

AD-A016 171

U. S. AERONAUTICAL L-BAND SATELLITE TECHNOLOGY TEST  
PROGRAM

E. H. Schroeder, et al

Boeing Commercial Airplane Company

Prepared for:

Transportation Systems Center  
Federal Aviation Administration

June 1975

DISTRIBUTED BY:



**Best  
Available  
Copy**

303139

Report No. FAA-RD-75-111

## U.S. AERONAUTICAL L-BAND SATELLITE TECHNOLOGY TEST PROGRAM

### Interim Test Results

E. H. Schroeder      R. W. Sutton  
A. D. Thompson      C. J. Kuo  
C. V. Paulson      I. R. Reese  
S. G. Wilson

1  
2  
3  
4  
5  
6  
7  
8  
9  
AD-A161-2



D D C  
RECORDED  
OCT 28 1975  
REGULATED  
B

June 1975

### INTERIM REPORT

Document is available to the public through the  
National Technical Information Service,  
Springfield, Virginia 22161

U.S. DEPARTMENT OF TRANSPORTATION  
FEDERAL AVIATION ADMINISTRATION  
Systems Research and Development Service  
Washington DC 20591

Reproduced by  
NATIONAL TECHNICAL  
INFORMATION SERVICE  
U.S. Department of Commerce  
Springfield, VA 22151

**NOTICE**

This document is disseminated under the sponsorship of the Department of Transportation in the interest of information exchange. The United States Government assumes no liability for its contents or use thereof.

**NOTICE**

The United States Government does not endorse products or manufacturers. Trade or manufacturers' names appear herein solely because they are considered essential to the object of this report.

ACCESSION NO.	
DTIB	<input checked="" type="checkbox"/> DATA SECTION
DCC	<input type="checkbox"/> DATA SOURCE
DATA CENTER	<input type="checkbox"/>
JULY 1984	
DW	
DISTRIBUTION, AVAILABILITY CODES	
DATA	MAIL, RDG OR SPECIAL
DATA	DATA
DATA	DATA

## TECHNICAL REPORT STANDARD TITLE PAGE

1 Report No <b>FAA-RD-75-111</b>	2 Government Accession No	3 Recipient's Catalog No	
4 Title and Subtitle <b>U.S. AERONAUTICAL L-BAND SATELLITE TECHNOLOGY TEST PROGRAM</b> Interim Test Results		5 Report Date <b>June 1975</b>	6 Performing Organization Code
7 Author(s) <b>E.H. Schroeder, R.W. Sutton, A.D. Thompson, C.V. Paulson, S.G. Wilson, C.J. Kuo, and I.R. Reese</b>		8 Performing Organization Report No <b>DOT-TSC-FAA-75-18</b>	
9 Performing Organization Name and Address The Boeing Commercial Airplane Company* P.O. Box 3707 Seattle WA 98124		10 Work Unit No <b>FA511/R6153</b>	11 Contract or Grant No <b>DOT-TSC-707</b>
12 Sponsoring Agency Name and Address <b>U.S. Department of Transportation Federal Aviation Administration Systems Research and Development Service Washington D.C. 20591</b>		13 Type of Report and Period Covered <b>Interim Report Dec. 1, 1974/June 1, 1975</b>	
15 Supplementary Notes U.S. Department of Transportation Transportation Systems Center Kendall Square		14 Sponsoring Agency Code	
*Under contract to: <b>Cambridge MA 02142</b>			
16 Abstract    The U.S. Aeronautical L-Band satellite test program was performed between September 1974 and April 1975 as part of an international ATS-6 L-Band satellite test program. The U.S. program consisted of both technology and ATC communications demonstration tests. Tests were in support of the aeronautical satellite (AEROSAT) program to collect satellite-aircraft signal propagation data, evaluate L-Band avionics hardware designs and perform preliminary satellite voice and data communications demonstration tests. All tests were conducted between an FAA KC-135 aircraft and the NASA-Rosman ground station via the geostationary ATS-6 satellite. This report presents data on the U.S. technology tests. The ATC demonstration test results will be presented by the FAA.			
<p>The technology tests were comprised of multipath channel characterization tests; modem tests of voice, data, and ranging; and aircraft antenna tests. Multipath results include delay-Doppler scatter function characteristics and calculations of spectra, spreads and autocorrelations for both over-ocean and CONUS multipath. Comparison of sample results with model prediction is given. Voice modem intelligibility scores, digital data bit error rates and ranging modem performance are presented parametrically as functions of <math>C/N_0</math> and S/I. Experimentally derived gain and multipath rejection performance data are given for the slot-dipoles, phased array, patch, and crossed-slot antennas for various aircraft/satellite geometries.</p>			
17 Key Words <b>Satellite communications, AEROSAT, multipath, delay-Doppler scatter function, modem evaluation, voice intelligibility, bit error rates, ranging, antennas, phased array, slot dipoles, L-band, ATS-6 satellite</b>	18 Distribution Statement Document is available to the public through the National Technical Information Service, Springfield Virginia 22161		
<b>PRICES SUBJECT TO CHANGE</b>			
19 Security Classif. (of this report) <b>Unclassified</b>	20 Security Classif. (of this page) <b>Unclassified</b>	21 No of Pages <b>174</b>	22 Price <b>\$ 6.25</b>

## PREFACE

Aeronautical tests were conducted by the U.S. Department of Transportation as part of the International ATS-6 L-Band Experiment. All tests were conducted between an FAA KC-135 airplane and the NASA/Rosman ground station via the geostationary ATS-6 satellite. Approximately 135 hours of flight testing were performed over a 7-month period starting September 1974 and ending April, 1975. Tests included Satellite Aeronautical Channel Prober (SACP) multipath characterization, evaluation of voice, digital data and ranging modems, and evaluations of various aircraft L-Band antennas. Results provide data for the evaluation of advanced system concepts and hardware applicable to the design of future satellite-based air traffic control systems. In addition, in support of the DOT/Federal Aviation Administration, aeronautical ATC demonstration tests were conducted to gain experience with satellite ATC systems as a prelude to the International Aeronautical Satellite AFROSAT program.

This interim report presents test results of the ATS-6 Aeronautical Technology tests. The FAA ATS-6 ATC Demonstration tests are reported elsewhere. Technology test conclusions are presented based on representative quantities of reduced data.

The U.S. ATS-6 program is under the direction of the Federal Aviation Administration, Systems Research and Development Service (SRDS), Satellite Branch. The U.S. aeronautical Technology tests were conducted by DOT/Transportation Systems Center supported by the Boeing Commercial Airplane Company under contract DOT-TSC-707.

The principal DOT/TSC contributing personnel are:

**Chief, Telecommunications**

System Branch:

J.M. Gutwein

Project Engineer:

R.G. Bland

Multipath:

L.A. Frasco

Modem Evaluation:

P.D. Engels, J.S. Golab, and P.Mauro

Antenna Tests:

L. Klein

The KC-135 flight operations were managed by Mr. Francis W. Jefferson who also provided auxiliary support at the FAA/National Aviation Facilities Experimental Center, Atlantic City, N.J.

## CONTENTS

	Page
<b>1.0 SUMMARY . . . . .</b>	<b>1</b>
1.1 Multipath Test . . . . .	1
1.2 Modem Evaluation Test . . . . .	2
1.3 Antenna Evaluation Test . . . . .	3
<b>2.0 GENERAL DESCRIPTION OF TEST PROGRAM . . . . .</b>	<b>5</b>
2.1 IOT/TSC Aeronautical Technology Tests . . . . .	5
2.2 KC-135 Terminal Equipment . . . . .	7
2.2.1 Airborne Terminal Function Description . . . . .	7
2.2.2 KC-135 L-Band Antennas . . . . .	7
2.2.3 Rosman Terminal Equipment . . . . .	12
<b>3.0 INDIVIDUAL AERONAUTICAL TECHNOLOGY TESTS . . . . .</b>	<b>15</b>
3.1 Multipath Test . . . . .	15
3.1.1 Test Objectives . . . . .	15
3.1.2 Multipath Test Configuration . . . . .	15
3.1.3 Multipath Test Geometry and Scenarios . . . . .	17
3.1.4 Multipath Data Acquisition Summary . . . . .	17
3.2 Modem Evaluation Test . . . . .	17
3.2.1 Test Objectives . . . . .	17
3.2.2 Modem Evaluation Test Configuration . . . . .	19
3.2.3 Transmission Formats and Modems Tested . . . . .	21
3.2.4 Modem Evaluation Data Acquisition Summary . . . . .	24
3.3 Antenna Evaluation Test . . . . .	26
3.3.1 Test Objectives . . . . .	26
3.3.2 Antenna Evaluation Test Configuration . . . . .	27
3.3.3 Antenna Test Geometries and Scenarios . . . . .	27
3.3.4 Data Acquisition Summary . . . . .	30
<b>4.0 MULTIPATH TEST RESULTS AND ANALYSIS . . . . .</b>	<b>31</b>
4.1 Multipath Data Analysis Procedures . . . . .	31
4.2 Oceanic Multipath Test Results . . . . .	35
4.2.1 Oceanic Scatter Function . . . . .	36
4.2.2 Integral and Fourier Operations on the Oceanic $S(\tau, \omega)$ Function . . . . .	37
4.2.3 Ocean Scatter Parameter Spread Values . . . . .	52
4.2.4 Comparison with Physical Optics Scatter Theory . . . . .	58
4.3 CONUS Multipath Test Results . . . . .	74
4.3.1 CONUS Delay Spectra Time History . . . . .	74
4.3.2 CONUS Scatter Function and Associated Integral and Fourier Relationships . . . . .	86
4.3.3 Airport Landing and Taxi Scatter Data . . . . .	98
4.3.4 Conclusions . . . . .	103

▼  
Previous page blank

## **CONTENTS (Continued)**

	<b>Page</b>
<b>5.0 MODEM EVALUATION TEST RESULTS AND ANALYSIS . . . . .</b>	<b>105</b>
5.1 Data Analysis Procedures . . . . .	105
5.1.1 Data Analysis Functional Flow . . . . .	105
5.1.2 C/N <sub>0</sub> and S/I Determination . . . . .	105
5.2 Voice Modem Test Results . . . . .	107
5.3 Digital Data Modem Test Results . . . . .	113
5.3.1 Reference Theoretical Performance Curves . . . . .	113
5.3.2 Type I Test Results . . . . .	115
5.3.3 Type II Test Results . . . . .	123
5.3.4 Block Error Statistics . . . . .	123
5.4 Ranging Modem Test Results and Analysis . . . . .	131
5.4.1 Data Analysis Procedures . . . . .	132
5.4.2 TSC Digital Ranging Modem . . . . .	132
5.4.3 NASA PLACE Ranging Modem . . . . .	134
<b>6.0 ANTENNA EVALUATION TEST RESULTS AND ANALYSIS . . . . .</b>	<b>137</b>
6.1 Data Analysis Procedures . . . . .	137
6.1.1 Bearing and Elevation Angles . . . . .	137
6.1.2 Antenna Gain Calculation . . . . .	137
6.1.3 Multipath Rejection Ratio Calculation . . . . .	138
6.2 Antenna Test Results . . . . .	138
6.2.1 Slot-Dipole Antenna . . . . .	138
6.2.2 Phased Array Antenna . . . . .	145
6.2.3 Patch Antenna . . . . .	151
6.2.4 Crossed-Slot Antenna . . . . .	154
<b>REFERENCES . . . . .</b>	<b>157</b>
<b>REPORT OF INVENTIONS APPENDIX . . . . .</b>	<b>159</b>

## FIGURES

	<b>Page</b>
<b>2-1</b> DOT/TSC U.S. Aeronautical Technology Test Configuration . . . . .	6
<b>2-2</b> KC-135 Terminal Block Diagram . . . . .	7
<b>2-3</b> KC-135 Antenna Locations . . . . .	11
<b>2-4</b> Rosman U.S. Aeronautical Terminal Block Diagram . . . . .	13
<b>3-1</b> Simplified KC-135 Terminal for Multipath Test . . . . .	16
<b>3-2</b> Simplified KC-135 Terminal for Modem Evaluation Test . . . . .	20
<b>3-3</b> DOT/TSC ATS-6 Voice Tape Composition . . . . .	23
<b>3-4</b> Simplified KC-135 Terminal for Antenna Evaluation Test . . . . .	28
<b>3-5</b> Antenna Evaluation Test Geometry . . . . .	29
<b>4-1</b> Data Reduction and Analysis Functional Flow . . . . .	32
<b>4-2</b> Multipath Algorithm Execution Sequence . . . . .	33
<b>4-3</b> $S(\tau, \omega)$ - Horizontal Polarization, In-plane Geometry . . . . .	38
<b>4-4</b> $S(\tau, \omega)$ - Horizontal Polarization, 45° Heading . . . . .	39
<b>4-5</b> $S(\tau, \omega)$ - Horizontal Polarization, Cross-plane Geometry . . . . .	40
<b>4-6</b> $S(\tau, \omega)$ - Vertical Polarization, In-plane Geometry . . . . .	41
<b>4-7</b> Spectra and Autocorrelation Parameters - Horizontal Polarization, In-plane Geometry . . . . .	42
<b>4-8</b> Spectra and Autocorrelation Parameters - Horizontal Polarization, 45° Heading . . . . .	44
<b>4-9</b> Spectra and Autocorrelation Parameters - Horizontal Polarization, Cross-plane Geometry . . . . .	46
<b>4-10</b> Spectra and Autocorrelation Parameters - Vertical Polarization, In-plane Geometry . . . . .	48
<b>4-11</b> Oceanic RMS Total Scatter Coefficients . . . . .	51
<b>4-12</b> 3-dB Oceanic Scatter Doppler Spread . . . . .	53
<b>4-13</b> Oceanic Scatter Delay Spread . . . . .	55
<b>4-14</b> Oceanic Scatter Coherence Bandwidth . . . . .	57
<b>4-15</b> 3-dB Oceanic Scatter Decorrelation Time . . . . .	59
<b>4-16</b> Model Predicted Oceanic Scatter Parameters - Horizontal Polarization, In-plane Geometry . . . . .	61
<b>4-17</b> Model Predicted Oceanic Scatter Parameters - Horizontal Polarization, 45° Heading . . . . .	64
<b>4-18</b> Model Predicted Oceanic Scatter Parameters - Horizontal Polarization, Cross-plane Geometry . . . . .	67
<b>4-19</b> Model Predicted Oceanic Scatter Parameters - Vertical Polarization, In-plane Geometry . . . . .	70
<b>4-20</b> Specular Point Overlay Leg FG February 20, 1975 . . . . .	75
<b>4-21</b> Delay Spectra Time History - February 20, 1975, Leg FG, Horizontal Polarization . . . . .	76
<b>4-22</b> Delay Spectra Time History - February 20, 1975, Leg FG, Vertical Polarization . . . . .	84
<b>4-23</b> Delay Spectra Time History, September 19, 1974 Lower New York Bay . . . . .	85
<b>4-24</b> CONUS Scatter Channel Parameters - February 19, 1975, Vertical Polarization . . . . .	87

## FIGURES (Continued)

	Page
<b>4-25 CONUS Scatter Channel Parameters - February 18, 1975, Horizontal Polarization . . . . .</b>	<b>89</b>
<b>4-26 CONUS Scatter Channel Parameters - February 19, 1975, Vertical Polarization . . . . .</b>	<b>91</b>
<b>4-27 CONUS Scatter Channel Parameters - February 20, 1975, Horizontal Polarization . . . . .</b>	<b>93</b>
<b>4-28 CONUS Scatter Channel Parameters - February 20, 1975, Horizontal Polarization . . . . .</b>	<b>95</b>
<b>4-29 Pilot's Log of Landing and Taxi at O'Hare, February 19, 1975 . . . . .</b>	<b>99</b>
<b>4-30 O'Hare Delay Spectra Time History . . . . .</b>	<b>100</b>
<b>4-31 O'Hare Delay Spectra (12-05-17 GMT) . . . . .</b>	<b>101</b>
<b>4-32 O'Hare Delay Spectra (12-06-24 GMT) . . . . .</b>	<b>102</b>
<b>5-1 Modem Evaluation DR&amp;A System Block Diagram . . . . .</b>	<b>106</b>
<b>5-2 Voice Modem Intelligibility Score, Voice Only Mode . . . . .</b>	<b>108</b>
<b>5-3 Voice Modem Intelligibility Score, Voice Only Mode . . . . .</b>	<b>109</b>
<b>5-4 Voice Modem Intelligibility Score, Voice Only Mode . . . . .</b>	<b>110</b>
<b>5-5 Voice Modem Intelligibility Score, Hybrid Mode . . . . .</b>	<b>111</b>
<b>5-6 Voice Modem Intelligibility Score, Voice Only Mode . . . . .</b>	<b>112</b>
<b>5-7 BER Performance, NASA DECPSK Demodulator . . . . .</b>	<b>116</b>
<b>5-8 BER Performance, Hybrid Number 1 Demodulator . . . . .</b>	<b>117</b>
<b>5-9 BER Performance, Hybrid Number 2 Demodulator . . . . .</b>	<b>118</b>
<b>5-10 BER Performance, CPSK Demodulator . . . . .</b>	<b>119</b>
<b>5-11 BER Performance, DPSK Demodulator . . . . .</b>	<b>120</b>
<b>5-12 BER Performance, Hybrid Number 1 Demodulator, Hybrid Mode . . . . .</b>	<b>121</b>
<b>5-13 BER Performance, Hybrid Number 2 Demodulator, Hybrid Mode . . . . .</b>	<b>122</b>
<b>5-14 BER Performance, NASA DECPSK Demodulator . . . . .</b>	<b>124</b>
<b>5-15 BER Performance, Hybrid Number 1 Demodulator . . . . .</b>	<b>125</b>
<b>5-16 BER Performance, Hybrid Number 2 Demodulator . . . . .</b>	<b>126</b>
<b>5-17 BER Performance, CPSK Demodulator . . . . .</b>	<b>127</b>
<b>5-18 BER Performance, DPSK Demodulator . . . . .</b>	<b>128</b>
<b>5-19 Type I Block Error Histograms . . . . .</b>	<b>129</b>
<b>5-20 Type II Block Error Histograms . . . . .</b>	<b>130</b>
<b>5-21 RMS Error Performance, TSC Ranging Modem . . . . .</b>	<b>133</b>
<b>5-22 RMS Error Performance, TSC Ranging Modem . . . . .</b>	<b>135</b>
<b>6-1 Gain and S/I, Slot Dipole Antennas, April 1, 1975 . . . . .</b>	<b>139</b>
<b>6-2 Gain and S/I, Slot Dipole Antennas, March 25, 1975 . . . . .</b>	<b>142</b>
<b>6-3 Gain and S/I, Slot Dipole Antennas, November 21, 1974 . . . . .</b>	<b>143</b>
<b>6-4 Aircraft Heading, Pitch and Roll Data, November 21, 1974 . . . . .</b>	<b>144</b>
<b>6-5 Slot-Dipole System Composite Gain at 20° Elevation . . . . .</b>	<b>146</b>
<b>6-6 Gain and S/I, Slot Dipole Antennas, September 24, 1974 . . . . .</b>	<b>147</b>

## **FIGURES (Continued)**

	<b>Page</b>
6-7 Phased Array Gain Data for "Straight-Line" Flight Segments . . . . .	148
6-8 Gain and S/I, Phased Array, September 24, 1974 . . . . .	150
6-9 Gain and S/I, Phased Array, November 21, 1974 . . . . .	152
6-10 Gain and S/I, Patch Antenna, November 21, 1974 . . . . .	153
6-11 Gain and S/I, Crossed Slot, April 1, 1975 . . . . .	155
6-12 Gain and S/I, Crossed Slot, March 25, 1975 . . . . .	156

## **TABLES**

	<b>Page</b>
3-1 Typical Oceanic Multipath Test Scenario . . . . .	17
3-2 Multipath Data Acquisition Summary . . . . .	18
3-3 Modem Evaluation Transmission Formats . . . . .	21
3-4 Modem Evaluation Data Acquisition, Type I . . . . .	25
3-5 Modem Evaluation Data Acquisition, Type II . . . . .	26
3-6 Antenna Evaluation Data Acquisition . . . . .	30
4-1 Cross-Reference for Model and Measurement Comparison . . . . .	73
4-2 Emulated Oceanic Scatter Channel Spread and RMS Energy Values . . . . .	73
4-3 Example Spread Values for CONUS Multipath . . . . .	98
5-1 PLACE Ranging Modem Results . . . . .	136
6-1 Antenna Test Summary, Slot Dipole System . . . . .	140
6-2 Phased Array Antenna Gain Data . . . . .	149
6-3 Patch Antenna Gain Data . . . . .	151

## **ABBREVIATIONS AND SYMBOLS**

<b>SACP</b>	- Satellite aeronautical channel prober
<b>NBFM</b>	- narrowband frequency modulation
<b>C/N<sub>0</sub></b>	- ratio of unmodulated carrier power to noise power density, dB-Hz
<b>S/I</b>	- ratio of direct path signal power to multipath signal power, dB
<b>ADVM</b>	- adaptive delta voice modulation
<b>DECPSK</b>	- differentially-encoded coherent phase-shift-keying
<b>DPSK</b>	- differential phase-shift-keying
<b>PN</b>	- pseudo-noise
<b>FMP</b>	- forward multipath antenna
<b>LWSD, (RWSD)</b>	- left (right) wing slot dipole antenna
<b>PHA</b>	- phased array antenna
<b>PAT</b>	- patch antenna
<b>SMP</b>	- side-mounted multipath antenna
<b>LSD, (RSD)</b>	- left (right) slot dipole antenna
<b>QH</b>	- quad-helix antenna
<b>XLT</b>	- crossed-slot antenna
<b>LHC (RHC)</b>	- left-hand (right-hand) circular polarization
<b>S(<math>\tau, \omega</math>)</b>	- delay-Doppler scatter power spectral density function
<b>R(<math>\xi, \Omega</math>)</b>	- time-frequency correlation function
<b>D(<math>\omega</math>)</b>	- Doppler spectrum
<b>Q(<math>\tau</math>)</b>	- delay spectrum
<b><math>\Gamma</math></b>	- mean-square scatter coefficient (normalized reflected signal power)
<b><math>\sigma_{\text{slope}}</math></b>	- rms surface slope

## **ABBREVIATIONS AND SYMBOLS (Continued)**

<b><math>\delta</math></b>	- grazing angle
<b><math>\sigma_H</math></b>	- rms surface height
<b>P.B.</b>	- phonetically balanced
<b>BER</b>	- bit error rate
<b>E/N<sub>0</sub></b>	- ratio of energy per data bit to noise power density, dB
<b>B<sub>F</sub></b>	- one-sided $c^{-1}$ Doppler bandwidth
<b>B<sub>L</sub></b>	- loop bandwidth
<b>T</b>	- symbol period
<b>SCIM</b>	- speech communication index meter

## 1.0 SUMMARY

The U.S. Aeronautical Technology Tests were conducted by DOT/TSC as part of the Integrated ATS-6 L-Band Experiment. All tests were conducted between an FAA KC-135 airplane and the NASA/Rosman ground station via the geo-stationary ATS-6 satellite. Approximately 135 hours of flight testing were performed over a 7-month period ending April 1975. Tests included overocean and overland multipath channel characterization, evaluation of voice, digital data and ranging modems and evaluation of various aircraft L-band antennas. Results provide data for the evaluation of advanced system concepts and hardware applicable to the design of future satellite-based air traffic control systems.

### 1.1 MULTIPATH TEST

The overall test objective is to characterize the multipath sufficiently to allow design of both the signal structure and the hardware for aeronautical satellite applications. Acquired data are analyzed to obtain a detailed delay-Doppler characterization and to verify an ocean scatter model for various test geometries and signal polarizations. Wideband PN-PSK probing signals operating at chip rates of 1 to 10 MHz are transmitted from the KC-135 aircraft using selected antennas and transmission polarizations. After relay by ATS-6, the signals are received at Rosman, processed by the Satellite Aeronautical Channel Prober (SACP) receiver and recorded for off-line analysis. Overocean testing was conducted on eighteen occasions at elevation angles ranging between 3° and 35°. Six CONUS multipath tests were conducted over the U.S. and Canada.

For oceanic multipath the properties of the scatter function were found to be in general accord with predictions based upon the physical optics very-rough surface model. Numerical surface area integration of this model's vector formulation appears to closely predict the delay-Doppler distributed nature of the multipath returns. In contrast, a closed-form solution based upon "steepest descent" integration techniques fails to account for the assymetrical Doppler spectra associated with geometries other than cross-plane.

The mean square total scatter coefficient data for the horizontal and vertical polarization probes were shown to be roughly equivalent to the product of divergence factor and smooth earth Fresnel reflection coefficient. Doppler spreads from a low of 25 Hz to a high of 215 Hz (3-dB values) were observed and display a marked tendency to increase with an increase in grazing angle. No appreciable grazing angle dependence was apparent for the delay spread data which varied over a range from 0.35  $\mu$ sec to 1.5  $\mu$ sec. The time autocorrelation function spread displayed, as expected, an inverse grazing angle dependence to that of the Doppler data; it was characterized by a low of 1.5 msec and a high of 9 msec. Coherence bandwidths ranging from 100 kHz up to 380 kHz were measured with the higher values typically being associated (very weakly) with high grazing angles and vice versa.

An obvious characteristic of the overland CONUS scatter data is its high degree of signal structure non-stationarity. The signature of the channel delay-Doppler scatter function varies markedly with experiment time and was used to isolate periods of very low spreading, modest spreading, biased positional scatter, large irregular Doppler spectra return, and mixed scatter process return. Data gathered during the airport landing taxi sequence give preliminary

indications of (a) fairly large amplitude fluctuations of the energy received in the direct signal taps when using the crossed-slot antenna and (b) the absence of substantial multipath return arriving with delays greater than 0.2  $\mu$ sec with respect to the direct path signal.

## 1.2 MODEM EVALUATION TEST

The test objective is to evaluate the performance of various voice, digital data and ranging modems which represent candidate approaches for aeronautical satellite link applications. Type I modem evaluation tests used a selected operational aircraft antenna to acquire overocean performance data at elevation angles ranging from 10° to 30°. Type II tests employed the quad-helix for reception of the direct path signal and the side multipath antenna for reception of the sea-reflected multipath signal. After preamplification these were combined at RF in the desired power ratio to simulate an antenna with a specified S/I ratio. Tests spanned  $C/N_0$  values between 38 and 52 dB-Hz in combination with S/I values ranging from heavy multipath fading S/I = 3 dB to essentially non-fading conditions (S/I > 20 db).

All voice modems tested meet the Aerosat system requirement of 60 percent intelligibility for unrelated phonetically-balanced words at 43 db-Hz. The Hybrid modem No. 1 consistently scored highest at all  $C/N_0$  values and the NBFM modem tested usually scored lowest. Adaptive delta voice modulation (ADVM) performance with analog processing was intermediate between Hybrids No. 1 and 2. ADVM with digital processing performed well above 45 dB-Hz but degraded rapidly below 43 dB-Hz as expected. When operating in the combined voice and data mode, the performance of the two hybrid modems was degraded by at least 3 dB relative to the voice only mode. The intelligibility scores for Type II tests compare favorably with the Type I tests both in terms of absolute performance and relative performance between modems. Voice modem performance was not strongly sensitive to the multipath contamination. Even for S/I values as low as 3 dB, the Type II results do not differ greatly from those of the Type I tests.

An assessment of relative demodulator performance at 1200 bps during Type I digital data tests ranks Hybrid No. 1 first, followed in order by Hybrid No. 2, FAA CPSK, and NASA DECPKS. The performance of the Hybrid No. 1 demodulator in the data mode was typically 1 dB from theoretical for DECPKS. The S/I values calculated from the carrier detector data for Type I tests were usually 15 dB or higher. These levels of multipath interference would not be expected to cause significant performance degradation at 1200 bps data rates over the range of bit error rates tested. Consistent with this observation, none of the demodulators exhibited a tendency for BER performance to diverge from the theoretical relationship at the higher  $C/N_0$  values as would be expected if multipath interference were significant. When operating in the hybrid mode, Hybrid No. 1 appeared to suffer less than 3 dB degradation (relative to data only mode) at low  $C/N_0$  and more than 3 dB at high  $C/N_0$  while Hybrid No. 2 experienced roughly 3-dB degradation over the entire  $C/N_0$  range.

For the Type II digital data tests all demodulators demonstrated performance degradation due to multipath in general agreement with the shape of the reference curves. There was little discernible difference in performance between Hybrid No. 1, Hybrid No. 2 and FAA CPSK but the NASA DECPKS did not perform as well as the other three. The BER performance of the DPSK demodulator was superior to that of the DECPKS units at low S/I but this

advantage in absolute BER performance disappeared at S/I values above 9 dB. Block error histogram data shows that under Type I conditions DECP SK reveals a propensity for paired errors while DPSK produces primarily single errors. Under Type II multipath fading conditions the proportion of single errors made by DECP SK increased with decreasing S/I while single errors continued to dominate for DPSK.

The TSC digital ranging modem has two operating bandwidth capabilities; a wideband mode which uses a 156 kHz clock frequency and a narrowband mode with a 19 kHz clock. Experimental results generally showed improving performance with increasing C/N<sub>0</sub> as expected. Best performance was achieved for the wideband mode for which the Type I test one-way rms error relative to the reference trajectory was in the order of 30 meters at a link quality of 45 dB-Hz. This modem, however, experienced difficulty resolving range ambiguity, especially at S/I below 10 dB. The two-way rms error relative to the reference trajectory for the NASA PLACE ranging modem was typically between 250 and 350 meters for the limited data available (mostly Type II). The performance of this ranging system was not consistent when the forward link C/N<sub>0</sub> was less than 43 dB-Hz.

### 1.3 ANTENNA EVALUATION TEST

The objective of this test is to quantitatively evaluate performance of aircraft antennas which are candidates for aeronautical L-band satellite link applications. Data were acquired and analyzed to determine gain and S/I over a range of satellite elevation and relative bearing angles for two contrasting antenna approaches, namely, the selectable 3-element slot-dipole system and the phased array. A limited amount of similar data was acquired for the patch and crossed-slot antennas.

An experimental composite gain conic for the 3-element slot dipole system for an elevation angle of about 20° is given. The experimentally derived gains agree reasonably well with scale model antenna range data. The computed values of S/I as derived from carrier detector data were found to exceed 16 dB for all azimuthal angles and elevation (10° to 40°) angles tested. This result is in accord with the observed digital data modem performance during Type I tests.

A portion of the phased-array data was acquired using straight-line flight segments rather than circular paths because of the optimum beam selection dependency upon azimuthal angle. The data tends to be in general agreement with expectation. Antenna S/I values were found to exceed 20 dB for all test geometries. Analyzed data for selected circular path flights are also given.

The crossed-slot performance data reveals antenna gain approximately 6 dB lower than expected indicating a possible antenna malfunction. The S/I values generally exceeded 10 dB at a nominal elevation angle of 15°.

## **2.0 GENERAL DESCRIPTION OF TEST PROGRAM**

**The U.S. Aeronautical Tests are part of the Integrated ATS-6 L-Band Experiment (Reference 2-1). Participants in the integrated experiment included**

**NASA/Goddard Space Flight Center (GSFC)  
DOT/Transportation Systems Center (TSC)  
DOT/Federal Aviation Administration (FAA)  
DOT/U.S. Coast Guard (USCG)  
DOC/Maritime Administration  
European Space Research Organization (ESRO)  
Canadian Ministry of Transport and Department of Communications**

**The integrated experiment included both aeronautical and maritime tests conducted by DOT/TSC in cooperation with DOT/FAA and DOT/USCG. Other participants frequently performed their tests simultaneously using shared ATS-6 satellite test time and coordinated transmission formats.**

### **2.1 DOT/TSC AERONAUTICAL TECHNOLOGY TESTS**

**The U.S. Aeronautical Technology Tests conducted by DOT/TSC provide data for the evaluation of advanced system concepts and hardware applicable to the design of future satellite-based air traffic control systems. All testing is between the FAA KC-135 airplane and the NASA/Rosman ground station using the geostationary NASA ATS-6 satellite, as shown in Figure 2-1. Specific tests are**

- 1. Multipath Channel Characterization.** Pseudo-noise (PN) code modulated signals are transmitted from the KC-135 using several different antennas and various polarizations. After relay by ATS-6, the signals are received at Rosman, processed by the SACP equipments, recorded and are later analyzed to obtain a characterization of the multipath channel.
- 2. Modem Evaluation.** Several voice, digital data, ranging and hybrid voice/data modems are tested using signals transmitted from Rosman through ATS-6 to the aircraft. Modem demodulator outputs are recorded onboard the aircraft and analyzed to determine performance for various carrier-to-noise density ( $C/N_0$ ) and signal-to-multipath interference (S/I) ratios.
- 3. Antenna Evaluation.** A CW signal radiated by Rosman through ATS-6 is received by the various aircraft antennas under test. Data is recorded and analyzed to evaluate antenna gain and multipath rejection as a function of geometry.

**Two additional U.S. Aeronautical Tests were conducted by other participants. These are:**

- ATC Demonstration Test    DOT/FAA**
- Two-Satellite Position Determination    NASA/GSFC**

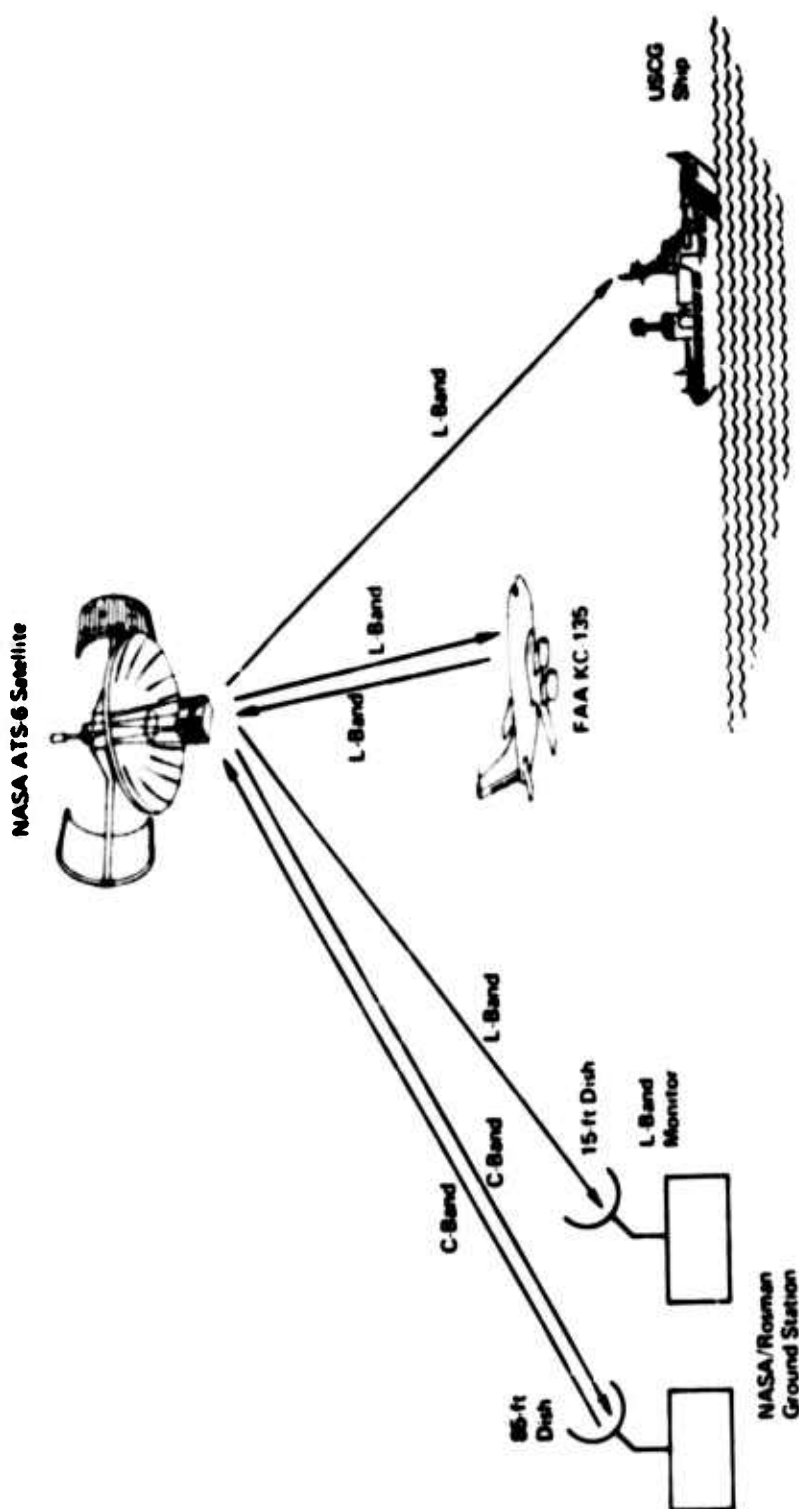


Figure 2.1.—DOT/TSC U.S. Aeronautical Technology Test Configuration

**Data acquired for these tests are being analyzed by the responsible participants. Detailed discussions of these two tests are not included in this report.**

Development of an overall flight test plan (Reference 2-2) necessitated consideration of requirements for each test, satellite antenna coverage and the various constraints of other participants. These constraints were best satisfied by spreading the tests over a 7-month period with each individual flight involving a mix of test types. A single flight for example, provided multipath, antenna, voice modem, data modem, and ranging modem tests. This has required a very flexible equipment configuration both on the aircraft and at Rosman so that the test modes could be changed with minimum delay.

Tests were conducted over 7 months ending April 3, 1975. The DOT/TSC Aeronautical Technology program acquired approximately 135 hours of flight test data during this period. Oceanic data were acquired over the North Atlantic at ATS-6 elevation angles between approximately 30° and 35°. CONUS data were acquired over various regions of the U.S. and Canada.

## **2.2 KC-135 TERMINAL EQUIPMENT**

A block diagram of the aircraft terminal showing the main signal flow paths is given in Figure 2-2. Seven racks in the aft section housed most of the equipment for modem evaluation, antenna evaluation and for system calibration. Equipment items for the multipath tests are contained in three racks located forward. Rack numbers and drawer locations of equipment items are indicated. The FAA ATC Demonstration data link terminal is not part of the Technology test instrumentation package but is included to show major interfaces.

### **2.2.1 AIRBORNE TERMINAL FUNCTION DESCRIPTION**

Distribution of L-band signals between the various antennas, preamplifiers, transmitters and receivers is performed by the Aft and Forward RF Control units. After preamplification, received L-band signals are down-translated to IF by the two receivers and are then tuned and distributed by the IF Tuning unit to the appropriate modem. Modem outputs, carrier detector data, time code and aircraft flight parameters are recorded by a 14-track instrumentation magnetic tape recorder. Multipath test parameters are recorded by a digital recording system. A chart recorder provides a test monitoring feature and yields a hard copy record of selected signals.

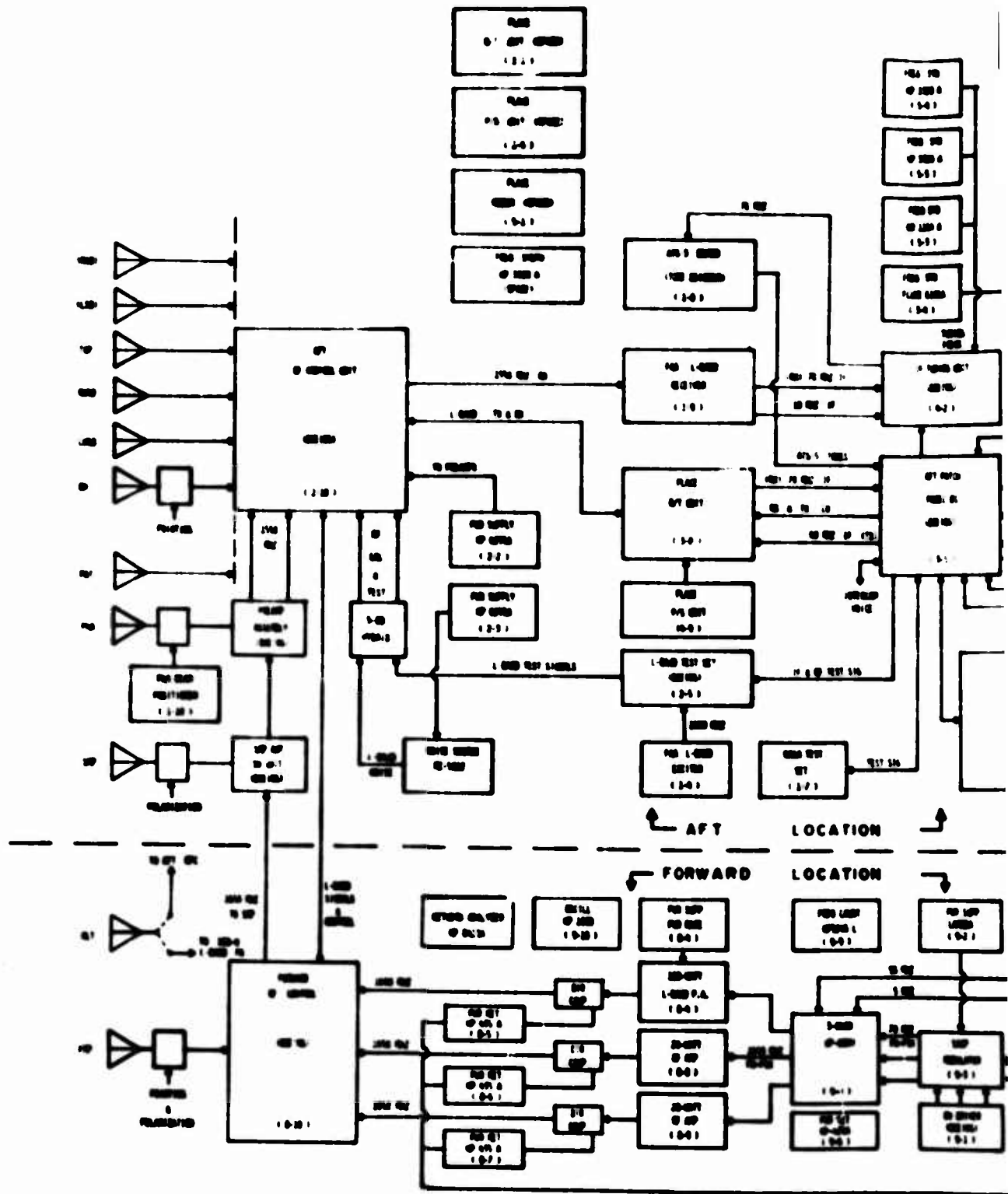
The terminal design incorporates a sophisticated test and calibration capability. A calibrated noise source allows the operating noise figure of all receiving systems to be measured. A composite L-band test signal simulating the ATS-6 and ATS-5 downlinks with appropriate 1200 bps digital data, ranging, NBFM voice and PLATE S&R modulations can be generated and injected into the receiving system inputs for test and calibration purposes.

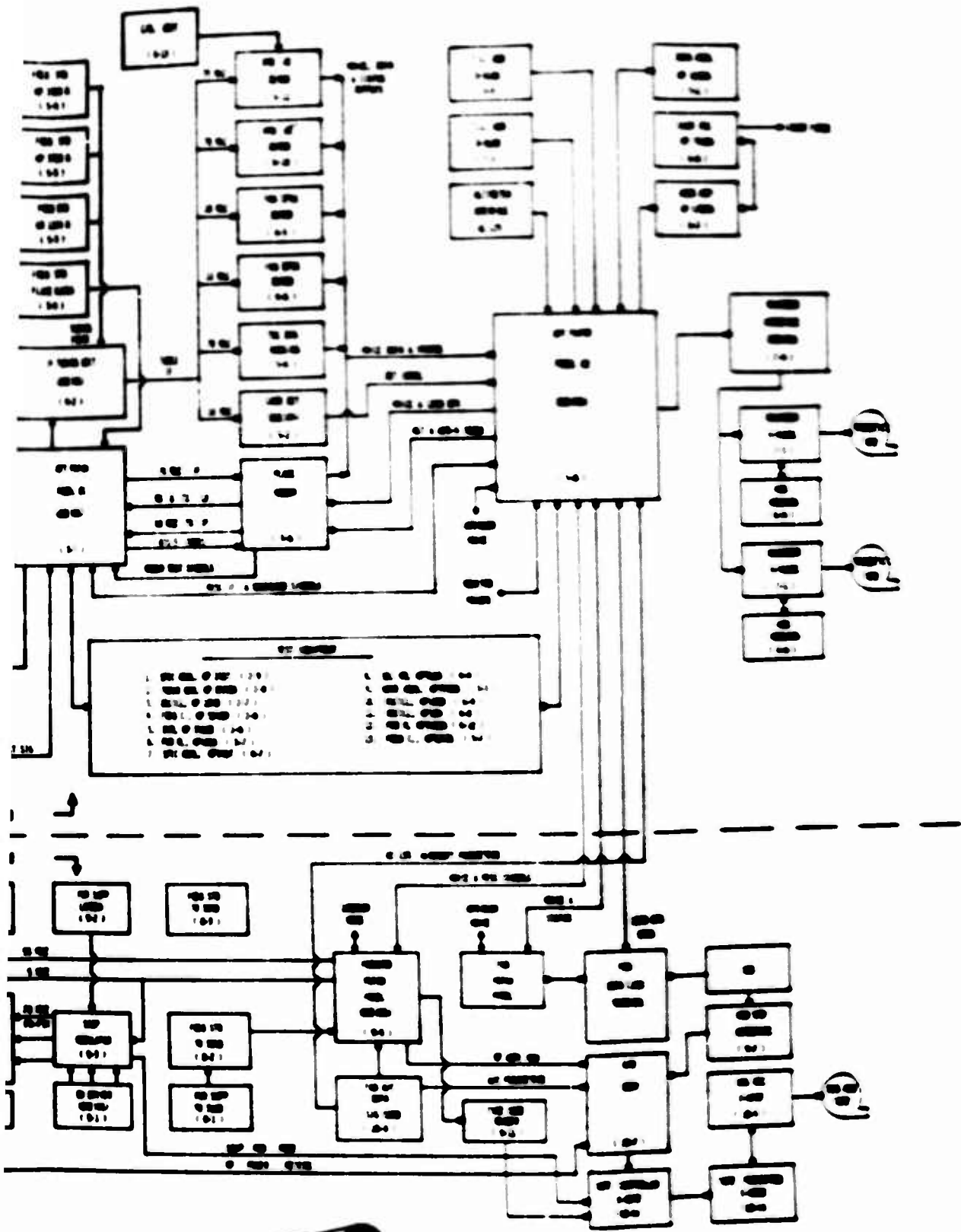
### **2.2.2 KC-135 L-BAND ANTENNAS**

The approximate locations of the L-band antennas used on the KC-135 test aircraft are shown in Figure 2-3. Major features of these antennas are summarized below. Unless otherwise noted, antenna polarization is right-hand circular.

1. **Front Multipath Antenna (FMP):** Gain is approximately 10 dB and polarization is selectable between right-hand circular (RHC), left-hand circular (LHC) and dual linear (the horizontal and vertical polarization ports are simultaneously accessible on separate transmission lines). It is mechanically steerable downward from the horizon in elevation and to both right and left of the aircraft nose in azimuth.
2. **3-Antenna Slot-Dipole System (LWSD, RWSD, TOP):** This system consists of three flush-mounted antennas. Side coverage is provided by the left (LWSD) and right (RWSD) side antennas mounted in the upper wing/body (wing root) fairing areas at station 766. High elevation angle and fore/aft coverage is provided by a third antenna (TOP) mounted near the top centerline at station 805.
3. **Phased Array (PHA):** The antenna is mounted on the right side of the aircraft at Station 420, 41° degrees down from the top centerline. With this location the main coverage is approximately broadside to the airplane. The beam is fixed in azimuth and is electronically steerable in elevation in increments of about 10°.
4. **Patch Antenna (PAT):** Because of its low power handling capability this antenna is used only for receiving. It is located near the top centerline of the fuselage at Station 270 to provide forward "fill-in" coverage for the RSD/LSD antenna system described in (6) below.
5. **Side-Mounted Multipath (SMP):** This antenna, located at Station 804 and waterline 150, has a fixed beam which points approximately 15° below the horizon and 10° aft of broadside. Gain is about 13 dB and polarization is selectable between dual linear, RHC or LHC.
6. **Right/Left Slot Dipoles (RSD, LSD):** These antennas are mounted at Station 1135 approximately 35° down from the top centerline as shown. Due to the more favorable location of the LWSD/RWSD/TOP slot-dipoles, the RSD/LSD antennas were used primarily as backups and for auxiliary transmission/reception functions.
7. **Quad-Helix (QH):** This antenna is mechanically steerable to provide coverage throughout the forward region of the upper hemisphere and provides about 15 dB gain towards the satellite.
8. **Crossed-Slot (XLT):** Also referred to as an orthogonal mode cavity, this antenna was installed at Station 746 near the top centerline specifically for acquisition of CONUS multipath data during the February 1975 tests.

The front multipath antenna and the LWSD/RWSD/TOP slot-dipoles were furnished by Boeing and installed specifically for this test program. The phased array and patch were furnished and installed by Ball Bros. Detailed description and evaluation of these antennas may be found in Refs. 2-3 to 2-5. The side multipath, RSD/LSD slot dipoles and quad helix were developed and installed by Boeing for the earlier FAA ATS-5 tests (Ref. 2-6). The crossed-slot was furnished by Boeing under an earlier contract (Ref. 2-7) and was first used by DOT/TSC for their balloon test program.





Reproduced from  
best available copy.

Figure 22 - KC-135 Terminal Block Diagram

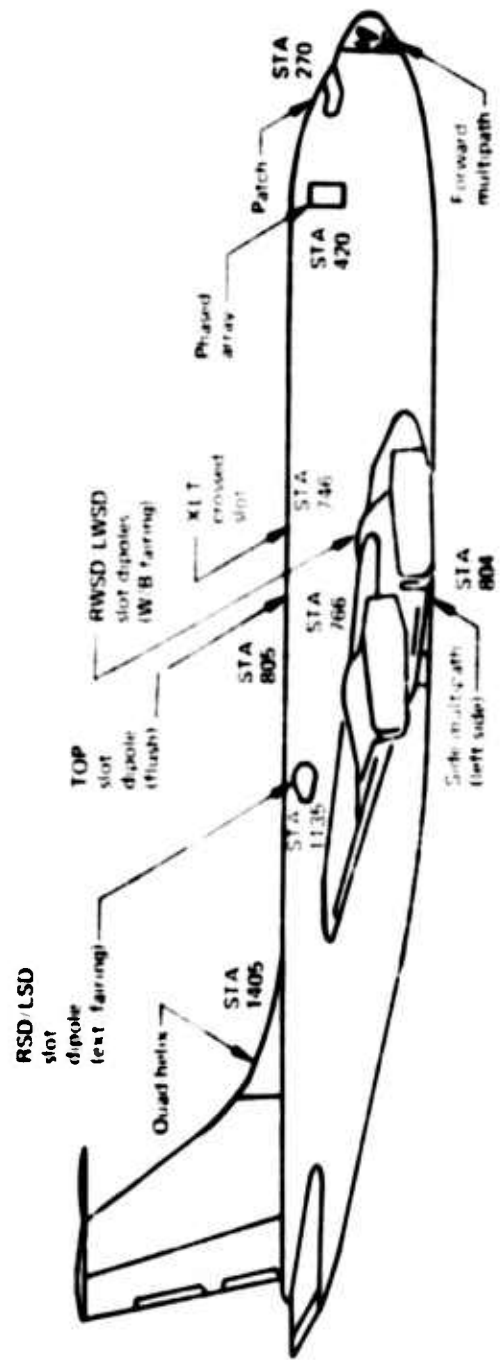


Figure 2.3 - KC-135 Antenna Locations

Preceding page blank

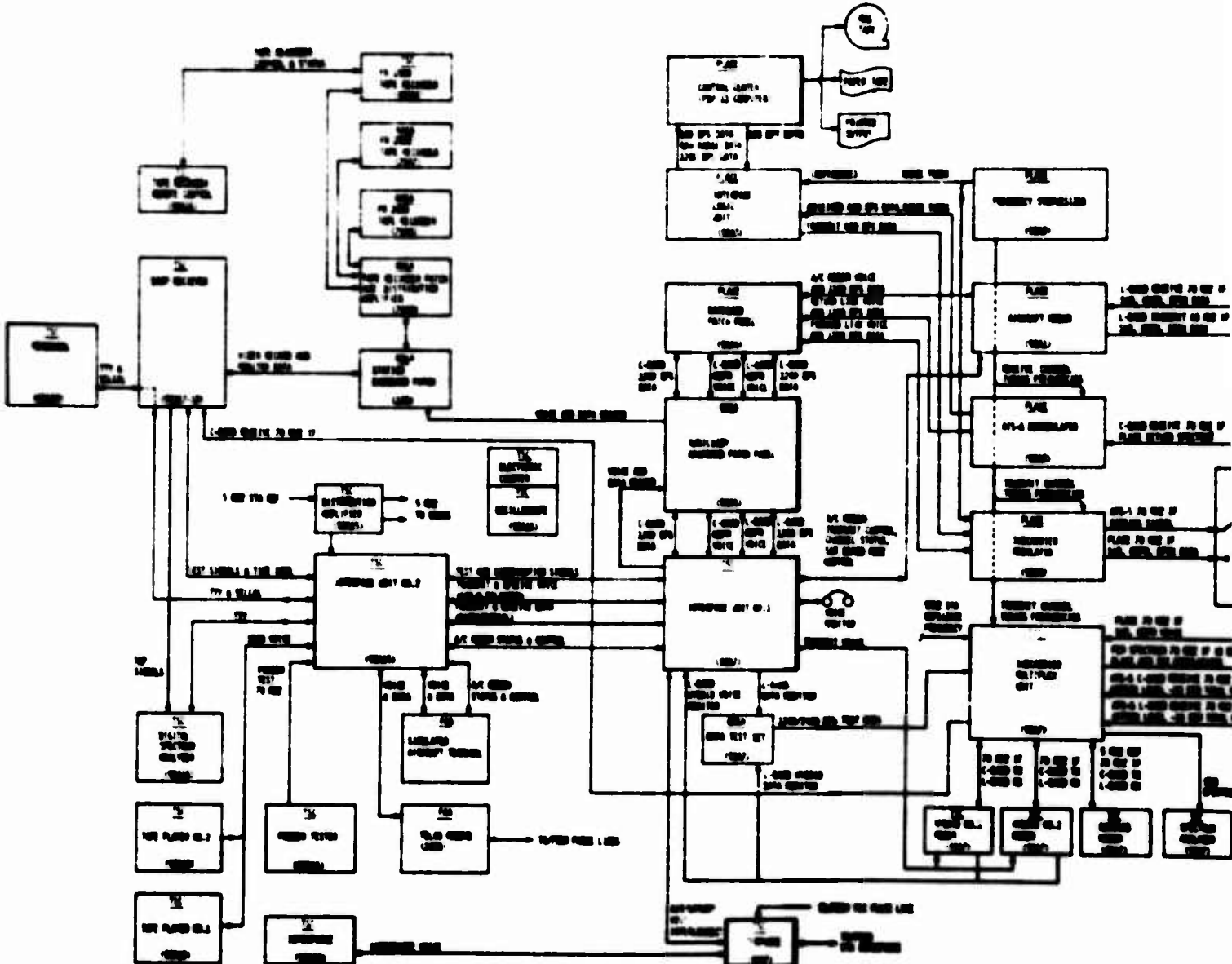
### **2.3 ROSMAN TERMINAL EQUIPMENT**

**A functional block diagram of U.S. Aeronautical L-Band Experiment equipment is shown in Figure 2-4. This diagram indicates equipments, functions, signal flow paths, signal types and equipment rack locations.**

**Baseband test signals for voice, digital data and ranging modem evaluation are generated locally at Rosman within the TSC and other experimenter equipment. Baseband test signals for the FAA ATC Demonstration tests are generated at the remote FAA NAFEC facility and received at the station via telephone. All test signals are modulated onto 70 MHz IF carriers by TSC test modems or by the PLACE Ground Equipment (PGE). The TSC Sub-carrier Multiplex Unit (SMU) translates and combines the subcarriers to form the frequency division multiplex (FDM) spectrum for transmission to ATS-6 via the Station C-Band transmitter and 85-foot antenna. For the NASA 2-Satellite Position Determination tests the PLACE Surveillance and Ranging (S&R) signals and similar signals for the ATS-5 link are generated in the PGE. These modulations are transmitted to ATS-5 and ATS-6 for relay to the aircraft.**

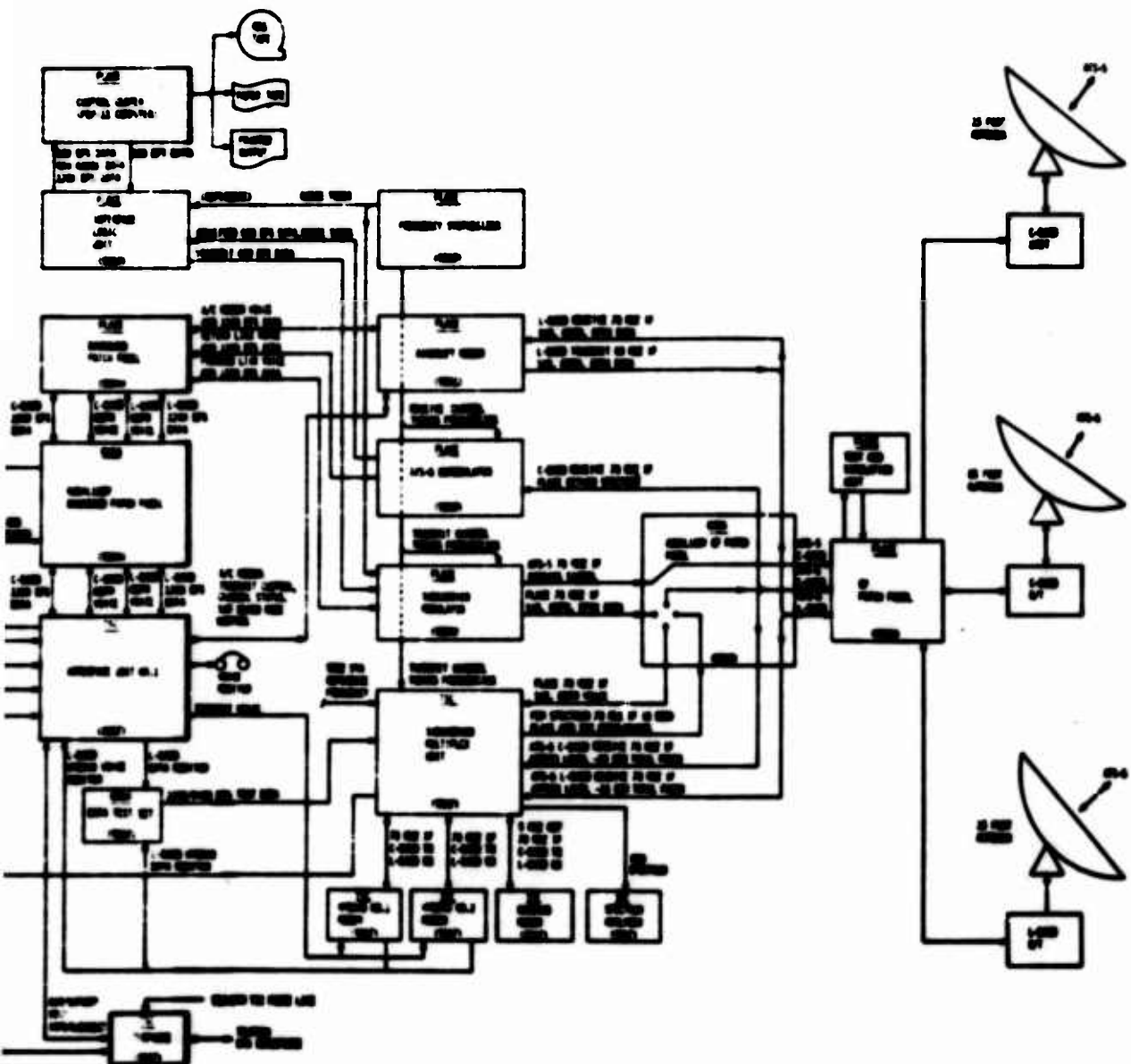
**Return-link signals received from ATS-6 via the 85-foot antenna and C-Band receiver are down-translated to the 70 MHz IF and distributed to the PGE and to the TSC experiment equipment for demodulation. The return-link S&R channel is demodulated by the PGE and the baseband voice and data are distributed to the experimenters for recording, for transmission to remote locations via telephone or for test coordination. When the multipath prober test is in progress the received signal is down converted to IF and routed to the SACP receiver where it is demodulated, processed and formatted along with time code for recording on wideband analog tape. The TSC Ampex FR-1900 and the Station Ampex FR-2000 tape recorders are used to record these signals.**

**In addition to the C-band operations described, transmission and reception of forward and return link signals at L-band to/from ATS-6 are provided by the station L-band receiver/transmitter and a 15-foot antenna. The received signal is down-converted to a 70 MHz IF and is distributed to the PGE and experimenter equipment. The PGE contains a PLACE aircraft modem that can be used as an L-band forward-link monitor or a simulated aircraft terminal. This 70 MHz signal is also tuned and routed to the TSC ranging and hybrid modems to monitor the L-band forward link. A spectrum analyzer in TSC rack 90A7 is used to monitor the 70 MHz IF signals on the ATS-6 forward link at either the C-band transmitter input or the L-band receiver output.**



Reproduced from  
best available copy.

*Figure 2-4.—Rosman*



Reproduced from  
best available copy.

Figure 2-4.—Rosman U.S. Aeronautical Terminal Block Diagram

## **3.0 INDIVIDUAL AERONAUTICAL TECHNOLOGY TESTS**

**This section provides a brief description of the multipath, modem evaluation and antenna evaluation technology tests.**

### **3.1 MULTIPATH TEST**

#### **3.1.1 TEST OBJECTIVES**

**For mobile communication systems operating in the vicinity of random rough surfaces, the received electromagnetic signal consists of the superposition of transmitted signal replicas having random amplitudes, time delays and Doppler shifts. The effects of such multipath should be accounted for in the system design of an aeronautical satellite communication system. The overall objective is to characterize the multipath sufficiently to allow design of both the signal structure and the hardware for aeronautical satellite applications. Specific objectives are to:**

- 1. Acquire and analyze multipath data to obtain a detailed delay-Doppler characterization for various test geometries, polarizations, sea states and terrain states.**
- 2. Analyze data to evaluate and verify the ocean scatter model.**

**Validation of a laboratory multipath channel simulator using multipath data acquired by SACP has also been identified as a DOT/TSC goal. Analysis of simulator requirements and processing of multipath data for simulator applications are planned future efforts to be conducted by DOT/TSC.**

#### **3.1.2 MULTIPATH TEST CONFIGURATION**

**A functional block diagram for the multipath test is shown in Figure 3-1. The SACP probe modulator generates three PN-PSK 70 MHz IF signals which are identical except for preset time delays between the PN codes. The triple up-converter coherently translates the three signals to 1650 MHz to drive the three multipath transmitters. Each transmitter is connected to an L-band antenna. The reference signal (with code delay,  $T_0$ ) is transmitted directly to ATS-6 via the quad helix antenna. The other two PN-PSK signals (with code delays,  $T_1$  and  $T_2$ ) drive the horizontal and vertical polarization arrays of the selected multipath antenna. If desired, a single transmitter may be used with the 1 WSD/RWSD/TOP slot dipoles, crossed-slot antenna (not shown) or with the FMP antenna operating in one of its circular polarization modes. Power monitors allow the transmitted RF power levels to be recorded. A digital recorder with A-D conversion records the transmitted power levels and other pertinent aircraft parameters.**

**At the receiving site at Rosman, the reference carrier frequency and PN code timing are established by acquiring and tracking the reference direct path signal. The reference carrier and code are used to demodulate the horizontally and vertically polarized signals in the 112 complex taps of the SACP receiver. Tap outputs are formatted and recorded on wideband (2 MHz) analog recorders for subsequent data analysis.**

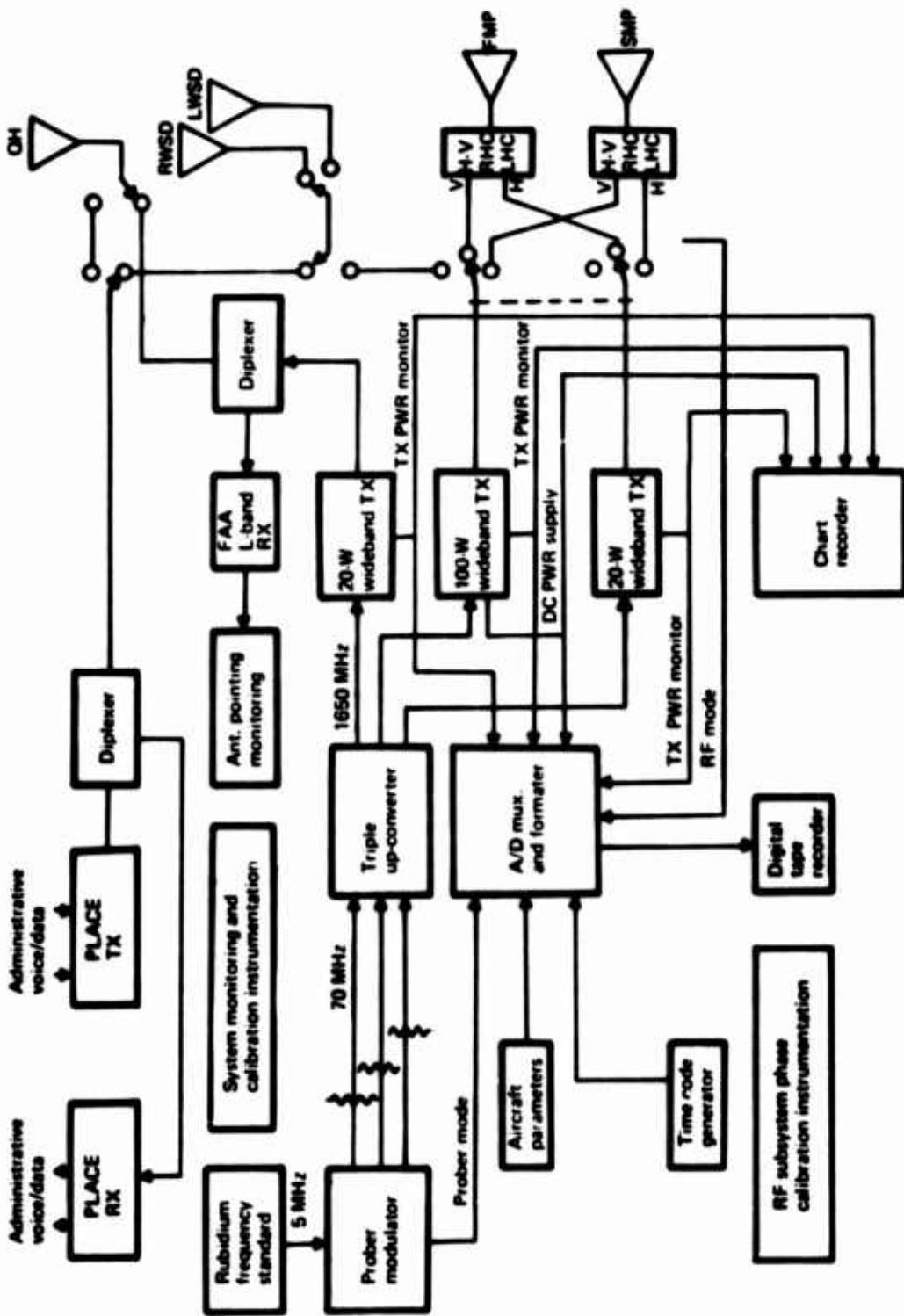


Figure 3-1.—Simplified KC-135 Terminal for Multipath Test

### 3.1.3 MULTIPATH TEST GEOMETRY AND SCENARIOS

A typical oceanic multipath test scenario, as shown in Table 3-1, consists of 4 legs with test headings directly towards, 45° offset and 90° offset relative to the ATS-6 subsatellite direction. The reference direct path signals are always transmitted via the quad helix antenna. The multipath test signals are usually transmitted via the forward multipath antenna. A limited amount of data has been acquired with the TOP and LWSD antennas. Code chip rates are typically either 5 MHz or 10 MHz and the maximum code length of 1023 bits has been used for all tests.

CONUS flight legs are typically of 20 minutes duration with test headings either directly towards or 90° offset relative to ATS-6. Enroute data was usually acquired with the forward multipath antenna. During the February 1975 tests, the crossed-slot antenna was used to acquire data during approach, landing and taxi phases at three airports: Namao (Edmonton, Alta.), O'Hare (Chicago) and JFK (New York) on three successive days.

*Table 3-1.- Typical Oceanic Multipath Test Scenario*

Leg	Heading (Relative to ATS-6)	Relative time	Direct antenna	Test antenna				Other parameters
				Type	Polarization	Az	Elev	
1	0°	0+00	QH	FMP	H&V	0°	-35°	$T_1=127$ $T_2=490$
		+18		TOP	RHC	--	--	
2	45°	0+18		FMP	H&V	315°	-35°	$CR=5\text{ MHz}$ $CL=1023$
		+27		LWSD	RHC	--	--	
3	0°	0+32		FMP	H&V	0°	0°	all legs
		+41		FMP	H&V	0°	-35°	
4	270°	0+46		RWSD	RHC	--	--	
		+55		FMP	H&V	90°	-35°	

### 3.1.4 MULTIPATH DATA ACQUISITION SUMMARY

The multipath flight tests actually conducted are listed in Table 3-2. Cancellations are not shown. Sea state data was not acquired as part of the Contractual effort described by this report. A limited amount of sea state buoy data was acquired by the TSC/USCG during the March 1975 tests. This data is not yet analyzed.

## 3.2 MODEM EVALUATION TEST

### 3.2.1 TEST OBJECTIVES

Various techniques are being considered for the transmission of voice, digital data and ranging/surveillance signals to and from aircraft via satellites. The objective of these tests is to evaluate

Table 3-2.-Multipath Data Acquisition Summary

Date	Elev. angle	Test duration hrs.	Remarks
<b>A. Oceanic</b>			
9-24-4	30°	1+00	Nominal
10-24-4	18° to 23°	1+00	Nominal
10-28-4	8° to 12°	1+00	Nominal
11-14-4	3° to 8°	1+00	
11-15-4	8° to 13°	1+00	
11-16-4	3° to 8°	1+00	
11-21-4	19° to 23°	1+00	
1-23-5	3° to 8°	1+00	Partial Data Acqn, Faulty 100-W PA
1-27-5	8° to 13°	1+00	Nominal
1-28-5	19° to 23°	1+20	Aircraft Maneuvers due to Weather Avoidance
1-30-5	3° to 8°	1+00	Nominal
2-27-5	30°	1+20	Nominal
3-26-5	15°	0+20	TOP Ant Only
3-27-5	10° to 15°	1+00	FMP Antenna Fault
3-28-5	3° to 8°	1+00	FMP Antenna Fault
3-31-5	10° to 15°	1+00	Nominal
4-02-5	7° to 11°	1+00	Nominal
4-03-5	16° to 21°	1+00	Nominal
		18 hrs.	Oceanic Test Hours
<b>B. CONUS</b>			
9-19-4	30° to 45°	4+00	Eastern U.S., Nominal
10-30-4	30° to 45°	4+00	Eastern U.S., Nominal
11-02-4*	30° to 45°	4+00	Northwest U.S., 50% of Data Acquired.
2-18-5*	16° to 27°	4+30	NW Canada to Edmonton, 50% of data acquired.
2-19-5*	27° to 40°	4+30	Central Canada to O'Hare, Nominal
2-20-5*	28° to 37°	4+30	N. Quebec to JFK, Nominal
		25.5 hrs.	CONUS Test Hours

\* Acquired data with both fan and pencil beams of ATS-6

the performance of various voice, digital data and ranging modems which represent candidate approaches for this application. Specific objectives are:

1. To evaluate modem performance over a range of flight geometries and  $C/N_0$  using the candidate operational LWSD/RWSD/TOP switchable slot-dipole antenna system.
2. To evaluate modem performance parametrically in terms of  $C/N_0$  and S/I over a wide range of the two parameters for the overocean flight environment.

### 3.2.2 MODEM EVALUATION TEST CONFIGURATION

All modem evaluation tests are performed in the forward link configuration. Test signals are transmitted from Rosman to the KC-135 via ATS-6. Return link transmissions from the aircraft are for test coordination purposes only except for the PLACE ranging tests which use a round-trip configuration.

#### Types I & II Test Scenarios

Tests are divided into two general categories:

1. **Type I:** These acquire modem performance data with operational antennas at elevation angles ranging from 10° to 30°. Bearing angles relative to ATS-6 are approximately 45°, 135°, 225° and 315°. About 65 percent of the modem evaluation data acquired is of the Type I variety. The signal to multipath interference ratio (S/I) for these tests is dependent upon the polarization and gain characteristics of the airborne operational antenna and the magnitude and polarization characteristics of the sea-reflected signals. Type I tests evaluate modem performance over a range of  $C/N_0$  values and with the S/I values inherent at the relative bearings and elevation angles tested.
2. **Type II Tests:** These employ the quad-helix antenna for reception of the direct path signal and the side multipath antenna for reception of the sea-reflected multipath signals. After preamplification these are combined at RF in the desired power ratio to simulate an antenna with a specified S/I ratio. The combining technique employed does not result in undesired lobing effects because the quad helix and SMP antennas do not have any significant spatial pattern overlap. All flights are approximately broadside to the satellite at an elevation angle of 15°. The test parameters varied are the direct path  $C/N_0$  and the combining ratio which determines S/I. Tests are designed to span  $C/N_0$  values between 38 and 52 dB-Hz in combination with S/I values ranging from heavy multipath fading ( $S/I = 3$  dB) to essentially non-fading conditions ( $S/I > 20$  dB).

#### Aircraft Terminal

A simplified block diagram of the modem evaluation test configuration is shown in Figure 3-2. For Type II tests the QH and SMP antennas are selected by RF switches. The variable resistor preceding the QH preamplifier allows the direct path  $C/N_0$  to be set at the desired value. The two variable resistors preceding the RF power combiner allow the ratio of S/I to be adjusted. Channel tuning is accomplished by the IF Tuning unit which employs frequency synthesizers for this purpose. For Type I tests the RF switches are set to select the desired operational

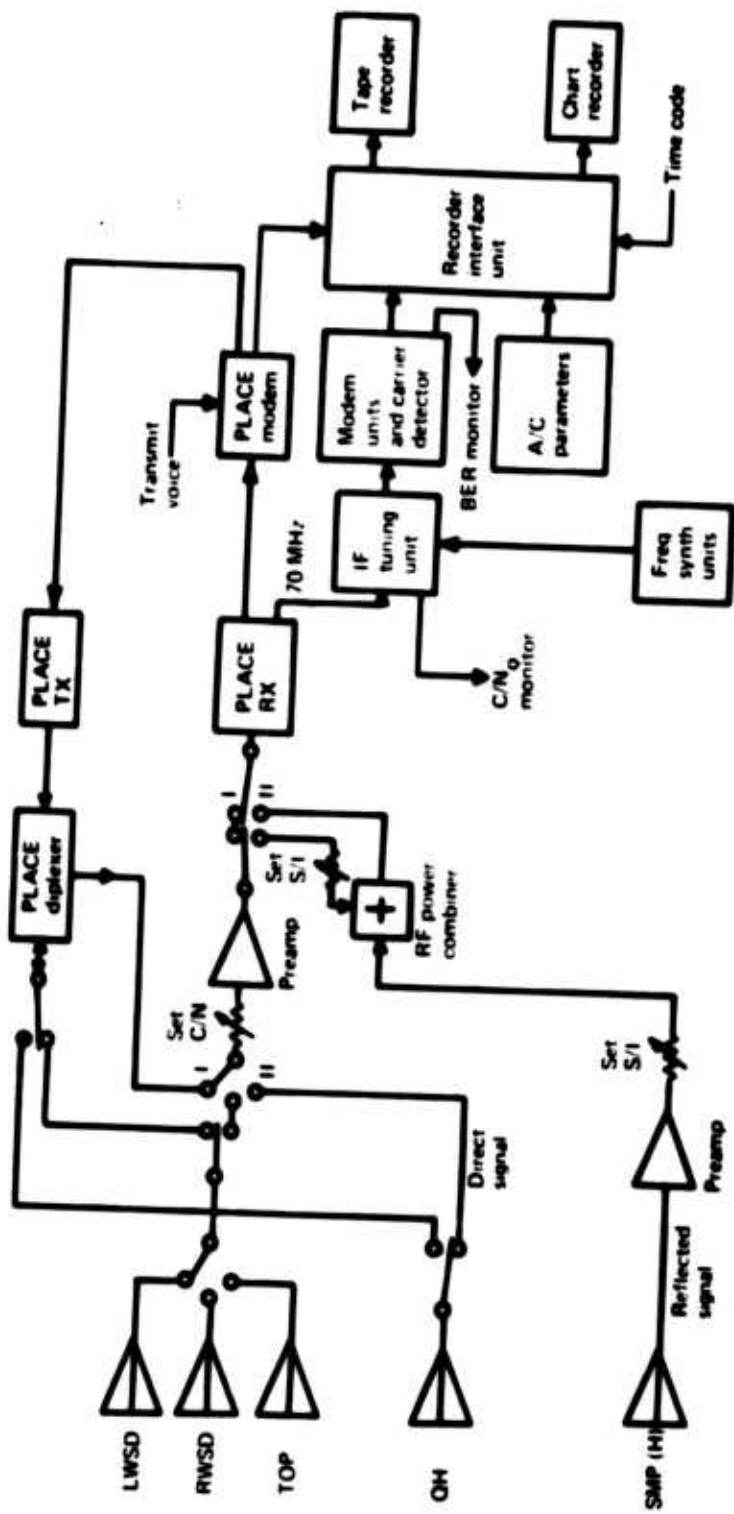


Figure 3-2.—Simplified KC-135 Terminal for Modem Evaluation Test

antenna and the RF power combiner is not used. If maximum available C/N<sub>0</sub> is required, the PLACE diplexer can be bypassed to reduce insertion loss preceding the preamplifier.

#### Aircraft C/N<sub>0</sub> Measurement

For all modem evaluation tests, the transmission format includes a CW carrier at a power level equal to that of other test channels. C/N<sub>0</sub> measurements can therefore be made on this channel to infer the C/N<sub>0</sub> on other channels. The CW signal was normally at 1550.6875 MHz for data modem test and at 1550.075 MHz for other modem tests.

The CW signal is also envelope detected in the Carrier Detector unit whose output is FM recorded for off-line computer analysis to determine C/N<sub>0</sub> and S/I on a more continuous basis in support of the detailed data analysis. This method of determining C/N<sub>0</sub> is referred to as "computer analyzed C/N<sub>0</sub>" or "computed C/N<sub>0</sub>" in the data presented later. Frequent independent measurements are made by separate operators at 70 MHz and 10 MHz IF points using an HP 1411 spectrum analyzer and an HP 312A wave analyzer. These measurements are used to establish the desired value of the C/N<sub>0</sub> test parameter during flight test conduct.

#### 3.2.3 TRANSMISSION FORMATS AND MODEMS TESTED

The principal forward link transmission formats used are given in Table 3-3. Uplink signals are transmitted from Rosman at relative power levels which cause the L-band down-link channel powers received at the airplane (with modulations applied) to be equal. Special precautions and monitoring techniques were employed to ensure that this was adequately achieved.

*Table 3-3.—Modem Evaluation Transmission Formats*

Test mode	Channel frequency - MHz					
	1550.000	1550.075	1550.250	1550.600	1550.675	1550.6875
Voice (1)	..	CW	NBFM	Hy #2	Hy #1	..
Voice (2)	..	CW	ADVM	Hy #2	NBFM	..
Voice (3)	..	CW	NBFM	ADVM	Hy #1	..
Voice (4)	..	CW	Hy #2	ADVM	Hy #1	..
Digital Data	..	CW	NBFM	..	PSK	CW
Voice/Data	..	CW	Hy #1	Hy #2	PSK	..
			V/D	V/D		
Ranging, NB (1)	CW	S&R	NBFM	R <sub>N</sub>	..	..
Ranging, NB (2)	..	S&R	CW	R <sub>N</sub>	PSK	..
Ranging, WB	CW	S&R	NBFM	R <sub>W</sub>	..	..

### **Voice Tests:**

**Four voice modems were tested:**

1. **Adaptive Narrow Band Frequency Modulation (ANBFM):** This narrow-band frequency modulation modem is part of the NASA PLACE Airborne Avionics. The demodulator is a phase-lock discriminator whose bandwidth adaptively narrows with decreasing  $C/N_0$  thus reducing occurrence of disruptive threshold effects.
2. **Hybrid No. 1: (Bell Aerospace Co.)** This modem employs narrow-band phase modulation for the voice channel and differentially-encoded PSK for the data channel. Simultaneous transmission of data and voice signals on a single carrier are achieved using quadrature modulations.
3. **Hybrid No. 2: (Magnavox Research Lab.)** This modem utilizes suppressed-carrier pulse duration modulation for the voice channel and differentially-encoded PSK for the data channel. Simultaneous transmission of data and voice signals on a single carrier are achieved using quadrature modulations.
4. **Adaptive Delta Voice Modulation (ADVM): (Bell Aerospace Co.)** This is a delta modulation voice modem which uses a 19.2 kHz clock rate and an adaptive step size dependent upon voice wave form slope. Either digital (hard decisions on data bits) or analog (no decisions on the data bits) processing is available at the demodulator.

The ADVM modem was not available for testing until February 1975. The test configuration and transmission channel capacity allowed for the simultaneous testing of 3 modems. Several transmission format options were therefore used as indicated in Table 3-3 for testing the 4 available modems during February and March 1975.

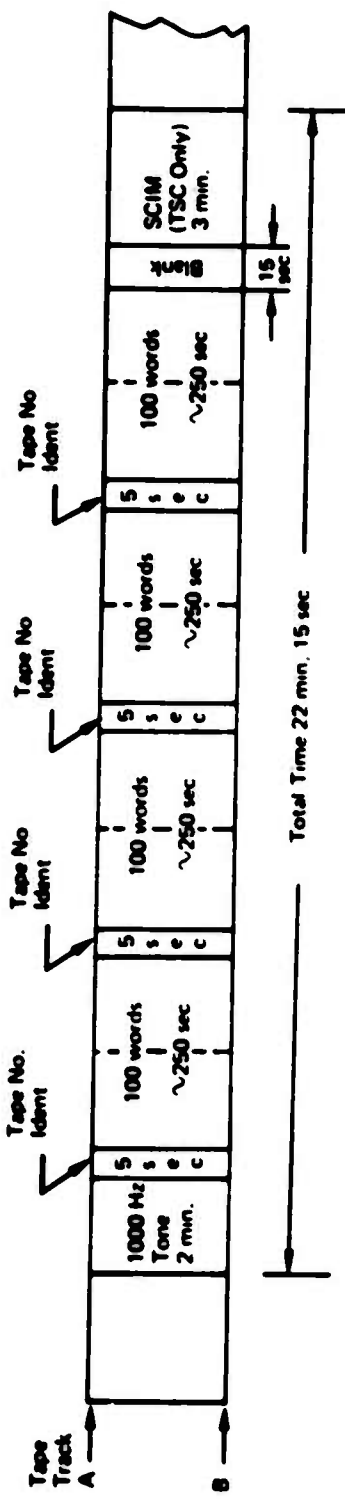
The voice source tapes include 2 minutes of 1-kHz tone, a 17-minute word list and 3 minutes of SCIM. The word list consists of 400 phonetically balanced words segmented into shorter lists which use separate talkers. The tape composition is depicted in Figure 3-3. Except for the September 1974 series, all tests used a single voice source tape simultaneously driving all voice modulators.

### **Digital Data Tests**

The performance of five binary data transmission systems were simultaneously evaluated on typical aeronautical satellite channels by transmitting a specific pseudo-random sequence at 1200 bps, recording the demodulated outputs, and analyzing error statistics in a general-purpose computer. Real-time onboard monitoring of bit-error-rate (BER) performance was also performed for quick-look evaluation of modem performance.

The five modems, all utilizing derivatives of phase-shift-keyed signalling are:

1. **NASA DECPSK** (differentially encoded, coherent PSK)
2. **Hybrid #1 - Bell Aerospace Co.** (same detection method)
3. **Hybrid #2 - Magnavox** (same detection)



#### Major Parameters

- 1) Record Speed: 7 1/2 ips (2 tracks, forward direction)
- 2) Record Level: 0 VU, average
- 3) Tape Type: 1/4 - inch, Scotch 260
- 4) Tape Capacity: 1200 feet, 30 min at 7 1/2 ips, 2 tracks one direction
- 5) Interpause Period: 2.5 sec (time between start of each word)
- 6) No. of words per track: 400 uniquely scrambled PB words (18 PB 50 word lists)
- 7) No. of speakers per track: 4 speakers (100 words each)
- 8) Total record time: (a) Without SCIM: 19.0 min.  
(b) With SCIM (TSC Only): 22 min. 15 sec

Figure 3-3.—DOT/TSC ATS-6 Voice Tape Composition

- 4. FAA CPSK - Philco Ford (same detection)**
- 5. FAA DPSK - Philco Ford (differentially coherent PSK)**

The first four are essentially similar in concept, employing Costas structure coherent reference loops with integrate-and-dump filtering followed by differential decoding to eliminate loop lock ambiguity. The fifth is an implementation of DPSK wherein the bit-to-bit relative phase is used to perform decisions rather than absolute channel phase.

All digital data demodulators operate on the same PSK downlink test signal eliminating any uncertainty regarding unequal modulation quality or unequal channel downlink powers. The CW carrier at 1550.6875 MHz is normally the signal used for aircraft operator and Carrier Detector unit C/N<sub>0</sub> measurements (computed C/N<sub>0</sub> values). It is also down translated to an IF of about 1.25 kHz for potential off-line CW probe multipath analysis.

#### **Hybrid Mode Voice and Data Tests**

These tests evaluate performance of the two hybrid modems in their hybrid voice and data (simultaneous) modes. A separate PSK data channel is transmitted for use by the NASA DECPKS Demodulator.

#### **Ranging Tests**

Two ranging modems are evaluated. These are:

- 1. NASA PLACE Surveillance and Ranging (S&R)**
- 2. DOT/TSC Digital Ranging (in-house DOT/TSC development)**

Testing of the NASA S&R technique is accomplished on a single-link round-trip basis using the ATS-6 satellite. Raw range measurements are obtained from NASA in the form of digital tapes and computer printouts. The testing of the DOT/TSC Digital Ranging modem is performed on a one-way single link basis with all measurements made onboard the aircraft and recorded for analysis off-line.

#### **3.2.4 MODEM EVALUATION DATA ACQUISITION SUMMARY**

Modem evaluation test legs were straight-line segments of 23 minutes duration. The first 3 minutes of a leg allowed for aircraft turns, antenna selection and C/N<sub>0</sub> (and S/I when applicable) setup. Data were acquired on the last 20 minutes of each leg. Approximately 12 different flight paths, (described in the Test Operation Plan for each flight series) were needed to fulfil the combined data acquisition requirements of the modem, multipath and antenna tests.

Table 3-4 and 3-5 summarize modem Type I and II tests which were conducted. The tables identify the number of test legs of each type flown. Additional information describing C/N<sub>0</sub> and S/I, antenna used, etc. is included in a data package submitted separately.

Table 3-4.-Modem Evaluation Data Acquisition, Type I

Date	Elevation angle	Number of 20-minute runs				
		Voice (no ADM)	Voice (with ADM)	Hybrid V/D	Digital data	Ranging (1)
9-24-4	30°	1	-	1	1	2
9-26-4	30°	5	-	-	5	-
9-30-4	30°	4	-	2	2	2
10-24-4	15° - 22°	2	-	1	1	-
10-25-4	15°	-	-	-	5	1
10-26-4	15° - 17°	2	-	-	2	1
11-13-4	12° - 15°	-	-	3	1	2
11-14-4	9° - 16°	4	-	-	3	-
11-15-4	15° - 17°	2	-	-	2	1
11-16-4	9° - 15°	4	-	-	1	2
11-19-4	15° - 17°	-	-	-	4	-
11-20-4	9°	5(2)	-	-	4(2)	2(2)
11-21-4	15° - 17°	3	-	1	1	-
1-23-5	8° - 15°	4	-	-	1	2
1-24-5	15° - 18°	-	-	-	4	-
1-27-5	15°	-	-	-	-	1
1-28-5	15° - 22°	2	-	1	1	-
1-30-5	8° - 15°	4	-	-	1	2
2-24-5	30°	-	7	-	3	-
2-26-5	30°	-	7	-	1	2
2-27-5	30°	-	-	3	-	2
3-25-5	15°	-	-	-	1	2
3-27-5	15°	-	3(3)	-	-	-
3-28-5	10° - 15°	3	-	-	2	-
3-31-5	15°	3	-	-	-	-
4-1-5	10° - 17°	-	3	1	-	-
4-2-5	10°	-	-	-	1	2

Notes:

- (1) Low percentage of success due to erratic modem performance.
- (2) Ground test parked at Azores.
- (3) No ADM data.

Table 3-5.-Modem Evaluation Data Acquisition, Type II

Date	Elevation angle	Number of 20-minute Runs				
		Voice (no ADM)	Voice (with ADM)	Hybrid V/D	Digital data	Ranging (1)
10-24-4	15°	3(2)	-	-	-	-
10-25-4		-	-	-	3(2)	1(2)
10-26-4		3	-	-	-	-
11-13-4		-	-	-	4	-
11-14-4		-	-	-	3	-
11-15-4		3	-	-	-	-
11-16-4		-	-	-	3	-
11-19-4		-	-	-	4	2
11-21-4		2	-	-	-	-
1-23-5		-	-	-	2	-
1-24-5		-	-	-	4	2
1-27-5		3	-	-	-	-
1-28-5		3	-	-	-	-
1-30-5		-	-	-	3	-
3-25-5		-	-	3	3	-
3-27-5		-	2(3)	-	1	1
3-28-5		1	-	-	2	1
3-31-5		2	-	-	2	1
4-1-5		-	3	-	-	-
4-2-5		1	-	1	1	-

Notes:

- (1) Erratic performance of modem.
- (2) Questionable data due to RF power combiner fault.
- (3) No ADM Data.

### 3.3 ANTENNA EVALUATION TEST

#### 3.3.1 TEST OBJECTIVES

The antenna evaluation test quantitatively evaluates the performance of candidate aircraft antennas for aeronautical L-band satellite applications. The antenna performance figures-of-merit of major interest are the gain (which directly determines achievable C/N<sub>0</sub>) and the S/I ratio.

The specific test objective is to acquire and analyze data to determine gain and S/I over a range of satellite elevation and relative bearing angles for the selectable 3-element slot-dipole system, phased array, patch and crossed-slot antennas.

### **3.3.2 ANTENNA EVALUATION TEST CONFIGURATION**

All tests are conducted in the forward mode with the receiving configuration of Figure 3-4. The test signal consists of an unmodulated carrier radiated by ATS-6. Either the quad-helix or the selected slot dipole may be connected to the PLACE receiver. The quad-helix is used as a reference gain antenna for a direct comparison with the selected slot dipole. Either the phased array, patch or crossed-slot (the latter by a cable change) may be connected to the other receiving system.

After amplification and down conversion to 10 MHz, the two signals are time multiplexed, at a 3-second switching rate, to an envelope detector. The detected output is recorded for off-line computer analysis which determines  $C/N_0$  and S/I for each receiving system. The attenuators preceding the preamplifiers adjust  $C/N_0$  to the desired value, while those following the preamplifiers approximately equalize levels, thus reducing the dynamic range requirements imposed on the envelope detector.

### **3.3.3 ANTENNA TEST GEOMETRIES AND SCENARIOS**

Antennas tested included the selectable 3-element slot-dipole system, phased array, patch and crossed-slot. The test concept (previously described in Ref. 3-1 and 3-2) involved flying the airplane in a large circle with low bank angle to acquire antenna data on a quasi-continuous basis. Figure 3-5 gives the basic test geometry. A test begins with a segment broadside to the satellite during which input levels to the carrier detector unit are adjusted, the elevation beam position of the phased array is selected to maximize the signal received and the QII reception is compared with the RWSD for gain calibration. The aircraft then performs a turn to the right at 180° per minute. Antennas are selected on the basis of relative heading to the satellite but no additional elevation beam steering of the phased array is performed. Following completion of the circle, a second 4-minute straight-line path is made providing a "back-up" calibration interval in case the first was missed.

During the 1974 fall series, 7 such tests were planned at elevation angles ranging between 10° and 40°. It was found that (1) the circular path was difficult for the flight crew to fly successfully, (b) the continually changing heading made manual  $C/N_0$  measurements (deemed useful as a check on the subsequent analysis) difficult to make accurately, and (c) the "conical" cuts through the phased array beam did not acquire the data desired. Due to the characteristic beam shape of the phased array antenna different elevation beam positions must be selected for optimum gain as the relative bearing angle to the satellite is changed. Design descriptions of the phased array and patch antennas are given in Ref. 2-3 through 2-5.

As a result, some additional antenna tests specifically designed to acquire data for the phased array were conducted during the spring 1975 series. For these, the planned flight path consisted of 7 straight-line segments, each of 13 minutes duration, offset 0°, 30°, 60°, 90°, 120°, 150°, and 180° relative to ATS-6 on the right side of the aircraft. These segments were easy to fly and were of sufficient time duration to allow phased array antenna beam selection optimization as well as manual measurement of  $C/N_0$  and gain calibration for each antenna under test. This flight path, however, also had several disadvantages, namely: (a) less efficient usage of satellite and flight time, (b) data is available at 30° azimuthal increments only rather than quasi-continuously, (c) the flight path spans a much larger geographical region

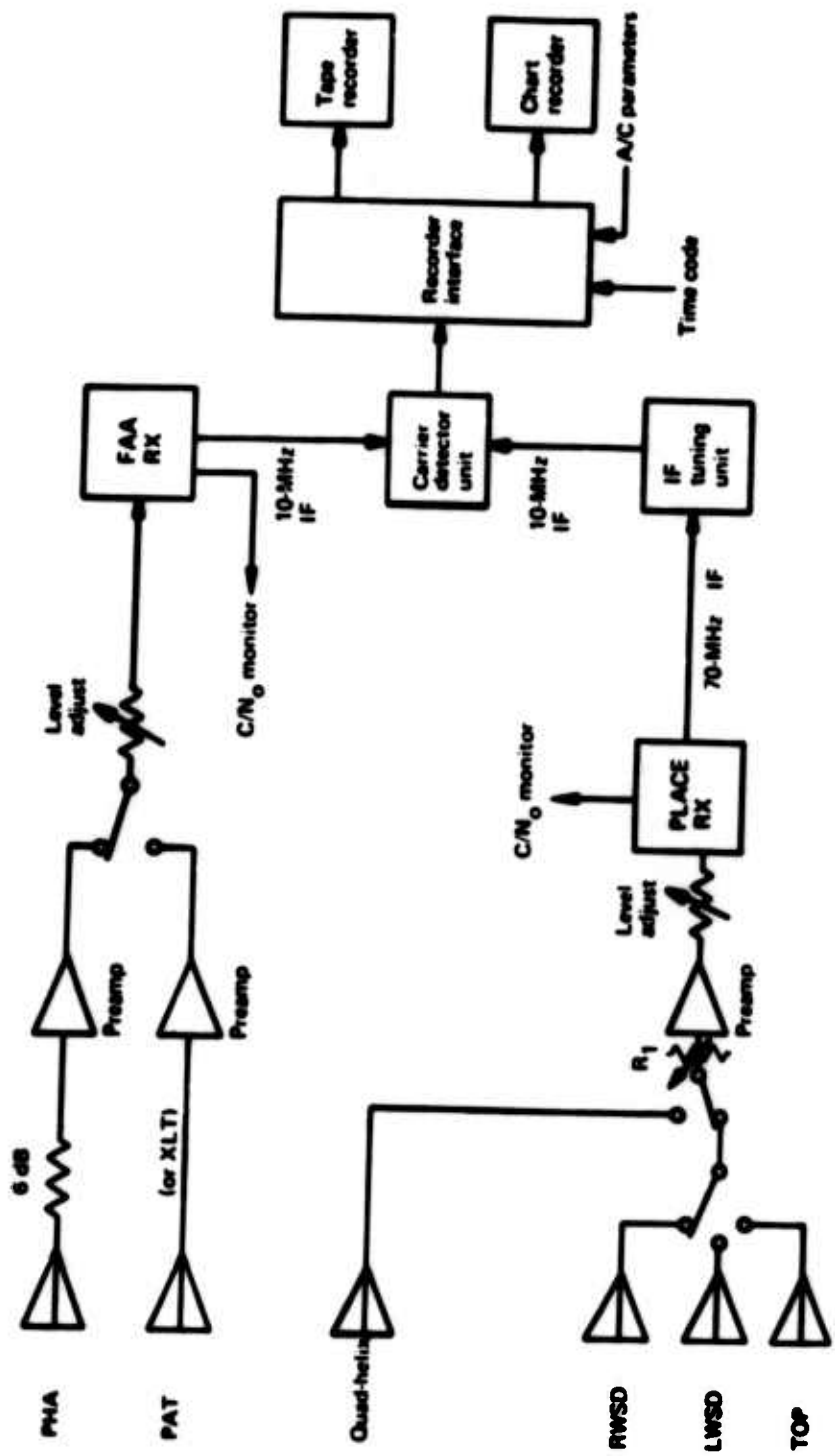
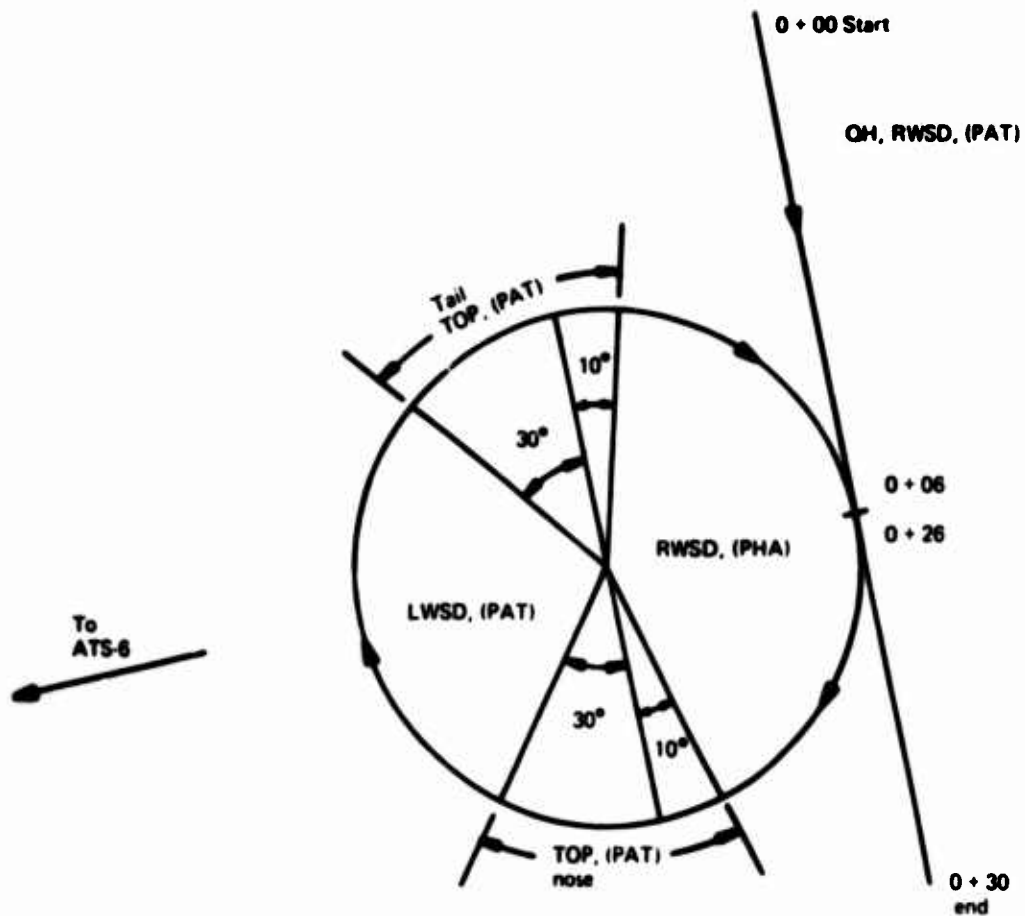


Figure 3-4.—Simplified KC-135 Terminal for Antenna Evaluation Test



Test segment	Hdg. relative to ATS-6	PLACE RX	FAA RX
Initial calibration Circle	270° 270° to 350° 350° to 30° 30° to 150° 150° to 180° 180° to 270°	OH, RWSD RWSD TOP LWSD TOP RWSD OH, RWSD	PHA PHA PAT PAT PAT PHA PHA
Circle Final calibration	270°		

Figure 3-5.—Antenna Evaluation Test Geometry

over which the ATS-6 antenna gain coverage may not be entirely constant, and (d) the duration of the test is much longer increasing the possibility of ATS-6 RF power output variation during test conduct.

For these reasons circular flight paths of the basic test geometry were used wherever the resultant conical pattern cuts yielded the requisite information. Some additional circular flights were made during the spring series for the 3-element slot dipoles and the crossed-slot antennas.

### 3.3.4 DATA ACQUISITION SUMMARY

A summary of the antenna evaluation tests conducted is given in Table 3-6.

*Table 3-6.—Antenna Evaluation Data Acquisition*

Date	Elev. angle	Flight geometry	Test duration	Remarks
9-24-4 10-1-4	30° 40°	Circular <sup>(1)</sup> Circular <sup>(1)</sup>	0+30 0+30	No quad helix gain calibration. Flight path deviations due to ATC conflicts.
10-23-4 10-24-4 10-28-4	25° 19° 15°	Circular <sup>(1)</sup> Circular <sup>(1)</sup> Circular <sup>(1)</sup>	0+30 0+30 0+30	As per Figure 3-3. As per Figure 3-3. As per Figure 3-3.
11-21-4	19°	Circular <sup>(1)</sup>	0+30	As per Figure 3-3.
1-21-5	40°	Linear	1+50	Ground test at NAFEC, various headings by taxiing aircraft.
1-22-5 1-27-5	9° 17°	Linear	0+30 1+30	Real time measures only (3 segments) 6 segments, slot dipoles, PHA, etc.
3-26-5 3-27-5 4-1-5	15° 14° 15°	Circular Linear Circular	0+20 1+30 0+20	Slot Dipoles and Crossed-Slot 7 segments, slot dipoles, PHA, etc. Slot Dipoles and Crossed-Slot.

Notes:

- (1) Phased array data acquired is of limited value due to characteristic beam shape of antenna (see discussion in text).

## 4.0 MULTIPATH TEST RESULTS AND ANALYSIS

Multipath tests were configured to measure several of the more important statistical parameters associated with the oceanic and overland (CONUS) forward scatter propagation channels. Prior to presenting some preliminary results of these tests, we briefly describe the data analysis procedures that have been employed.

### 4.1 MULTIPATH DATA ANALYSIS PROCEDURES

Figure 4.1 depicts the processing steps involved in the formatting, reduction, and analysis of the recorded multipath SACP signal arrays and the aircraft-transmitter parameter tape.

Received SACP signals are direct recorded in a standard telemetry analog format (serial PCM, NRZ-L). Redundant recording was employed on the analog source tape with each of the PCM data bit streams and IRIG A time code signals recorded on two separate tracks. At the Boeing ground station facility, the data and the time tracks are initially processed by telemetry front end (TFe) equipment which for this particular application routes the played-back serial signals through its PCM subsystem to the programmable data distributor (PDD). The PDD merges time words with the data and distributes the information to one or both of the PDP-11/45 computer I/O buses. The dual PDP computer system is called upon to perform three basic functions: (a) conversion of the analog recorded data tapes into digital format computer compatible tapes, (b) quick-look processing of the multipath data, and (c) calculation of the time-ordered delay spectra arrays that are used to generate the time history of the multipath channel delay spectra. The normalization and 3-dimensional plotting of this data is performed in the CDC 6600.

Detailed analysis of the probe data is performed in the CDC 6600 machine. This analysis provides a comprehensive characterization of the multipath channel for horizontal and vertical polarization, gathered over a down-looking antenna and for data gathered over an operational antenna. The primary output of this routine is the time-frequency scatter function of the channel. Also included are the channel's total scattered intensity, delay spectrum, Doppler spectrum, frequency autocorrelation function, and time autocorrelation function. The spreads of these parameters are also calculated.

The algorithm execution sequence for processing the multipath channel data is given in Figure 4.2. A brief description of the analytical objective of each of the major processing blocks follows:

#### 1. Quick-Look Real Time Playback Data Analysis

This output is directly available from the PDP 11/45 system and provides both oscilloscope display plots and hard copy numerical output. From these the operator may investigate receiver parameter configuration, tap frequency spread, delay power spectral density and analog magnetic tape status descriptors. Primary uses of these data include isolation of time intervals which provide both steady-state receiver conditions and multipath scatter phenomena of particular importance.

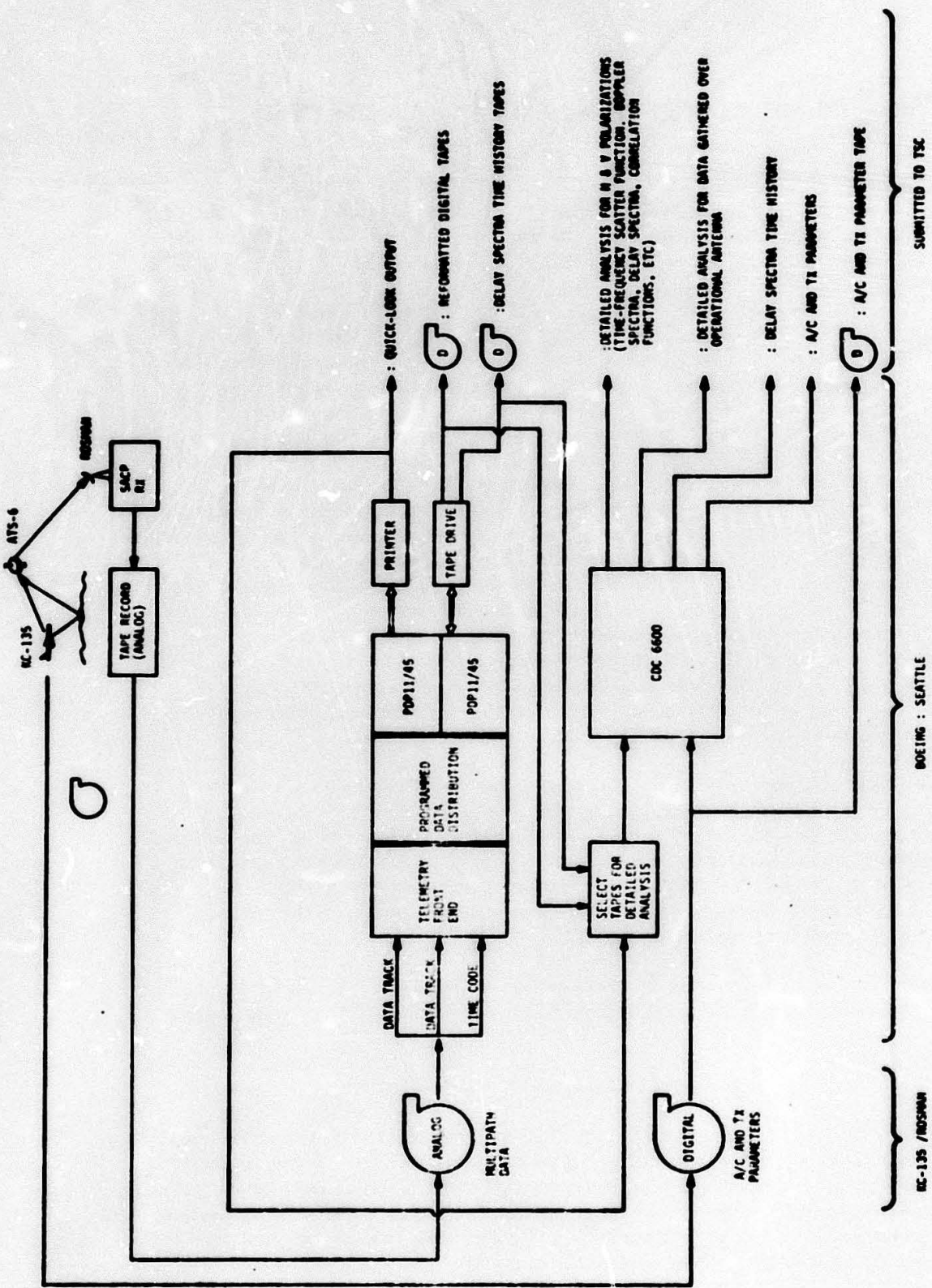


Figure 4.1 - Data Reduction and Analysis Functional Flow

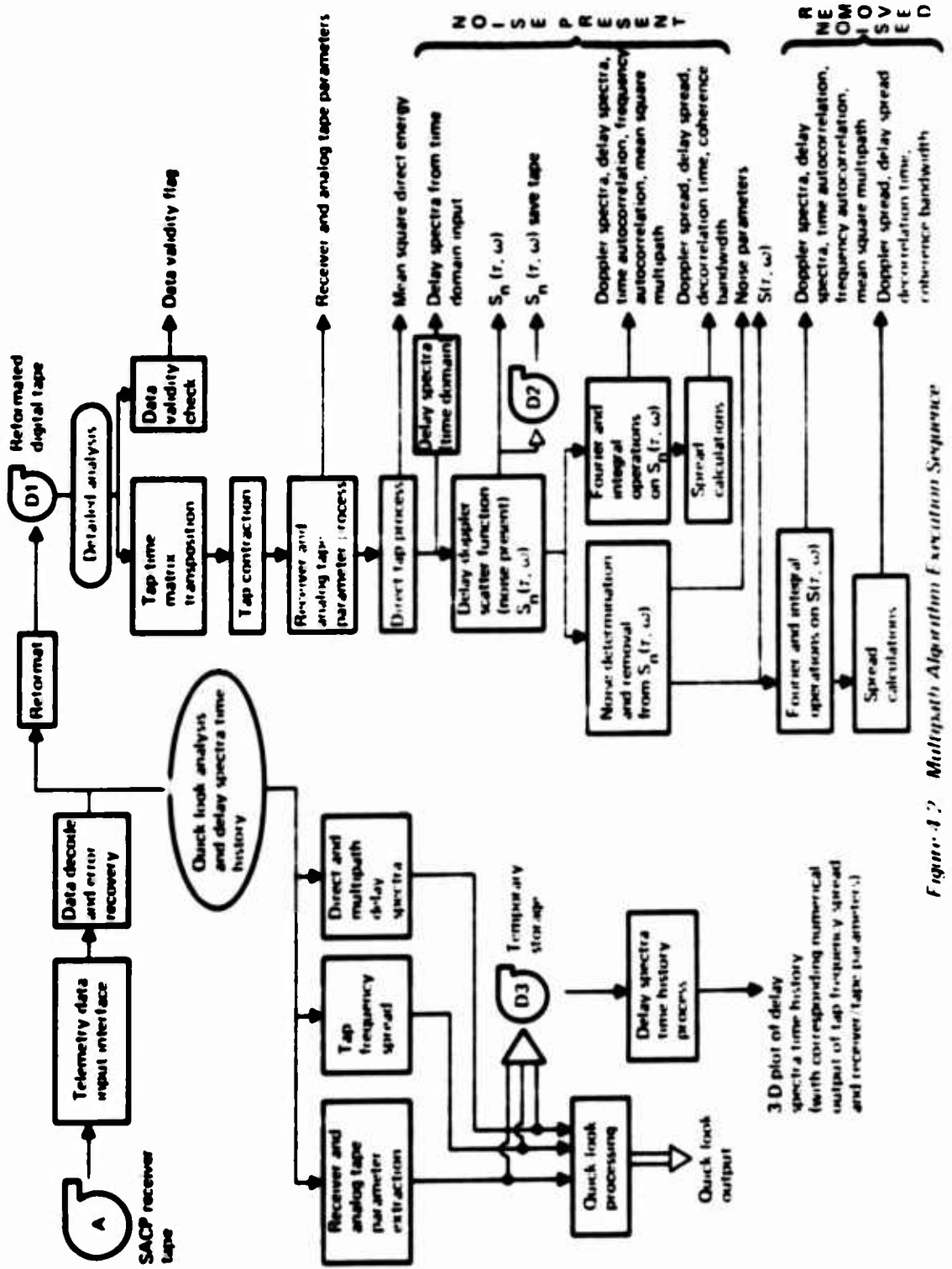


Figure 3.2 Multipath Algorithm Execution Sequence

## **2. Reformatted SACP Digital Tapes**

**Source analog tapes are processed to provide computer compatible digital tapes which represent the complex tap voltage time domain data of the SACP receiver. Typically, those periods of data identified by the "quick-look" analysis as being of particular interest are reformatted for the CONUS tests. For the oceanic tests the bulk of the valid data has been converted to digital format.**

## **3. Delay-Spectra Time History**

**For all periods of valid data collection the scatter channel's delay power spectral density (psd) is determined in a time running manner with discrete psd outputs being given every 2 seconds. For typical SACP low-pass digital filter bandwidth settings (i.e. 300 Hz) the 2-second interval spans a total of roughly 1220 samples. In the computer algorithm every fourth point is selected for the delay spectra computation thereby yielding a sample space of 305 points. The outputs are given in both numerical and 3-dimensional plotted formats. Respectively, these data provide both a quantitative and a comprehensive overview description of the channel's time variant delay spectra characteristics. This analysis is of particular importance for the CONUS scatter where terrain roughness and electrical characteristics vary rapidly with distance. One use of the 3-D overview plot is for isolation of time and tap bank intervals which possess data for which it is desirable to either i) reference the numerical output to obtain quantitative delay-spectra information or ii) subject the data input string to detailed delay-Doppler power spectral density computer processing.**

## **4. Delay-Doppler Scatter Power Spectral Density $S(\tau, \omega)$**

**This function represents the distribution of diffusely scattered power arriving at the receiver with Doppler frequency  $\omega$  and time delay  $\tau$ . For the zero-mean complex Gaussian random scatter process,  $S(\tau, \omega)$  completely characterizes the channel statistics. For each test condition, including probes conducted over the multipath and operational antenna systems, at least one detailed- $S(\tau, \omega)$  function is generated. The output is given in numerical and 3-dimensional plotted form. Furthermore, since this parameter is of such fundamental importance for the interpretation, modeling and application of the scatter channel phenomena,  $S(\tau, \omega)$  is also preserved on magnetic tape. This provides a convenient and compact basis from which future analysis may be conducted without going through the time consuming and expensive computer processing steps required to obtain the delay-Doppler psd from the reformatted SACP digital tapes.**

## **5. Integral and Fourier Operations on $S(\tau, \omega)$ :**

**The scatter function  $S(\tau, \omega)$  contains all the needed ingredients for the derivation of equivalent and lower order channel parameters. Three of the more commonly referred to parameters are the multipath's joint time-frequency correlation function  $R(\xi, \Omega)$ , Doppler spectra  $D(\omega)$ , and delay spectra  $Q(\tau)$ , i.e.,**

$$R(\xi, \Omega) = \int \int S(\tau, \omega) e^{i(\Omega\tau + \xi\omega)} d\tau d\omega \quad (4.1)$$

$$D(\omega) = \int S(\tau, \omega) d\tau \quad (4.2)$$

$$Q(\tau) = \int S(\tau, \omega) d\omega \quad (4.3)$$

The functions  $D(\omega)$  and  $Q(\tau)$  are calculated in the basic software package. The function  $R(\xi, \Omega)$  measures the degree of correlation between two signals delayed in time by  $\xi$  and separated in frequency by  $\Omega$ . Data is processed to evaluate the following special cases:  $R(\xi, 0)$ , the time autocorrelation function and  $R(0, \Omega)$  the frequency autocorrelation function.

#### 6. Channel Spread Parameters

From the  $D(\omega)$ ,  $Q(\tau)$ , and  $R(\xi, 0)$  and  $R(0, \Omega)$  distributions, lower echelon first-order channel parameters such as the Doppler spread, delay spread, de-correlation time and coherent bandwidth of the scatter channel are easily estimated.

#### 7. Noise Determination and Removal (ND and R)

The outputs of the SACP multipath correlator contain desired signal data, spurious signal terms, low-pass additive thermal noise and receiver arithmetic noise. Under normal SACP operating conditions the ND and R algorithm statistically eliminates these noise terms from the data on a tap-by-tap basis. The noise-free estimate of the delay-Doppler function may then be subjected to the integral, Fourier transform, and spread determination steps as previously outlined.

#### 8. System Calibration Parameter Data

Magnetically recorded data pertaining to receiver system operation (i.e., direct and multipath channel gains, etc.), transmitter power amplifier outputs and aircraft flight parameter descriptors are computer reduced to aid in the normalization of the scatter channel power returns. These data also serve as a data collection integrity measure and are used primarily to augment the logged flight test data.

### 4.2 OCEANIC MULTIPATH TEST RESULTS

Probes of the oceanic multipath phenomena were conducted on eighteen separate occasions covering a range of grazing angles from  $3^\circ$  to  $30^\circ$  and a variety of North Atlantic sea conditions. A limited amount of sea surface data was acquired during March 1975 using a sea state buoy. Reduced buoy data is not available for inclusion in this report. Experimental multipath data is presented to illustrate the delay-Doppler scatter function, results of integral and Fourier operations on the scatter function, and the spread values of the delay spectra, Doppler spectra and autocorrelation functions. Most of the data given are for simultaneous probing transmissions which have vertical and horizontal linear polarizations. A limited amount of data for circularly polarized transmissions from the forward multipath antenna is included.

For mid grazing angles (about 19°), results are compared with predictions based upon surface integration of the physical optics vector-scatter model as applied to a very rough surface\* possessing an isotropic slope distribution of the gaussian form with assumed mean square value. Measured spread values are also compared with theoretical predictions based upon "steepest descent" solutions to the integral formulation for the appropriate channel parameter and discussions of these comparisons are given.

#### 4.2.1 OCEANIC SCATTER FUNCTION

For oceanic scatter at L-band frequency there are compelling reasons to believe that the multipath channel is adequately described as a zero-mean complex gaussian random scatter process\*\*. Since the experimental test conditions are processed in time segments on the order of 6 seconds we may also in general assume that the effective scatter region traverses a surface area over which its significant electrical and physical parameters are relatively constant. Under these conditions  $S(\tau, \omega)$  completely characterizes the statistics of the channel (Ref. 4-1).

Several fundamental observations have been made relative to the energy distribution dependencies of  $S(\tau, \omega)$  upon grazing angle, flight direction and polarization. Typically, these dependencies are most easily discussed when  $S(\tau, \omega)$  is reduced to lower echelon relationships such as the channel Doppler spectra spreads, etc. Observations relative to quantities derived from  $S(\tau, \omega)$  will be delineated in Sections 4.2.2 and 4.2.3. In this section we restrict our attention to some of the more distinct spectral characteristics that  $S(\tau, \omega)$  itself displays as a function of flight direction and polarization. To augment this discussion several three-dimensional plots of the scatter function are given for a test conducted on April 3, 1975 during the final series of flight tests. The grazing angle for this test was on the order of 19 degrees. Scatter function plots are presented for in-plane, 45° relative heading, and cross-plane geometries for horizontal polarization. The horizontal data is given in Figures 4-3 through 4-5. Vertical polarization data for the in-plane case is found in Figure 4-6.

By far the most striking observation pertains to the pronounced velocity direction dependency of the energy distribution of  $S(\tau, \omega)$  in the Doppler variable coordinate. For cross-plane flight (i.e., KC-135 flying broadside to ATS-6 direction) the scatter function possesses a high degree of symmetry (the bias towards a slightly higher energy content in the positive frequency realm may be attributed to nose-bulkhead shielding effects upon the front multi-path antenna for cross-plane pointing angles). On the other hand, as the flight geometry approaches the in-plane direction (i.e., KC-135 flying at constant altitude towards ATS-6) the asymmetry of the spectra becomes increasingly significant. We also note that for a specified delay  $\tau$  the resultant Doppler spectrum has pronounced energy in the tails of its distribution\*\*\* for the in-plane case as compared to the two alternate headings. These results are

\*Very rough in the sense that the surface height variations are significantly greater than the electromagnetic wavelength.

\*\*The evaluation of this hypothesis will be documented in the Final Report.

\*\*\*For a given  $\tau$  these distinct spectral "humps" correspond to the lower and upper frequency limits over which physically possible returns may arrive.

in accord with theoretical modelling (see Section 4.2.4) and are explainable in terms of surface area to Delay-Doppler co-ordinate mapping functions as weighted by the scatter cross-section of the multipath source.

With respect to polarization influences upon the  $S(\tau, \omega)$  distribution we note that the vertical and horizontal data sets are in fairly close agreement to each other (compare Figure 4-3 and 4-6). One important difference that we are able to discern relates to the relative enhancement of the vertically polarized energy content contained in the negative frequency tail of a tap's Doppler distribution. With respect to the "specular point" of the surface the positive Doppler returns, for this flight geometry, are associated with scatter from the direction of the sub-satellite point (lower local grazing angles, hence lower vertical reflection coefficients) and the negative returns with scatterers towards the sub-aircraft point (higher local grazing angles, hence higher vertical reflection coefficients). Thus, the observed negative Doppler tail enhancement for vertical polarization illustrates the effect of the reflection coefficient magnitude upon the rough surface scatter cross-section. This effect is more noticeable for lower elevation angles where the vertical reflection coefficient changes more rapidly (and not necessarily monotonically over the effective scatter surface) and is referred to as Brewster angle fill-in\* in subsequent sections of this report. We also note that these results are substantiated by surface integration model predictions as illustrated by Figures 4-16(a) and 4-19(a) of Section 4.2.4.

#### 4.2.2 INTEGRAL AND FOURIER OPERATIONS ON THE OCEANIC $S(\tau, \omega)$ FUNCTION

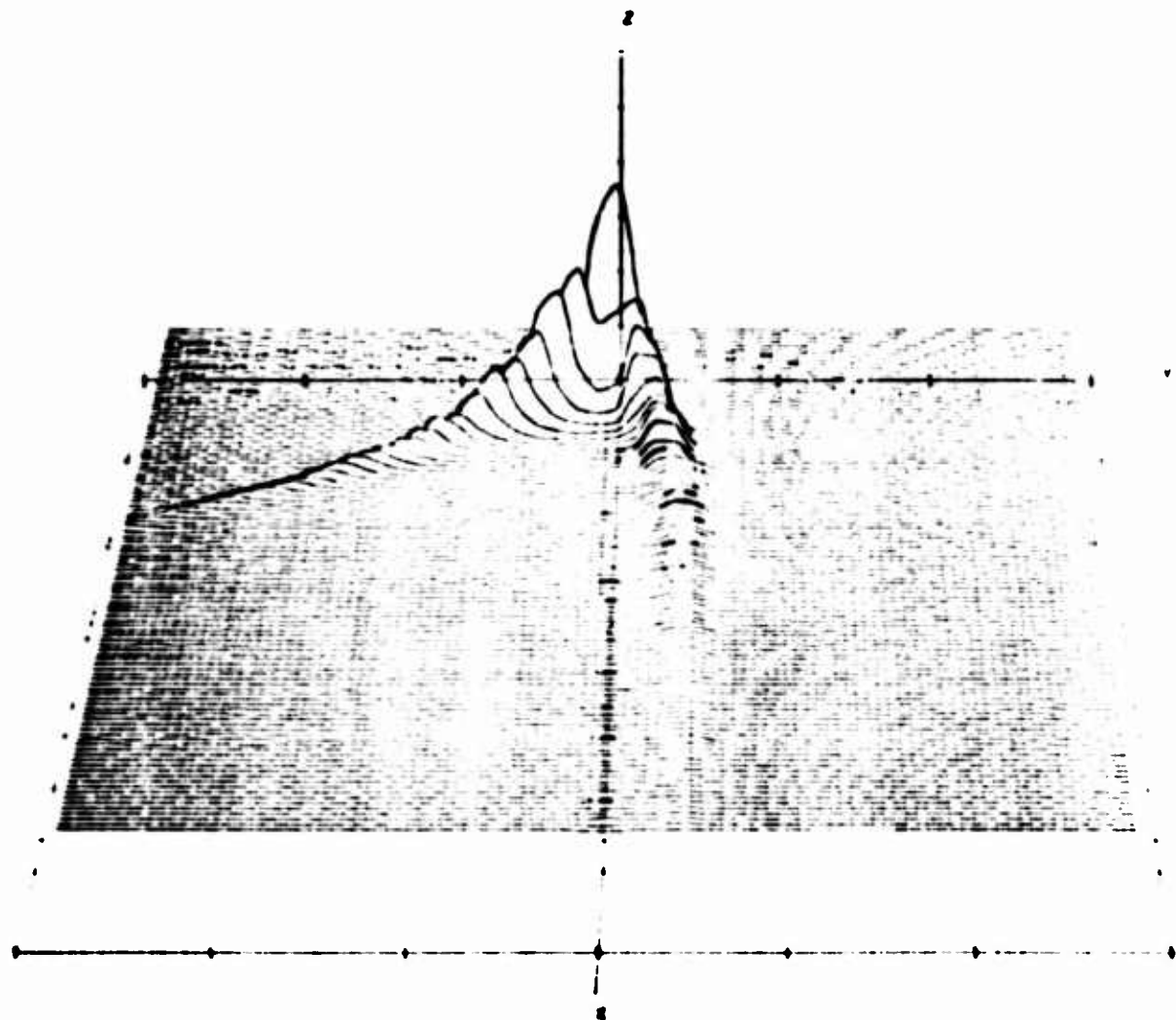
The oceanic  $S(\tau, \omega)$  function is subjected to integral and Fourier transform operations to yield the delay spectrum, Doppler spectrum, frequency autocorrelation function, time autocorrelation function and rms composite reflection coefficients for the multipath channel.

Representative spectra and autocorrelation (magnitude) distributions, derived from the  $S(\tau, \omega)$  functions presented in the previous section, are given in Figures 4-7 through 4-10. These data correspond to medium ( $\approx 190^\circ$ ) grazing angle conditions and are presented for both horizontal and vertical polarizations. The data set includes in-plane,  $45^\circ$  relative heading, and cross-plane geometries. Aircraft altitude ( $\approx 10$  km) and speed ( $\approx 200$  m/sec) are to close approximation held constant for all multipath probe oceanic flights. These presented results lead to the following observations

1. As expected, the delay spectra and frequency autocorrelation distributions are essentially independent of aircraft heading (any slight dissimilarities observed are thought to be related to aircraft antenna pattern effect).
2. The Doppler spectra distribution is quite symmetrical for the cross-plane flight geometry but becomes highly assymetrical as the geometry approaches the in-plane case. Also for the in-plane geometry, the Doppler distribution has a right-triangle like shape with a low end in the negative frequency realm and a high end followed by a sharp cut-off at the positive frequency end of the spectrum. On the other hand the cross-plane

\*This terminology is used since it is the same phenomena which was first observed to produce an increased vertical polarization reflection magnitude in the vicinity of Brewster's angle.

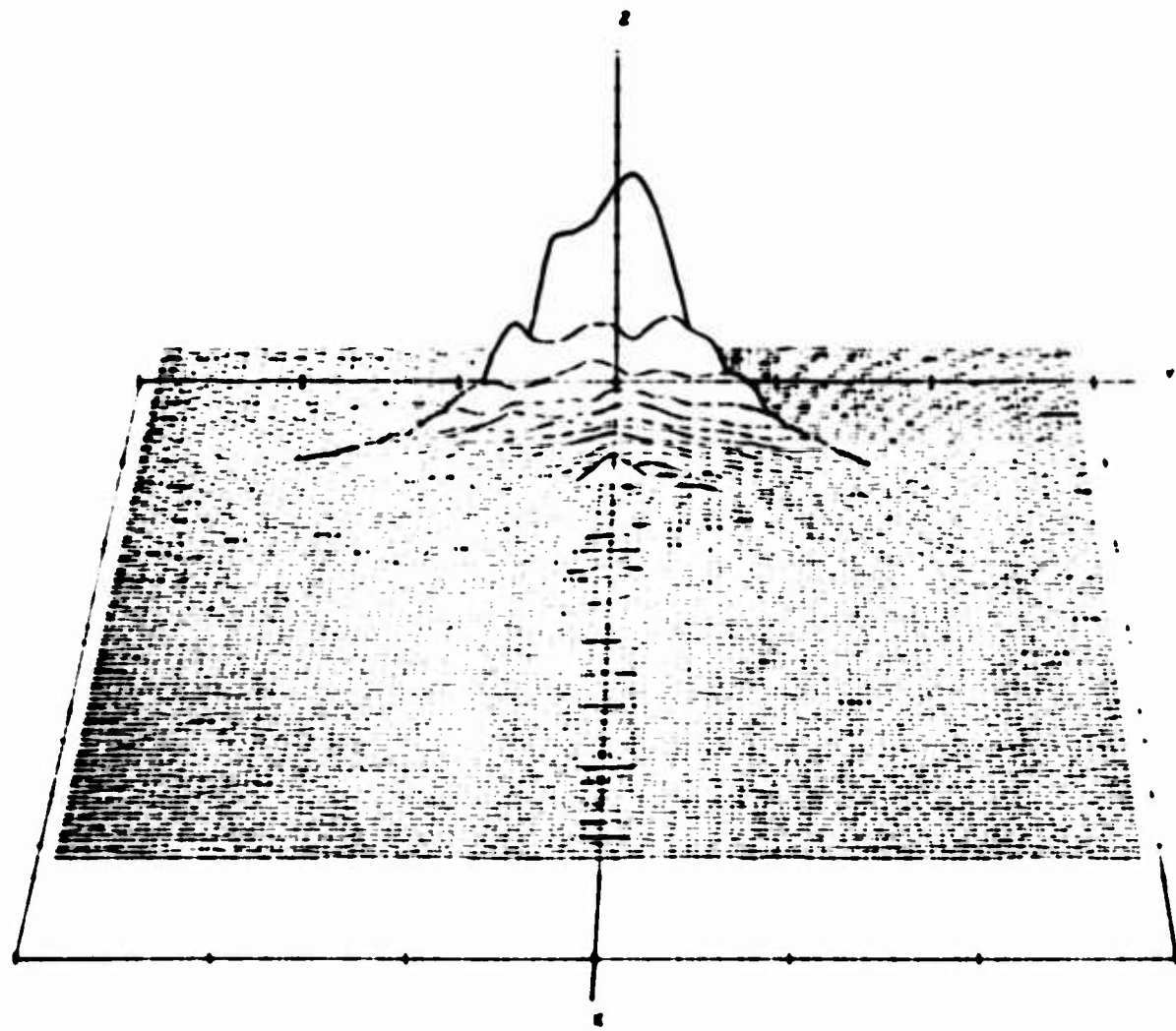
DELAY-DOPPLER SCATTERING FUNCTION  
 DATE 4/3/75 HORIZONTAL POLARIZATION  
 TAP RESOLUTION .2 MICROSEC  
 TIME INTERVAL 9/5// -.521 TO 9/5// 6.463  
 NOISE REMOVED



AXIS	MINIMUM	MAXIMUM	INCREMENT
X DELAY TAP 1 .2 MICROSEC. WIDTH 1	.00	120.00	20.00
Y DOPPLER FREQUENCY (HERTZ)	-300.00	300.00	100.00
Z DELAY-DOPPLER PSD (LINEAR)	-5.00	25.00	5.00

Figure 4-3.- $S(t, \omega)$ -Horizontal Polarization, In-plane Geometry

DELAY-DOPPLER SCATTER FUNCTION  
 DATE 4/3/75 HORIZONTAL POLARIZATION  
 TAP RESOLUTION .2 MICROSEC  
 TIME INTERVAL 10/16/30.492 TO 10/16/36.395  
 NOISE REMOVED



AXIS

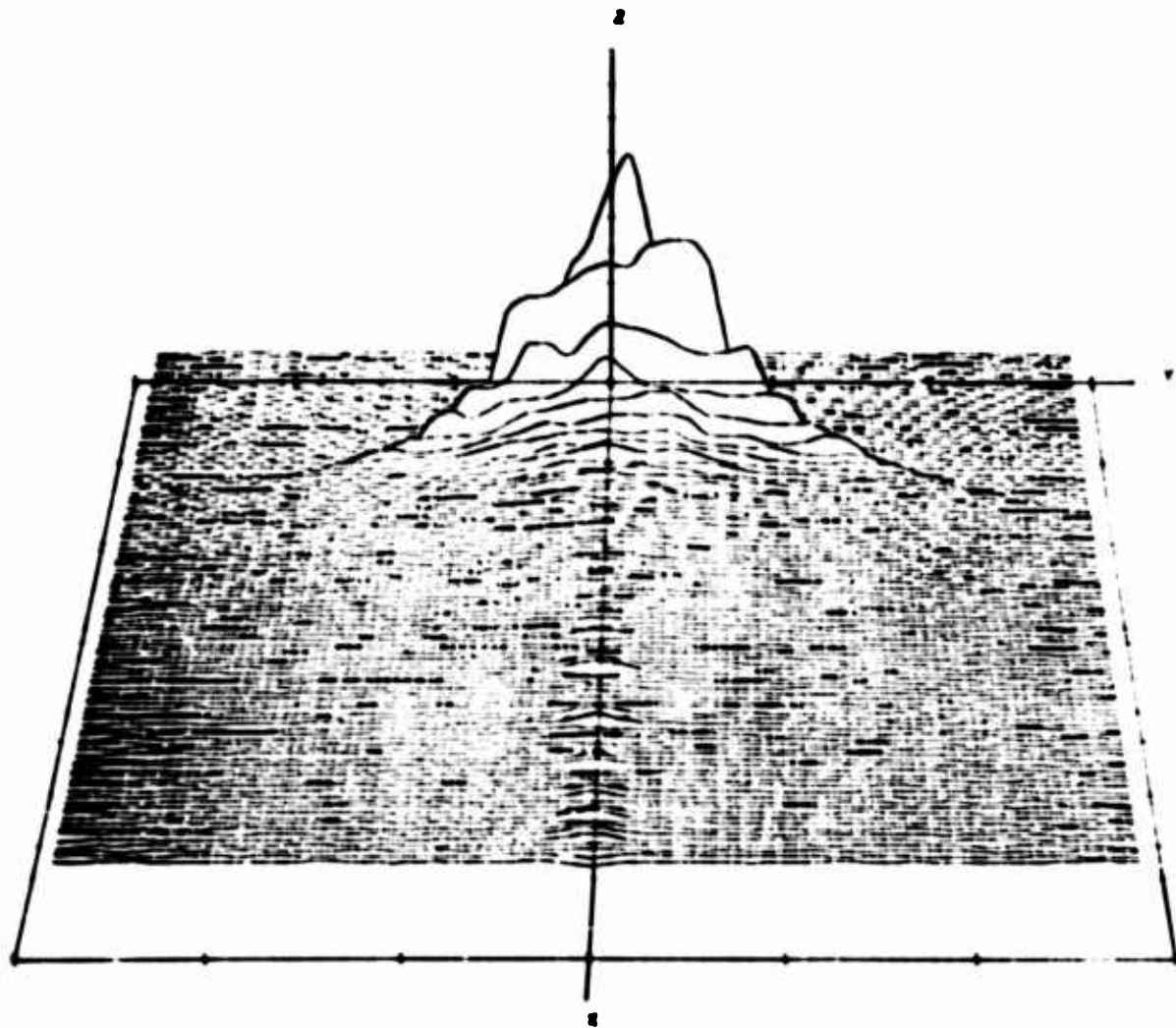
- DELAY TAP 1 .2 MICROSEC. WIDTH 1
- ▼ DOPPLER FREQUENCY 1 HERTZ 1
- DELAY-DOPPLER PSD LINEAR 1

MINIMUM MAXIMUM INCREMENT

.00	120.00	20.00
-300.00	300.00	100.00
-2.00	16.00	2.00

Figure 4-4.- $S(\tau, \omega)$ -Horizontal Polarization, 45° Heading

ELLAT CIRPHLN S A714 09114  
 DATE 05/19/70 HORIZONTAL POLARIZATION  
 TAP RESOLUTION .2 MICROSEC  
 TIME INTERVAL 10/39/ -492 TO 10/39/ 6.365  
 NOISE REMOVED



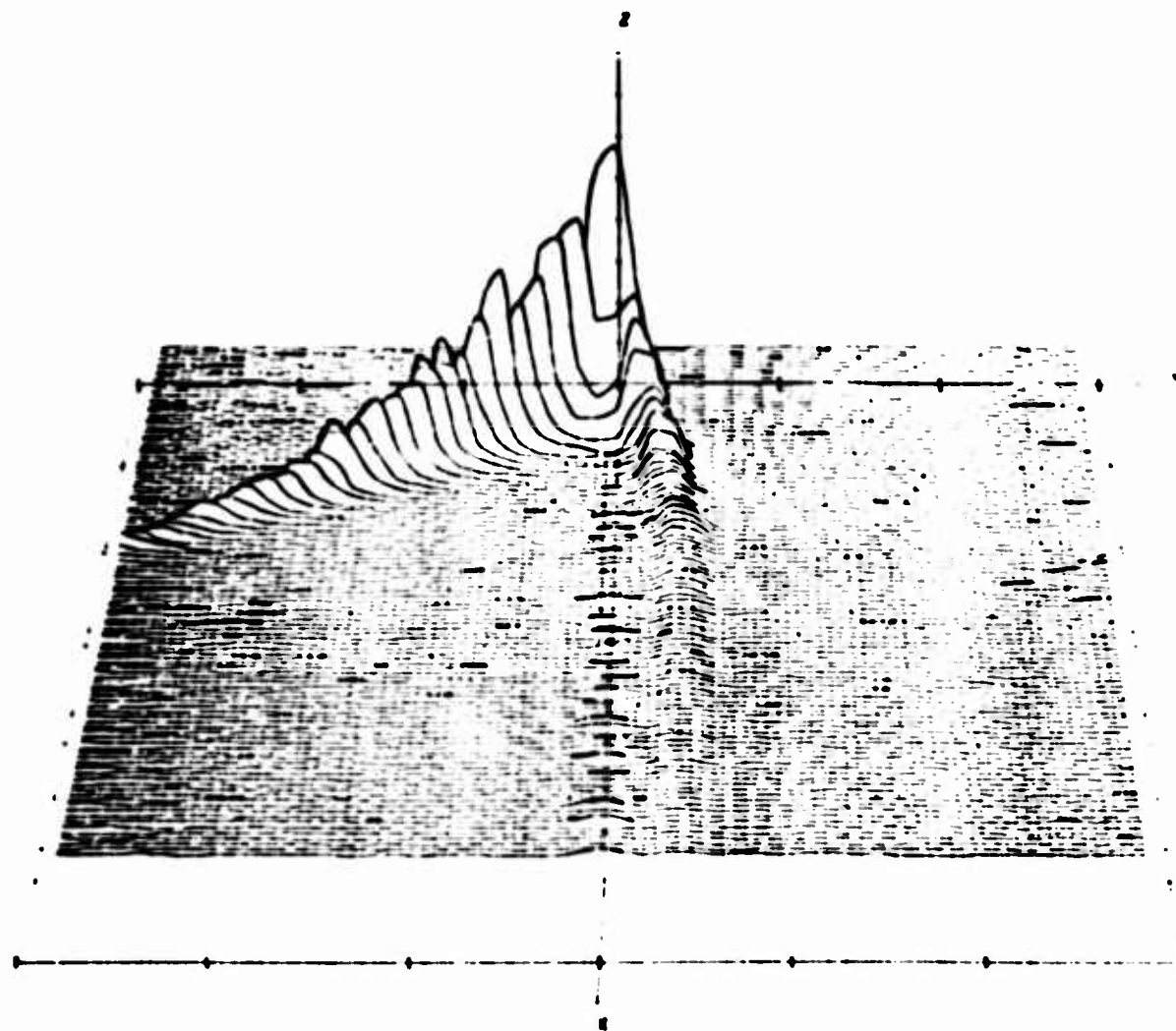
**AXIS**

X DELAY TAP 1 .2 MICROSEC. 810THI  
 Y DOPPLER FREQUENCY 1 MERTZI  
 Z DELAY-DOPPLER PSD LINEAR

	MINIMUM	MAXIMUM	INCREMENT
.00	120.00	20.00	
-300.00	300.00	100.00	
-1.00	9.00	1.00	

Figure 4-5.  $S(\tau, \omega)$ -Horizontal Polarization, Cross-plane Geometry

DELAY-DOPPLER SCATTER FUNCTION  
 DATE 4/3/75 VERTICAL POLARIZATION  
 TAP RESOLUTION .2 MICROSEC  
 TIME INTERVAL 9/5// -492 TO 9/5// 6.36  
 NOISE REMOVED



AXIS	MINIMUM	MAXIMUM	INCREMENT
X DELAY TAP (1 .2 MICROSEC. WIDTH)	.00	120.00	20.00
Y DOPPLER FREQUENCY (HERTZ)	-300.00	300.00	100.00
Z DELAY-DOPPLER PSD (LINEAR)	-1.00	1.00	.10

Figure 4-6.  $S(t, \omega)$  - Vertical Polarization, In-plane Geometry

DELAY AND DOPPLER SP. C184  
DATE 4/3/76 HORIZONTAL POLARIZATION  
TAP RESOLUTION .2 MICROSEC  
TIME INTERVAL 9/5// .531 TO 9/5// 6.463  
NOISE REMOVED

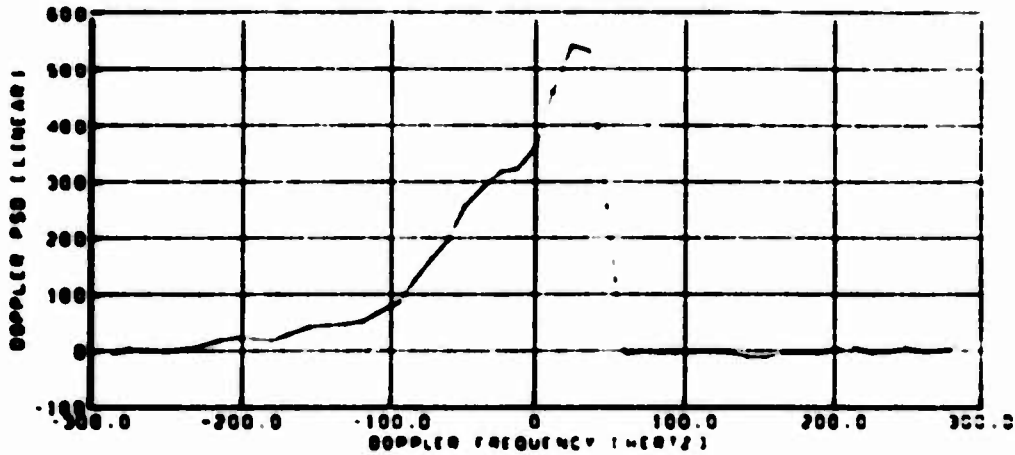
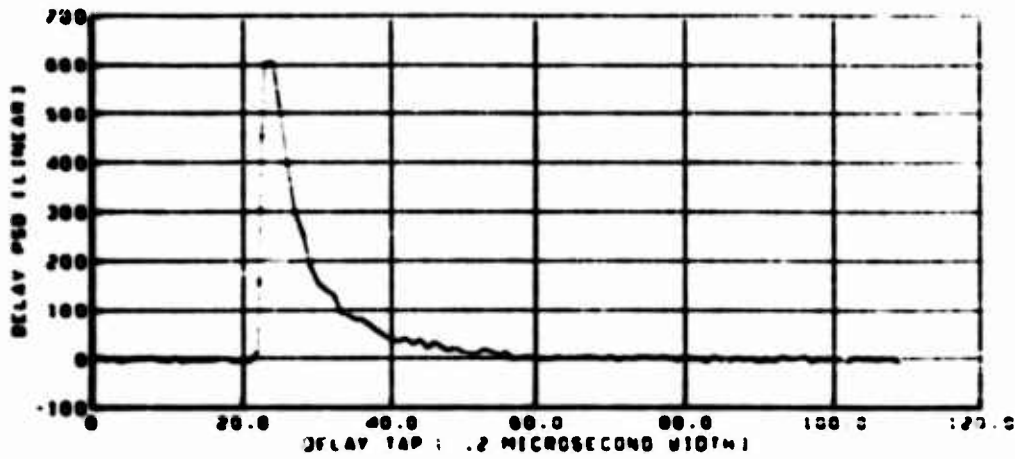


Figure 4-7(a).—Spectra and Autocorrelation Parameters—Horizontal Polarization,  
In-plane Geometry

AUTOCORRELATION FUNCTION  
DATE 6/3/75 HORIZONTAL POLARIZATION  
TAP RESOLUTION .2 MICROSEC  
TIME INTERVAL 8/5/71 .531 TO 8/5/71 6.463  
NOISE REMOVED

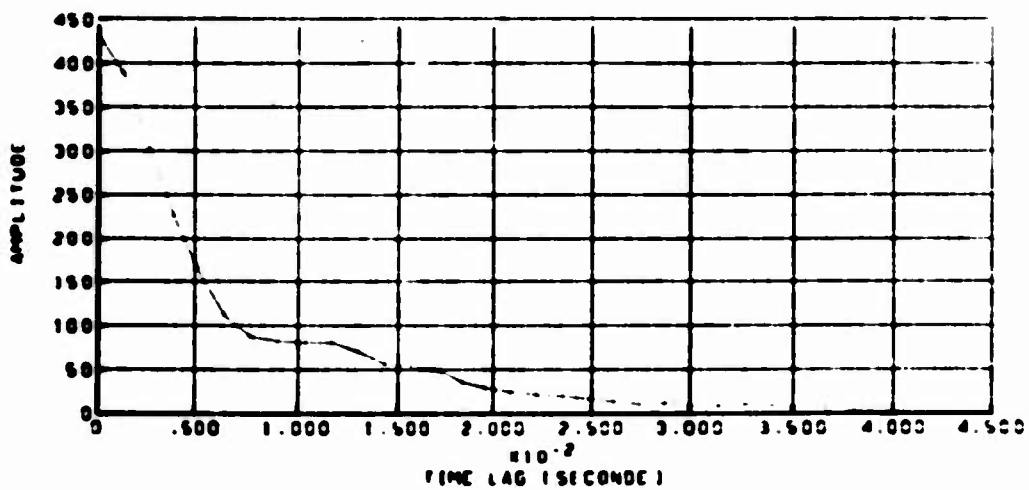
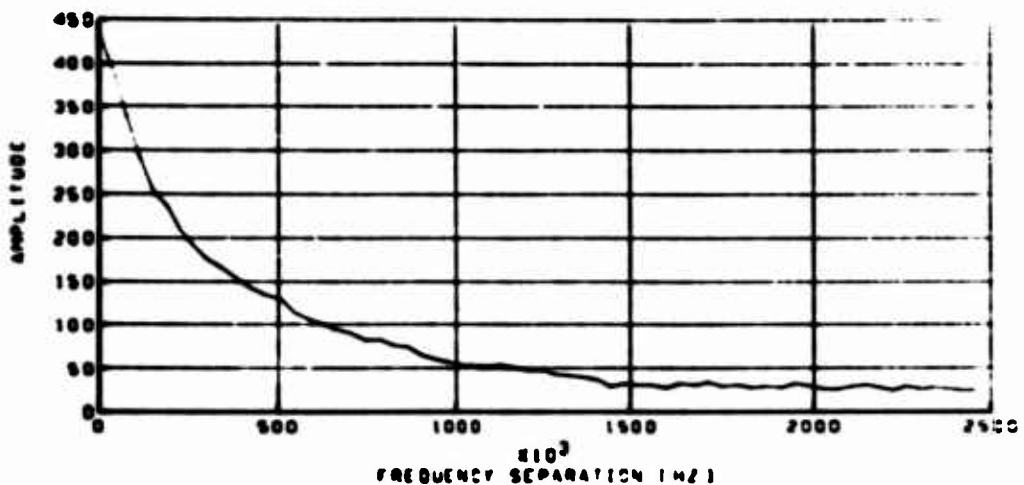


Figure 4.7(b).—Spectra and Autocorrelation Parameters—Horizontal Polarization,  
In-plane Geometry

DELAY AND DOPPLER SPECTRA  
DATE 4/3/75 HORIZONTAL POLARIZATION  
TAP RESOLUTION .2 MICROSEC  
TIME INTERVAL 10/16/30.462 TO 10/16/36.165  
NOISE REMOVED

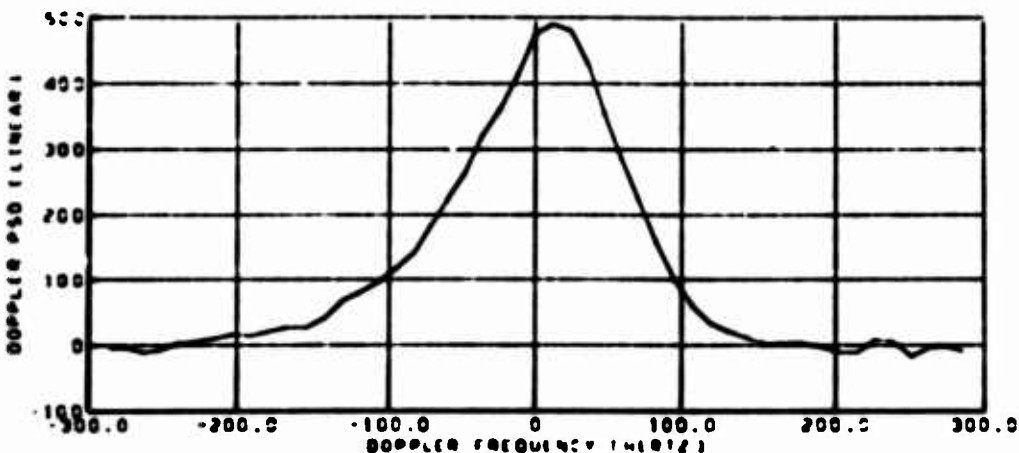
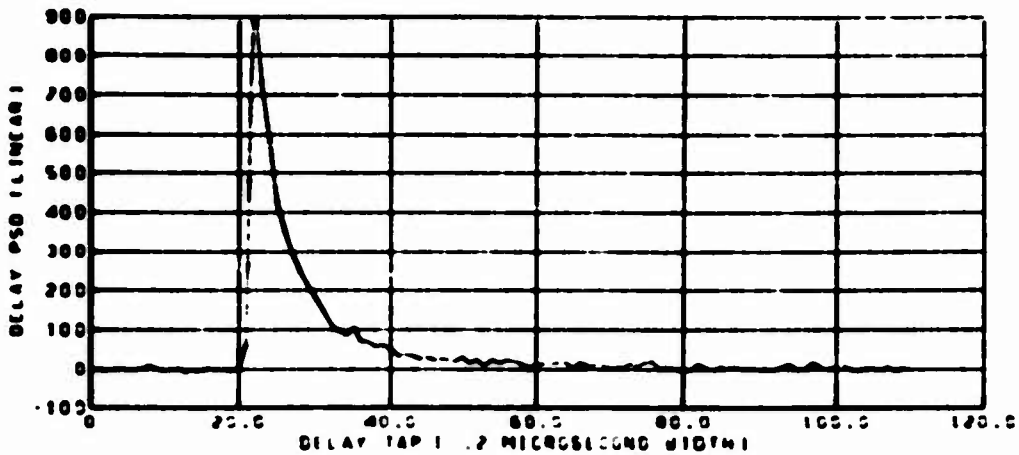


Figure 4-8(a).-Spectra and Autocorrelation Parameters—Horizontal Polarization,  
45° Heading

AUTOCORRELATION FUNCTION  
DATE 4/3/75 HORIZONTAL POLARIZATION  
TAP RESOLUTION .2 MICROSEC  
TIME INTERVAL 10/16/30.492 TO 10/16/36.165  
NOISE REMOVED

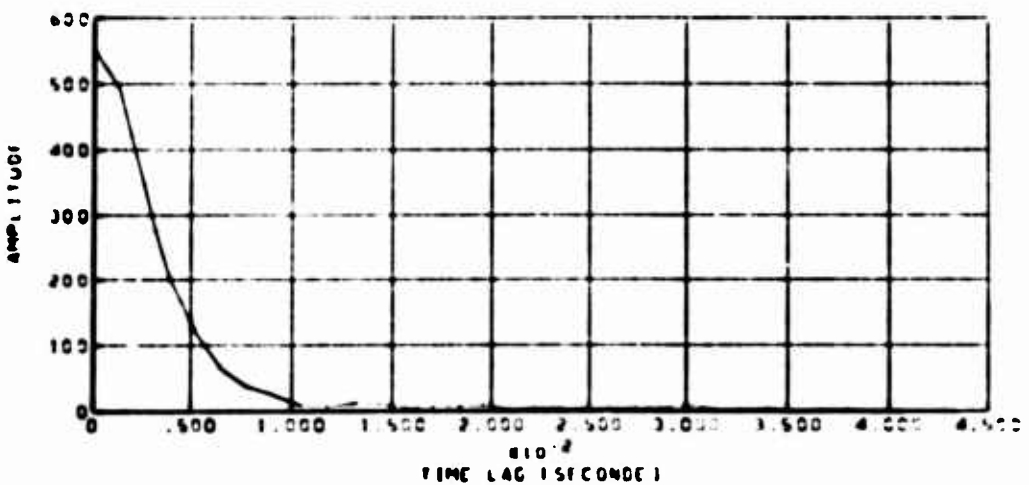
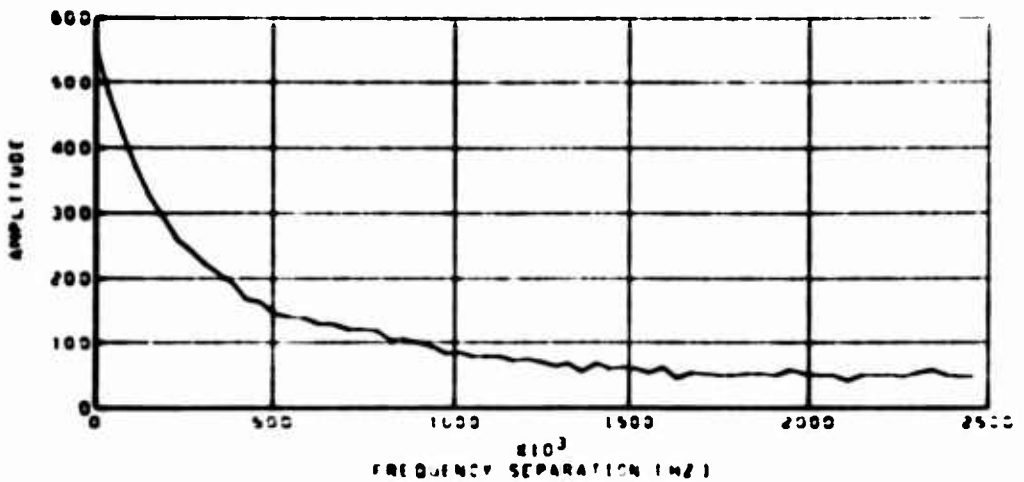


Figure 4-8(b). - Spectra and Autocorrelation Parameters—Horizontal Polarization,  
45° Heading

DELAY AND DOPPLER SPECTRA  
DATE 6/1/75 HORIZONTAL POLARIZATION  
TAP RESOLUTION .2 MICROSEC  
TIME INTERVAL 10/397 .492 TO 10/397 6.365  
NOISE REMOVED

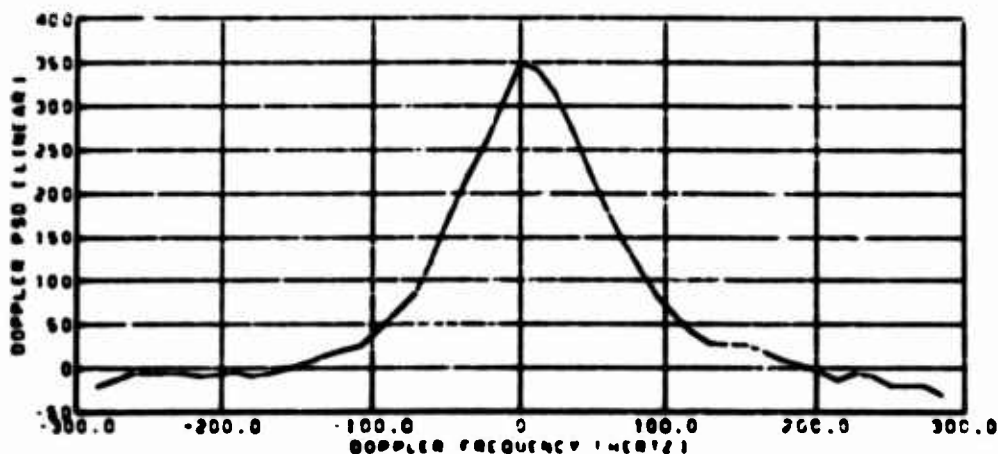
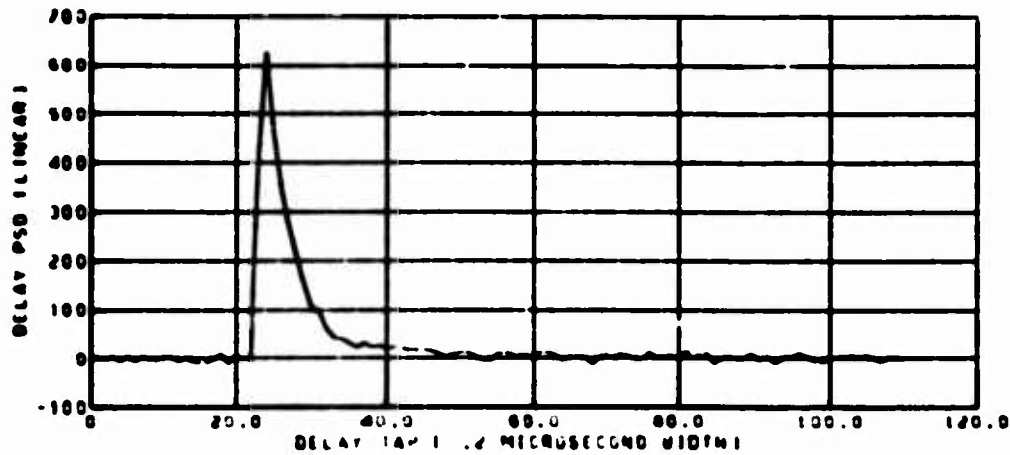


Figure 4-9(a).—Spectra and Autocorrelation Parameters—Horizontal Polarization,  
Cross-plane Geometry

AUTOCORRELATION - HORIZONTAL  
DATE 6/1/75 HORIZONTAL POLARIZATION  
TAP RESOLUTION .2 MICROSEC  
TIME INTERVAL 10/397 -.492 TO 10/397 6.116  
NOISE REMOVED

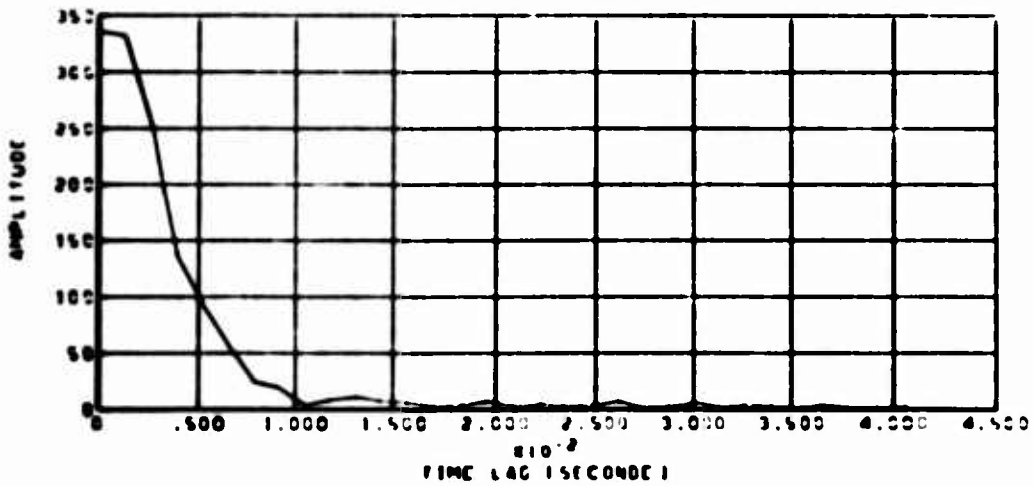
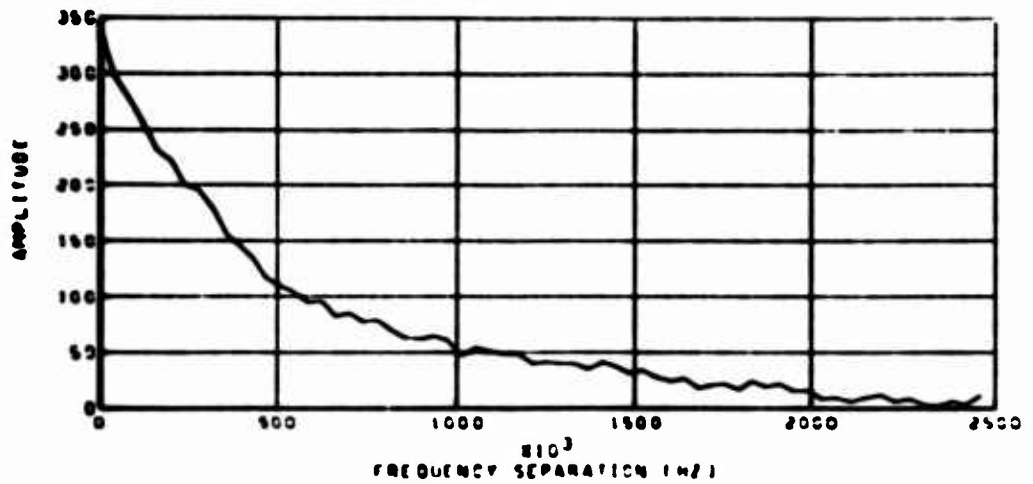


Figure 4.9(b). - Spectra and Autocorrelation Parameters-Horizontal Polarization,  
Cross-plane Geometry

DELAY AND DOPPLER SPECTRA  
DATE 4/3/75 VERTICAL POLARIZATION  
TAP RESOLUTION .2 MICROSECS  
TIME INTERVAL 9/5/74 .482 TO 9/5/74 6.365  
NOISE REMOVED

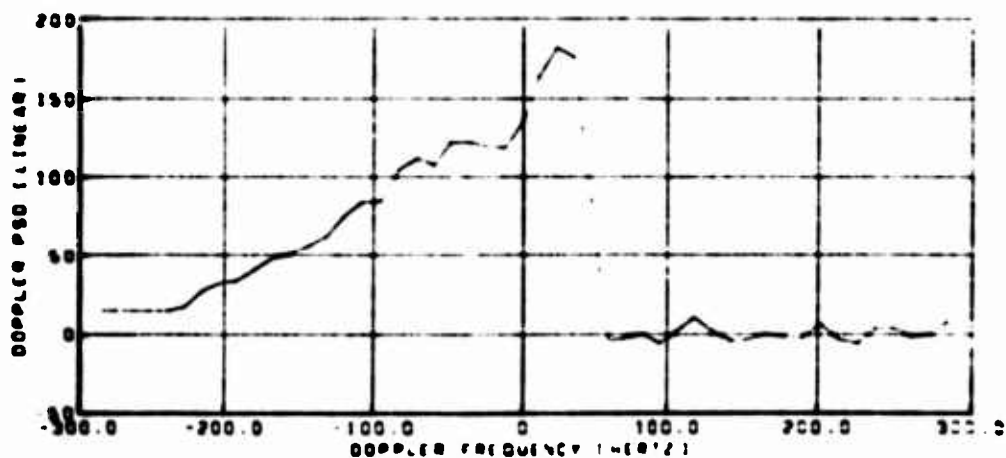
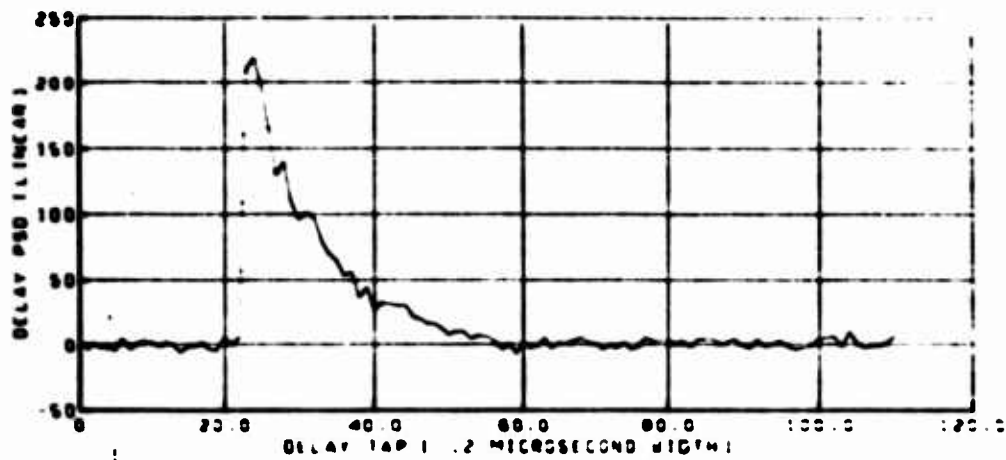


Figure 4-10(a).—Spectra and Autocorrelation Parameters—Vertical Polarization,  
In-plane Geometry

AUTOCORRELATION FUNCTION  
DATE 4/3/78 VERTICAL POLARIZATION  
TAP RESOLUTION .2 MICROSEC  
TIME INTERVAL 9/5/77 .492 TO 9/5/77 6.365  
NOISE REMOVED

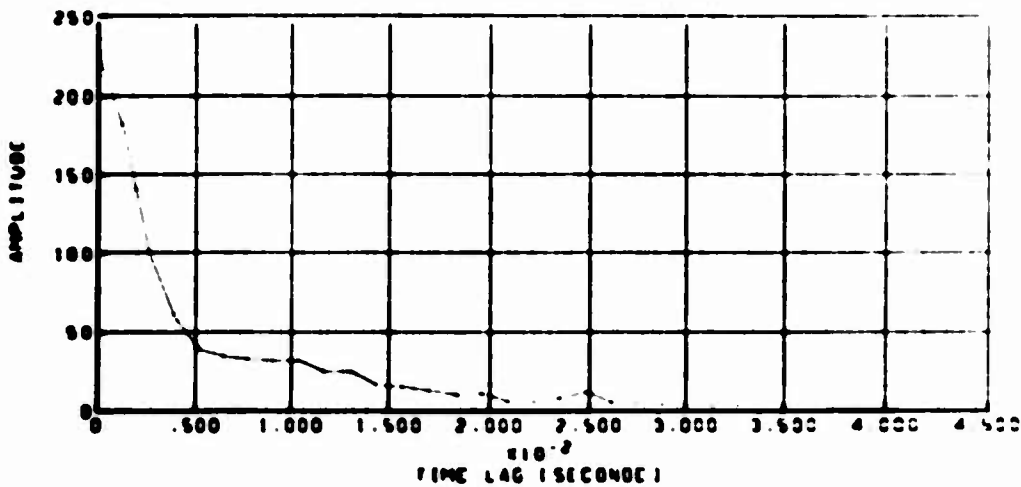
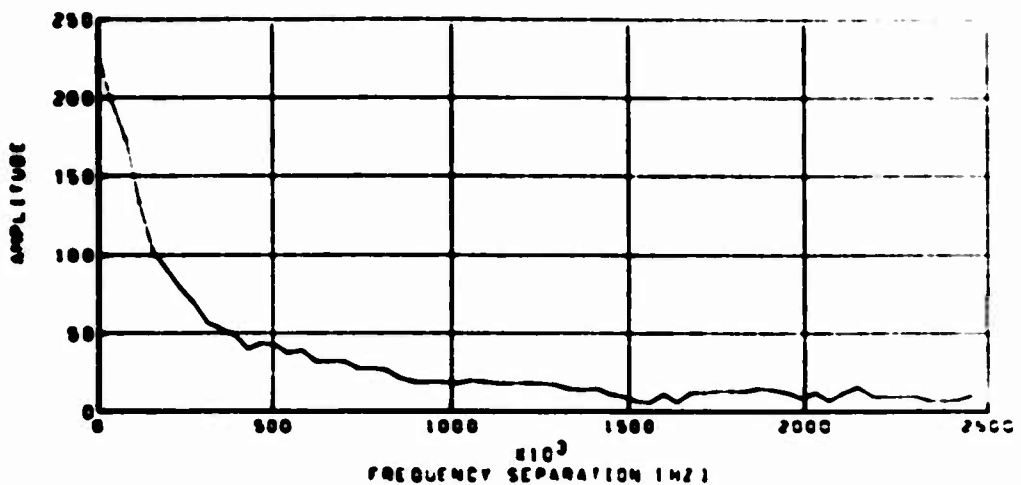


Figure 4-10(b).—Spectra and Autocorrelation Parameters—Vertical Polarization,  
In-plane Geometry

Doppler distribution has a shape which closely resembles gaussian. Both cases are readily explained in terms of the geometrical relationships relating the propagation time delay and Doppler frequency shifts associated with the co-ordinates of the scatter surface. The results are also in accord with theoretical modeling as illustrated in Section 4.2.4 (see Figures 4-16(b) and 4-18(b)).

3. Even though the time autocorrelation function is a Fourier transform pair to the Doppler spectrum we note that its shape is not nearly so dependent upon the aircraft heading. However, it does appear that the in-plane autocorrelation function is somewhat heavier tailed than the cross-plane result. This is a result predicted by the scatter model of Section 4.2.4 (see Figure 4-16(c) and 4-18(c)).
4. In general, the vertical polarization data has heavier tailed delay and Doppler spectra than its horizontal counterpart. This in turn causes the opposite conclusion to hold valid for the time and frequency autocorrelation function. We attribute this to the concept of "Brewster angle fill-in" as previously outlined.
5. Observations pertaining to the grazing angle influence upon the spread of the spectra and autocorrelation functions are given in Section 4.2.3.

In order to relate the intensity of the multipath scatter process to a quantitative measure we derive the channel mean square scatter coefficient. This is defined as the ratio of total scattered energy to the energy incident upon the surface and is obtained for both the horizontal and vertical polarization cases through the use of the following formulation:

$$\Gamma = \frac{\langle |I|^2 \rangle}{\langle |D|^2 \rangle} (G_D/G_I) \quad (4.4)$$

where  $\Gamma$  = mean square scatter coefficient

$\langle |D|^2 \rangle$  = mean square direct path signal; obtained from the quad-helix or multipath antenna direct path component.

$\langle |I|^2 \rangle$  = mean square multipath power obtained by integrating  $S(\tau, \omega)$  over both its delay and Doppler variables.

$G_D/G_I$  = adjustment factor to account for parameters such as the differences between direct and indirect signal ERP\*, gains of the receiver direct and indirect channels, gains of receiver low-pass digital filters, etc.

Figure 4-11 presents the experimentally derived values of  $\Gamma$  as a function of grazing angle. Also shown are relationships corresponding to the product of the Fresnel reflection coefficient ( $R$ ) and the smooth earth divergence factor ( $D$ ) illustrating the result predicted by

\*For the multipath signal the antenna gain is taken to be equivalent to the gain directed toward the specular point. This should not introduce an appreciable error due to the relatively broad-beam characteristics of the antenna and the capability for pointing the antenna toward the effective "glistening" area of the surface.

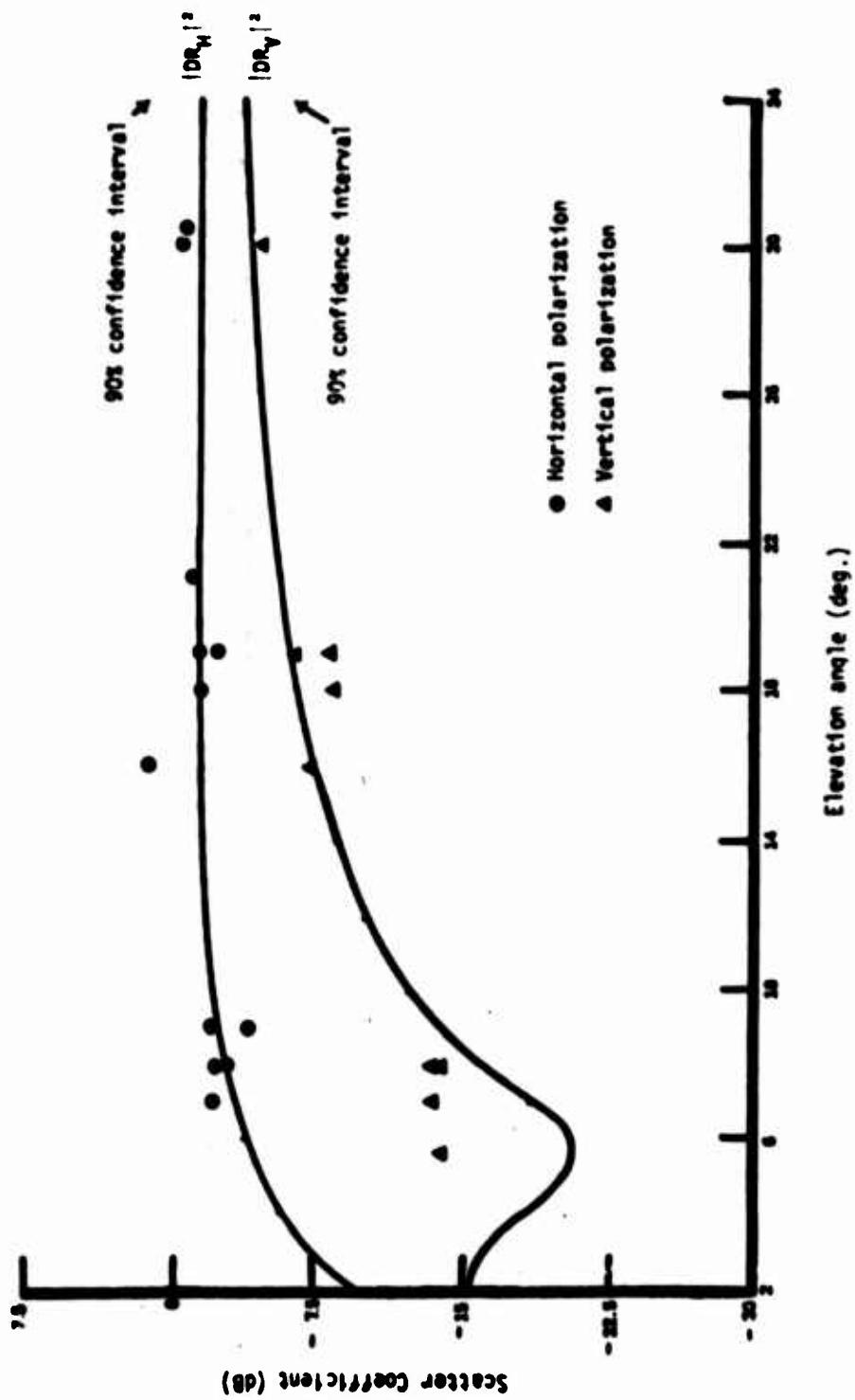


Figure 4.11.—Oceanic RMS Total Scatter Coefficients

"steepest descent" integration technique (Ref. 4-2). Statistical confidence limits have been assumed to be dependent only upon the normalization factors used for the relative ERP of the direct and multipath signals and have been calculated in a similar fashion to that employed in the ATS-5 data analysis (Ref. 4-3). To avoid an appreciable loss of intelligibility the confidence intervals have been plotted about the steepest descent predictions as opposed to placing them on the individual data points.

In general, the data trend, with the exception of the low angle vertical polarization coefficients, is in agreement with the appropriate  $|DR|$  relationship. The positive bias associated with the vertical polarization data for low angles is a result observed for numerous VHF experiments (Ref. 4-4, page 320) and also for ATS-5 L-band multipath (Ref. 4-3). It is attributed to the concept of "Brewster angle fill-in" and is predicted by the surface integration model described in Section 4.2.4 (e.g., at an elevation angle of 7 degrees and rms sea slope of 6 degrees the model yields total mean square relative scattered powers of -2.2 dB and -14.1 dB for horizontal and vertical polarization respectively).

#### 4.2.3 OCEAN SCATTER PARAMETER SPREAD VALUES

The data reduction computer routine determines the 3-dB, 1/e, first moment and second moment spread values of the multipath channel Doppler psd, delay psd, frequency autocorrelation function and time autocorrelation function. In this section we present the 3-dB spread values as a function of grazing angle and polarization. As presented, this spread parameter refers to the expanse over which the function does not drop below one-half the peak value of the distribution. For the delay and Doppler spectra it is the total two-sided value whereas for the autocorrelation functions it is the one-sided value.

The grazing angle dependence of the Doppler spread data is well illustrated in Figure 4-12. That is for an increase in grazing angle we in general observe an increase in Doppler spreading. This is in accord with ATS-5 data (Ref. 4-3) and theoretical predictions based upon "steepest descent" integration which, neglecting minor aircraft altitude variations, yields a Doppler bandwidth relationship of the form:

$$f_s(\gamma) \propto \frac{(f_c)}{c} \sigma_{slope} \sin \gamma |V_1^2 + V_2^2|^{\frac{1}{2}} \quad (4.5)$$

where  $f_s(\gamma)$  = 3-dB Doppler spread

$f_c$  = carrier frequency

$\sigma_{slope}$  = rms surface slope

$V_1$  = aircraft in-plane velocity

$V_2$  = aircraft cross-plane velocity

c = velocity of light

$\gamma$  = grazing angle.

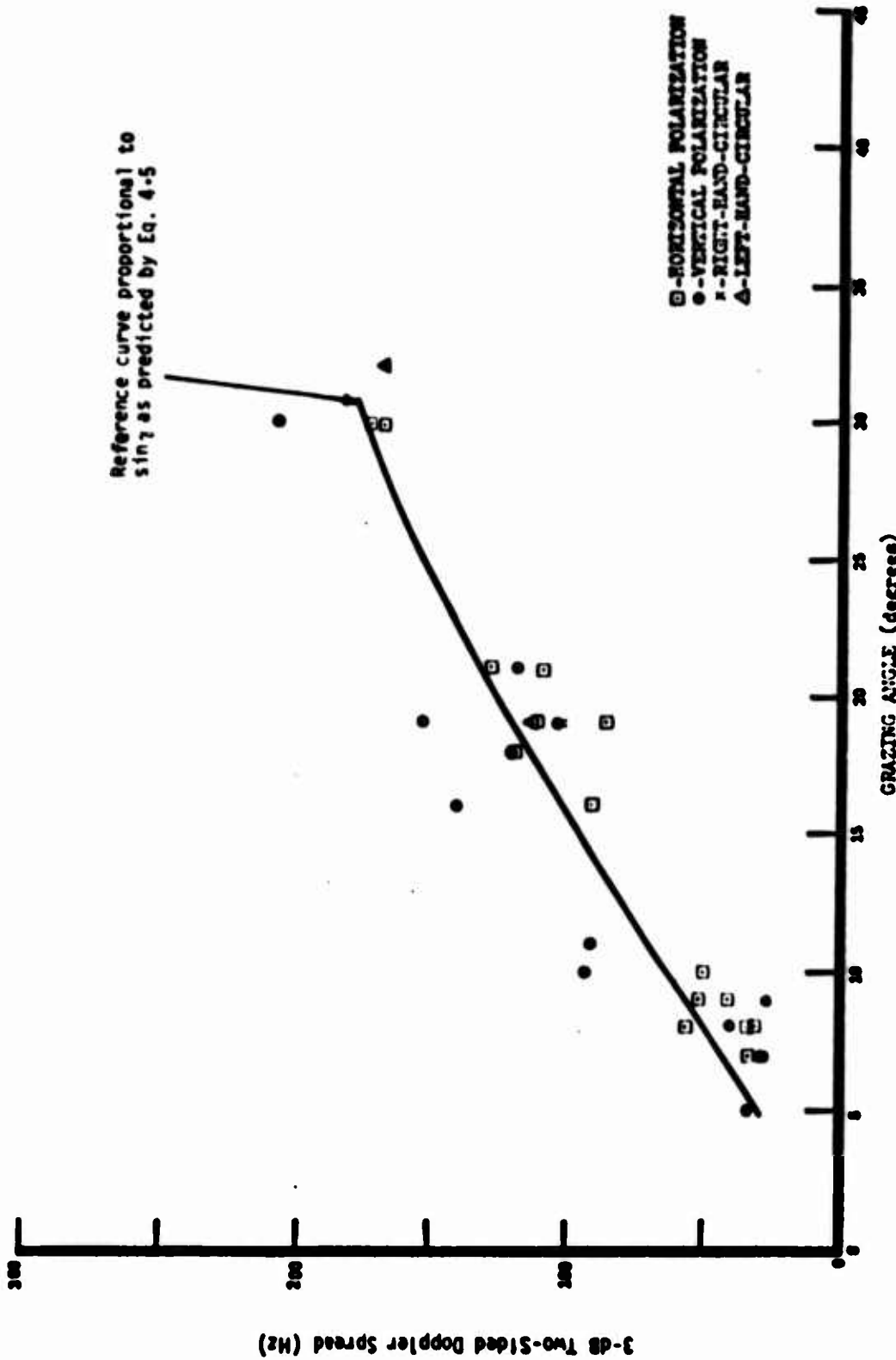


Figure 4-12.-3-dB Oceanic Scatter Doppler Spread

For the flight tests  $(V_1^2 + V_2^2)^{1/2}$  was generally on the order of 200m/sec. Sea surface slope data is not available at this time, thus, we cannot directly relate experiment to theory. However, the trend of the data does appear to substantiate the  $\sin \gamma$  relationship. This is illustrated in Figure 4-12 where we have superimposed an adjusted  $\sin \gamma$  curve on the graph. It is of interest to note that the "steepest descent" derivation of Doppler spread also predicts a gaussian spectral distribution. But as previously outlined the observed Doppler distribution for non cross-plane flight geometry is highly unsymmetrical and thus by definition non-gaussian. However, by folding one side of the Doppler psd over onto the other (e.g., the negative frequencies onto the corresponding positive frequencies) and combining the two we do obtain, a one-sided spectral distribution which resembles a gaussian shape. Heuristically this may account for applicability of the above equation to the data.

One further observation that is to be made concerning the Doppler spread data relates to the noticeable tendency of the vertical polarization results to have a larger spread than the horizontal data. Since horizontal and vertical probes occur simultaneously this cannot be attributed to surface non-stationarity. It is thought to be most likely caused by the previously mentioned concept of "Brewster angle fill-in" which particularly for in-plane geometry will, on a relative basis, cause the negative realm of the Doppler spectra to be heavier tailed for vertical polarization as compared to horizontal polarization (see Section 4.2.4, Figures 4-16(b) and 4-19(b) for model predictions relating to this observation).

The distribution of the observed 3-dB delay spreads as a function of grazing angle is given in Figure 4-13. Typically, the majority of the data indicates that the spreads are contained within the range of 0.3  $\mu$ sec. to 1.5  $\mu$ sec. In comparison with the Doppler spread data it is noted that the grazing angle dependence of the delay spread is relatively unpronounced. The steepest descent integration solutions of Mallincrodt (Ref. 4-5) and Bello (Ref. 4-1) for the delay spectra may be used to obtain an estimate of the 3-dB delay spread grazing angle dependence. Using Bello's formulation we write the delay spectra as:

$$Q(\tau) = \frac{1}{K} \exp \left[ -\frac{\sin \gamma + 1/\sin \gamma}{2K} \tau \right] \times I_0 \left( \frac{(1/\sin \gamma) - \sin \gamma}{2K} \tau \right) \quad (4.6)$$

where  $Q(\tau)$  = delay psd

$\tau$  = delay time

$\gamma$  = grazing angle

$K$  = a parameter embodying the rms sea slope, aircraft altitude and the speed of light.

As previously stated the aircraft altitude was roughly constant for the entire flight series. Thus, in our case  $K$  varies according to the rms slope changes only. Assuming a constant slope we may use the above relationship to predict the grazing angle dependence of the 3-dB spread values. Relative to the spread at 5 degrees,  $\tau_{.5}$  ( $5^\circ$ ), these are:

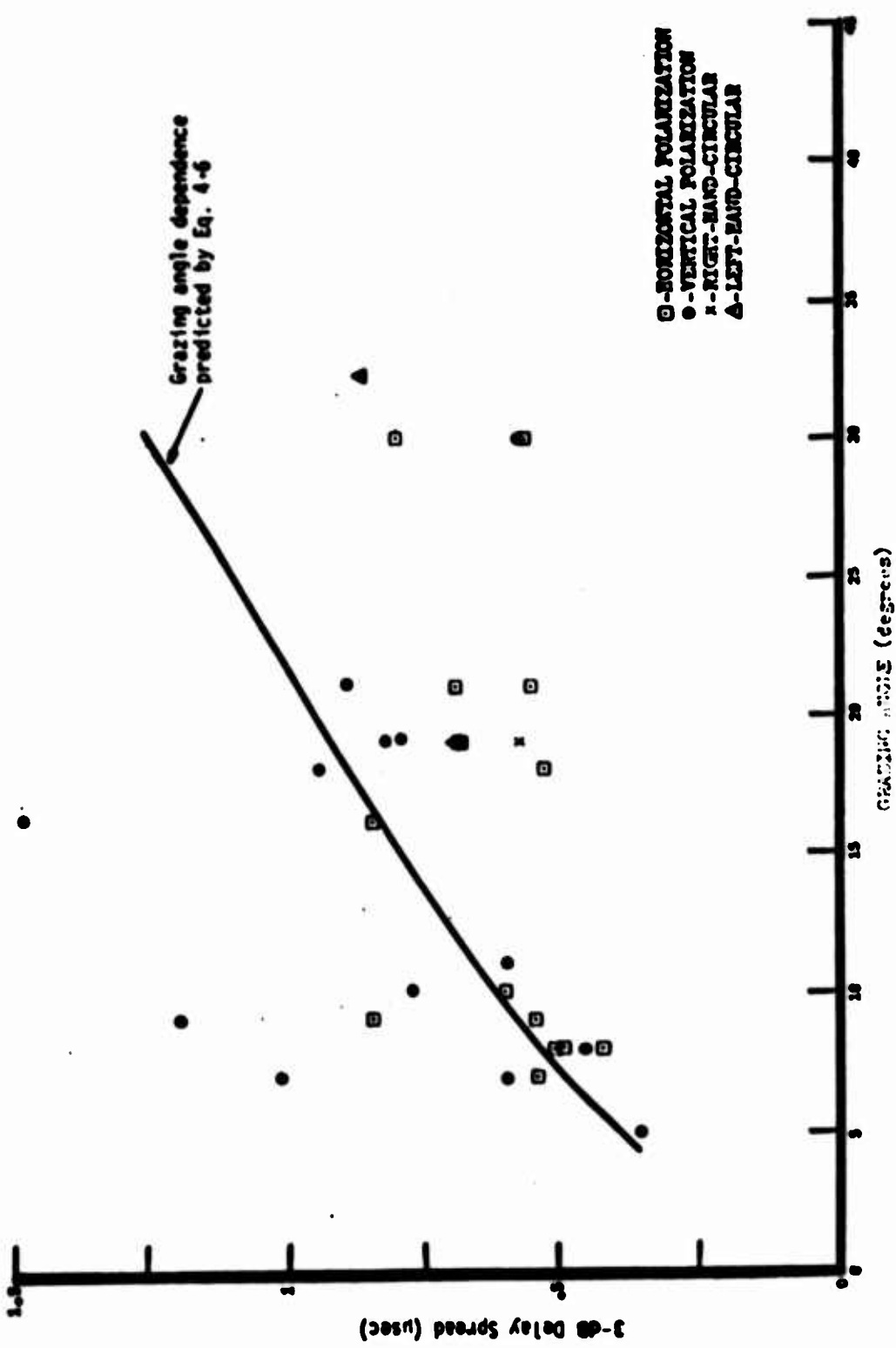


Figure 4-13.—Oceanic Scatter Delay Spread

$$\tau_s(10^\circ)/\tau_s(5^\circ) = 1.5$$

$$\tau_s(20^\circ)/\tau_s(5^\circ) = 2.4$$

$$\tau_s(30^\circ)/\tau_s(5^\circ) = 3.1$$

An adjusted curve representing this relationship has been plotted with the data of Figure 4-13. This indicates an expectation for the 3-dB delay spreads to increase with an increase in grazing angle\*. The dependence is somewhat weak however, (compared to the Doppler spread for example) and thus changes in the surfaces slope on a test-to-test basis could very easily override the grazing angle dependence. This is especially significant since the parameter K is proportional to the square of the rms surface slope.

Data pertaining to the 3-dB frequency coherence bandwidth values for the oceanic scatter are given in Figure 4-14. The observed results are bracketed by a lower limit of 100 kHz and an upper limit of 380 kHz, it is also noted that the coherence bandwidth in general shows a slight tendency to increase with an increase in grazing angle. This is in accord with steepest descent integration predictions [see Staras (Ref. 4-2) or Bello (Ref. 4-1)] which yields the following expression for the frequency correlation function.

$$R(0,\Omega) = \left[ (1+j \frac{2\pi K \Omega}{\sin \gamma}) \cdot (1+j 2\pi K \Omega \sin \gamma) \right]^{-1/2} \quad (4.7)$$

where  $R(0,\Omega)$  = complex frequency correlation function

$\Omega$  = frequency separation

$\gamma$  = grazing angle

K = parameter, as in Equation 4.6, embodying the surface slope, aircraft altitude, and speed of light.

As in the delay spread discussion one may assume K to be constant and thereby generate the grazing angle dependence of  $R(0,\Omega)$ . Relative to the  $5^\circ$  grazing angle the following 3-dB coherence bandwidth relationships are obtained

$$\Omega_s(10^\circ)/\Omega_s(5^\circ) = 1.95$$

$$\Omega_s(20^\circ)/\Omega_s(5^\circ) = 3.3$$

$$\Omega_s(30^\circ)/\Omega_s(5^\circ) = 4.0$$

The curve plotted in Figure 4-14 represents the above grazing angle dependence of the 3-dB coherence bandwidth. Like the delay spread this dependence is somewhat weak, however.

\*It is noted that for larger spread values, e.g., the 20-dB value, the opposite functional relationship is predicted to hold true with the delay spread decreasing for an increase in grazing angle (i.e., the low-grazing angle cases are heavier tailed than the high angle cases).

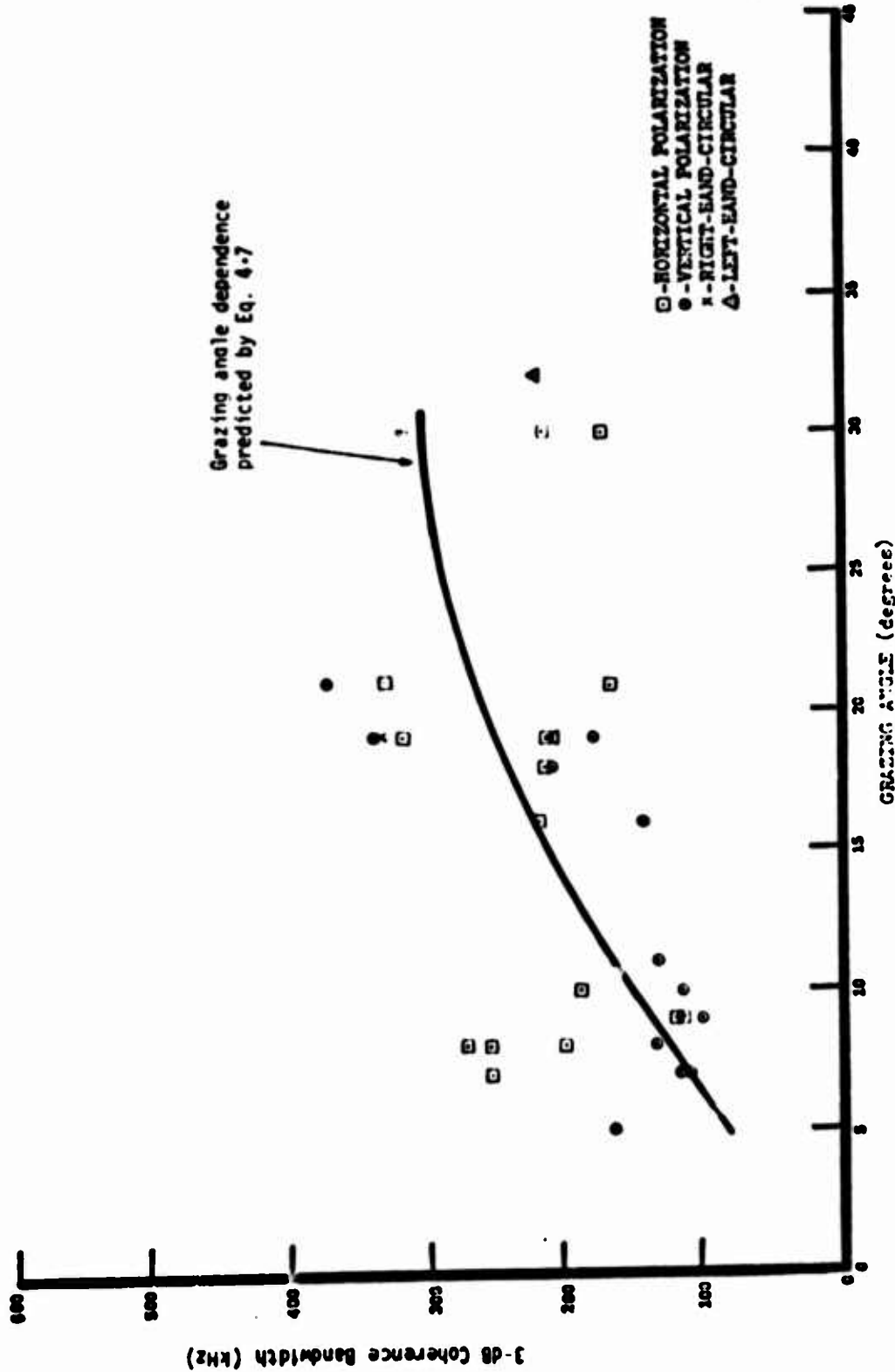


Figure 4-14.—Oceanic Scatter Coherence Bandwidth

the data points appear to bracket theoretical expectation fairly well. The variance of the data about the curve is most likely associated with the differences in rms sea slope that each flight test encountered. It is also noted that for low angle scatter the vertical polarization data is associated with a lower coherence bandwidth than the horizontal data.

The 3-dB values of the oceanic multipath's decorrelation time are plotted versus grazing angle in Figure 4-15. A range from a low of 2 msec to a high of 9 msec is noted together with an increase in decorrelation time for a decrease in grazing angle. Since the Doppler psd and time correlation function are Fourier transform pairs the steepest descent solution to the time correlation function yields a gaussian distribution with spread bandwidth inversely proportional to Equation 4.5; i.e.,

$$\xi_5(\gamma) = \frac{1}{\pi f_5(\gamma)} \propto 1/\sin \gamma \quad (4.8)$$

where  $\xi_5(\gamma)$  = decorrelation time

$f_5(\gamma)$  = Doppler bandwidth spread

$\gamma$  = grazing angle.

In Figure 4-15 the plotted line corresponds to a  $(\sin \gamma)^{-1}$  relationship. Typically the data values tend to bracket this curve although the agreement is not nearly as good as for the Doppler spread data. This is particularly the case for the low angle vertical polarization data and may be attributed to the influence of the enhanced energy in the tails of the Doppler spectra (Brewster angle fill-in) which will result in an increase in the  $\xi=0$  portion of the time autocorrelation function.

#### 4.2.4 COMPARISON WITH PHYSICAL OPTICS SCATTER THEORY

The choice of an appropriate model for the analysis of electromagnetic surface scattering is determined almost exclusively by the roughness characteristics of the reflecting medium. Surfaces are usually classified as slightly rough, very rough, or composite depending upon the magnitude of the height irregularities. In general, different scatter theories are utilized in each of these situations.

For the case of L-band Aerosat oceanic scatter the surface will almost always appear to be very rough; this implies that the following is approximately satisfied:

$$\frac{2\pi}{\lambda} \sigma_H \cos \theta_i > 1.0 \quad (4.9)$$

where  $\lambda$  = electromagnetic wavelength

$\sigma_H$  = standard deviation of surface height irregularities

$\theta_i$  = incident angle of ray upon the surface as measured from the normal.

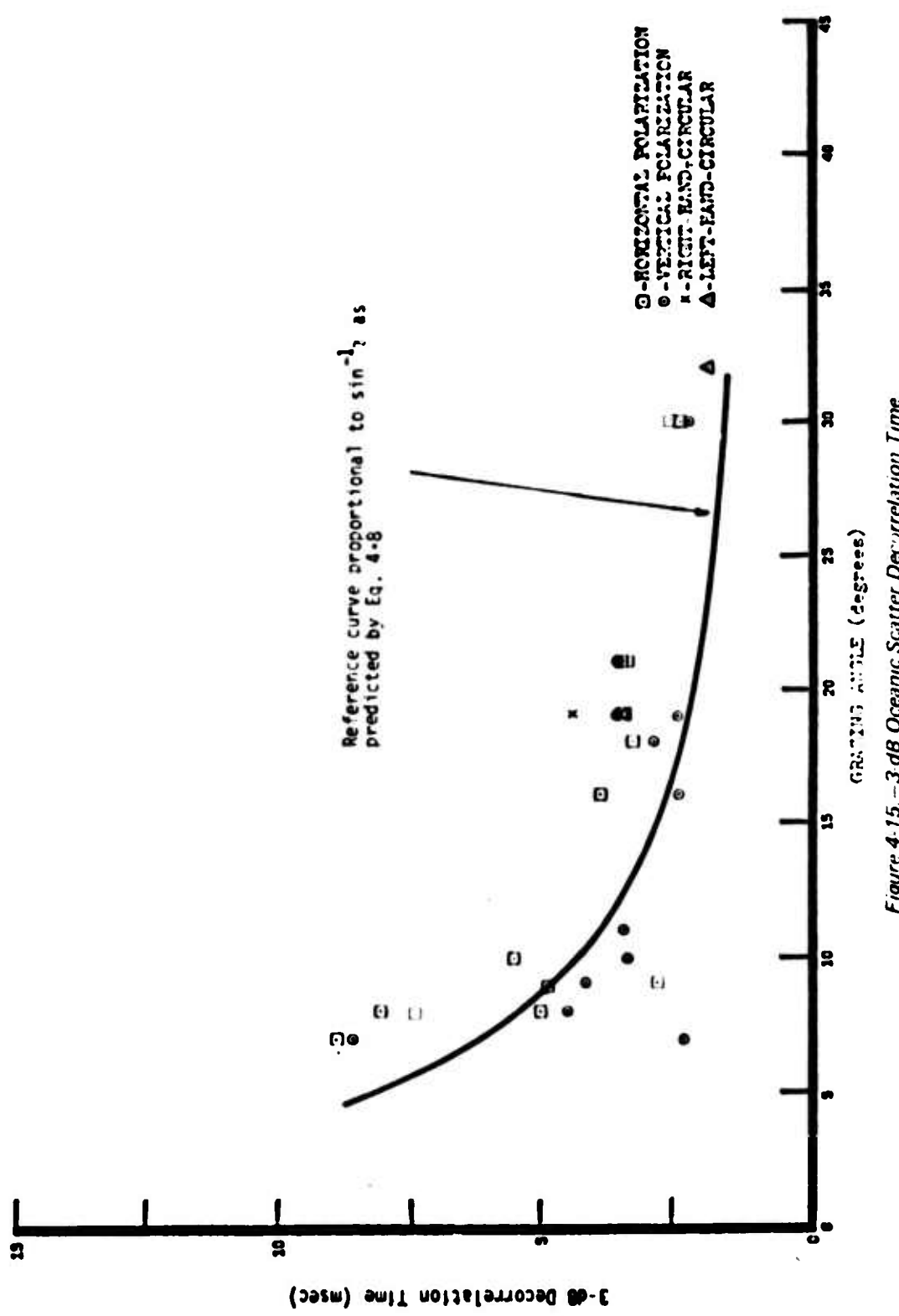


Figure 4-15.-3 dB Oceanic Scatter Decorrelation Time

**Analysis of scattering from very rough surfaces is usually developed through the physical optics tangent-plane method. Commonly called the Kirchhoff approximation, this model is based upon the assumption of a locally plane surface over the distance of many wavelengths. This is considered to be satisfied if the radius of curvature of the surface undulations is much greater than  $\lambda$ .**

**Under the assumption that the surfaces height probability distribution and spatial correlation function are gaussian\* the "very rough" surface configuration of the physical optics scatter model is completely described by the surfaces electrical characteristics and rms slope.**

**For this report we employ the vector formulation of the physical optics model and are thus able to properly account for the polarization dependencies of each particular scattering facet on the surface. Due to the immense complexity of this model it is not possible to arrive at adequate channel parameter solutions in a closed form. This is circumvented through use of a computerized technique suggested by Peake's work (Ref. 4-7), which subdivides the spherical scatter surface into incrementally small areas and then determines the scatter cross-section (including polarization transformation factors), Doppler shift, and time delay associated with each area. At the receiver the complex vector representation of the scattered signal is coupled to the antenna characteristics; this provides an estimation of the received power from the particular surface patch and allows the channel delay-Doppler scatter function to be constructed. From  $S(\tau, \omega)$ , steps identical to those described in Section 4.1 are employed to determine the channel delay spectrum, Doppler spectrum, time autocorrelation function, frequency autocorrelation function and total energy content.**

**To correlate the experimental observations with model predictions, the model is applied for a mid-angle case ( $\sim 190^\circ$ ) where the transmitted polarization is horizontal with flight geometries corresponding to in-plane,  $45^\circ$  relative heading and cross-plane. These sets of theoretically predicted results are given in Figures 4-16 through 4-18 respectively. Channel parameter predictions for vertically polarized in-plane flight geometry are given in Figure 4-19. In all cases the rms sea slope (total) was assumed to be 6 degrees\*\* the rms surface height was taken as 1 meter and the aircrafts altitude and velocity were set at 10 km and 200 m/sec, respectively.**

**As an aid in visually comparing the predicted results with the experimental measurements a cross-reference in Table 4-1 is given. In general we observe that a high degree of similarity between the theoretical model predictions\*\*\* and experimental distributions is in evidence.**

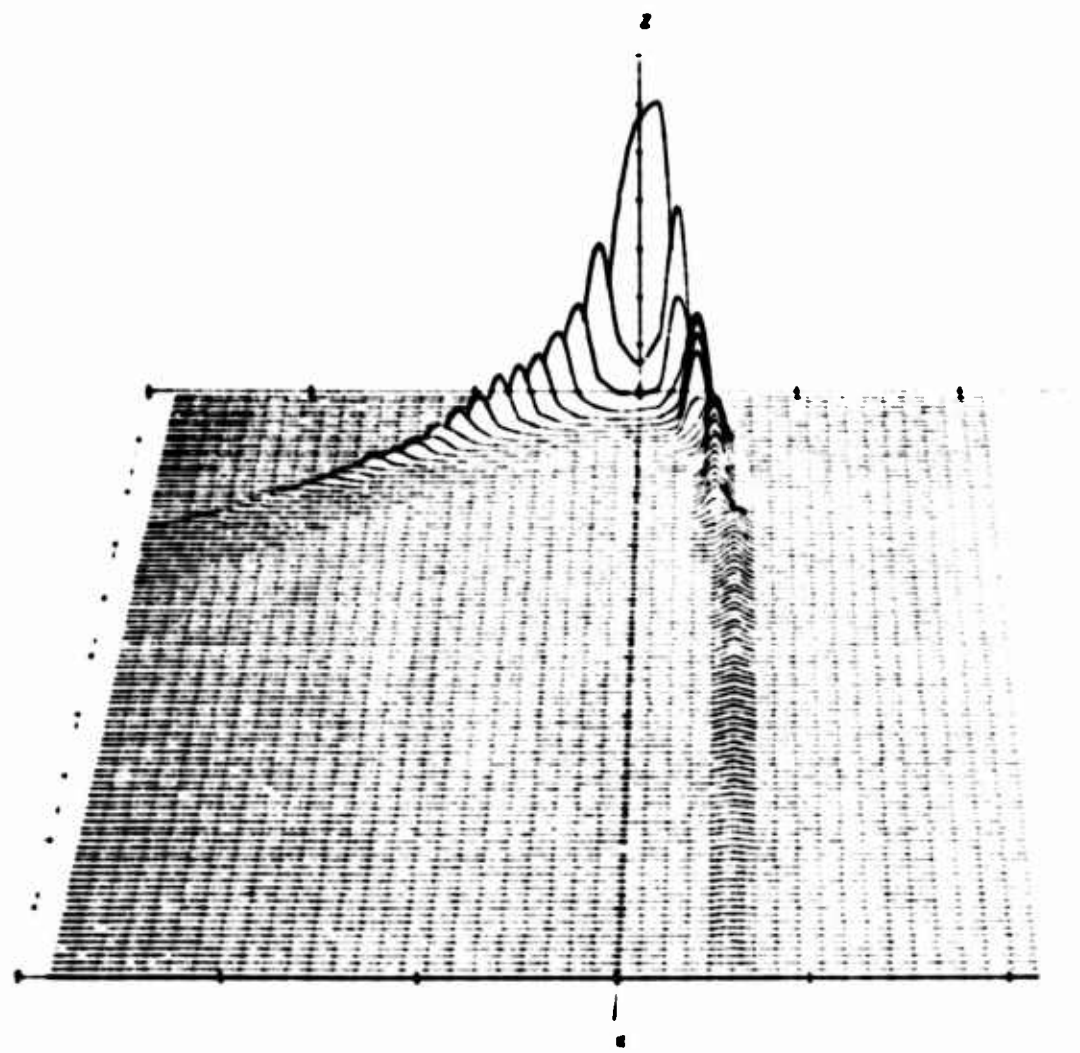
---

\*Assumptions in accord with experimental findings of Cox and Munk (Ref. 4-6).

\*\*Roughly equivalent to the average rms filtered slope associated with the ATS-5 sea state data.

\*\*\*The prediction model segregates the multipath returns into Doppler bins of specified width, which for this analysis were on the order of 12 Hz. This accounts for the piecewise constant, step-like appearance for the delay time dependence of the positive Doppler spectral "hump" associated with the in-plane  $S(\tau, \omega)$  function. The modest dc frequency bias that is visible on the cross-plane Doppler spectrum also results from the quantized nature of the Doppler bins in the model. These program artifacts are reduced by decreasing the width of the Doppler bins.

DELAY-DOPPLER SCATTER FUNCTION



AXIS  
 X DELAY TAP (.8 MICROSEC. WIDTH)  
 Y DOPPLER FREQUENCY (1000 Hz)  
 Z DELAY-DOPPLER PSD (LINEAR)

	MINIMUM	MAXIMUM	INCREMENT
X	00	100.00	10.00
Y	-300.00	300.00	100.00
Z	.00	.03	.03

*Figure 4-16(a). - Model Predicted Oceanic Scatter Parameters - Horizontal Polarization, In-plane Geometry*

DELAY AND DOPPLER SPECTRA

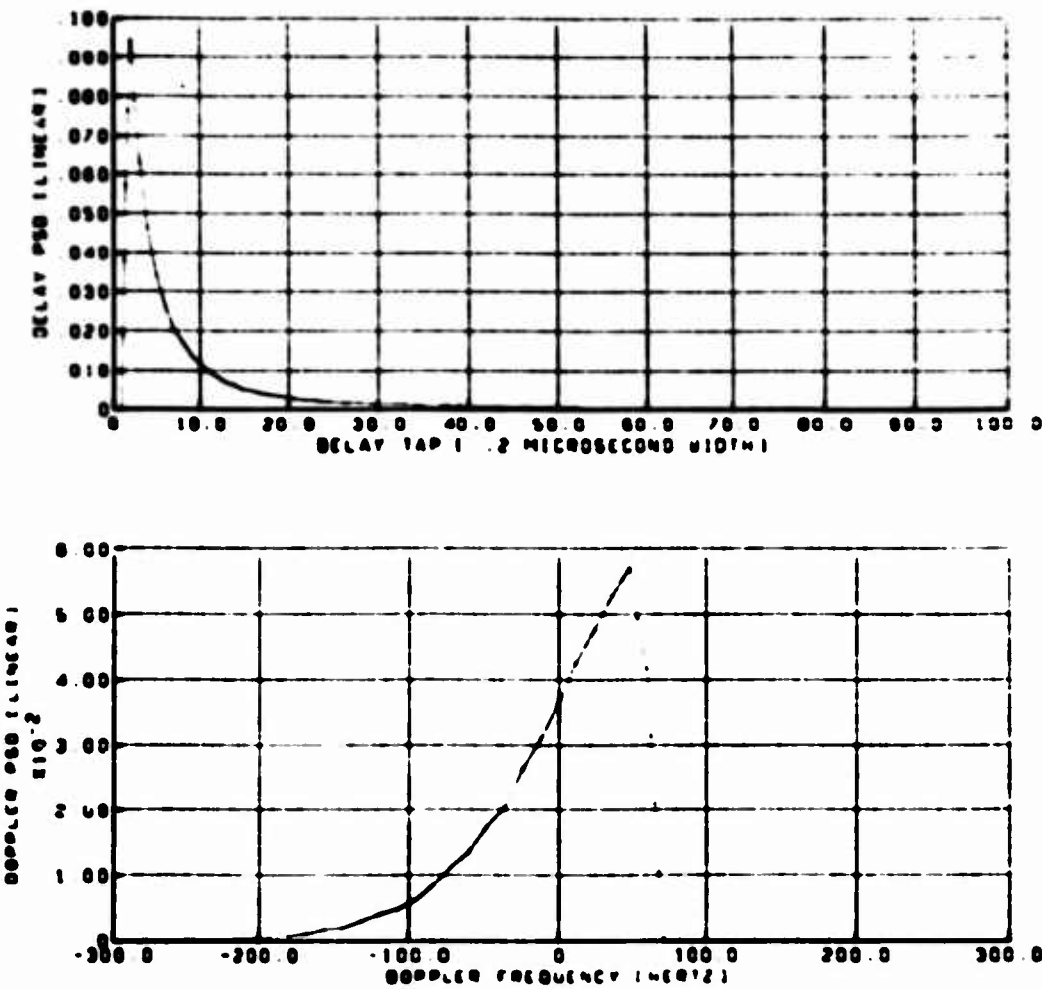


Figure 4-16(b).—Model Predicted Oceanic Scatter Parameters—Horizontal Polarization,  
In-plane Geometry

AUTOCORRELATION FUNCTION

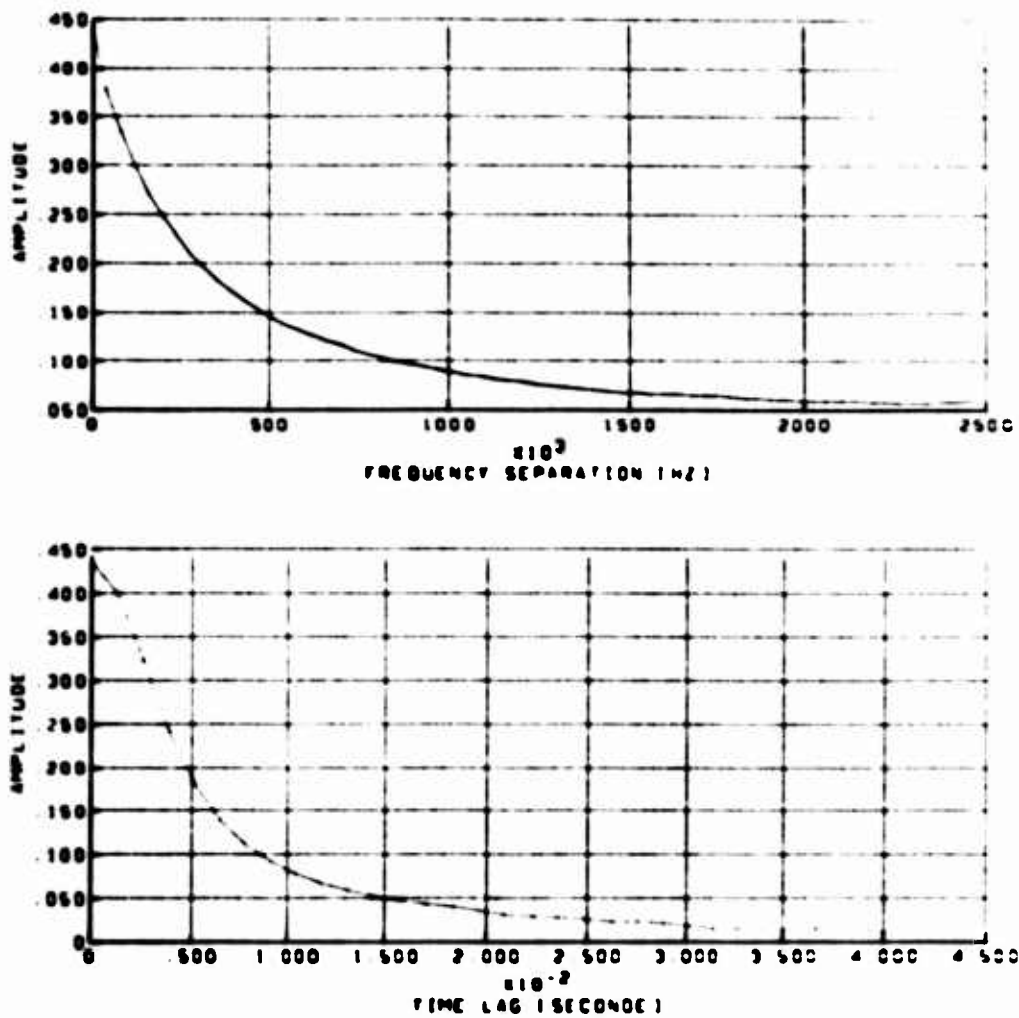
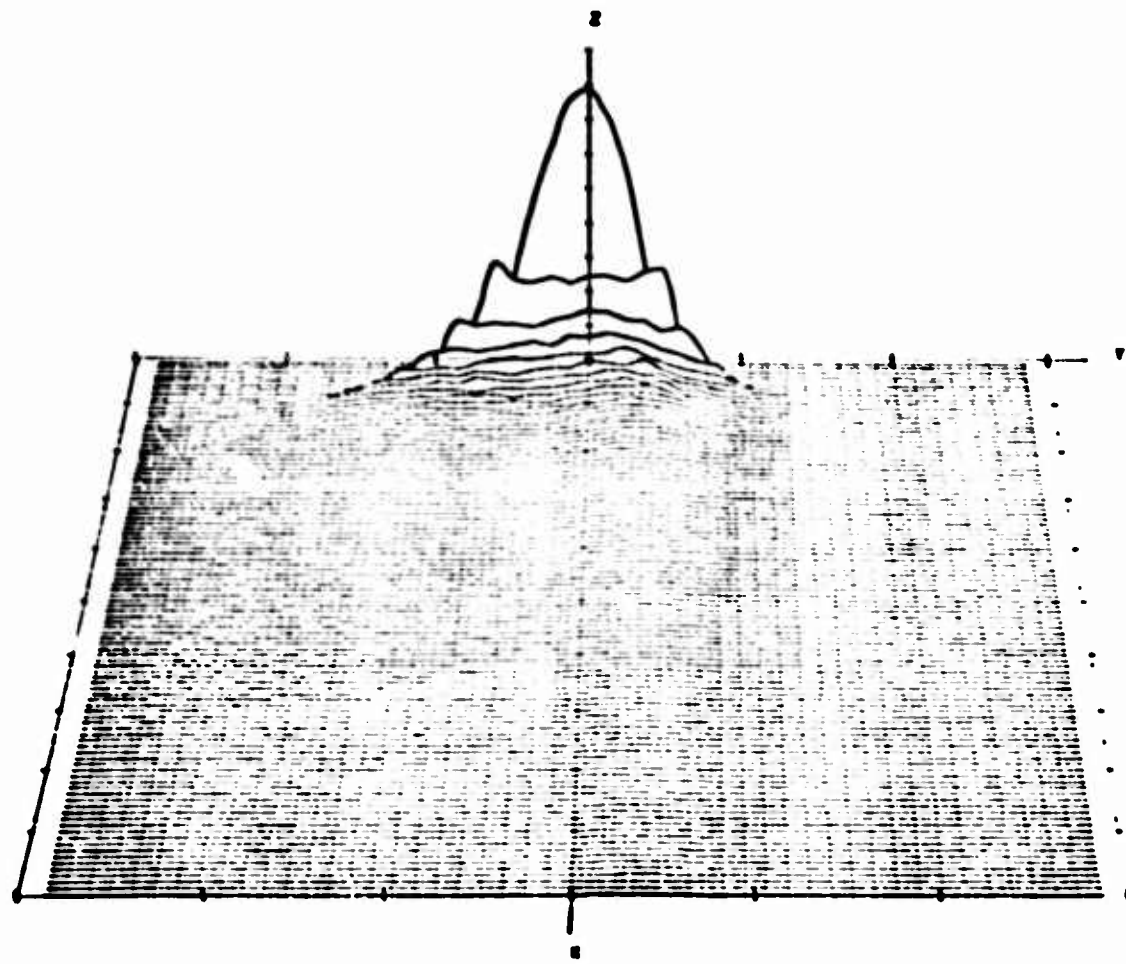


Figure 4-16(c).—Model Predicted Oceanic Scatter Parameters—Horizontal Polarization,  
In-plane Geometry

DELAY-DOPPLER SCATTER FUNCTION



AXIS

X DELAY TAP 1 .8 MICROSEC (10741)  
Y DOPPLER FREQUENCY 1MFR121  
Z DELAY-DOPPLER PSD (LENEAR1)

MINIMUM MAXIMUM INCREMENT

	MINIMUM	MAXIMUM	INCREMENT
X	.00	100.00	10.00
Y	-300.00	300.00	100.00
Z	.00	.02	.00

Figure 4-17(a).—Model Predicted Oceanic Scatter Parameters—Horizontal Polarization,  
 $45^{\circ}$  Heading

DELAY AND DOPPLER SPECTRA

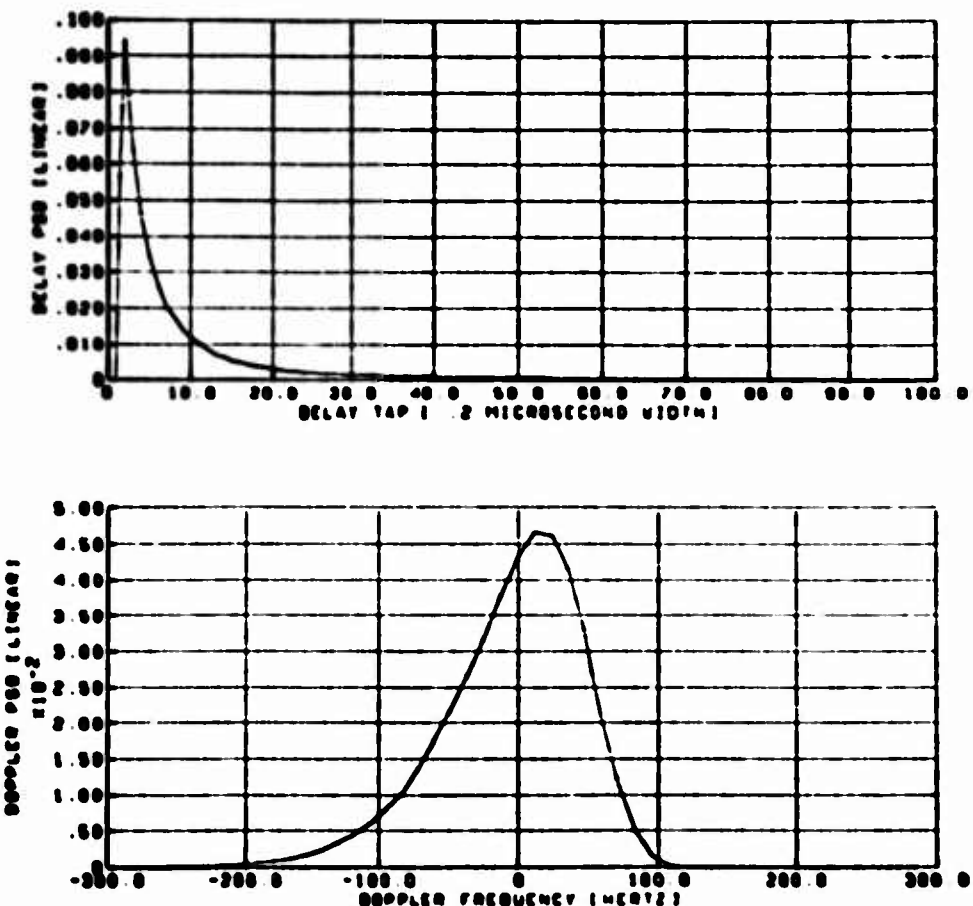


Figure 4-17(b).—Model Predicted Oceanic Scatter Parameters—Horizontal Polarization,  
45° Heading

AUTOCORRELATION FUNCTION

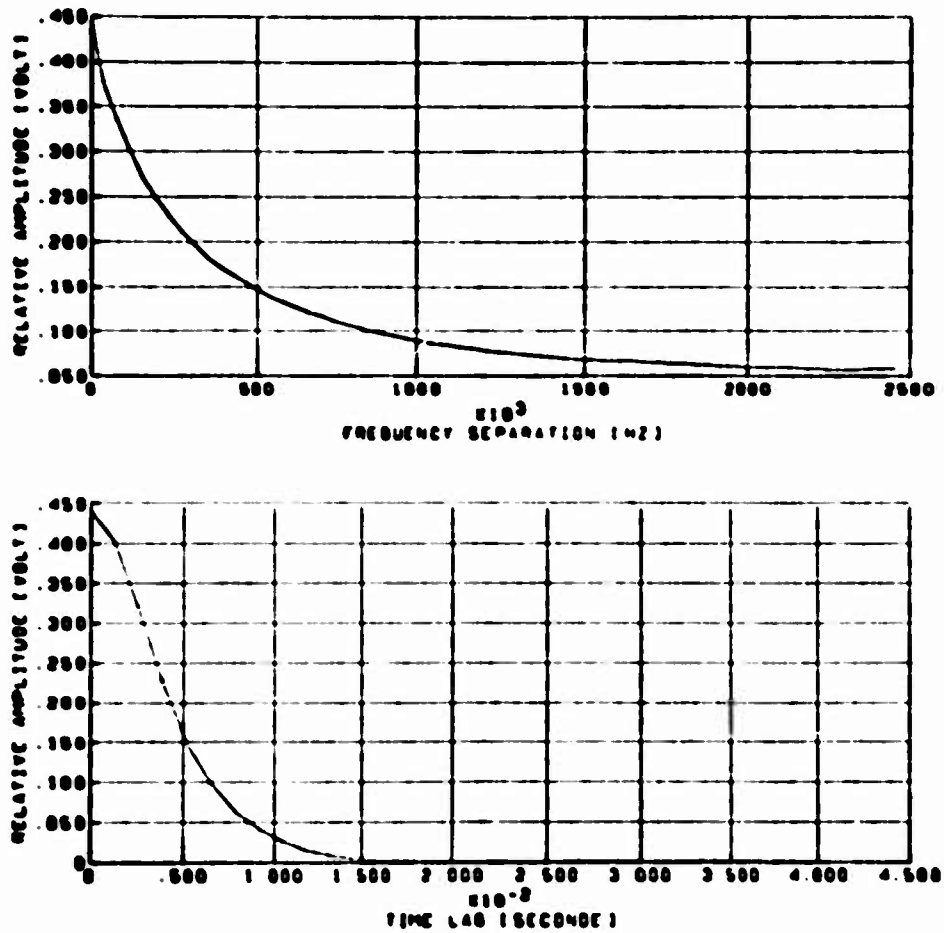
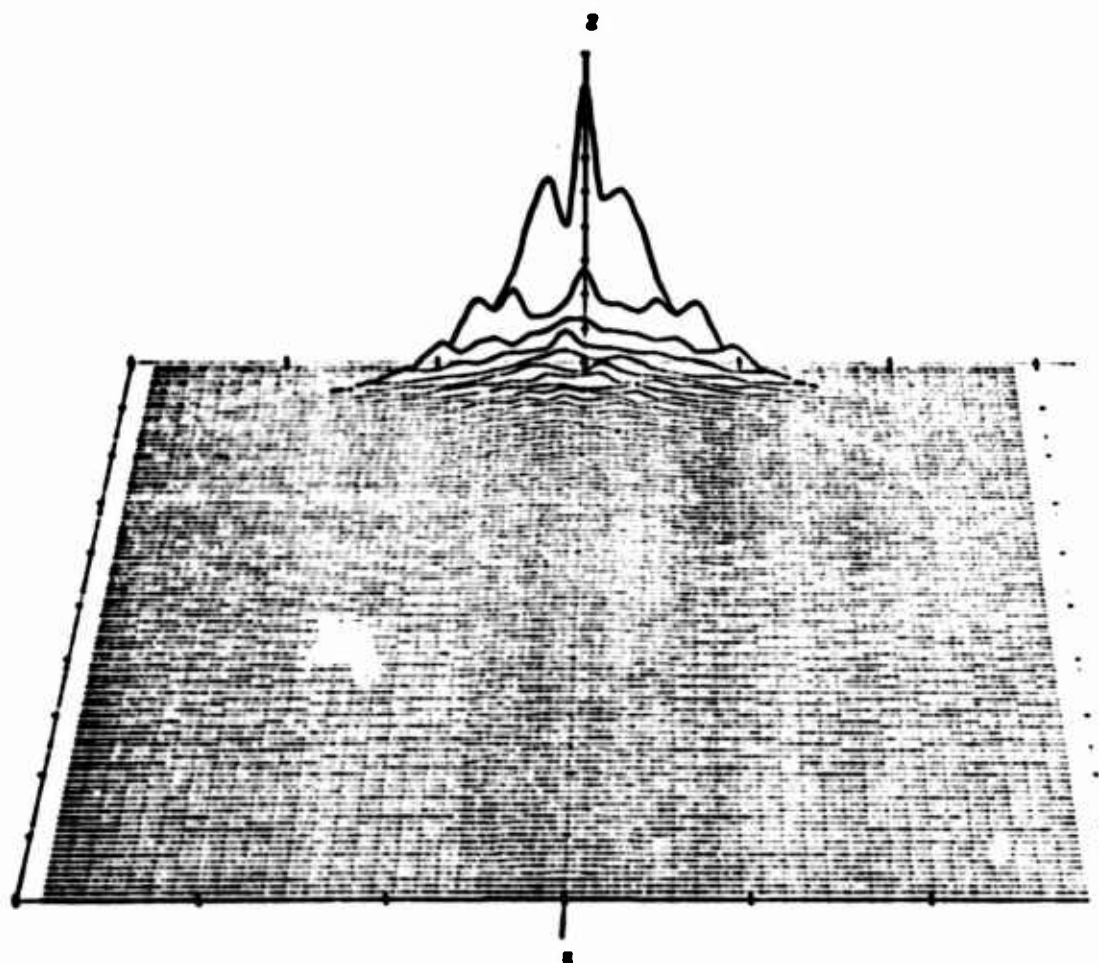


Figure 4-17(c).—Model Predicted Oceanic Scatter Parameters—Horizontal Polarization,  
45° Heading

DELAY-DOPPLER SCATTER FUNCTION



AXIS  
X DELAY TAP 1 .2 MICROSEC. (MSEC)  
Y DOPPLER FREQUENCY (HERTZ)  
Z DELAY-DOPPLER PSD (LINEAR)

MINIMUM MAXIMUM INCREMENT  
.00 100.00 10.00  
-300.00 300.00 100.00  
.00 .02 .00

Figure 4-18(a). - Model Predicted Oceanic Scatter Parameters—Horizontal Polarization,  
Cross-plane Geometry

DELAY AND DOPPLER SPECTRA

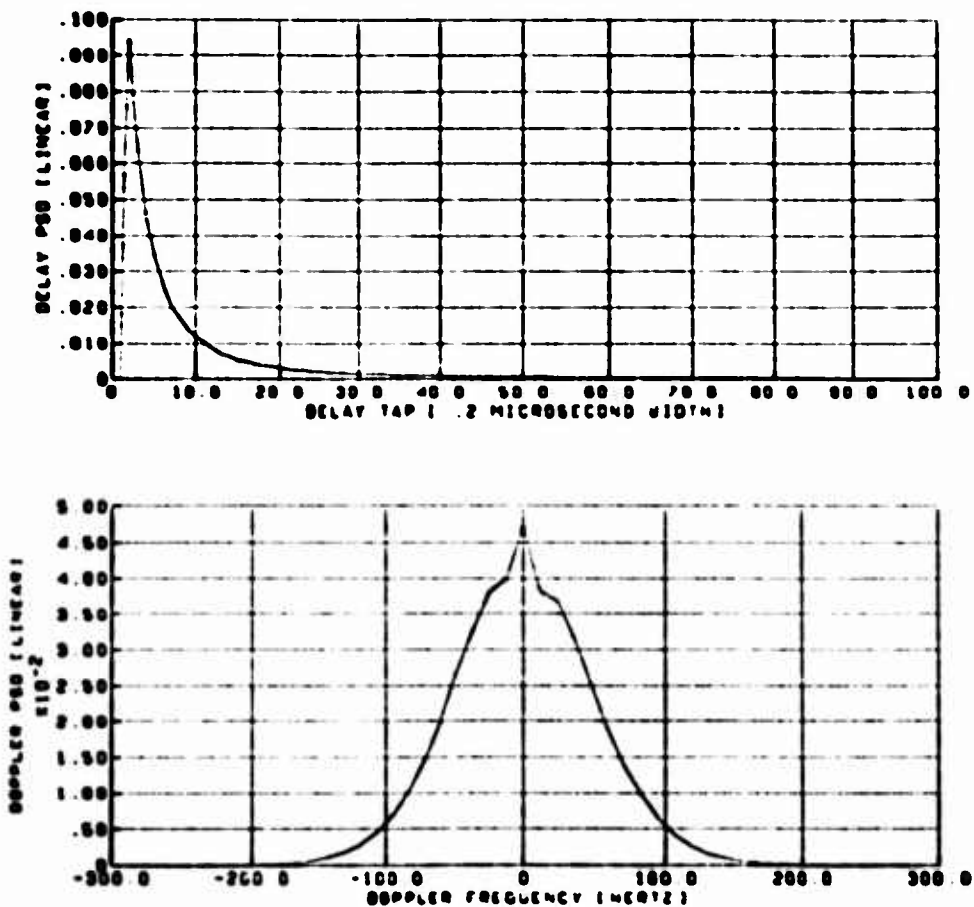


Figure 4-18(b). -Model Predicted Oceanic Scatter Parameters-Horizontal Polarization,  
Cross-plane Geometry

AUTOCORRELATION FUNCTION

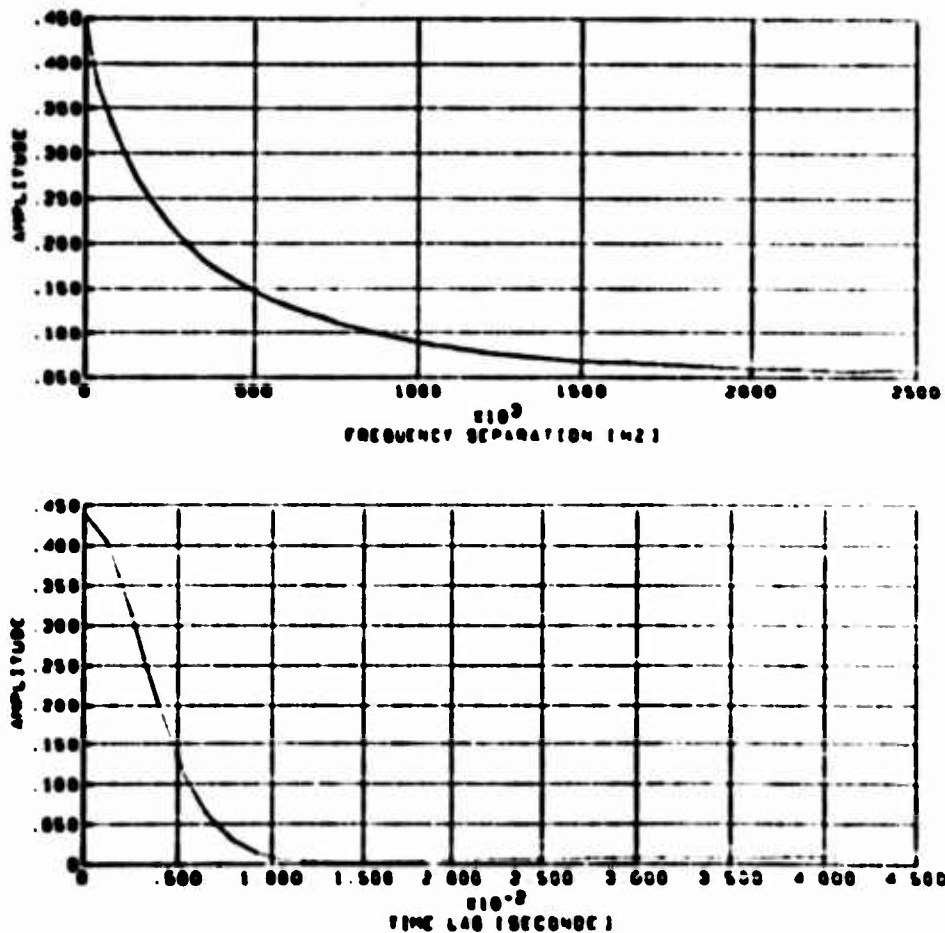
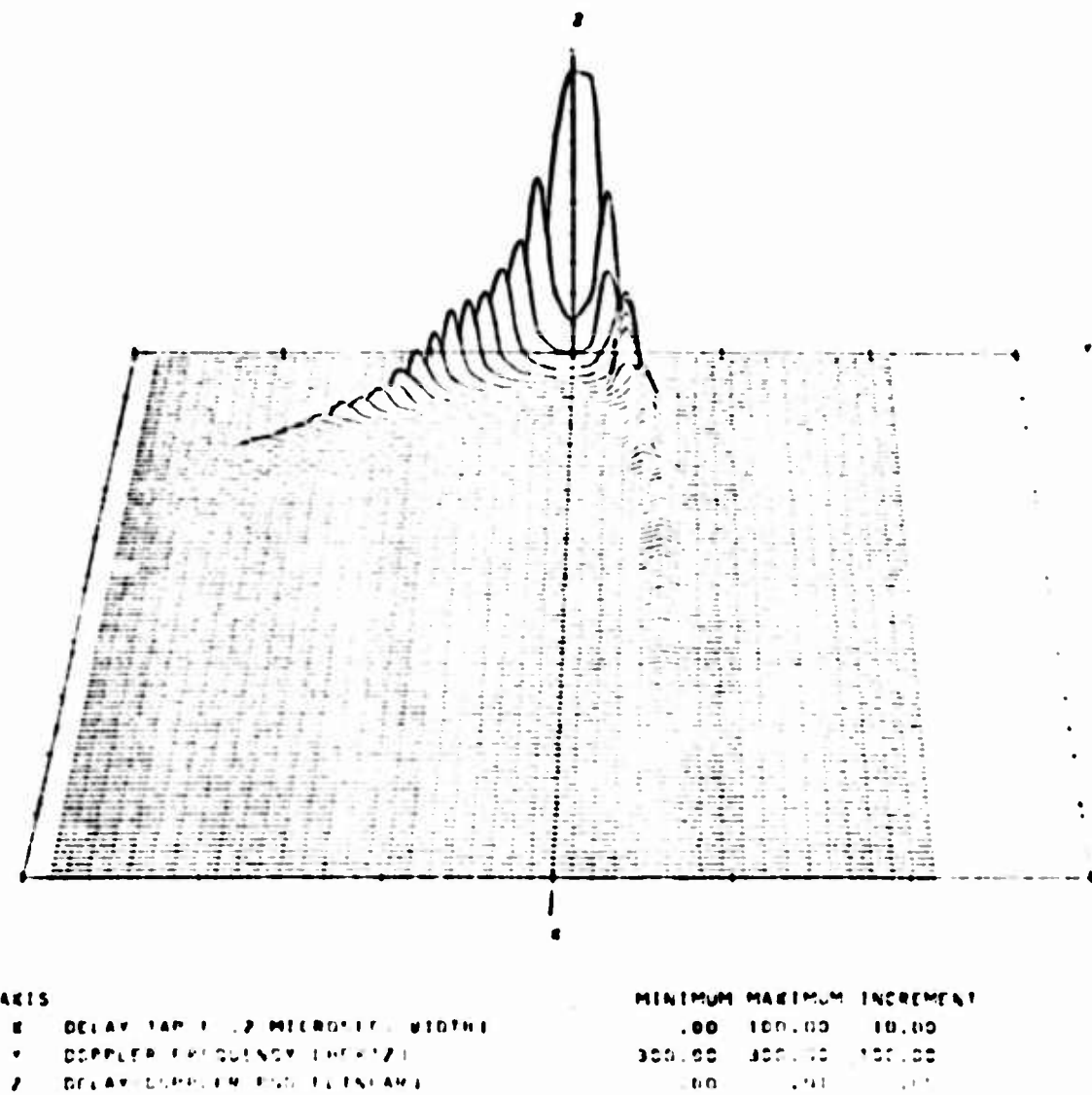


Figure 4-18(c). - Model Predicted Oceanic Scatter Parameters - Horizontal Polarization, Cross-plane Geometry

DELAY-DOPPLER SCATTER FUNCTION



*Figure 4-19(a). - Model Predicted Oceanic Scatter Parameters - Vertical Polarization, In-plane Geometry*

DELAY AND COUPLED SPECTRA

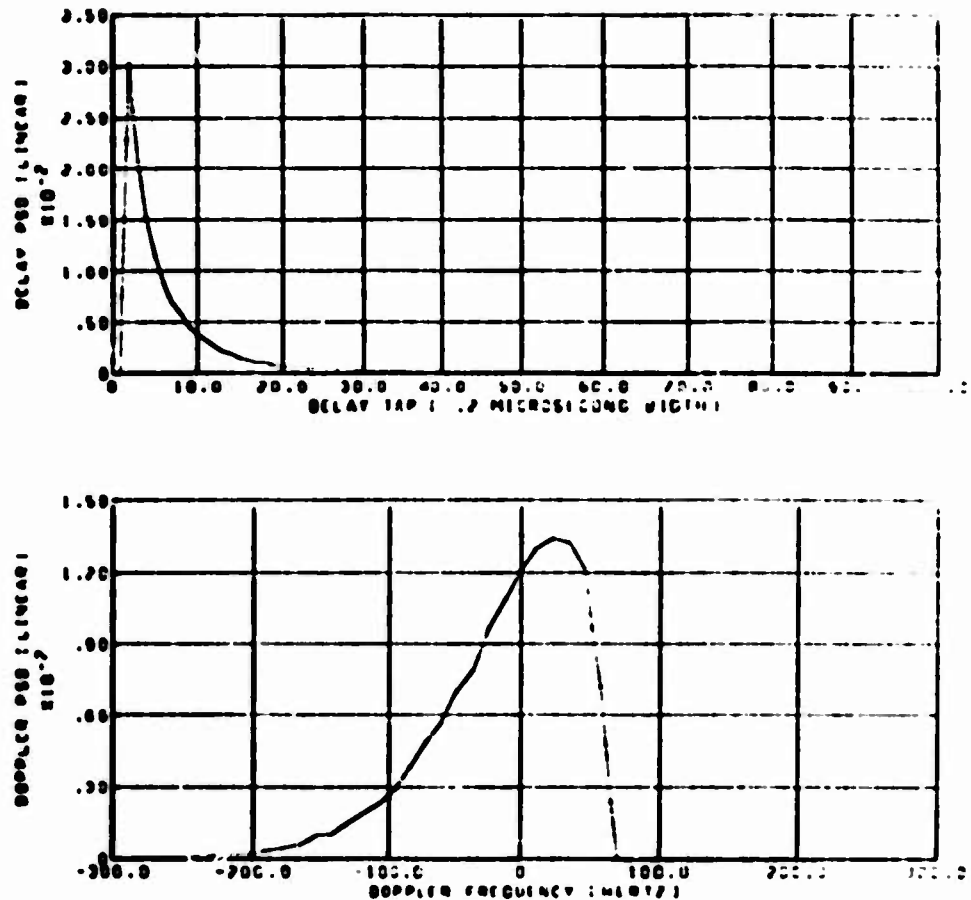


Figure 4-19(b).—Model Predicted Oceanic Scatter Parameters—Vertical Polarization,  
In-plane Geometry

AUTOCORRELATION FUNCTION

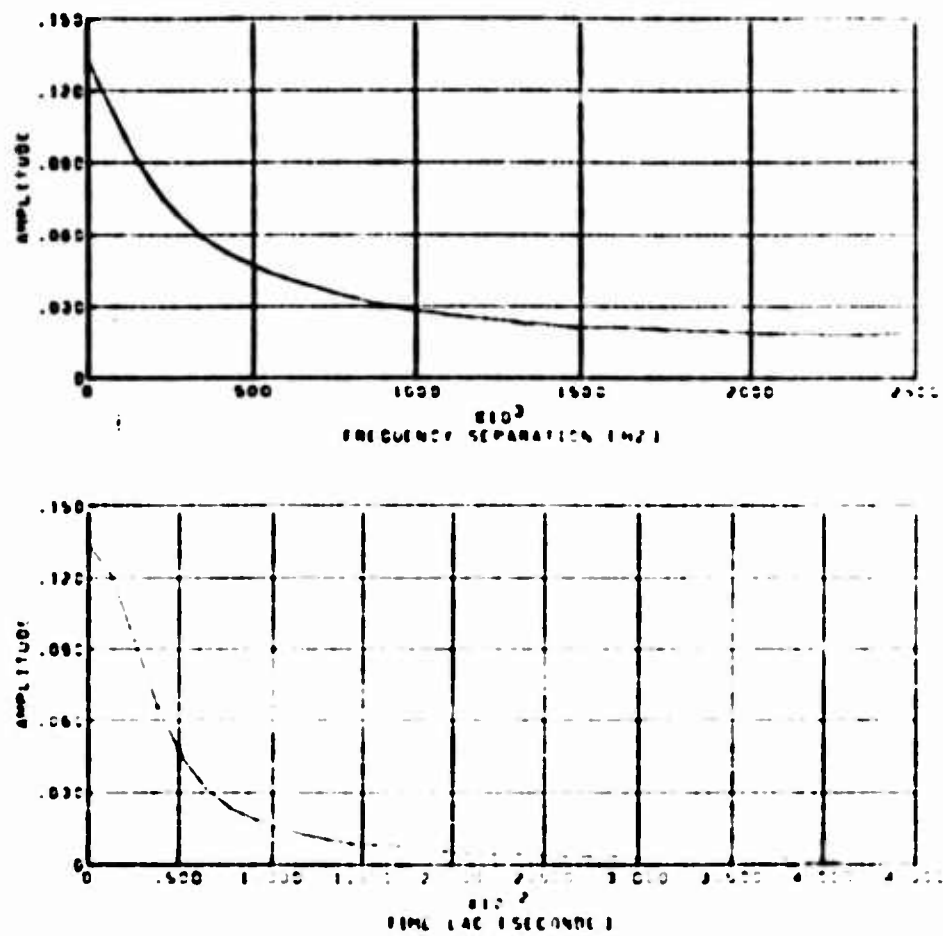


Figure 4-19(c). -Model Predicted Oceanic Scatter Parameters--Vertical Polarization,  
2-D plane geometry

The majority of these correlations have been referred to in previous sections during discussions pertaining to observed channel parameter characteristics. Slight departures between the two data sets could be caused by modeling deficiencies or, as is thought to be the case, by differences in the actual and assumed slopes and also by the fact that the probing antenna is not perfectly isotropic.

A listing of the scatter model predicted 3-dB spread values and rms total energies is given in Table 4.2. Comparing these results to the test data presented in Figures 4-12 through 4-15 indicates that the model emulation is in general accord with the experimental observation.

**Table 4-1.-Cross-Reference for Model and Measurement Comparison**

Parameter	Polarization	Flight geo	Predicted (figure)	Measured (figure)
$S(\tau, \omega)$	Horizontal	In-Plane	4-16(a)	4.3
$Q(\tau), D(\omega)$	"	"	4-16(b)	4.7(a)
$R(\xi, \omega), R(0, \Omega_2)$	"	"	4-16(c)	4.7(b)
$S(\tau, \omega)$	"	45° Heading	4-17(a)	4.4
$Q(\tau), D(\omega)$	"	"	4-17(b)	4.8(a)
$R(\xi, \omega), R(0, \Omega_2)$	"	"	4-17(c)	4.8(b)
$S(\tau, \omega)$	"	Cross-Plane	4-18(a)	4.5
$Q(\tau), D(\omega)$	"	"	4-18(b)	4.9(a)
$R(\xi, \omega), R(0, \Omega_2)$	"	"	4-18(c)	4.9(b)
$S(\tau, \omega)$	Vertical	In-Plane	4-19(a)	4.6
$Q(\tau), D(\omega)$	"	"	4-19(b)	4.10(a)
$R(\xi, \omega), R(0, \Omega_2)$	"	"	4-19(c)	4.10(b)

**Table 4.2.-Emulated Oceanic Scatter Channel Spread and RMS Energy Values**

Test condition	3-dB Spread parameter				RMS scatter coefficient
	$\tau_{.5}$	$\tau_{.5}$	$\xi_{.5}$	$\Omega_{.5}$	
Vertical Polarization In-Plane	105 Hz	.58 $\mu$ sec	3.9 msec	270 kHz	5.7 dB
Horizontal Polarization In-Plane	86 Hz	.58 $\mu$ sec	4.5 msec	255 kHz	0.6 dB
Horizontal Polarization Cross-Plane	105 Hz	.58 $\mu$ sec	3.8 msec	255 kHz	0.6 dB
Horizontal Polarization 45° Heading Offset	105 Hz	.58 $\mu$ sec	3.9 msec	255 kHz	-0.6 dB

### **4.3 CONUS MULTIPATH TEST RESULTS**

A rather extensive data base of CONUS forward scatter multipath has been obtained. This collection covers a range of grazing angles from  $20^\circ$  to  $45^\circ$ , and a variety of terrain electrical characteristics (snow covered to salt flats), surface roughness (flat plains to mountainous), and vegetation coverages (heavily forested to barren). In addition several hours of data pertaining to multipath reflections in the approach, landing, and taxi phases of large airport environments was obtained.

Due to the non-isotropic nature of the overland scatter surface the analysis and modeling of the CONUS multipath channel is not nearly as straight forward as the oceanic case and almost necessitates that each return signal structure be treated as a separate entity. In this section we present sample delay-spectra time histories which dramatically illustrate the non-stationarity of the multipath return. Data is also provided to illustrate a portion of the analyzed scatter function signatures and their associated two-dimensional integral and transformation properties.

With respect to the airport landing taxi scatter data we present several sample delay spectra which are representative of the data obtained for the majority of the airport maneuvers.

The results presented herein pertain primarily to the winter series (February) and thus for the most part correspond to snow covered terrain. Representative data for the fall campaign are available in a previous Interim Technical Report (Ref. 4-8). A subset of one of the most interesting fall campaign delay spectra time histories is also included in this document. In total, both sets of data represent, what is considered to be, sufficient information to achieve a general familiarity with the non-stationarity of the CONUS channel and to obtain some first order estimates of its Doppler and delay spectra characteristics.

#### **4.3.1 CONUS DELAY SPECTRA TIME HISTORY**

To date, several hours of CONUS data have been analyzed to determine the channel delay spectra time history. An obvious observation from this collection of data has been the expected high degree of signal structure non-stationarity. We present an example of this for a particular leg associated with the flight test conducted on February 20, 1975. Pertinent system parameters are given below:

flight direction: in-plane (towards ATS-6)  
airplane speed: approx. 190 m/sec.  
airplane altitude: approx. 9.5 km (31,000 ft)  
elevation angle: approx. 30 degrees

Using a log of the KC-135's INS latitude and longitude outputs, the specular point trajectory for this leg has been superimposed upon a terrain profile map as shown in Figure 4-20. The channel delay spectra time history for horizontally polarized signals is illustrated in Figure 4-21. A probing rate of 5 MHz was employed for this test. To enhance the output resolution the mean-square energy outputs corresponding to only a 40-tap region in the vicinity of the most active return (rather than all 112 taps) have been plotted. Sample space averaging was performed over a time interval of roughly 2 seconds (305 points); this accounts for the

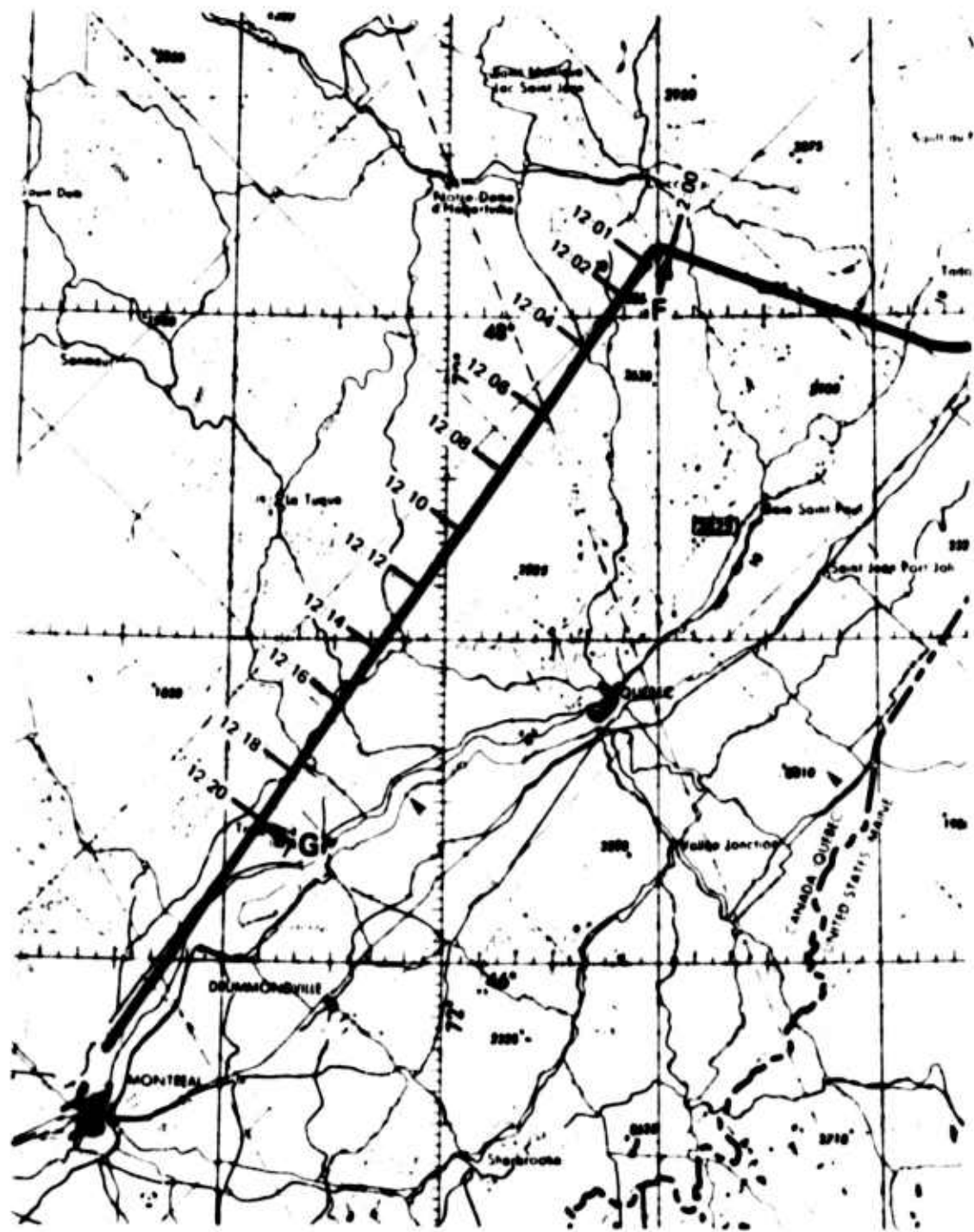
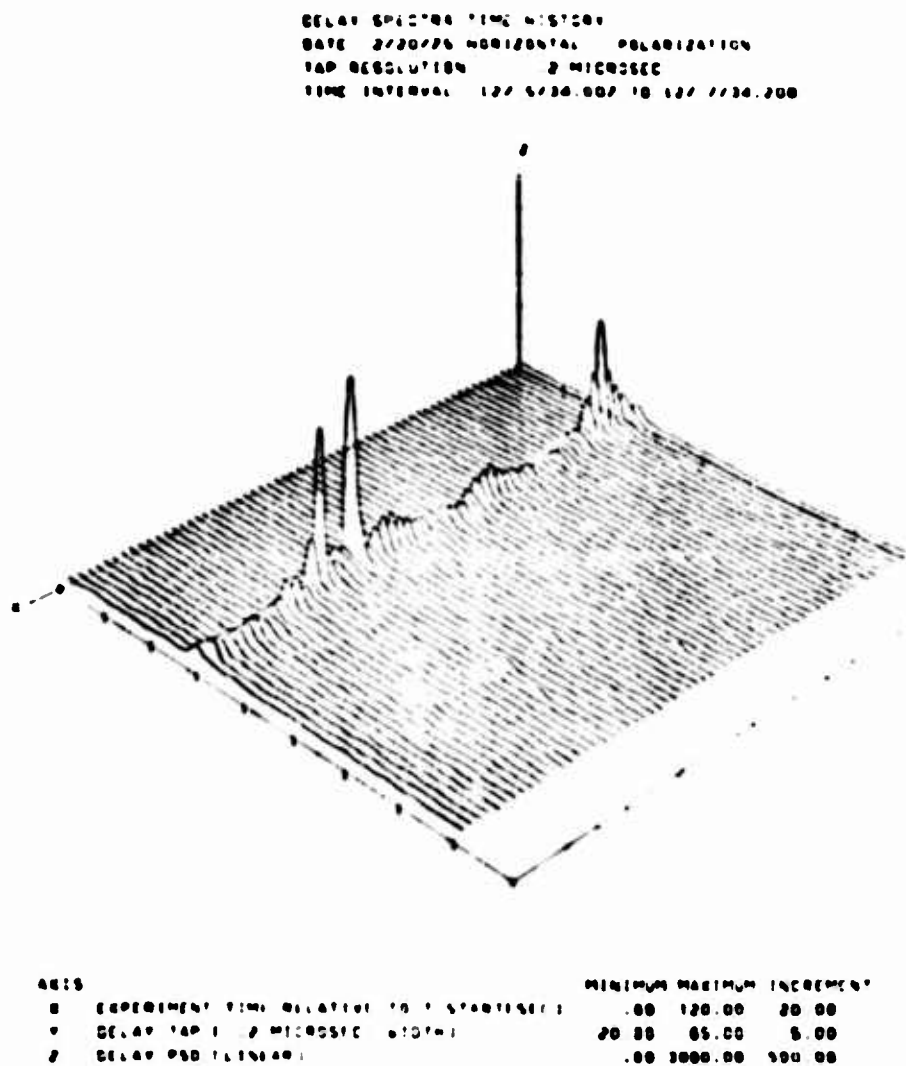
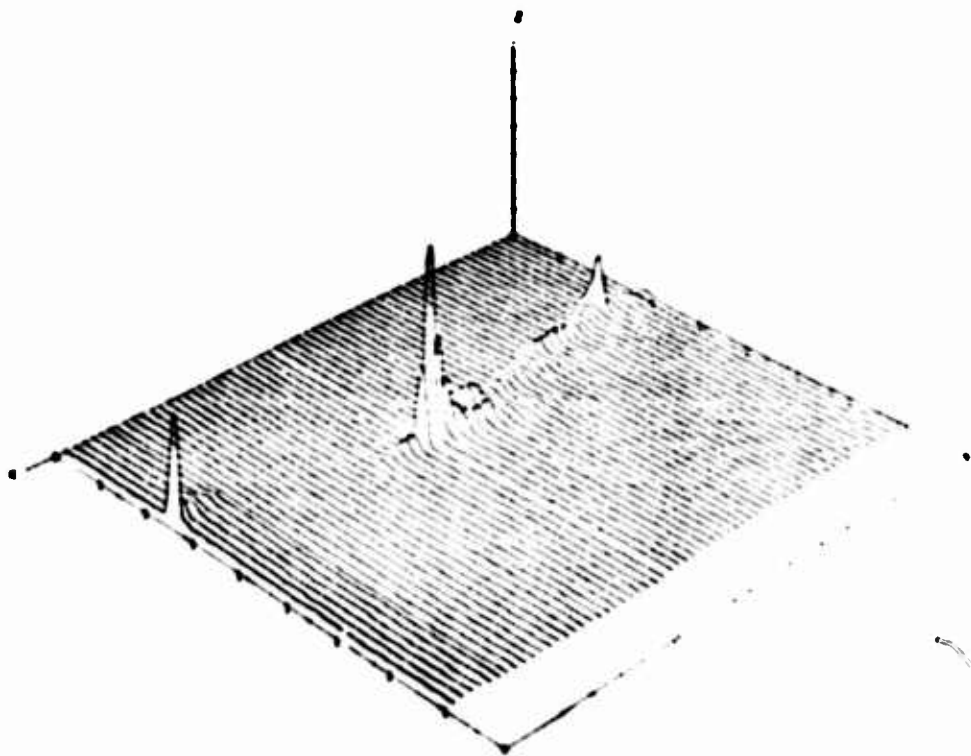


Figure 4-20. - Specular Point Overlay Leg FG February 20, 1975



**Figure 4-21(a). -Delay Spectra Time History—February 20, 1975, Log FG, Horizontal Polarization**

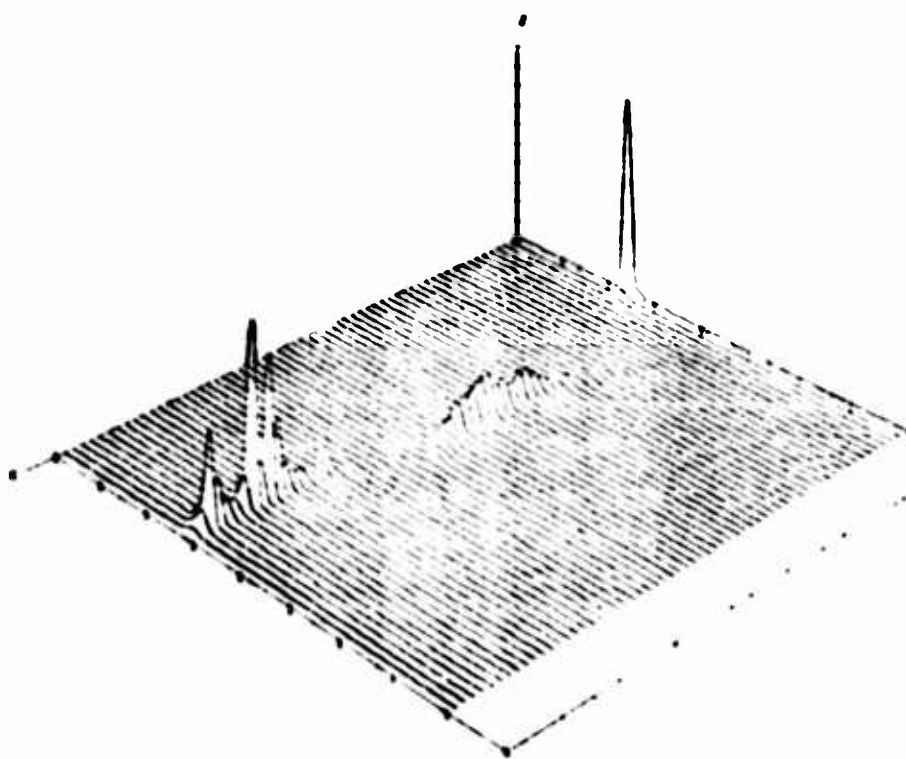
DELAY SPECTRA TIME HISTORY  
DATE 2/20/75 HORIZONTAL POLARIZATION  
TAP RESOLUTION 1.2 MICROSEC  
TIME INTERVAL 127.7736.216 TO 127.9736.616



	MINIMUM	MATERIAL	INCREMENT
1. EXPERIMENT TIME RELATIVE TO 1.2 MICROSEC	00	120.00	20.00
2. DELAY TAP 1.2 MICROSEC. (1024)	20.00	05.00	5.00
3. DELAY PSD (1.2 MICROSEC)	00	7000.00	1000.00

Figure 4-21(b).-Delay Spectra Time History February 20, 1975, Leg FG, Horizontal Polarization

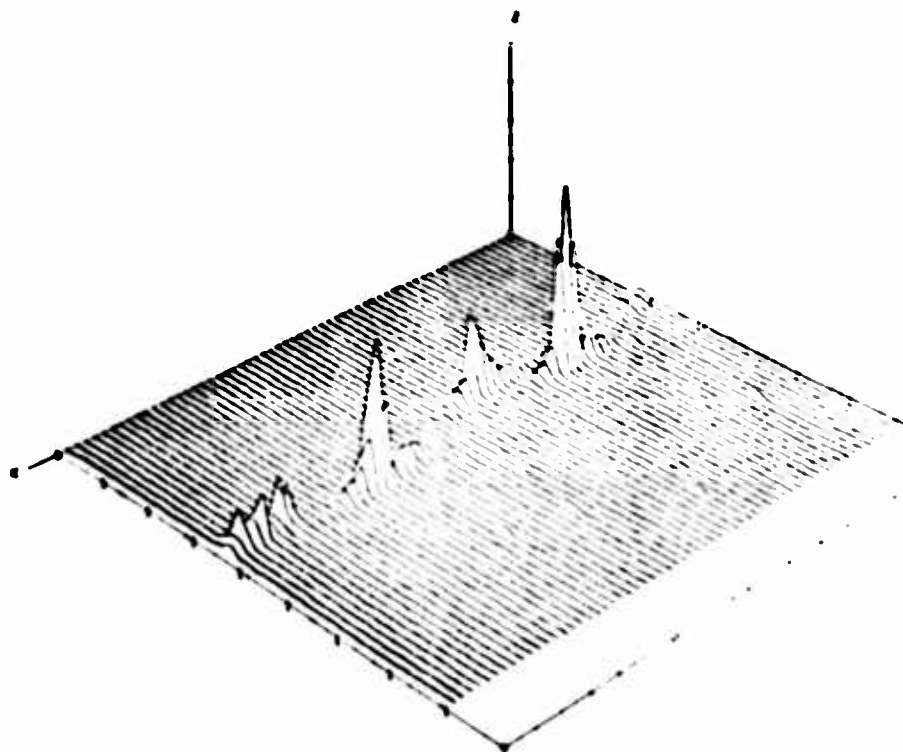
DELAY SPECTRA TIME HISTORY  
DATE 2/20/75 HORIZONTAL POLARIZATION  
TAP RESOLUTION 1.2 MICROSEC  
TIME INTERVAL 127 0730.622 TO 12711730.622



ITEM	MINIMUM	MAXIMUM	INCREMENT
1 EXPERIMENT TIME DELAY IN SEC	00	120.00	.20 .00
2 DELAY TAP 1 1.2 MICROSEC	20.00	65.00	.5 .00
3 DELAY PSS FREQUENCIES	.00	3000.00	.50 .00

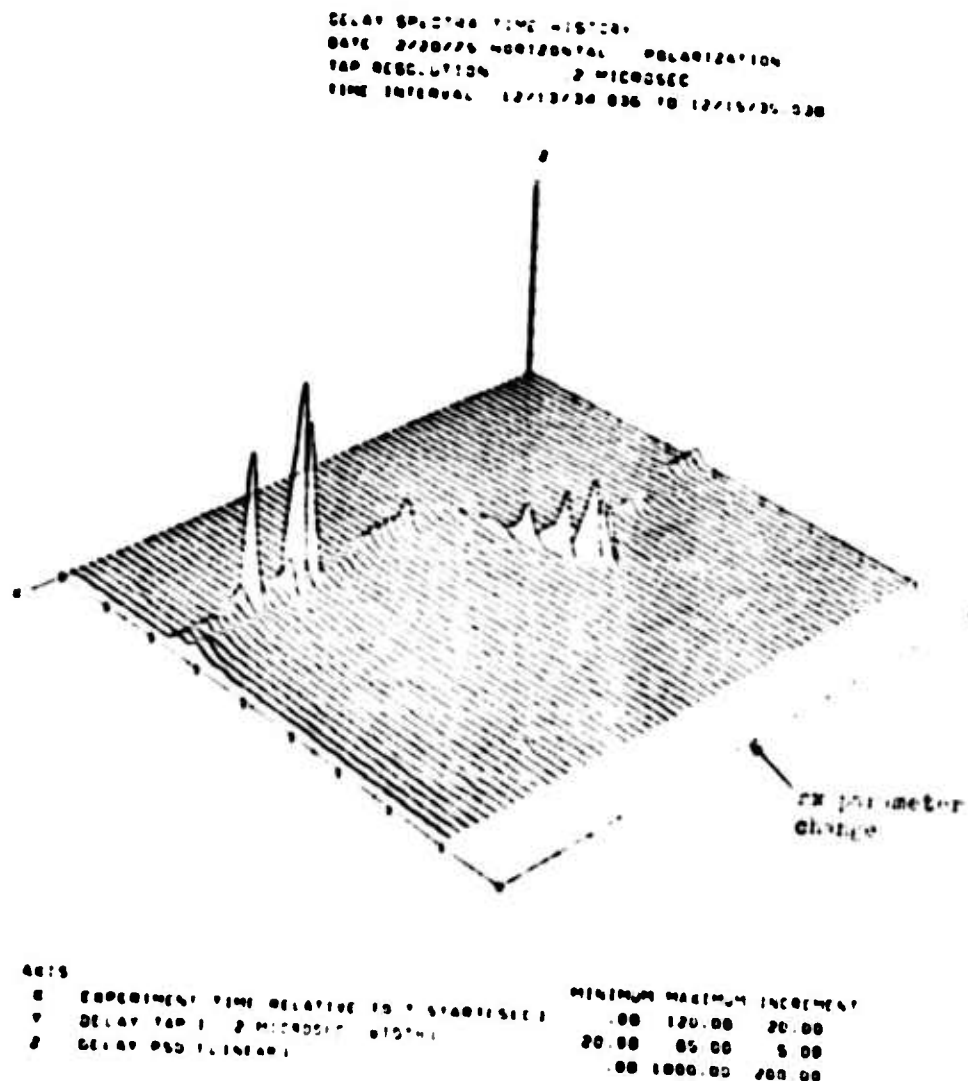
Figure 4-21(c). - Delay Spectra Time History—February 20, 1975, Leg FG, Horizontal Polarization

DELAY SPECTRA TIME HISTORY  
DATE 2/20/75 0001200740 POLARIZATION  
TAP RESOLUTION 2 MICROSEC  
TIME INTERVAL 12/11/74 020 TO 12/11/74 020



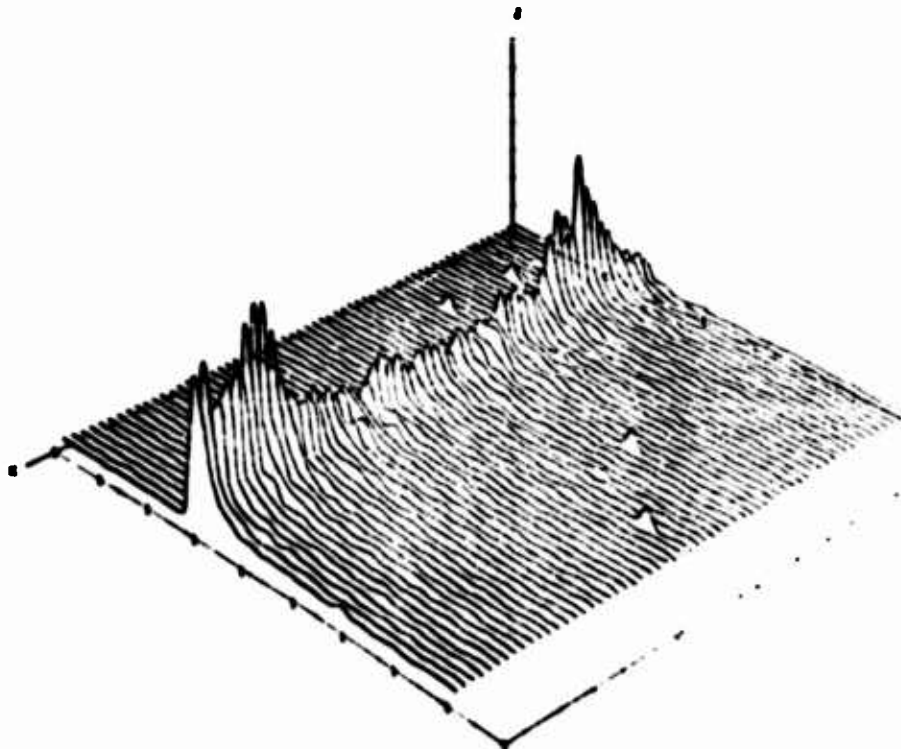
Axes	MINIMUM	MAXIMUM	INCREMENT
E	0.0	120.00	20.00
V	20.00	65.00	5.00
Z	0.00	2500.00	500.00

Figure 4-21(d).-Delay Spectra Time History—February 20, 1975, Leg FG, Horizontal Polarization



**Figure 4-21(e). - Delay Spectra Time History - February 20, 1975, Log FG, Horizontal Polarization**

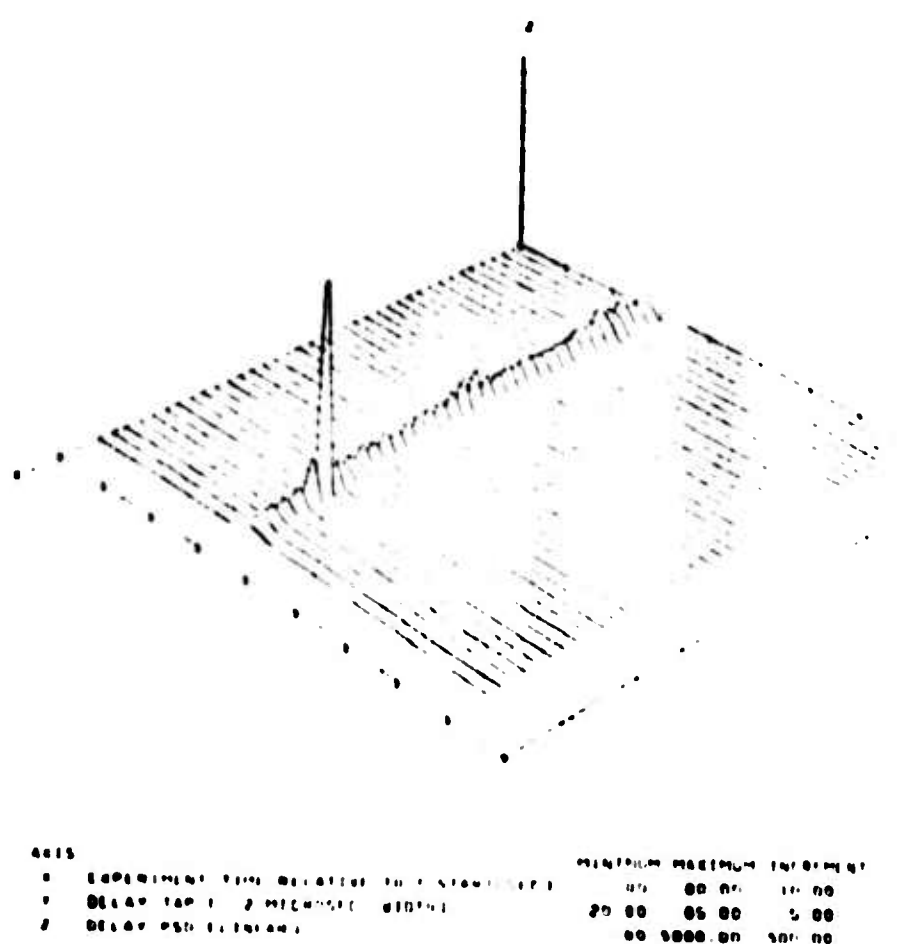
DELAY SPECTRA TIME HISTORY  
DATE 2/20/75 HORIZONTAL POLARIZATION  
TAP RESOLUTION .2 MICROSEC  
TIME INTERVAL 12/15/75 000 TO 12/17/75 246



ACID	MINIMUM	MATERIAL	MAXIMUM	INCREMENT
0	EXPERIMENT TIME RELATIVE TO T-SAMPLE SEC	1.00	120.00	20.00
1	DELAY TAP 1 .2 MICROSEC. VERTICAL	20.00	05.00	5.00
2	DELAY PGS (LINEAR)	.00	700.00	100.00

Figure 4-21(1).-Delay Spectra Time History-February 20, 1975, Log FG, Horizontal Polarization

BELAY SPECTRA TIME HISTORY  
DATE 2/20/75 0801Z0000Z POLARIZATION  
TAP RESOLUTION 2 MICROSEC  
TIME INTERVAL 12212206.252 TO 12210751.126



Axis	MINIMUM	MIDDLE	MAXIMUM
EXPERIMENT TIME (SEC)	00	00 00	10 00
BELAY TAP 1 (2 MICROSEC)	20 00	05 00	5 00
BELAY PSD (dBm)	00 0000.00	300 00	00 00

Figure 4-21(g). Delay Spectra Time History February 20, 1975, Lay FG, Horizontal Polarization

discrete nature of the output along the experiment time axis. For amplitude reference purposes the data for the direct line-of-sight tap bank together with the appropriate normalization parameters indicate that for a lossless non-spread signal arriving at the center of a delay tap, the corresponding Z-axis reading would be on the order of 4200 for the total time segment (with the exception of the intervals 12:05:34 to 12:08:41 and 12:09:24 to 12:09:36, where it would be increased by 6-dB, and the interval 12:08:41 to 12:08:57, where it would be reduced by 6-dB). A cursory analysis of the data reveals the presence of a variety of spectra signatures ranging from high energy single-tap to relatively low energy multi-tap occupancy. We also observe on a number of occasions the occurrence of what appears to be a multi-mode reflection process (e.g., 12:08:30). At this writing no definitive correlations of these phenomena with terrain features have been attempted although it does appear that whenever the specular point traverses a body of fresh water (probably frozen for the February series) such as a river the return has a characteristic high energy uni-tap reflection component in its delay spectra.

For comparison purposes, the vertical polarization counterpart of the above data for a two minute segment is presented in Figure 4-22. It is to be noted that the vertical and horizontal probes occur simultaneously and that for reference purposes the lossless non-spread vertical return would produce a z-axis reading of roughly 17,000. Comparing the horizontal data (Figure 4-21(d)) to the vertical data reveals that the two sets vary in concert with each other to a relatively high degree.

In Figure 4-3 of reference 4-8 a comprehensive delay spectra time history, similar to that presented above, was given for an East Coast CONUS fall campaign flight test leg. The time history begins north of Long Island Sound, subtends the sound, New York City, Lower New York Bay (LNYB) and ends well past the bay's southern extremity. Correlation of these data with the specular point trajectory (also given in reference 4-8) may be used to illustrate the delay spectra signature associated with several markedly different terrain features. A sample of this is illustrated in Figure 4-23 where data for a 2-minute time segment for horizontal polarization scatter is presented. With the exception of the grazing angle, which was on the order of 39°, system parameters were roughly equivalent to those given for the data sets of Figure 4-21 and 4-22.

The data of Figure 4-23 presents three rather distinct signature intervals. The first interval roughly spans the time range from 12:42:00 to 12:42:30. This return is attributed to scatter from the industrial/residential area to the north of LNYB and is seen to be characterized by a high intensity, somewhat erratic low delay spread return. The second identifiable interval extends from approximately 12:42:30 to 12:43:30 and represents the multipath return from LNYB. Its signature is observed to be fairly stationary with the energy being dispersed over a relatively large number of taps. The third interval which extends from 12:43:30 to 12:43:57 possesses similar multipath characteristics to the first interval and is interpreted as resulting from scatter return immediately south of LNYB. Integration over the delay variable shows that the total scattered power from LNYB return and the more intense portion of the industrial/residential signatures are to close approximation within 1.5 dB of each other.

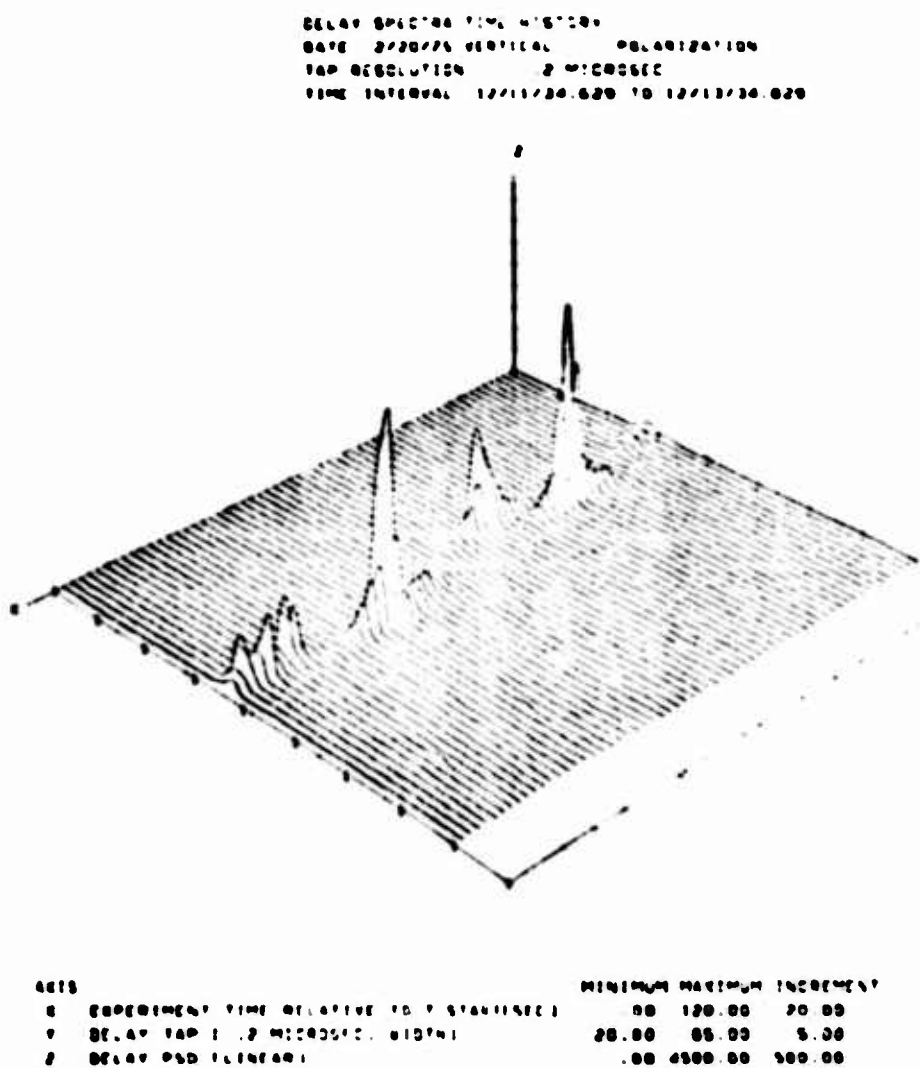
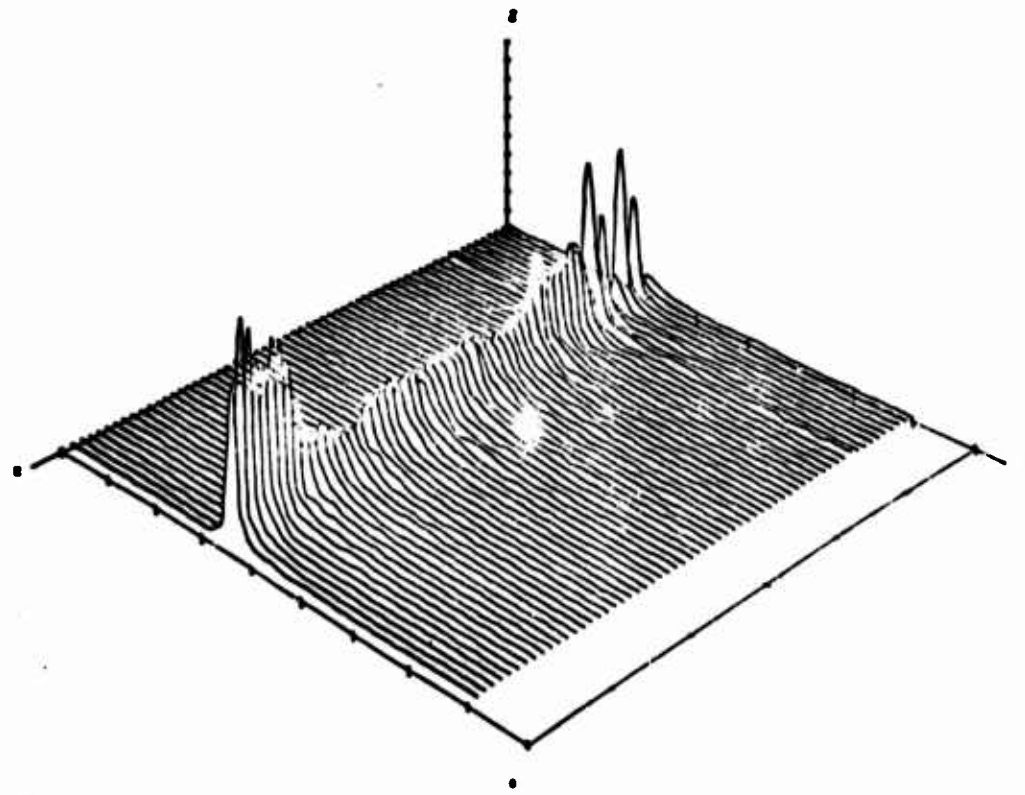


*Figure 4-22.—Delay Spectra Time History—February 20, 1975, Leg FG, Vertical Polarization*

DELAY SPECTRA TIME HISTORY  
DATE 09/19/74 HORIZONTAL POLARIZATION  
TAP RESOLUTION .1 MICROSEC  
TIME INTERVAL 12/41/80.140 TO 12/42/82.176



AXIS	MINIMUM	MAXIMUM	INCREMENT
X EXPERIMENT TIME RELATIVE TO T-START (SEC)	.00	120.00	20.00
Y DELAY TAP 1 (.1 MICROSEC. WIDTH)	30.00	76.00	6.00
Z DELAY PSD (LINEAR)	.0010000.00	1000.00	

Figure 4-23.—Delay Spectra Time History, September 19, 1974 Lower New York Bay

### **4.3.2 CONUS SCATTER FUNCTION AND ASSOCIATED INTEGRAL AND FOURIER RELATIONSHIPS**

The preceding discussion provided a sample overview of the CONUS channel delay spectra signatures. As one would expect when a high degree of non-stationarity in the channel delay spectra is observed there exists a corresponding degree of delay-Doppler scatter function non-stationarity. In this section we present several samples which illustrate a portion of the various CONUS scatter functions that have been observed. These, together with their delay spectra, Doppler spectra and one example of autocorrelation function distributions are given in Figures 4-24 through 4-28. These data are roughly categorized as being representative of the following scatter signatures.

1. Near-zero spread in both Doppler and Delay variables.

Figure 4-24, vertical polarization, in-plane geometry, grazing angle roughly 33 degrees.

2. Modest spread for both Doppler and Delay variables:

Figure 4-25, horizontal polarization, cross-plane geometry, grazing angle roughly 27 degrees.

3. Assymetrical spatial return with appreciable energy being obtained from sub-aircraft side of specular point only:

Figure 4-26, vertical polarization, in-plane geometry, grazing angle roughly 33 degrees.

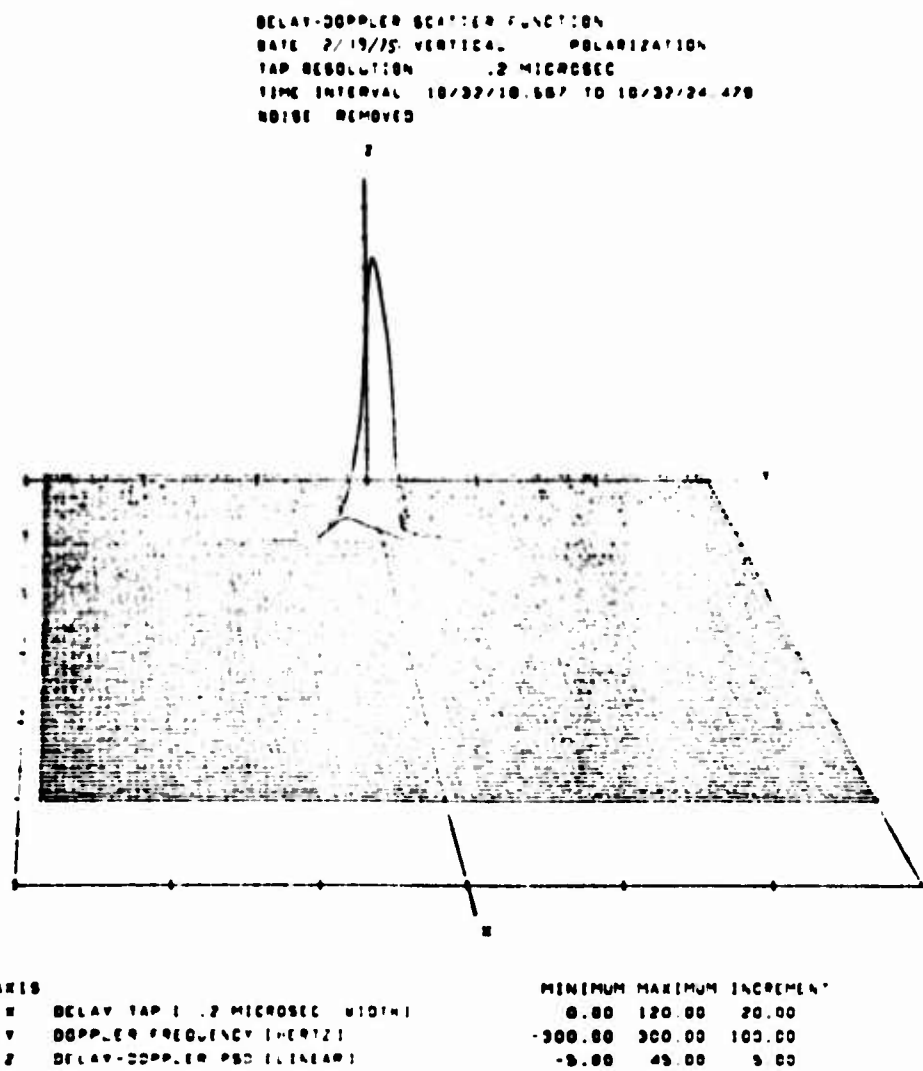
4. Multi-mode signature with large specular point region return superimposed upon an underlying low energy broadly spread signal

Figure 4-27, horizontal polarization, in-plane geometry, grazing angle roughly 29 degrees

5. Broadly spread return with persistence in delay spectra tail and highly irregular Doppler spectra

Figure 4-28, horizontal polarization, in-plane geometry, grazing angle roughly 29 degrees.

The 3-dB spread values associated with the channel parameters of the above data sets are given in Table 4-3.



*Figure 4-24(a).—CONUS Scatter Channel Parameters—February 19, 1975, Vertical Polarization*

DELAY AND DOPPLER SPECTRA  
 DATE 2/19/75 VERTICAL POLARIZATION  
 TAP RESOLUTION .2 MICROSEC  
 TIME INTERVAL 10/32/18.587 TO 10/32/24.479  
 NOISE REMOVED

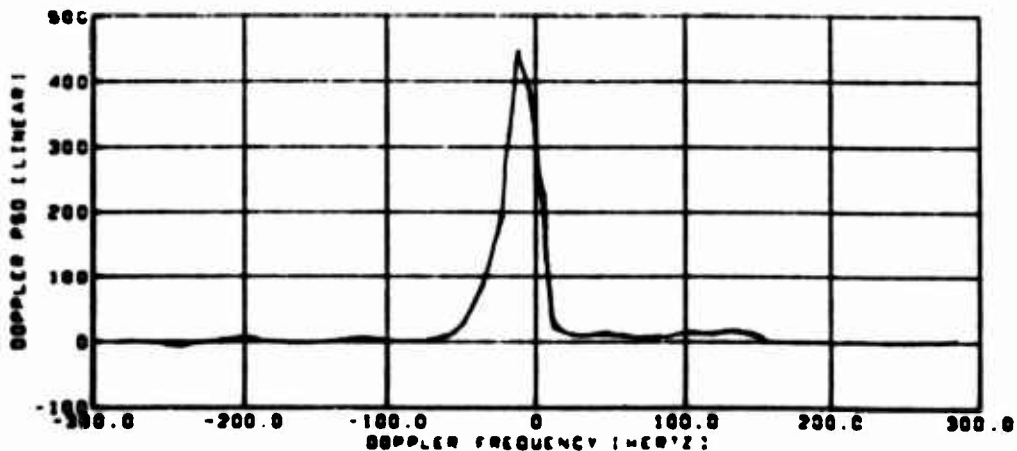
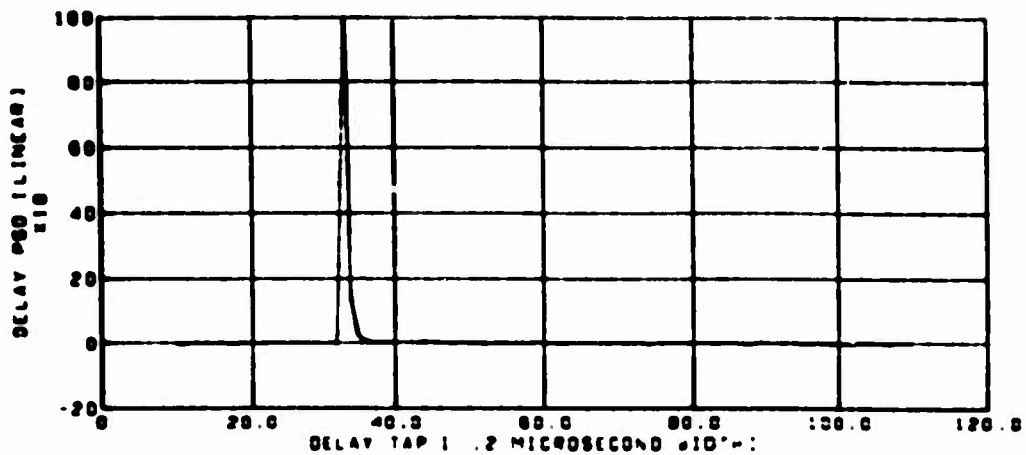
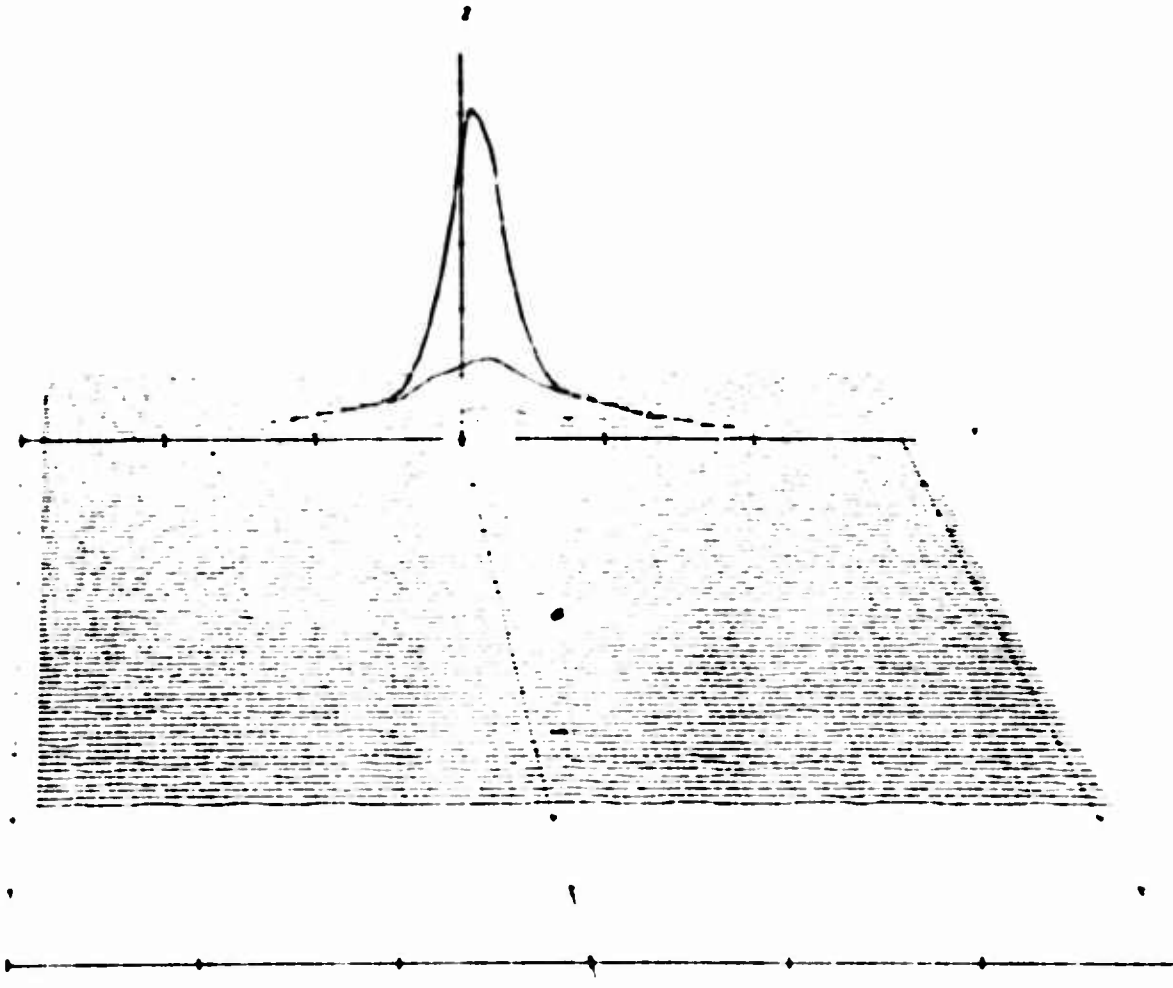


*Figure 4-24(b).—CONUS Scatter Channel Parameters—February 19, 1975, Vertical Polarization*

DELAY-DOPPLER SCATTER FUNCTION  
 DATE 2/18/75 HORIZONTAL POLARIZATION  
 TAP RESOLUTION .2 MICROSEC  
 TIME INTERVAL 12/577 .997 TO 12/577 0 .377  
 NOISE REMOVED



AXIS	MINIMUM	MAXIMUM	INCREMENT
X DELAY TAP 1 .2 MICROSEC. 6127+1	30.00	120.00	10.00
Y DOPPLER FREQUENCY (HERTZ)	-300.00	300.00	100.00
Z DELAY-DOPPLER PSD (LINEAR)	-10.00	50.00	10.00

Figure 4-25(a).—CONUS Scatter Channel Parameters—February 18, 1975, Horizontal Polarization

DELAY AND DOPPLER SPECTRA  
 DATE 2/18/75 HORIZONTAL POLARIZATION  
 TAP RESOLUTION .2 MICROSEC  
 TIME INTERVAL 12/57/.007 TO 12/57/.377  
 NOISE REMOVED

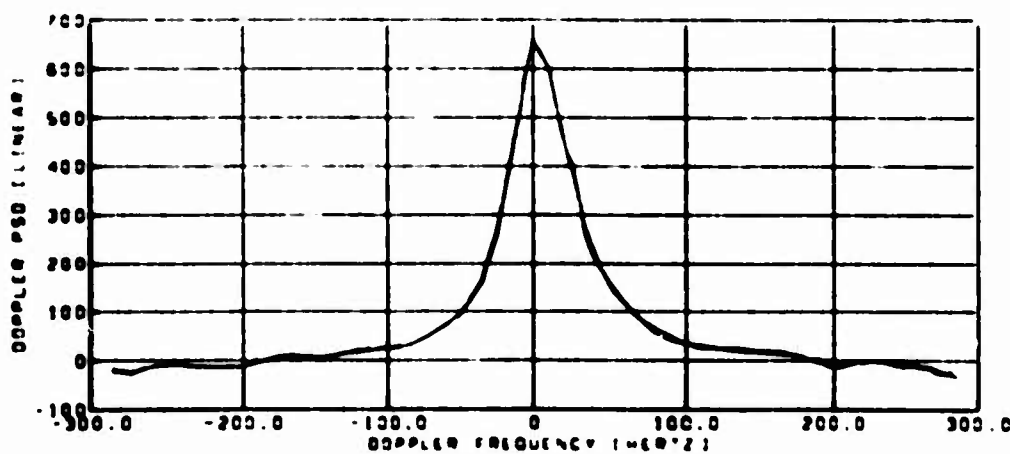
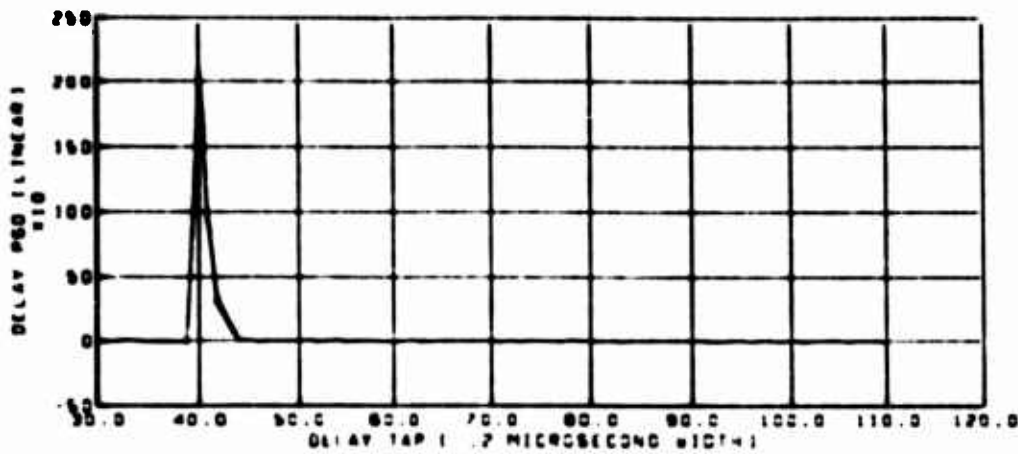
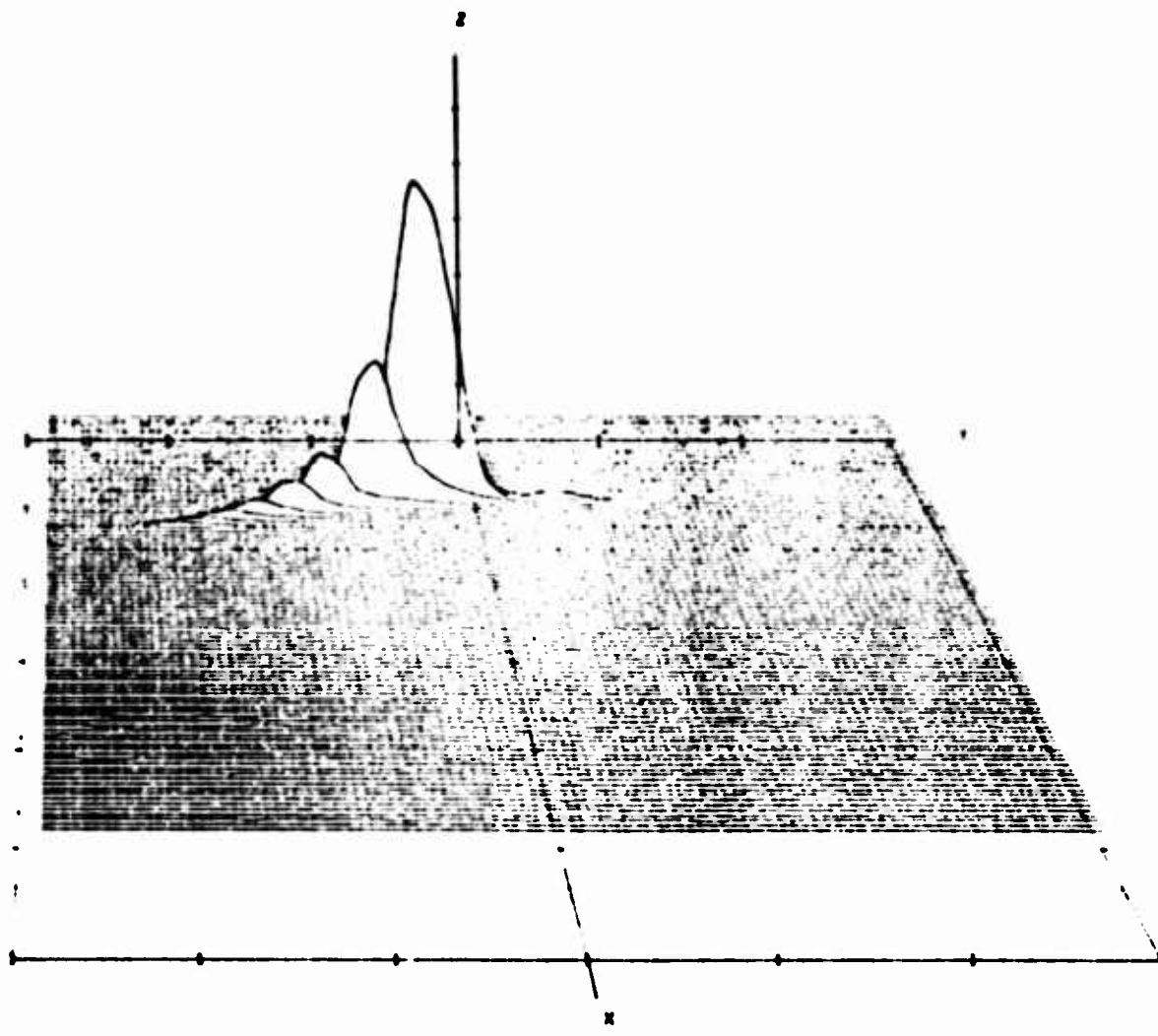


*Figure 4-25(b).—CONUS Scatter Channel Parameters, February 18, 1975, Horizontal Polarization*

DELAY-DOPPLER SCATTER FUNCTION  
 DATE 2/19/75 VERTICAL POLARIZATION  
 TAP RESOLUTION .2 MICROSEC  
 TIME INTERVAL 10/31/46.170 TO 10/31/52.861  
 NOISE REMOVED



AXIS		MINIMUM	MAXIMUM	INCREMENT
X	DELAY TAP ( .2 MICROSEC. WIDTH)	0.00	120.00	20.00
Y	DOPPLER FREQUENCY (HERTZ)	-300.00	300.00	100.00
Z	DELAY-DOPPLER PSD (LINEAR)	-1.00	8.00	1.00

Figure 4-26(a).—CONUS Scatter Channel Parameters—February 19, 1975, Vertical Polarization

DELAY AND DOPPLER SPECTRA  
 DATE 2/19/75 VERTICAL POLARIZATION  
 TAP RESOLUTION .2 MICROSEC  
 TIME INTERVAL 10/31/48.170 TO 10/31/52.051  
 NOISE REMOVED

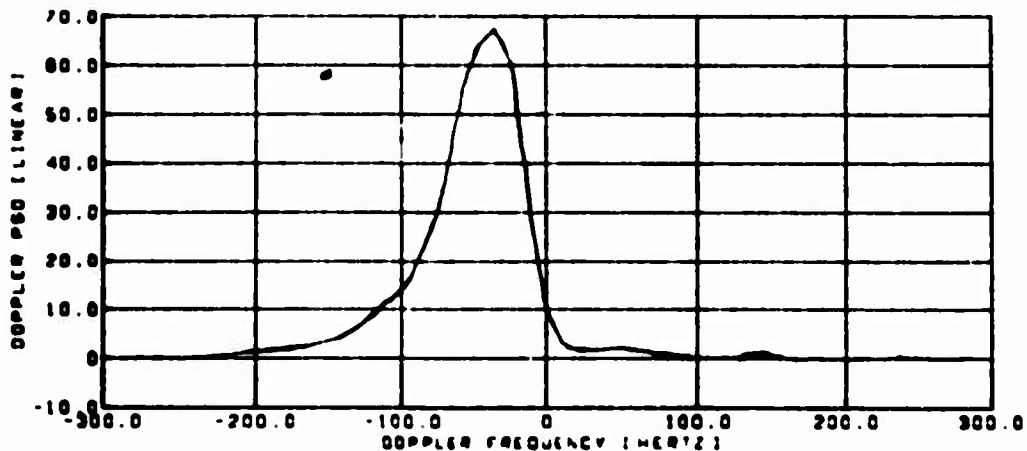
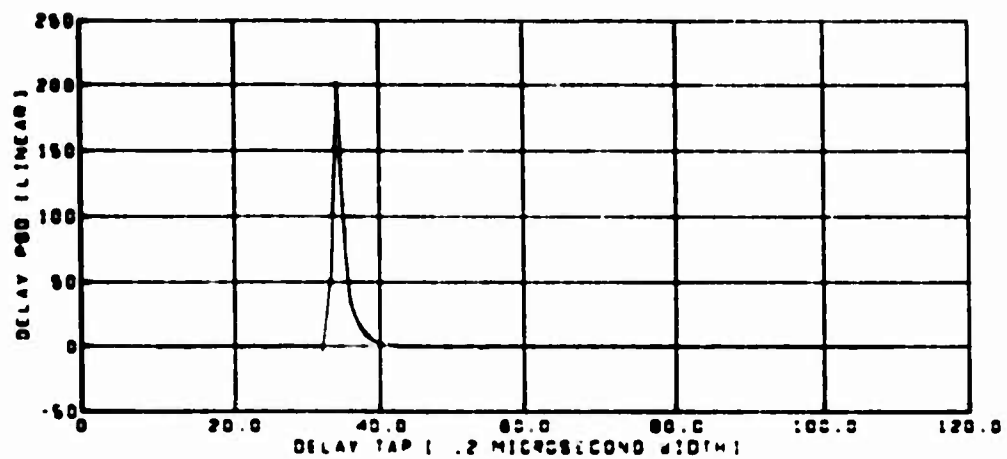
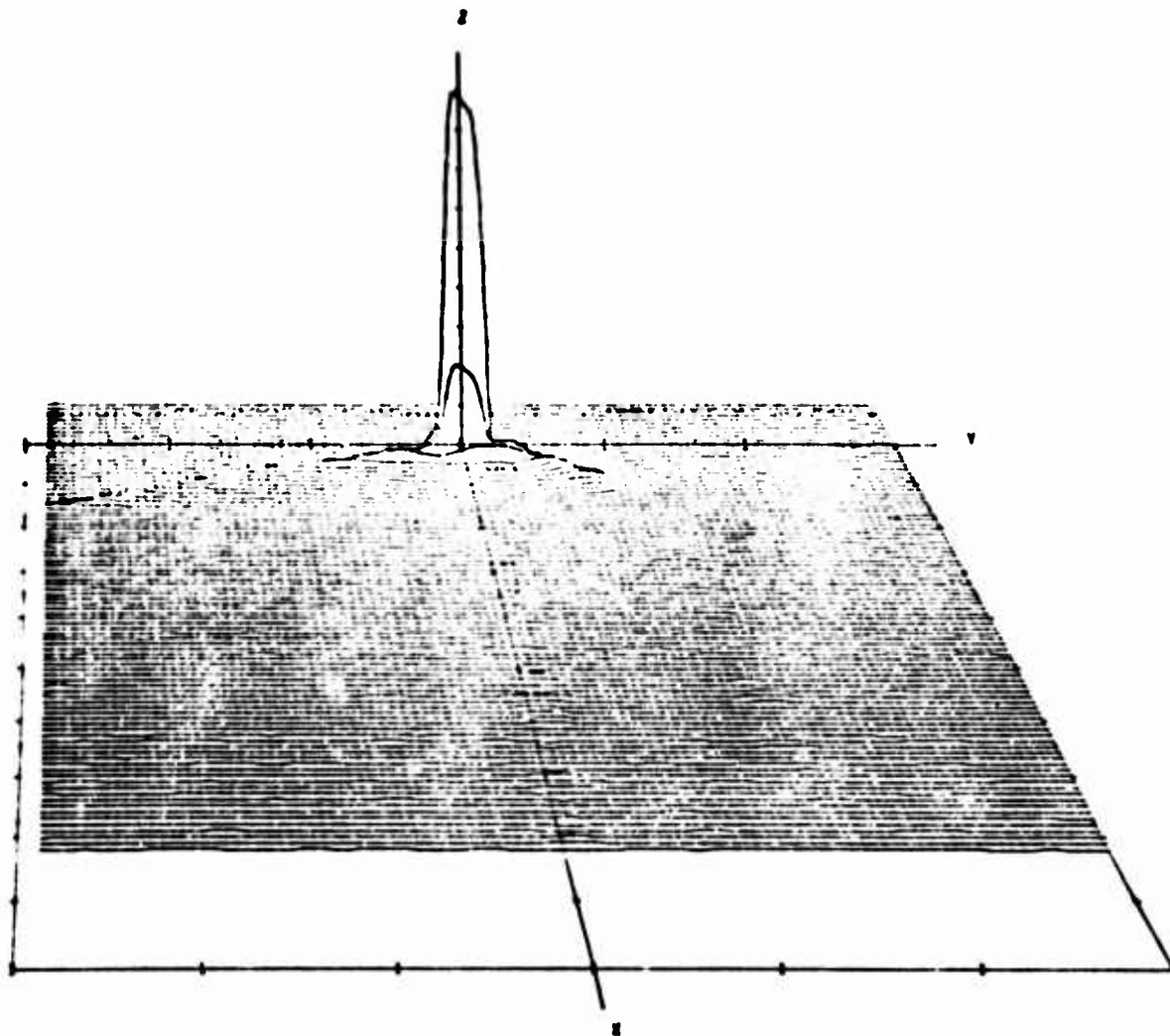


Figure 4-26(b).—CONUS Scatter Channel Parameters—February 19, 1975, Vertical Polarization

DELAY-DOPPLER SCATTER FUNCTION  
 DATE 2/20/75 HORIZONTAL POLARIZATION  
 TAP RESOLUTION .2 MICROSEC  
 TIME INTERVAL 12/ 8/51.160 TO 12/ 8/57.033  
 NOISE REMOVED



AXIS	MINIMUM	MAXIMUM	INCREMENT
X DELAY TAP (0.2 MICROSEC, WIDTH)	20.00	120.00	10.00
Y DOPPLER FREQUENCY (HERTZ)	-300.00	300.00	100.00
Z DELAY-DOPPLER PSD (LINEAR)	-5.00	45.00	5.00

Figure 4-27(a).—CONUS Scatter Channel Parameters—February 20, 1975, Horizontal Polarization

DELAY AND DOPPLER SPECTRA  
 DATE 2/20/75 HORIZONTAL POLARIZATION  
 TAP RESOLUTION .2 MICROSEC  
 TIME INTERVAL 12/ 6/51.160 TO 12/ 6/57.033  
 NOISE REMOVED

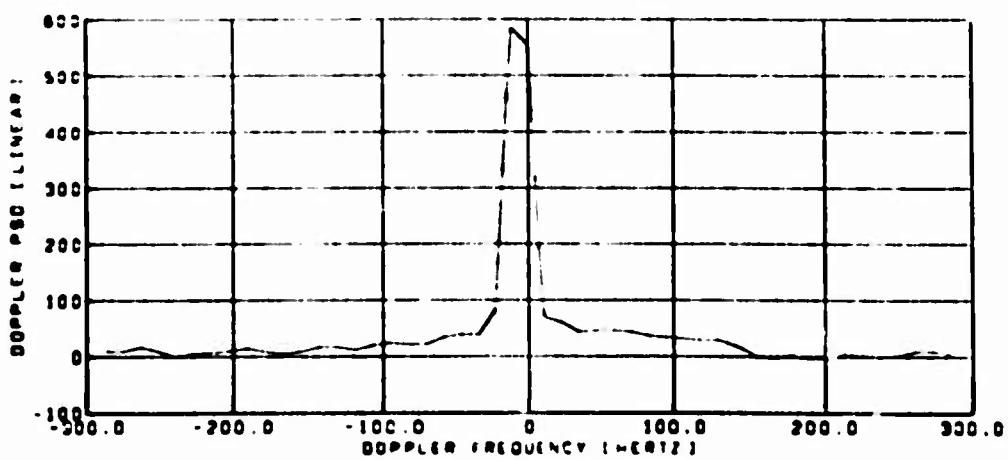
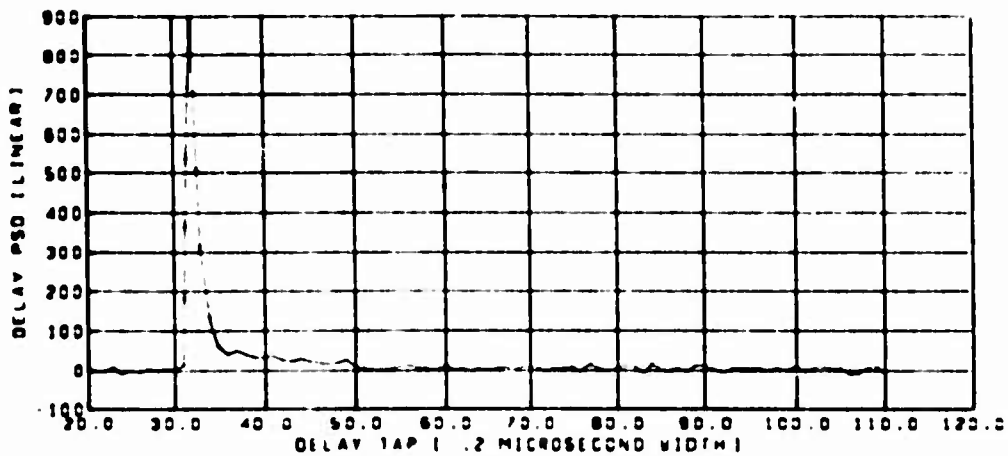
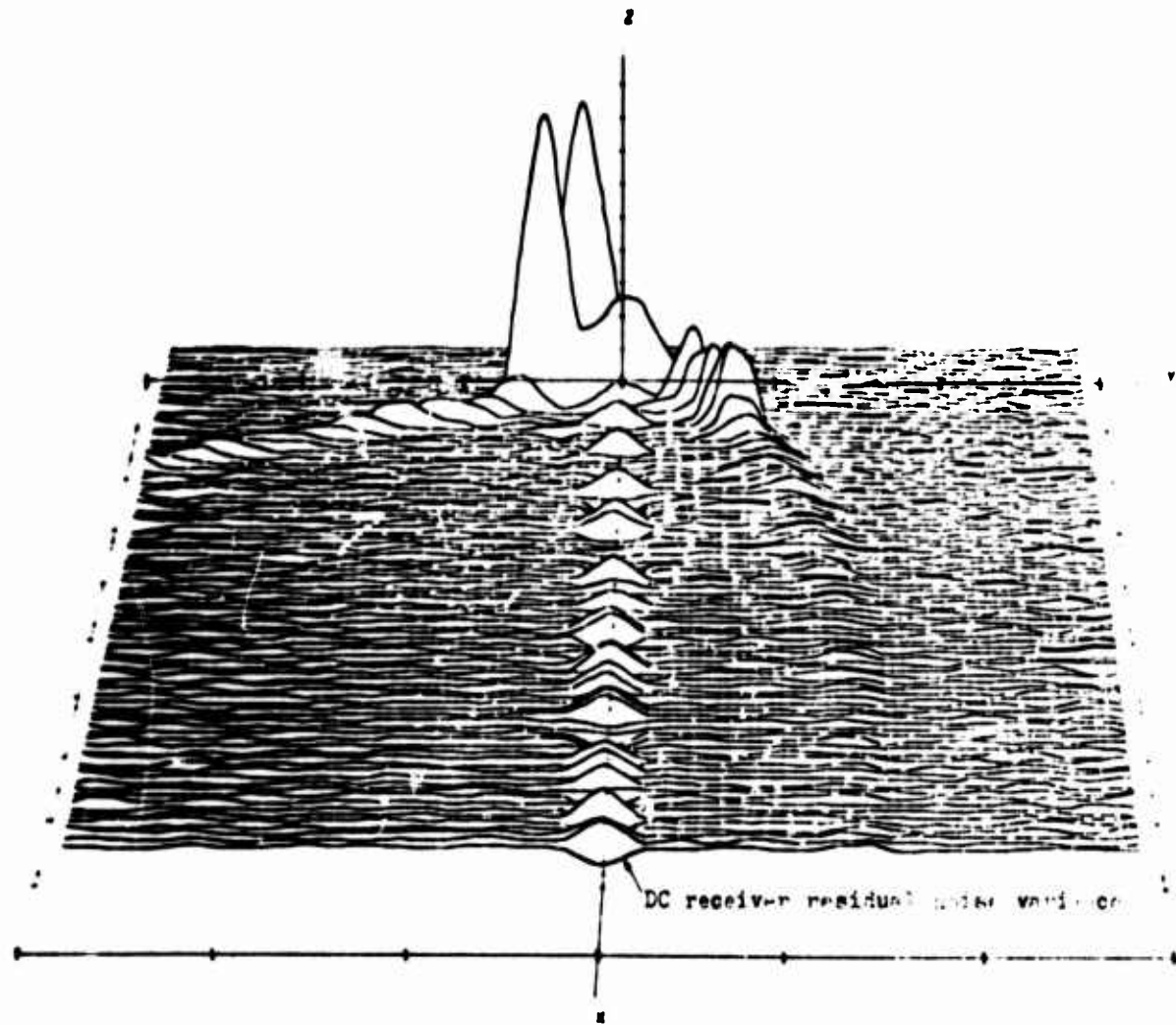


Figure 4 27(b).—CONUS Scatter Channel Parameters—February 20, 1975, Horizontal Polarization

DELAY-DOPPLER SCATTER FUNCTION  
 DATE 2/20/75 HORIZONTAL POLARIZATION  
 TAP RESOLUTION .2 MICROSEC  
 TIME INTERVAL 12/ 5/48.642 TO 12/ 5/55.615  
 NOISE REMOVED



AXIS	MINIMUM	MAXIMUM	INCREMENT
X DELAY TAP 1 .2 MICROSEC. WIDTH	20.00	120.00	10.00
Y DOPPLER FREQUENCY (HERTZ)	-300.00	300.00	100.00
Z DELAY-DOPPLER PSD (LINEAR)	- .50	4.50	.50

Figure 4-28(a).—CONUS Scatter Channel Parameters—February 20, 1975, Horizontal Polarization

DELAY AND DOPPLER SPECTRA  
 DATE 2/20/75 HORIZONTAL POLARIZATION  
 TAP RESOLUTION .2 MICROSEC  
 TIME INTERVAL 12/ 5/49.642 TO 12/ 5/50.515  
 NOISE REMOVED

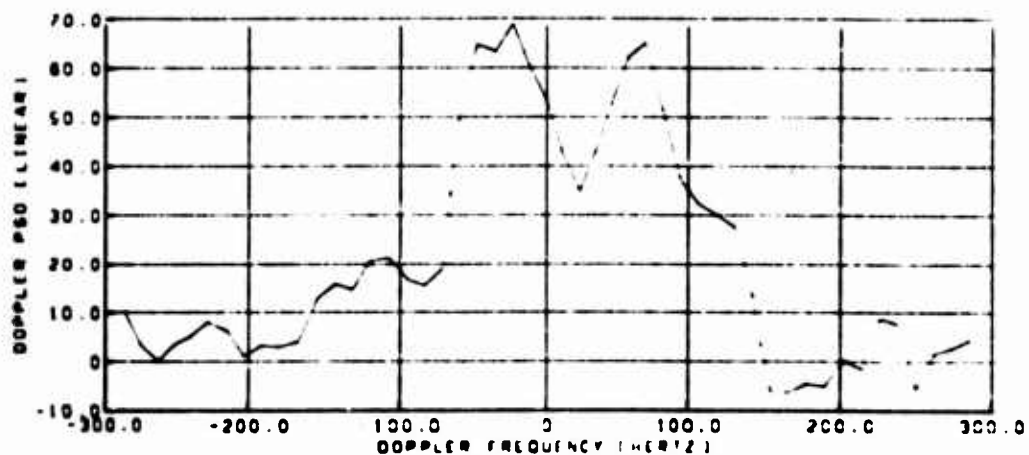
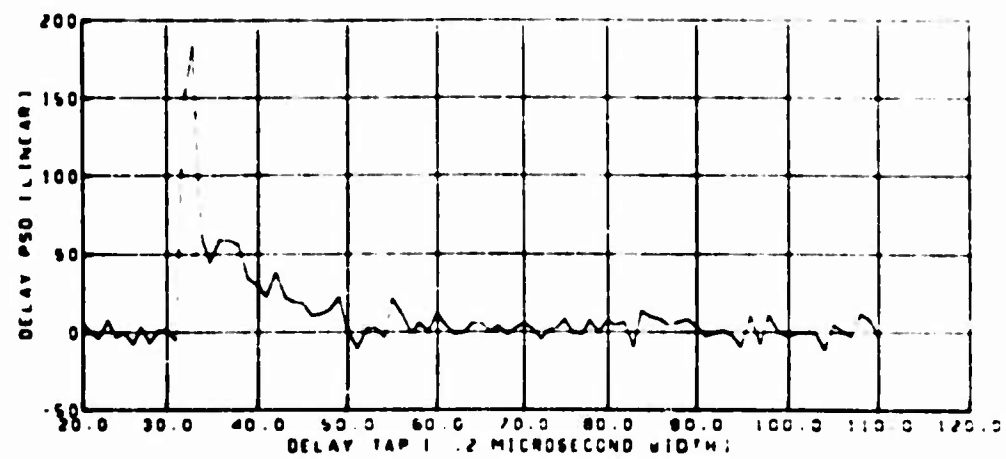


*Figure 4-28(b).—CONUS Scatter Channel Parameters—February 20, 1975, Horizontal Polarization*

AUTOCORRELATION FUNCTION  
DATE 2/20/75 HORIZONTAL POLARIZATION  
TAP RESOLUTION .2 MICROSEC  
TIME INTERVAL 12/ 5/49.542 TO 12/ 5/55.515  
NOISE REMOVED

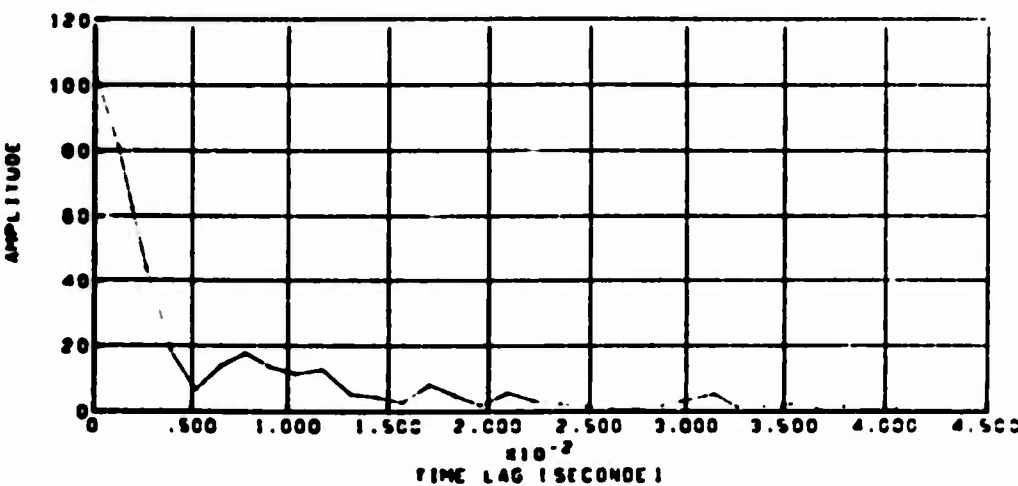
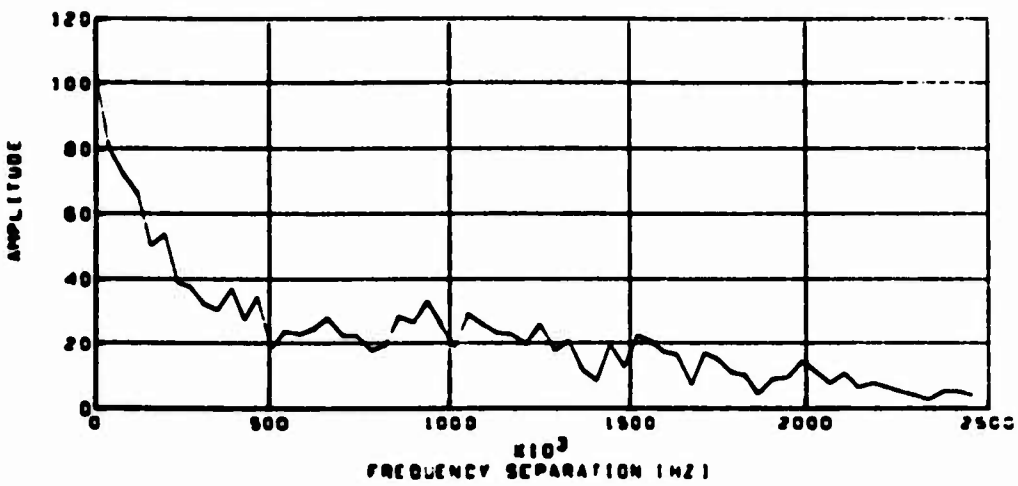


Figure 4-28(c).-CONUS Scatter Channel Parameters—February 20, 1975, Horizontal Polarization

*Table 4-3.—Example Spread Values for CONUS Multipath*

Figure reference	Spread parameter			
	Delay	Doppler	Time autocorrelation	Frequency autocorrelation
4-23	<.2 $\mu$ sec	24 Hz	13 msec	>2600 kHz
4-24	~.2 $\mu$ sec	50 Hz	6 msec	1600 kHz
4-25	.2 $\mu$ sec	61 Hz	5.5 msec	1020 kHz
4-26	.2 $\mu$ sec	20 Hz	8.5 msec	720 kHz
4-27	.6 $\mu$ sec	165 Hz	2.4 msec	160 kHz

#### 4.3.3 AIRPORT LANDING AND TAXI SCATTER DATA

Experimental scatter data for the airport landing and taxi test condition is still in a preliminary state of analysis. With the airplane on the ground and conducting typical taxi maneuvers the results analyzed to date indicate the following:

1. Significant amplitude fluctuation on the received direct tap\* signal of the crossed-slot operational antenna. This may be attributed to a number of occurrences such as building shielding of the direct line-of-sight signal, antenna pattern variation as a function of aircraft orientation, and interference (both constructive and destructive) due to multipath arrivals falling within the direct tap bank.
2. Very little energy (< 20 dB down from total) is returned with delays greater than .2  $\mu$ sec from the direct signal arrival.

These observations are illustrated with the following sample results taken from the February 19 O'Hare airport test sequence. Presented in Figure 4-29 is a time log of the airplane location superimposed upon a runway-building structure descriptor of O'Hare, also included is an arrow indicating the direction toward ATS-6. The delay spectra time history presented in Figure 4-30 demonstrates the variations in the direct tap signal amplitude when using the crossed-slot antenna during the time interval 12:04:50 to 12:07:30. The direct signal is located midway between taps 22 and 23 of the bank and corresponds to the plateau-like signal in the display. Through analysis of the corresponding numerical output the direct signal is observed to have peak-to-trough variations in excess of 5.2 dB. More detailed plots illustrating the delay spectra of the total (direct plus multipath) signal from the crossed-slot antenna are given in Figures 4-31 and 4-32. These data correspond to 2-second sample spaces centered about experiment times 12:05:17 and 12:06:24 respectively and are representative of the typical delay spectra signatures obtained for the taxi scenarios. They have been subjected to a first order noise removal process wherein noise is determined from delay spectra of a multipath-free region of the tap bank and then subtracted from all taps. Results generally indicate that the bulk of the delay returns arrive no later than 0.1 or 0.2 microseconds after the direct signal.

\*With the aircraft on the ground, the 10 MHz chip rate (the highest available with the SACP equipment) resolution is insufficient to completely discriminate against terrain and building scatter returns falling into the direct path taps.

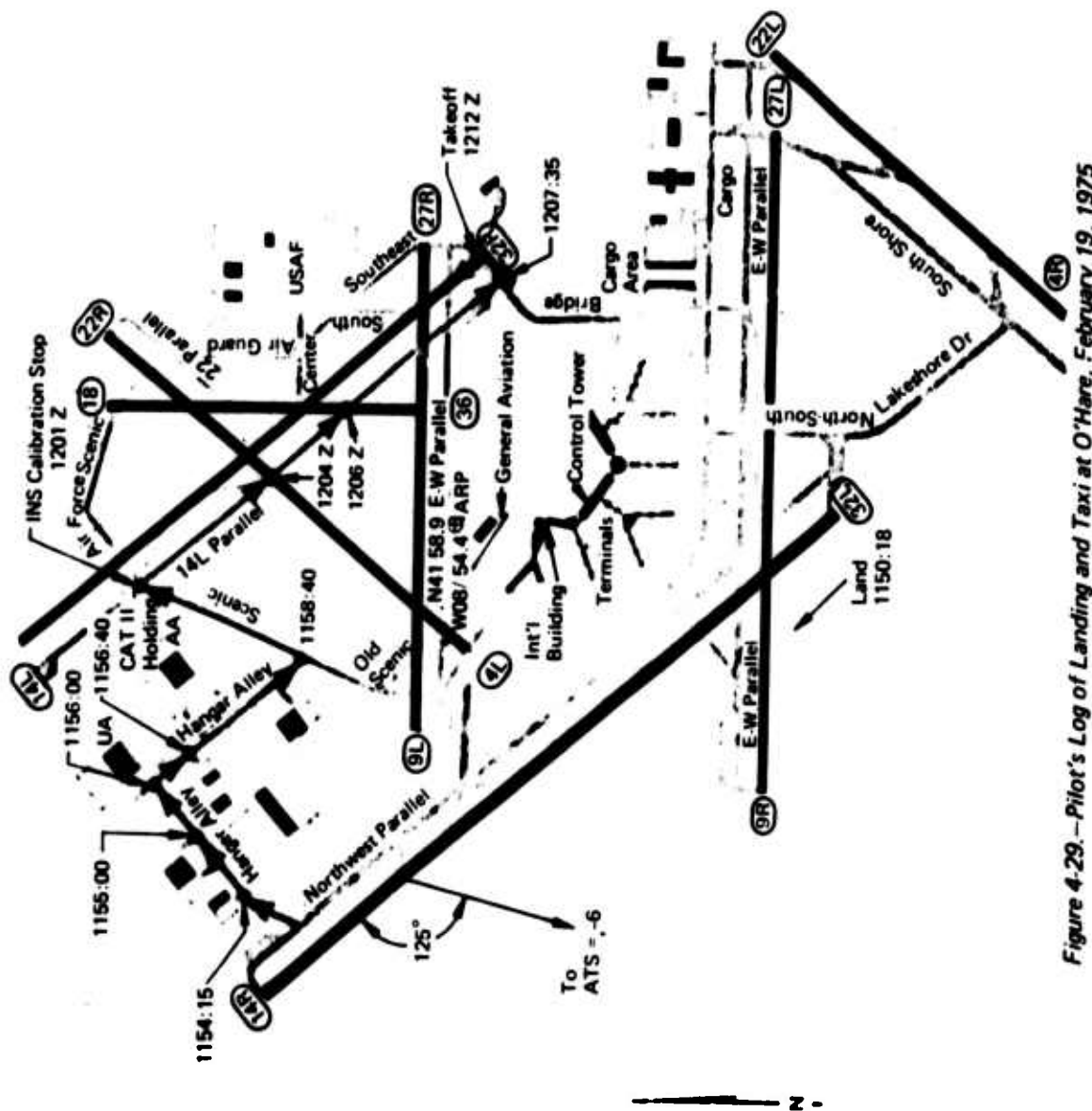
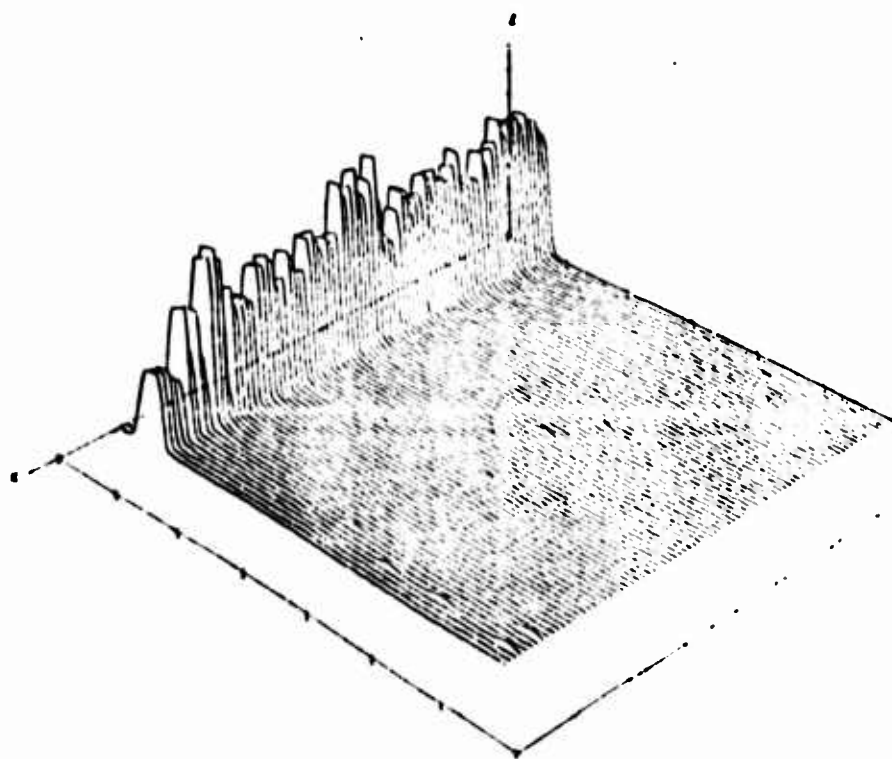


*Figure 4-29.—Pilot's Log of Landing and Taxi at O'Hare, February 19, 1975*

DELAY SPECTRA TIME HISTORY  
DATE 8/10/76 O'HARE  
TAP RESOLUTION .2 MICROSEC  
TIME INTERVAL 127.4750.007 TO 127.7730.357



AXIS	MINIMUM	MAXIMUM	INCREMENT
X EXPERIMENT TIME RELATIVE TO T START (SEC)	00	180.00	.20 00
Y DELAY TAP (.2 MICROSEC. VISTH)	20.00	55.00	5.00
Z DELAY PSD (LINEAR)	.00	4000.00	500.00

Figure 4-30.—O'Hare Delay Spectra Time History

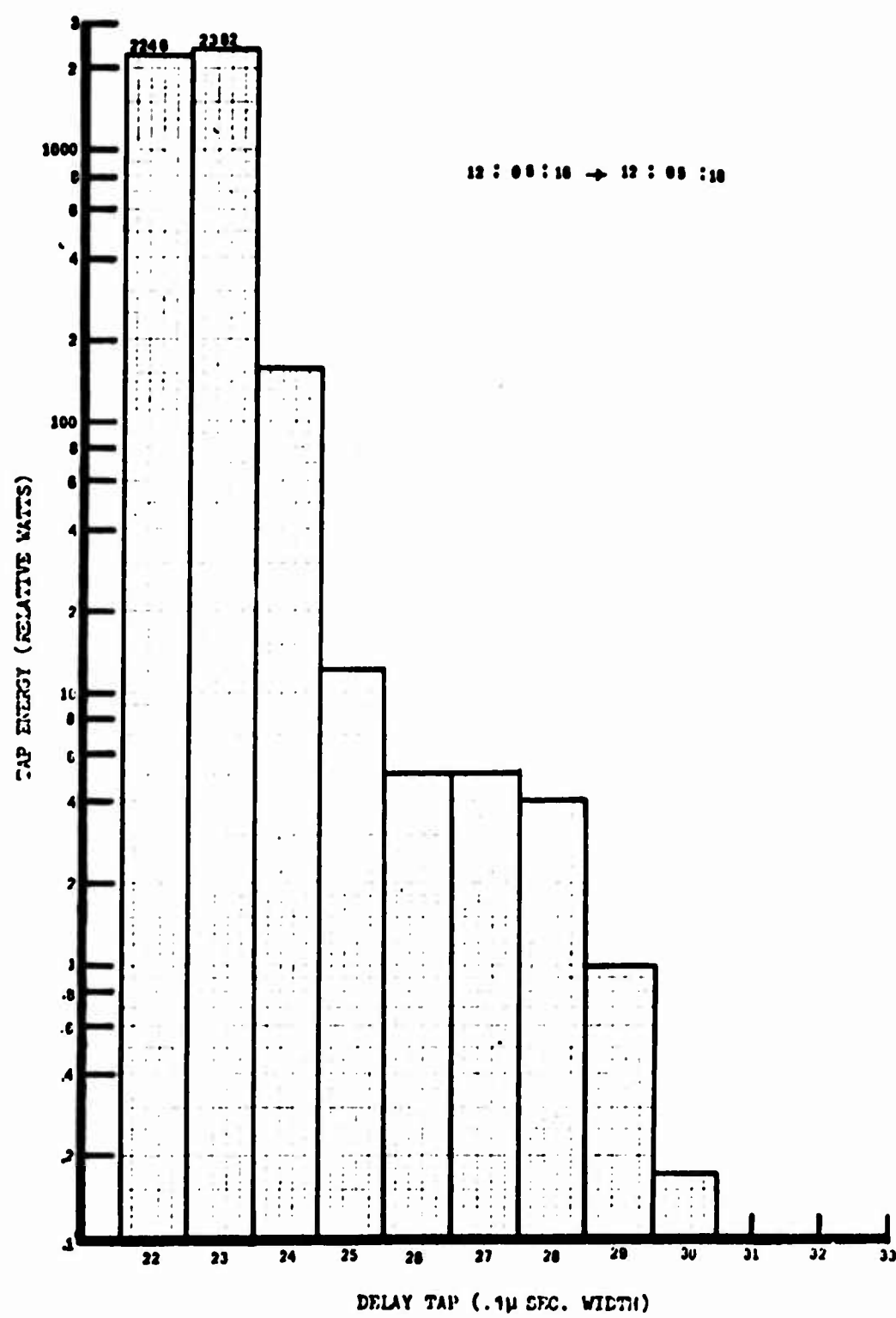


Figure 4-31.—O'Hare Delay Spectra (12:05:17 GMT)

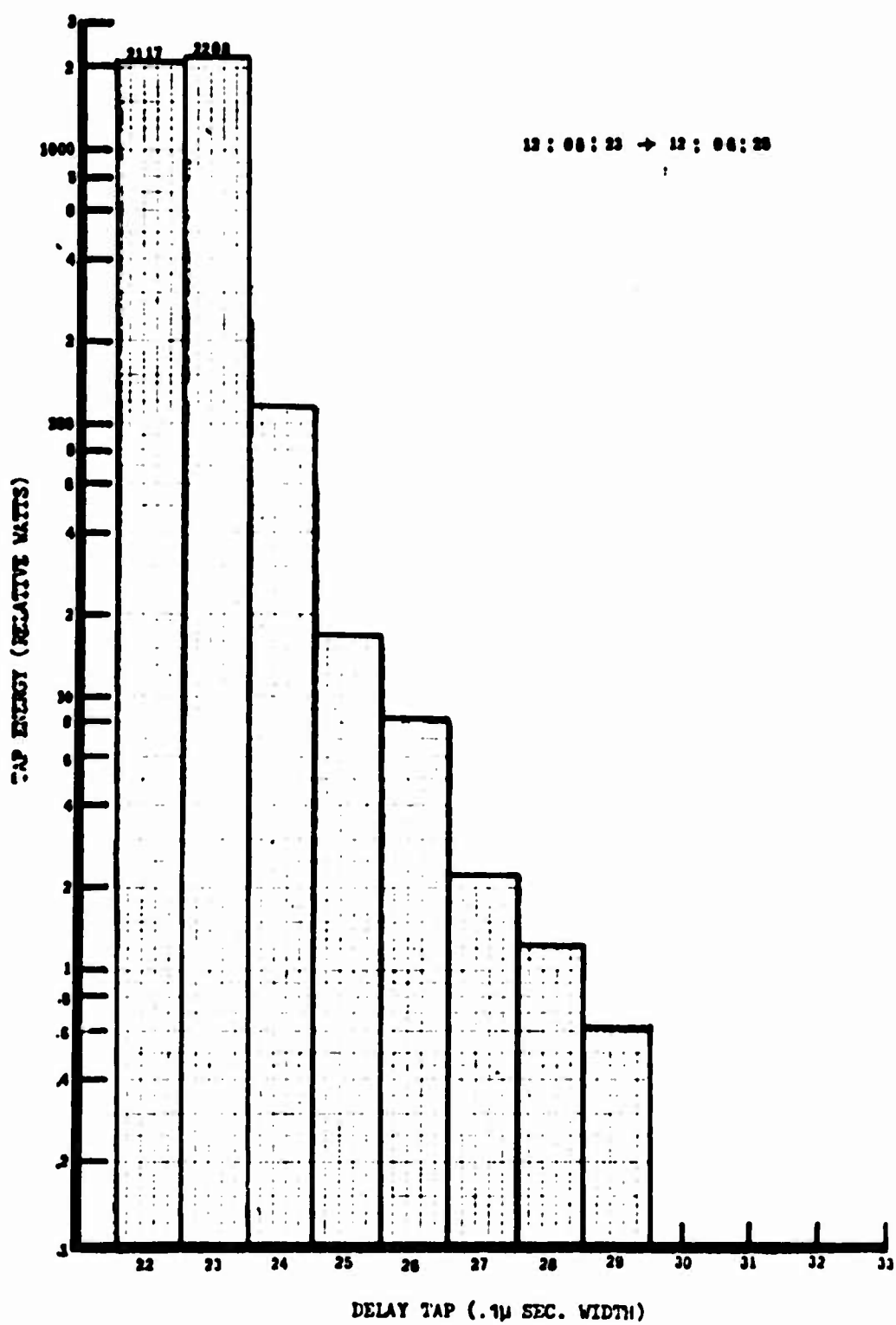


Figure 4-32.—O'Hare Delay Spectra (12:06:24 GMT)

#### **4.4 CONCLUSIONS**

**Forward scatter multipath data has been collected for a comprehensive set of oceanic and CONUS test conditions. Analysis of this data has concentrated primarily upon determining the channels delay-Doppler scatter function and its associated integral and Fourier parameters.**

**For oceanic multipath properties of the scatter function were found to be in general accord with predictions based upon the physical optics very-rough surface model. Numerical surface area integration of this model's vector formulation appears to closely predict the delay-Doppler distributed nature of the multipath returns. A closed form solution based upon "steepest descent" integration techniques fails to account for the assymetrical Doppler spectra associated with other than cross-plane geometries.**

**The mean square total scatter coefficient data for the horizontal and vertical polarization probes were shown to be roughly equivalent to the product of divergence factor and smooth earth Fresnel reflection coefficient. At the lower grazing angles, however, it was observed that the vertical data typically exceeded this relationship. This is in accord with expectation based upon previous experiments and is predicted by the surface integration scatter model.**

**Channel parameter 3-dB spread values were presented as a function of grazing angle. Doppler spreads from a low of 25 Hz to a high of 215 Hz were observed and display a marked tendency to increase with an increase in grazing angle. No appreciable grazing angle dependence was apparent for the delay spread data which varied over a range from 0.35  $\mu$ sec to 1.5  $\mu$ sec. The time autocorrelation function spread displayed, as expected, an inverse grazing angle dependence to that of the Doppler data; it was characterized by a low of 1.5 msec and a high of 9 msec. Coherent bandwidth ranging from 100 kHz up to 380 kHz were measured with the higher values typically being associated (very weakly) with high grazing angles and vice versa.**

**One of the most obvious characteristics of the overland CONUS scatter data is its high degree of signal structure non-stationarity. This was readily confirmed through a visual observation of a fifteen-minute delay spectra time history segment. Similarly, the signature of the channel delay-Doppler scatter function varies markedly with experiment time and was used to isolate periods of very low spreading, modest spreading, biased positional scatter, large irregular Doppler spectra return, and mixed scatter process return.**

**Results for a limited portion of the data gathered during the airport landing/taxi sequence were presented to indicate two rather preliminary conclusions. These relate to the fairly large amplitude fluctuations of the energy received in the direct signal taps when using the crossed-slot antenna and to the absence of substantial multipath return arriving with delays greater than 0.2  $\mu$ sec with respect to the direct path signal.**

## **5.0 MODEM EVALUATION TEST RESULTS AND ANALYSIS**

Analyzed test results for each of the voice, digital data and ranging modems tested are presented and discussed.

### **5.1 DATA ANALYSIS PROCEDURES**

#### **5.1.1 DATA ANALYSIS FUNCTIONAL FLOW**

Figure 5-1 illustrates the various machine and human judgment processes which make up the total modem data reduction and analysis (DR&A) system. Time periods for which valid voice data were acquired are identified from the airborne logs and strip charts. Corresponding voice channels are transcribed to 1/4-inch tapes for intelligibility scoring by CBS Labs (Ref 5-1). A limited quantity of transcribed SCIM data has been submitted to NASA/GSFC for processing.

Analog source tapes are sent to the Boeing Test Data Processing Center (TDPC) where (a) specified time segments and tape tracks are digitized to provide 7-track, 800-bpi digital tapes compatible with the CDC 6600 computer, and (b) aircraft heading, pitch, roll and modem monitor signals are stripped out on chart paper.

Airplane logs, onboard stripcharts, and TDPC stripcharts are used to identify which time segments of the digital tapes are to be analyzed. These time segments are subjected to detailed CDC 6600 processing using the applicable analysis programs (Ref. 5-2). Output from the CDC 6600 includes C/N<sub>0</sub> and S/I statistics, bit error rates, error pattern statistics and ranging data analysis. The above quantities are manually merged with other data such as voice intelligibility scores and aircraft parameters to give final outputs.

#### **5.1.2 C/N<sub>0</sub> AND S/I DETERMINATION**

The calculation of C/N<sub>0</sub> and S/I is basic to all modem and antenna evaluation tests. The CW carrier transmitted from Rosman to the aircraft via ATS-6 is processed by an envelope detector in the Carrier Detector unit. The detected envelope output is FM recorded and computer analyzed to determine C/N<sub>0</sub> and S/I. The algorithm makes it possible to obtain these estimates as often as every 15 seconds for modem evaluation and every 3 seconds for antenna tests.

Specifically, the envelope detected signal is digitized at a 2kHz rate using 10-bit quantization to obtain 1025 signal strength samples in approximately 0.5 second. The 1025 samples are processed to remove sample bias and linear drift components. The sample mean, ( $S$ ), mean-squared values ( $S^2$ ) and variance ( $\sigma^2$ ) are then determined. After tapering of the time domain samples to minimize spectral window sidelobes peaks the discrete Fourier Transform (FFT) is performed on the time domain data. The output of the FFT provides power spectral density versus frequency for the range 0 to 800 Hz.

The output spectrum can be expanded as a mathematical series involving direct signal power, multipath spectrum, and the noise spectrum. The spectral data is used to calculate a quantity termed noise floor which is computed as the weighted average of the spectral density from

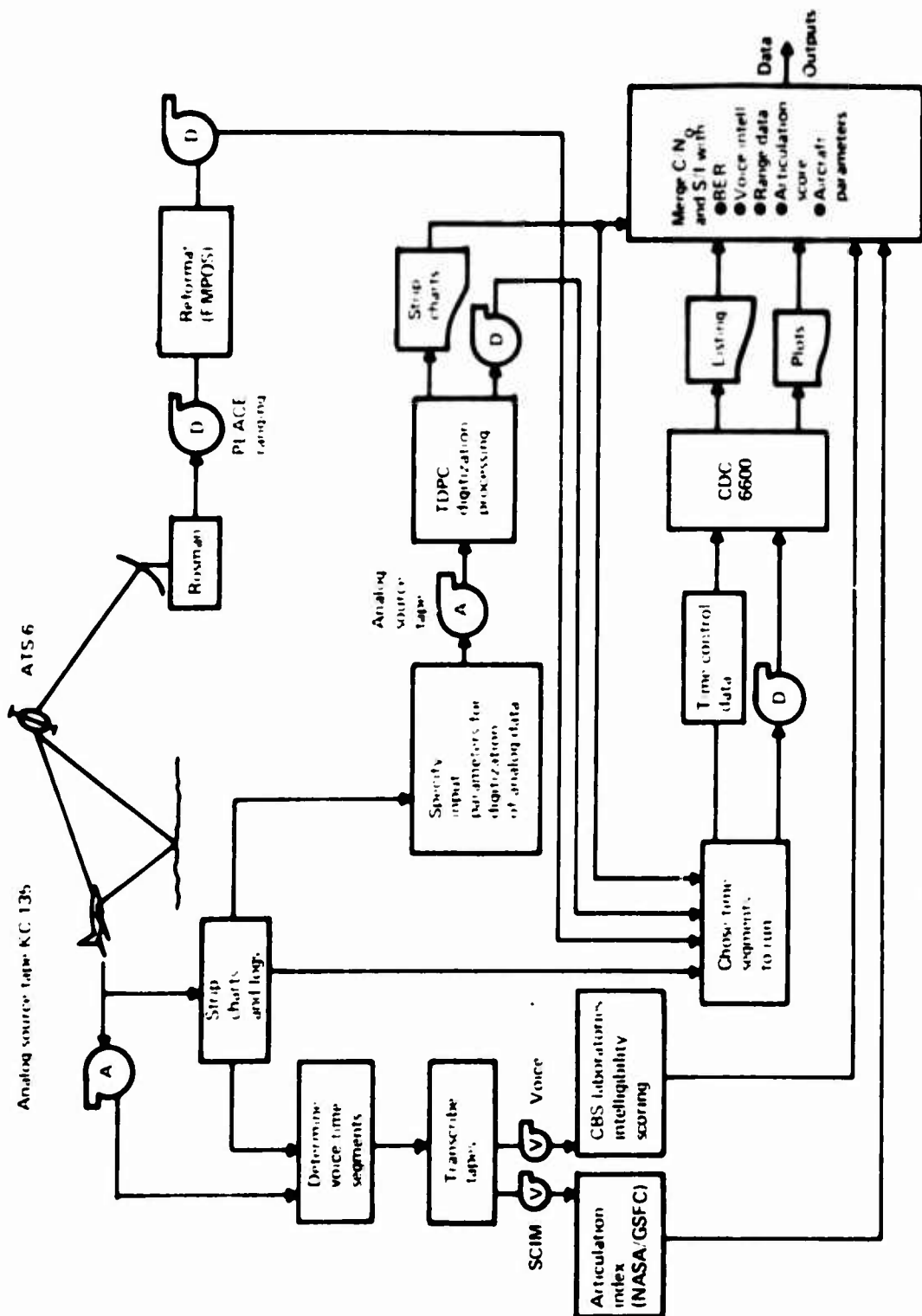


Figure 5.1 *Agile DR&A System Block Diagram*

250 Hz to 800 Hz. This frequency range is chosen with the **apriori knowledge** that there will be little multipath power above 250 Hz in comparison to noise power. The ratio of the squared mean signal strength to the noise floor value is calculated and used to determine  $C/N_0$  using a computer look-up table. The look-up table is based upon analytical modeling of the Carrier Detector output. The modeling has been experimentally verified for additive noise environment.

To estimate S/I, the spectral data is numerically integrated from 2 Hz to 250 Hz to yield a band-limited variance figure caused by the combined effects of multipath power and noise. This calculation uses the **apriori knowledge** that virtually all multipath related energy will fall within the range of 0-250 Hz. The ratio of squared mean to the above band-limited variance is calculated and used together with  $C/N_0$  to estimate S/I by graphical methods. These graphical relationships are also based upon careful analytical modeling.

Typically, several values of  $C/N_0$  and the S/I statistic are calculated over a time segment, from which the mean and standard deviation of these parameters are calculated. The mean  $C/N_0$  is the value used in plotting data in the final output format and the standard deviation gives an indication of the constancy of  $C/N_0$ . Similarly the mean of the S/I statistic is used to determine the mean S/I during the data time segment and the standard deviation indicates the constancy of that parameter estimate.

Reference 5-2 and 5-3 describe the envelope detector algorithm and provide the mathematical basis for the analysis.

## 5.2 VOICE MODEM TEST RESULTS

Voice modem test results are presented beginning with data from voice-only mode Type I tests. These data are plotted in Figures 5-2 through 5-6 as P.B. word list intelligibility scores versus  $C/N_0$  derived by computer analysis of the envelope detected CW channel. One set of points as noted on each of Figures 5-5 and 5-6, however, have been plotted with directly measured (HP 312A)  $C/N_0$  because of questionable data from the computer analyzed  $C/N_0$  for these points.

Figures 5-2 and 5-3 for the September, October, and November Type I tests show that the NBFM and both hybrid modems have word intelligibility of 60 percent or greater at 43 dB-Hz. It is also apparent that Hybrid modem No. 1 scored highest at all values of  $C/N_0$  tested and that the NBFM modem usually scored lowest. Figure 5-4 for the February Type I tests shows approximately the same relative performance for NBFM and the two hybrid modems. Also included in this figure is the limited amount of data analyzed to date for the ADVM modems. These data indicate that performance of the analog ADVM configuration is superior to Hybrid No. 2 but inferior to Hybrid No. 1. The ADVM digital implementation appears to perform better than Hybrid No. 2 above 45 dB-Hz but is inferior below 43 dB-Hz where performance degradation is rapid with decreasing  $C/N_0$ . This is expected because with a delta modulation data rate of 19.2 Kbps  $E_b/N_0$  will be less than zero dB for  $C/N_0$  below 43 dB-Hz and the decoded BER will be greater than  $10^{-1}$ .

Intelligibility scores for Type I tests of the Hybrid modems operating in the combined voice and data mode are shown in Figure 5-5. Comparing these data with Figures 5-2 through 5-3

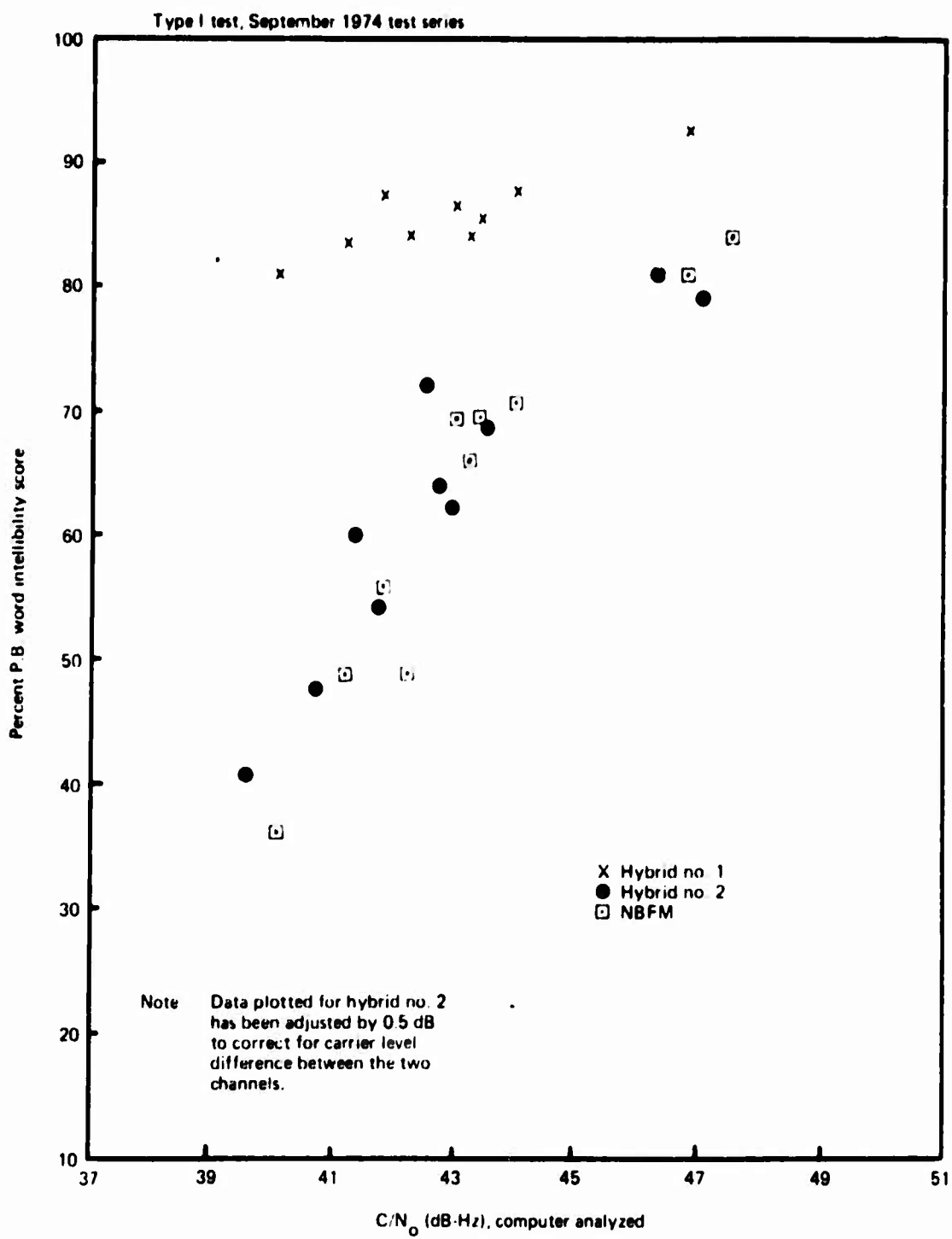


Figure 5-2.—Voice Modem Intelligibility Score, Voice Only Mode

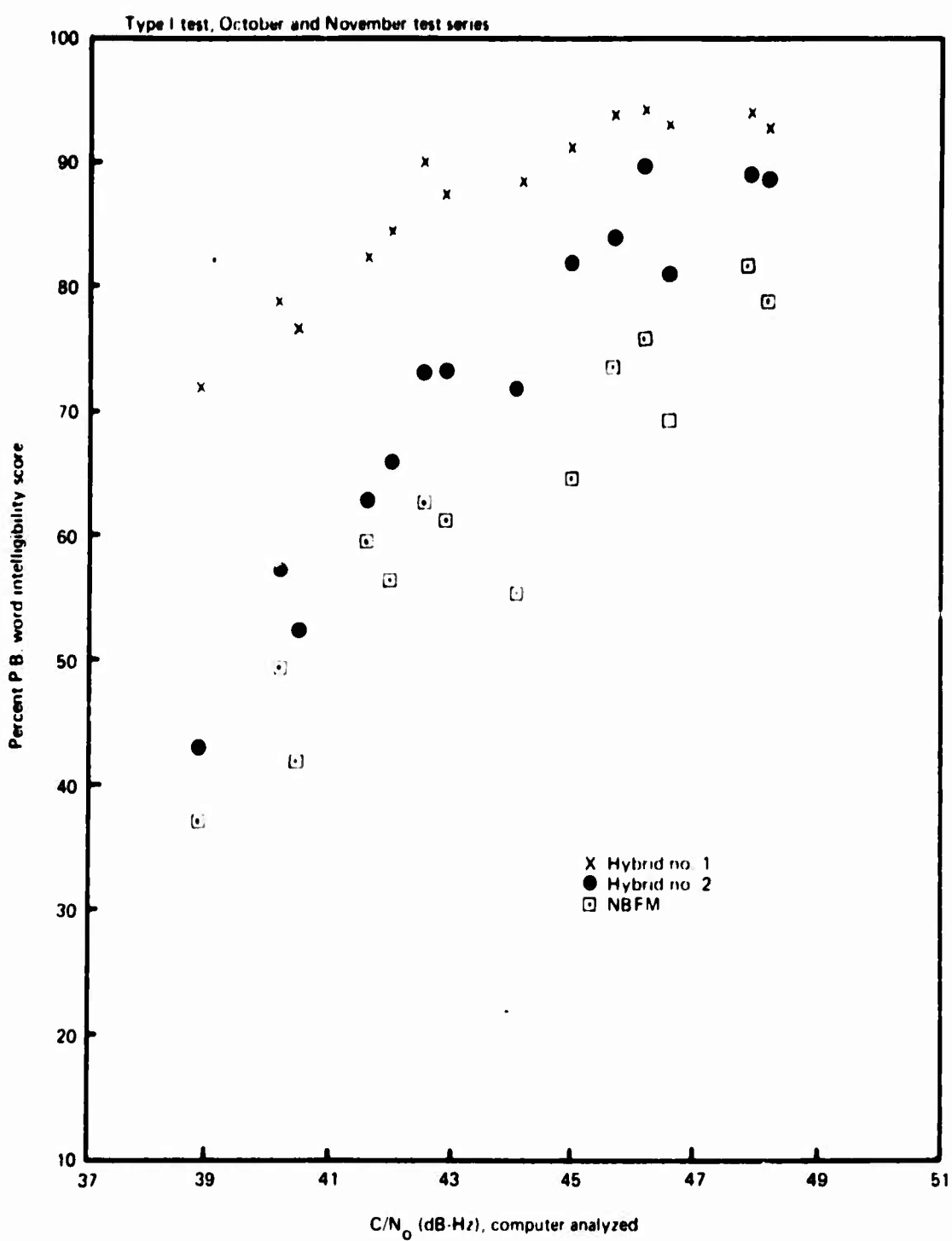


Figure 5-3.—Voice Modem Intelligibility Score, Voice Only Mode

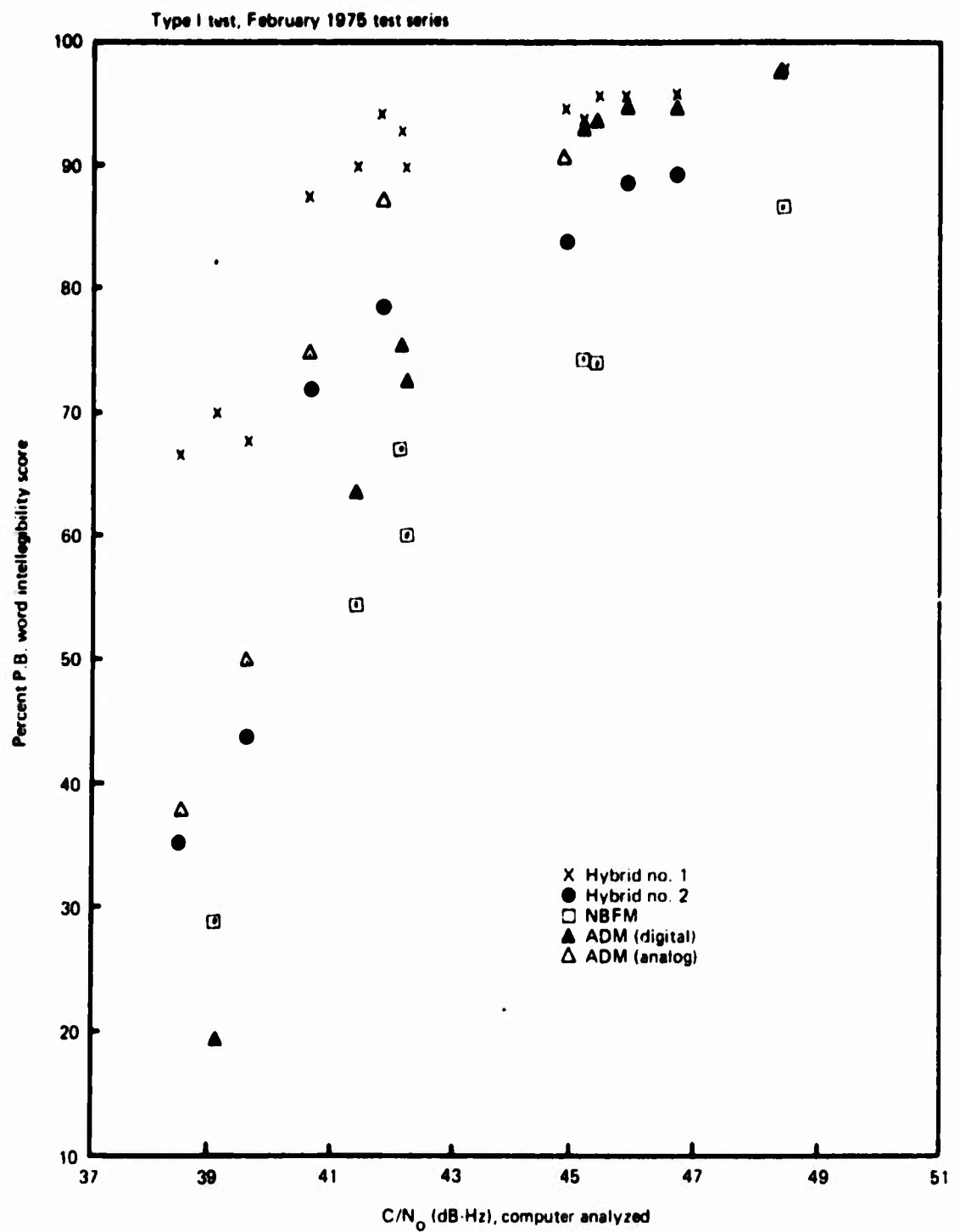


Figure 5-4.—Voice Modem Intelligibility Score, Voice Only Mode

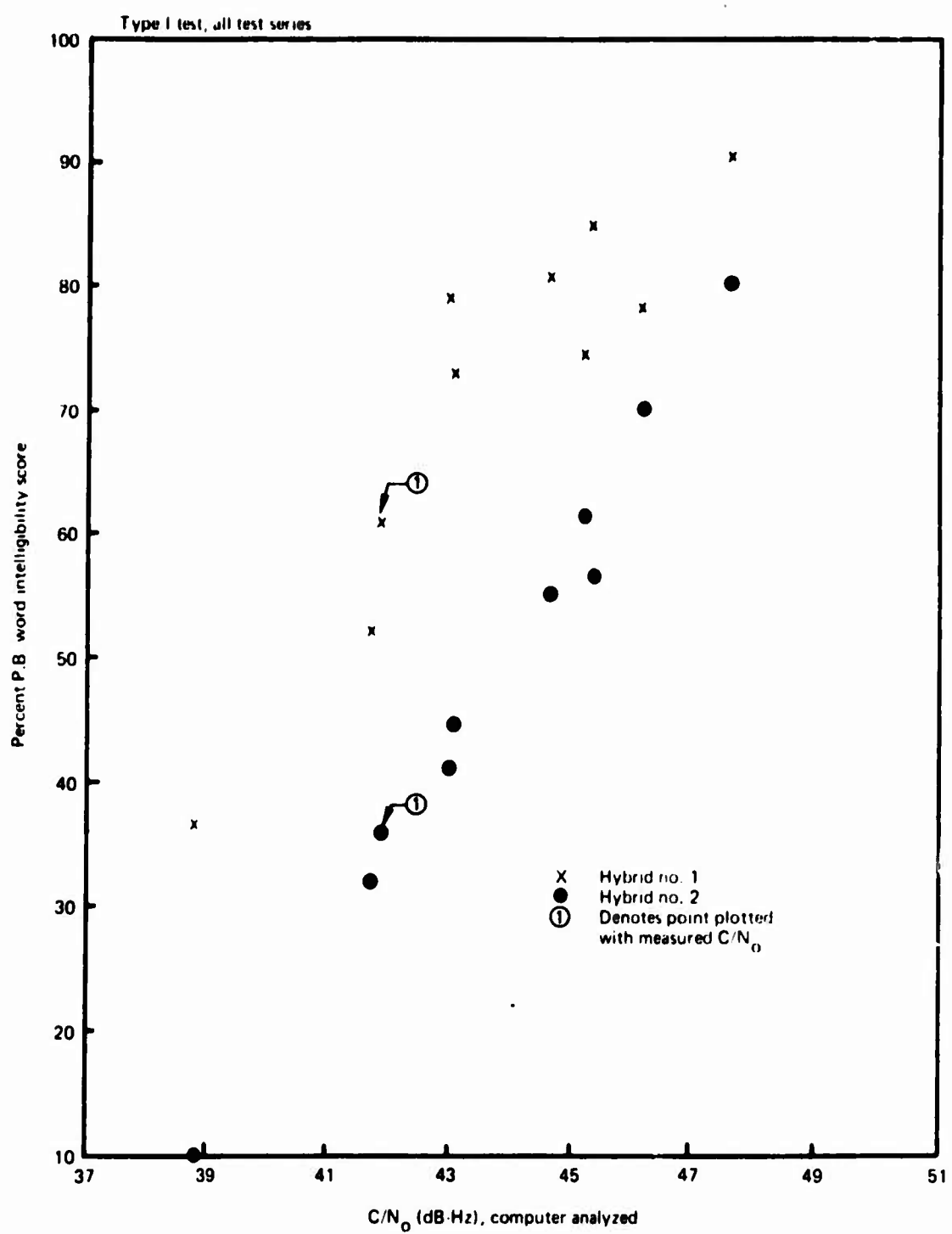


Figure 5-5.—Voice Modem Intelligibility Score, Hybrid Mode

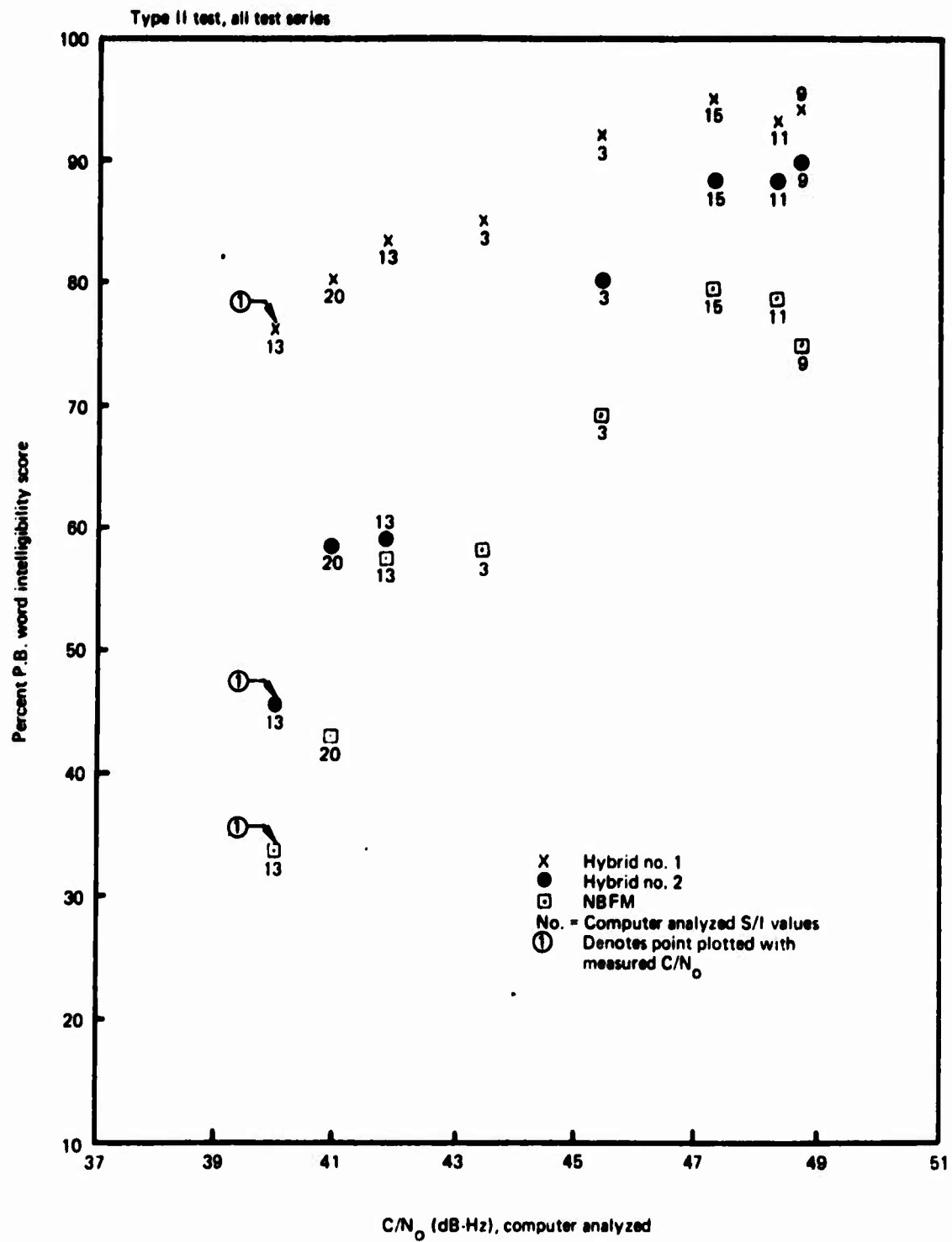


Figure 5-6.—Voice Modem Intelligibility Score, Voice Only Mode

it is noted that the performance of each hybrid modem is degraded by at least 3 dB relative to performance in the voice only mode. An exact 3 dB degradation is predictable for Hybrid No. 2 since the data/voice power sharing is exactly equal. A more complex relationship is in effect for Hybrid No. 1 but the results follow intuitive predictions and are consistent with acceptance test results.

Intelligibility scores of Type II voice only tests from all series are plotted in Figure 5-6. The Type II intelligibility scores for the three modems compare favorably with the Type I tests reported by Figure 5-3 in terms of both absolute performance and relative performance between modems. Study of Figure 5-6, where intelligibility scores are plotted versus  $C/N_0$  with S/I as a parameter, shows that performance of the modems is not strongly sensitive to the multipath contamination. Even for S/I as low as 3 dB the Type II test results do not differ greatly from those of the Type I tests.

The observed insensitivity of the analog voice modems to multipath is an important finding of this test program. It is intuitively believed to be due to natural waveform redundancy and the fact that demodulator output noise induced by multipath is largely sub-audio in frequency.

The voice modem performance results presented above represent most of the voice test data from the ATS-6 program. The January Type II data are in the process of being analyzed and will be included in the Final Report. The January Type I and all of the March voice tapes have been transcribed and sent directly to TSC. Selected tapes from these data sets have been forwarded by TSC to CBS Labs for intelligibility scoring.

### 5.3 DIGITAL DATA MODEM TEST RESULTS

Test results from the digital data modem Type I and Type II tests are presented in this section. These data are presented primarily as plots of bit error rate (BER) versus  $C/N_0$  on charts against reference curves of theoretical performance for similar modems. A brief description of the reference performance curves is followed by presentation and discussion of the test results. Results of the hybrid voice and data tests are presented also.

#### 5.3.1 REFERENCE THEORETICAL PERFORMANCE CURVES

Type I test results are plotted on charts containing reference curves for ideal theoretical performance of the applicable demodulation technique in an additive white gaussian noise (AWGN) channel. The classical error expressions for these idealized cases are:

DECP SK (differential encoding, coherent detection)

$$P(E) = \frac{2}{\sqrt{\pi}} \operatorname{erfc} \sqrt{2 E/N_0} \quad (1 - \operatorname{erfc} \sqrt{2 E/N_0}) \quad (5.1)$$

DPSK (differential encoding, differentially-coherent detection)

$$P(E) = (e^{-E/N_0})/2 \quad (5.2)$$

In these expressions,  $E/N_0$  is the ratio of bit energy to single-sided noise density and the abscissa values of  $C/N_0$  for the curves are obtained by adding  $E/N_0$  (in dB) to  $10 \log r_b$ , where  $r_b$  is the data clock rate.

The idealized performance curves are based on the assumption that perfect carrier phase (or frequency) coherence is achieved by the DECPSK and DPSK modems respectively and that perfect bit timing synchronization is also achieved. Because of implementation losses dictated by practical considerations, such as signal acquisition and tracking performance, perfect carrier and bit timing synchronization are not achieved. Thus, the reference curves represent a lower bound on bit error probability.

Type II test results are plotted on charts with reference curves so BER versus  $C/N_0$ , with signal to multipath interference ratio ( $S/I$ ) as a parameter. The reference curves are based on reception of a direct signal combined with ocean reflected multipath and modeled as a Rician fading channel, i.e., a coherent direct component plus a complex gaussian component representing the multipath.

Although, to our knowledge, no general analysis of DECPSK performance in such a channel has been published, an upper bound on BER can be found as twice the BER for CPSK as calculated by Blair and Balcewicz (Ref. 5-4 and 5-5). In the application of this analysis an additional parameter,  $\gamma$ , is defined and is related to the bandwidth ratio:

$$\gamma = \frac{B_L}{B_F + B_L} \quad (5.3)$$

where  $B_L$  is the modem carrier tracking loop bandwidth and  $B_F$  is the channel fading bandwidth. For an elevation angle of  $15^\circ$  and a speed of 400 knots the one-sided  $e^{-1}$   $B_F$  was found to be approximately 60 Hz via the ATS-5 tests which is commensurate with the value from A.TS-6 tests at  $15^\circ$  elevation. Thus, with assumed values of  $B_F = 60$  Hz and  $B_L = 210$  Hz (FAA CPSK demodulator)  $\gamma = 0.78$ . Thus, the  $\gamma = 0.75$  curves from (Ref. 5-5) provide the basis for the DECPSK reference curves for Type II data plotted herein. Because the different DECPSK modems tested have carrier loop bandwidths somewhat different from one another a single set of ideal theoretical performance curves cannot strictly apply to each. Therefore, the selected set of performance curves must be viewed as simply a common reference for comparison of modem performance.

Performance of DPSK under the assumption of long term fading has been treated by Jones (Ref. 5-6) and can be calculated as:

$$P(E) = \left[ \frac{1/2}{1 + \frac{E/N_0}{S/I}} \right] \exp - \left[ \frac{E/N_0}{1 + \frac{E/N_0}{S/I}} \right] \quad (5.4)$$

If the long-term fading assumption is relaxed to the point where small fluctuations in channel complex gain are allowed during detection time, then the work of Bello and Nellin (Ref. 5-7) and of Frasco and Goldstein (Ref. 5-8) is pertinent. Dependent on fading bandwidth relative to symbol rate, an effective signal-to-noise ratio is developed in terms of non-fading  $E/N_0$  and  $S/I$ . The equivalent  $E/N_0$  is:

$$E/N'_0 = \frac{E/N_0}{1 + (1-\rho)(S/I)^{-1}(E/N_0)} \quad (5.5)$$

where  $\rho$  is a measure of correlation of channel gain over a bit period. Using a Gaussian correlation function, the factor  $(1-\rho)$  is defined (Ref. 5-8) as:

$$(1-\rho) = 1 - e^{-\frac{(\pi^2 B_F^2 T^2)}{2}} \approx \frac{\pi^2 B_F^2 T^2}{2} \quad (5.6)$$

where  $B_F$  is the one-sided  $e^{-1}$  fading bandwidth and  $T$  is the data bit period. For the ATS-6 Type II test conditions and a 1200 bps data rate this yields:

$$(1-\rho) \approx .025 \text{ or } \rho \approx .975 \quad (5.7)$$

The reference performance curves for the DPSK Type II tests (Figure 5-18) were derived as described above.

### 5.3.2 TYPE I TEST RESULTS

Type I test results for each of the four DECPKS demodulators presented in Figures 5-7 through 5-10. The data plotted are BER versus computer analyzed  $C/N_0$ . Factors which contribute to data point scattering are uncertainties in the  $C/N_0$  measurement data and uncertainty of error probability, due to finite sample size. This last factor is particularly relevant at high  $C/N_0$  values where few errors are observed. In these cases the number of errors and number of bits analyzed have been shown on the plots.

Examination of the Type I DECPKS data of Figures 5-7 through 5-10 leads to several observations. An assessment of relative demodulator performance, though somewhat subjective, ranks the Hybrid No. 1 demodulator first, followed by Hybrid No. 2, FAA CPSK, and NASA DECPKS demodulators in that order. A "best-fit" curve to the experimental data generally falls about 1 dB to the right of theoretical performance for the two hybrid modems and slightly more displaced for FAA CPSK and NASA DECPKS.

Further examination of Figures 5-7 through 5-10 reveals no obvious tendency to exhibit behavior which would be expected in the presence of multipath. (The expected behavior in the presence of multipath is discussed in the following section.) The S/I values calculated from the carrier detector data for Type I tests were usually 15 dB or higher and, hence, this is the performance which was expected.

Type I test results for the FAA DPSK demodulator are presented in Figure 5-11. The data has been identified as preliminary information because of a discrepancy in the data reformatting process, peculiar to the channel which is used for the DPSK demodulator test data. This discrepancy, when present, causes the occasional addition of data bit errors not present in the demodulator output data stream thus giving the appearance of degraded demodulator performance. Those data runs, for which the discrepancy is known to have existed, have been re-submitted for processing but complete results are not available at the time of this writing. Some of the outliers have been found to fall much closer to ideal DPSK. The reprocessed data will be presented in the final report and further comment will be reserved until that time.

Type I digital data test results for the hybrid modems operating in the voice and data mode are shown in Figures 5-12 and 5-13. The reference curves assume the total signal power is

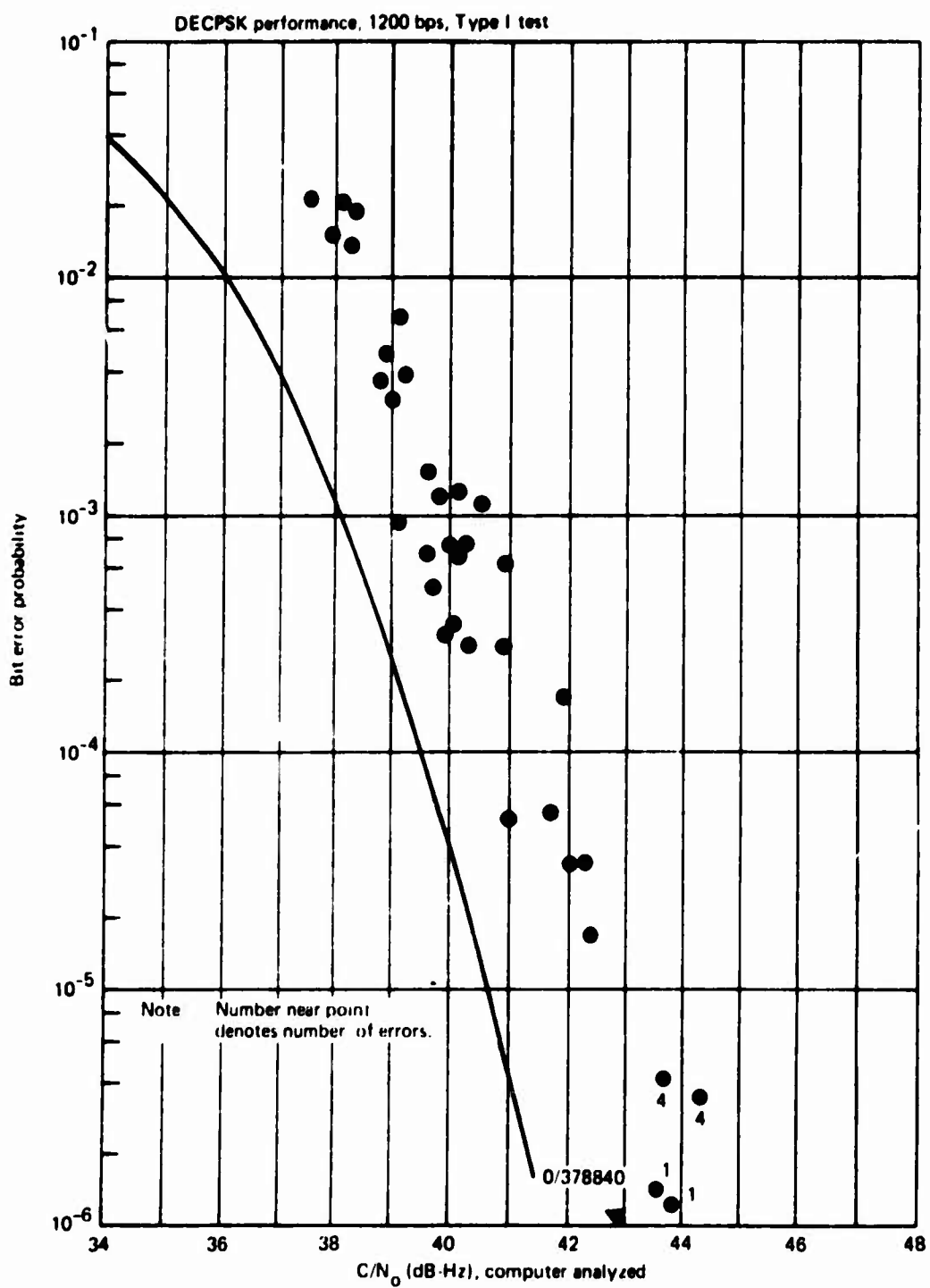


Figure 5.7.- BER Performance, NASA DECPSK Demodulator

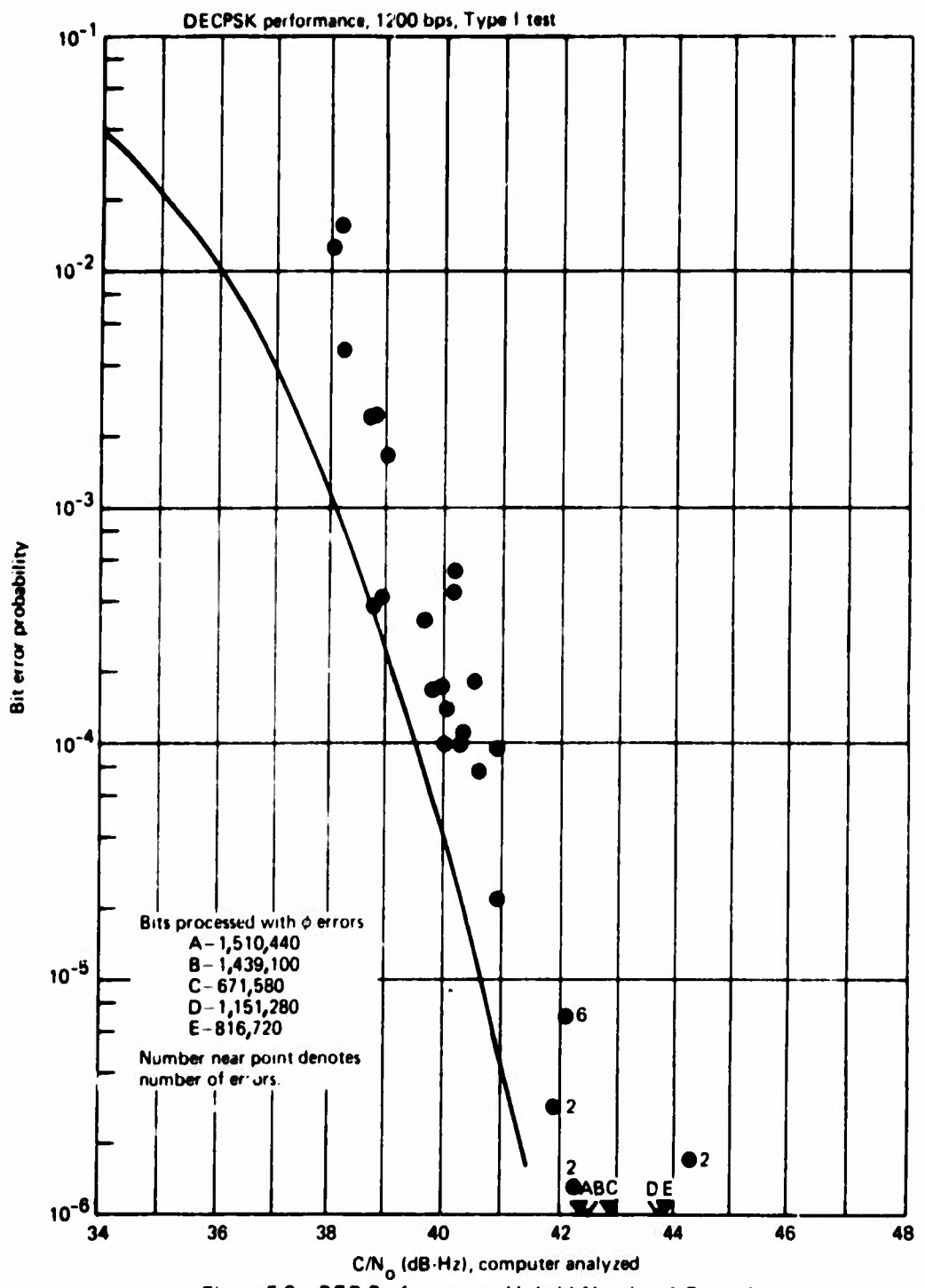
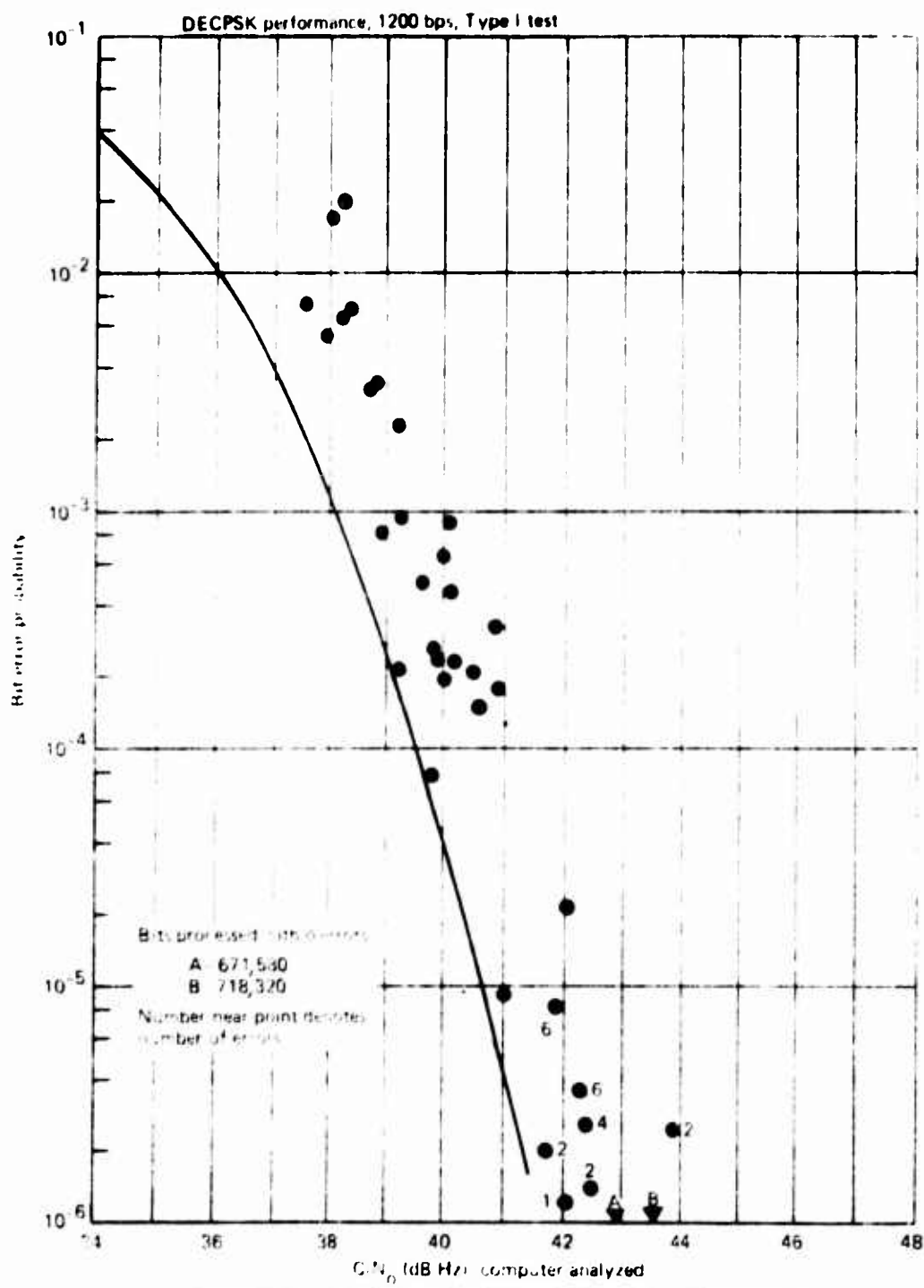


Figure 5-8.—BER Performance, Hybrid Number 1 Demodulator



**Figure 5-9.—BER Performance, Hybrid Number 2 Demodulator**

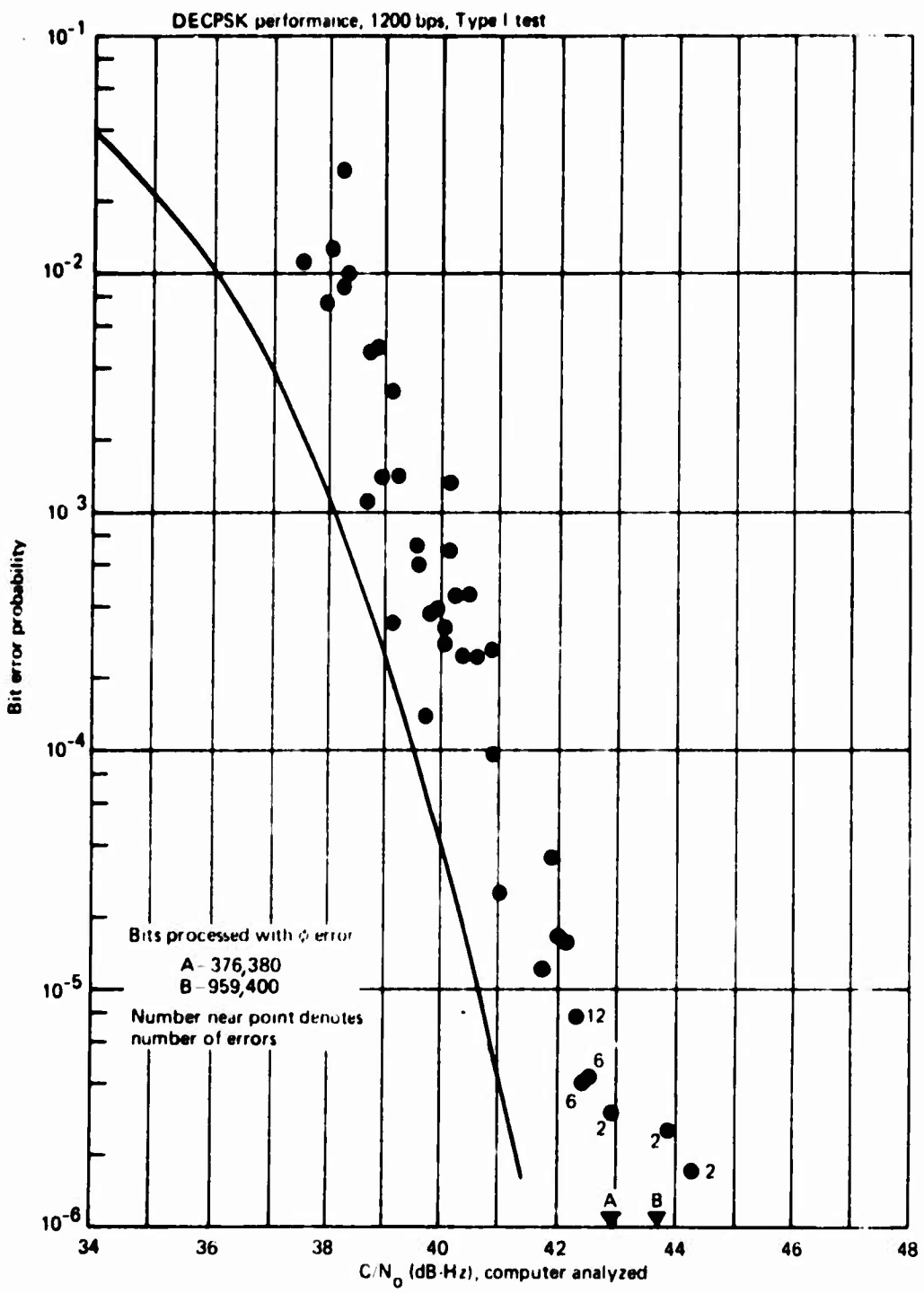


Figure 5 10.—BER Performance, CPSK Demodulator

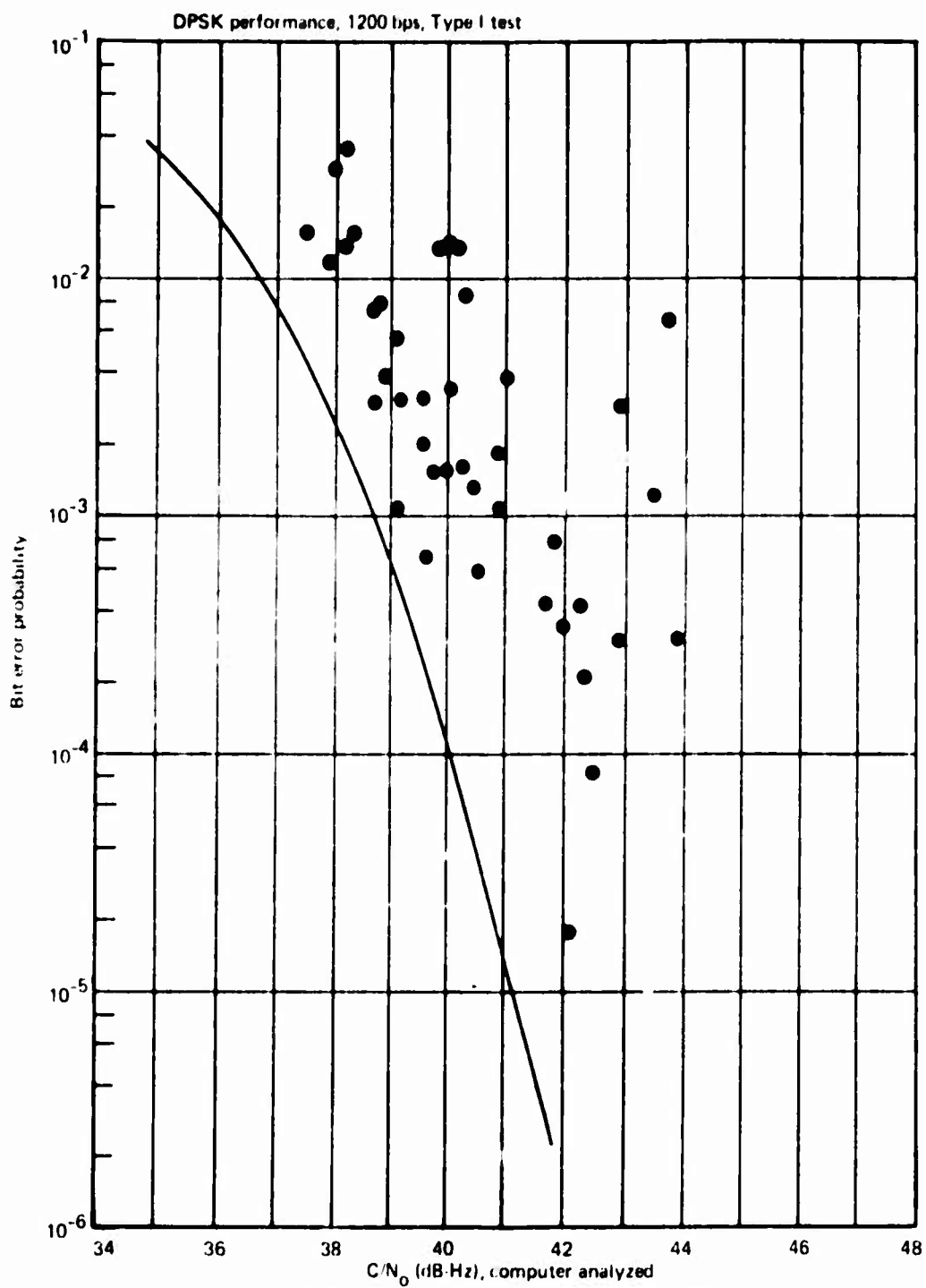


Figure 5.11. -BER Performance, DPSK Demodulator

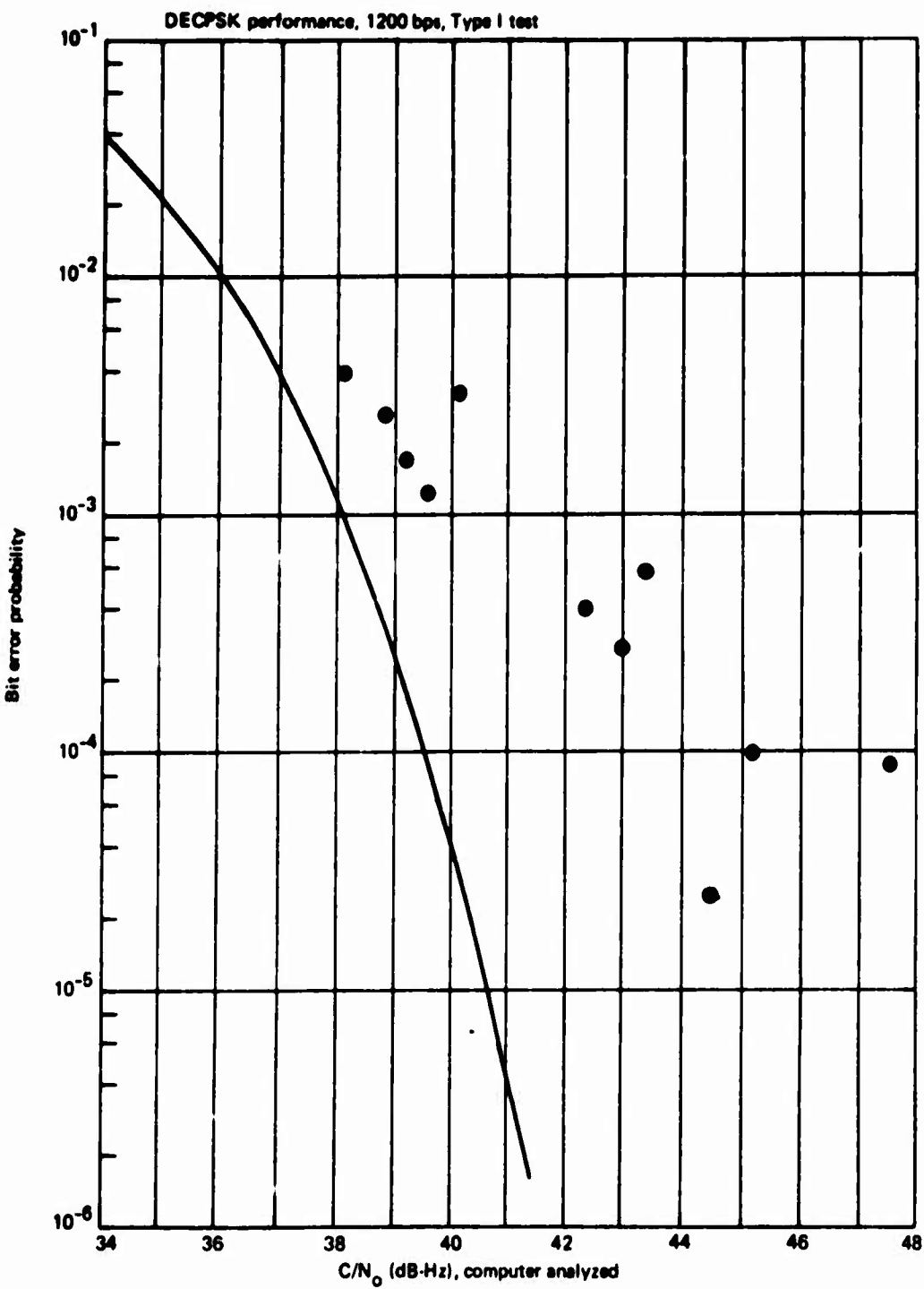


Figure 5-12.—BER Performance, Hybrid Number 1 Demodulator, Hybrid Mode

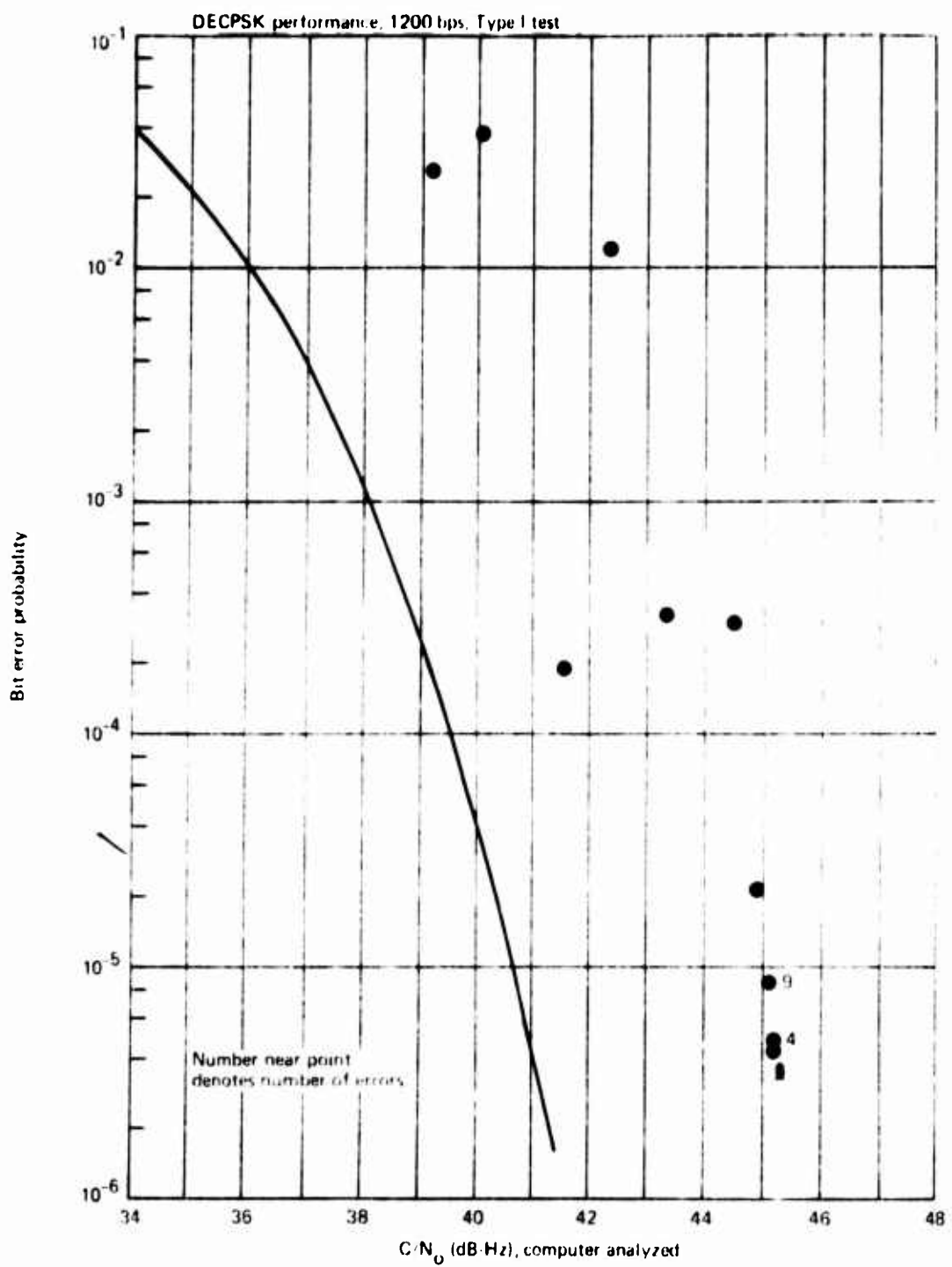


Figure 5-13. - BER Performance, Hybrid Number 2 Demodulator, Hybrid Mode

devoted to the data channel, although this is obviously not the case. Although these data are rather limited in quantity, some tentative observations can be made. Hybrid modem No. 1 appears to suffer less than 3 dB degradation (relative to the data only mode) at low  $C/N_0$  and somewhat more than 3 dB degradation at high  $C/N_0$  values. (A stochastically-based rationale for this effect will be presented in the final report.) No data points were recorded for BER values smaller than  $10^{-5}$ . Hybrid modem No. 2, however, experienced roughly 3 dB degradation over the range of  $C/N_0$  tested and logged three data points at less than one error in  $10^5$  bits. As for voice intelligibility, a 3 dB degradation is predictable.

### 5.3.3 TYPE II TEST RESULTS

The Type II, data only, test results for each demodulator are presented in Figures 5-14 through 5-18. Factors contributing to the scatter of these data points, in addition to those described previously, are uncertainty in measurement of S/I and resolution of the presentation. The S/I measurement uncertainty is  $\pm 2$  dB and the computed values of S/I are plotted with a resolution of  $\pm 1.5$  dB, i.e. all values falling within  $\pm 1.5$  dB of the respective values are treated as having common S/I to enhance readability.

The reference performance curves for the Type II data show an expected decreasing dependence of BER on  $C/N_0$  as S/I is decreased. In general, all of the data demodulators demonstrated performance in agreement with the shape of the reference curves. In contrast with the Type I test results, however, there is little discernible difference in performance between demodulators Hybrid No. 1, Hybrid No. 2, and FAA CPSK as shown in Figures 5-15 through 5-17. Figure 5-14, however, shows that the NASA DECPKS demodulator does not perform as well as do the other three DECPKS demodulators.

Although some of the DPSK demodulator Type II data suffered from the same data processing problems experienced with the Type I data, Figure 5-18 shows that performance of this demodulator is superior to that of the DECPKS demodulators at low S/I. At S/I values above approximately 9 dB, however, this advantage in absolute BER performance is seen to disappear. As with Figure 5-11, Figure 5-18 will be revised for the final report when the re-processed DPSK data are available.

### 5.3.4 BLOCK ERROR STATISTICS

The preceding sections presented digital data demodulator performance in terms of average error rate without regard to the distribution of errors. Additional insight into the behavior of the DECPKS and DPSK demodulation techniques can be obtained from the test data block error statistics. Block errors in this case refer to errors occurring within 24 bit blocks of the demodulator output data stream. Block error frequency histograms for selected DECPKS and DPSK Type I and Type II tests are presented in Figures 5-19 and 5-20. The FAA CPSK demodulator was selected as the DECPKS representative for comparison with the DPSK demodulator because these units have several design features in common. The test data for the histograms were taken from test intervals for which the DPSK data are not affected by the data processing difficulties discussed previously.

Block error histograms for Type I tests with two values of  $C/N_0$  are presented in Figure 5-19. (Note that total errors represented by each bar in the histogram are the product of the

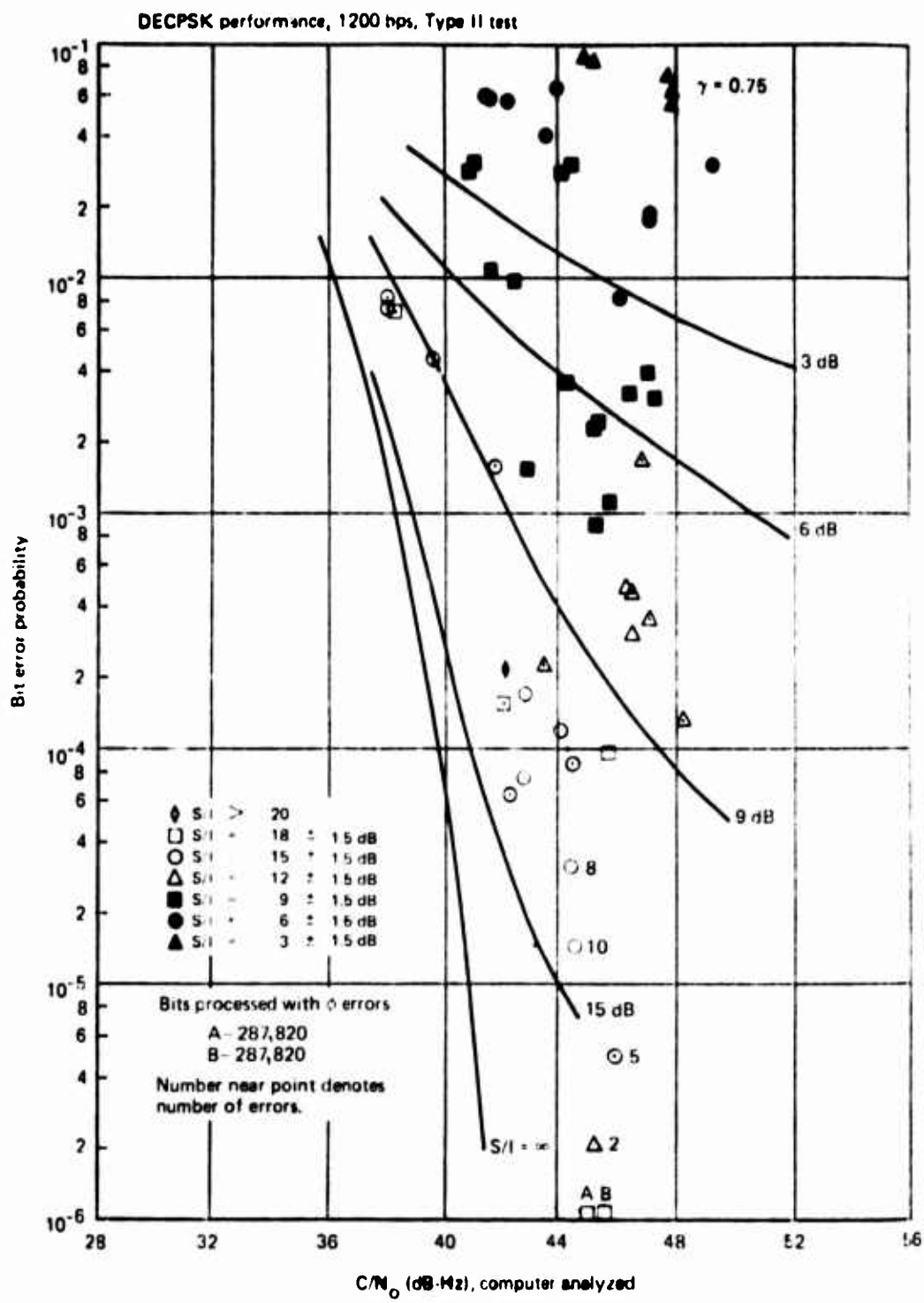


Figure 5-14.—BER Performance, NASA DECPSK Demodulator

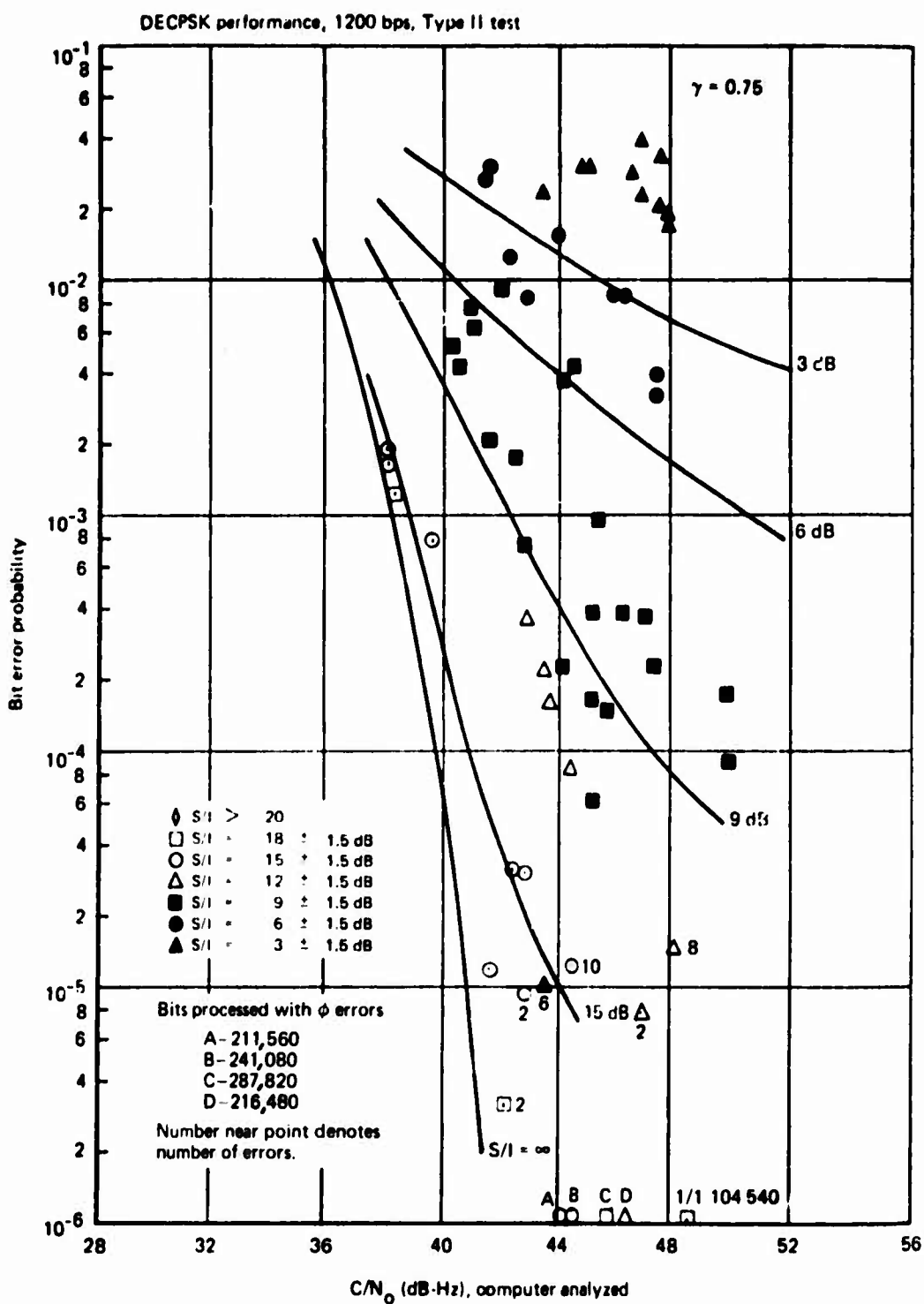


Figure 5-15.—BER Performance, Hybrid Number 1 Demodulator

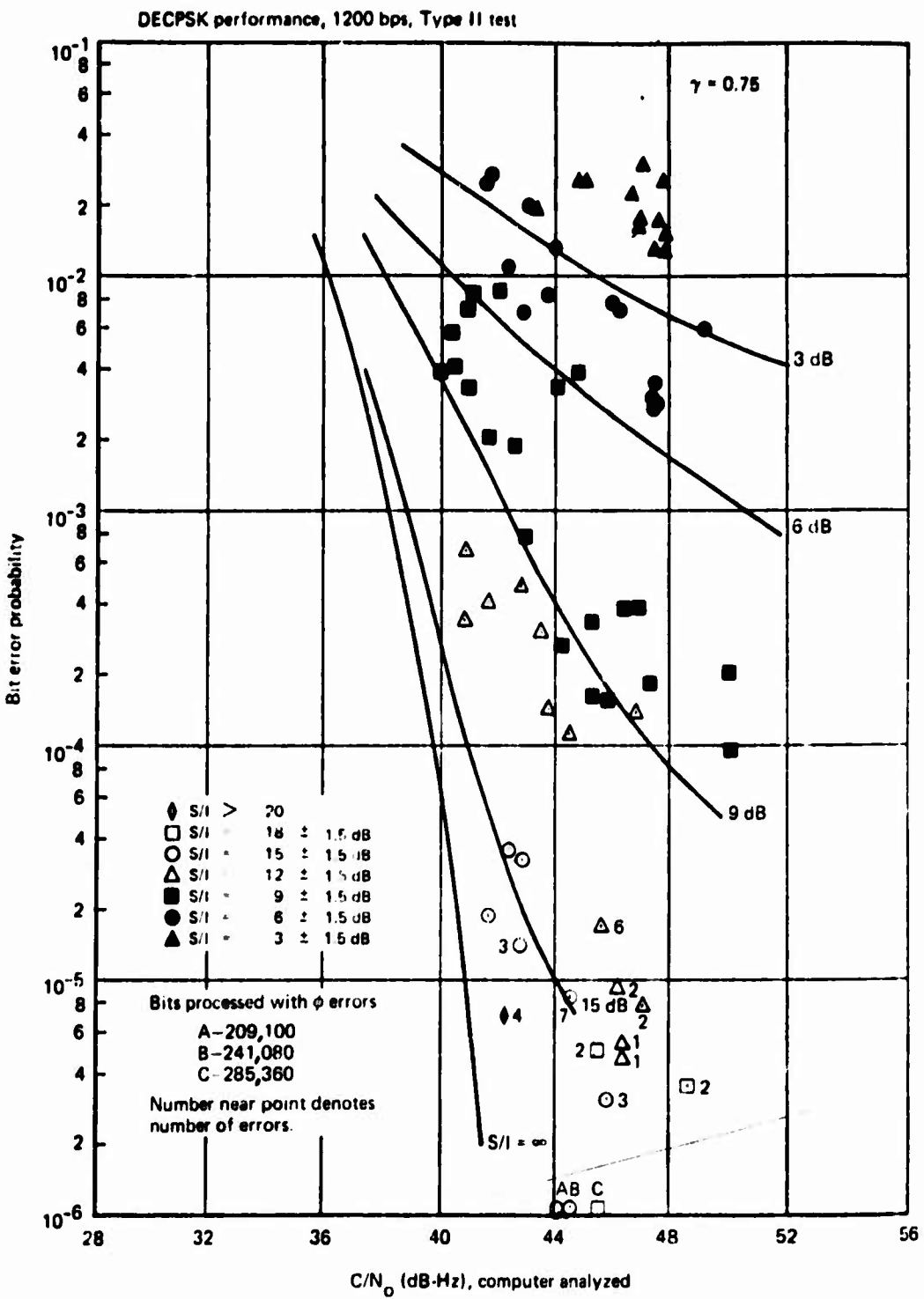


Figure 5-16.—BER Performance, Hybrid Number 2 Demodulator

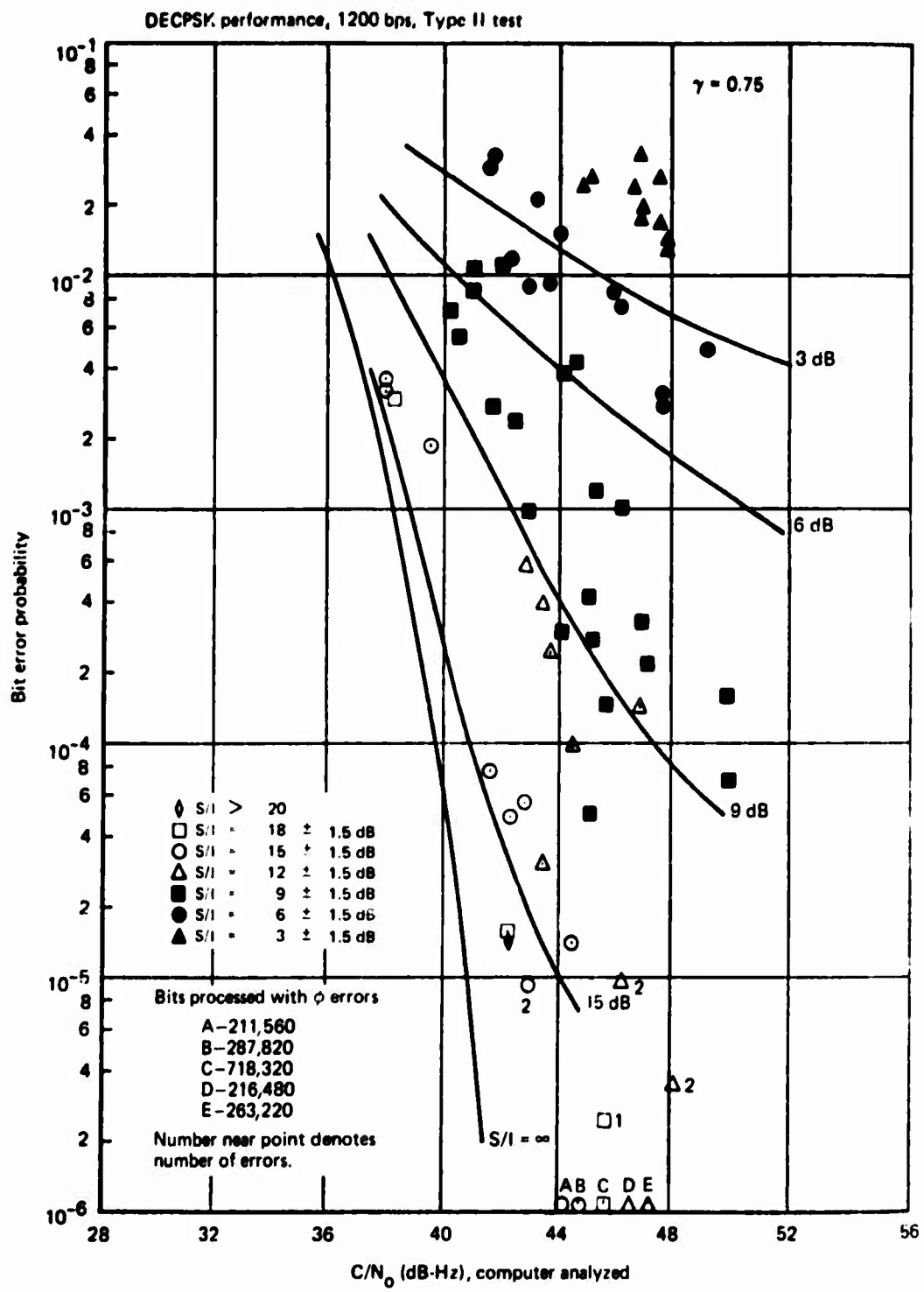


Figure 5-17.—BER Performance, CPSK Demodulator

10-1 DPSK performance, 1200 bps. Type II test

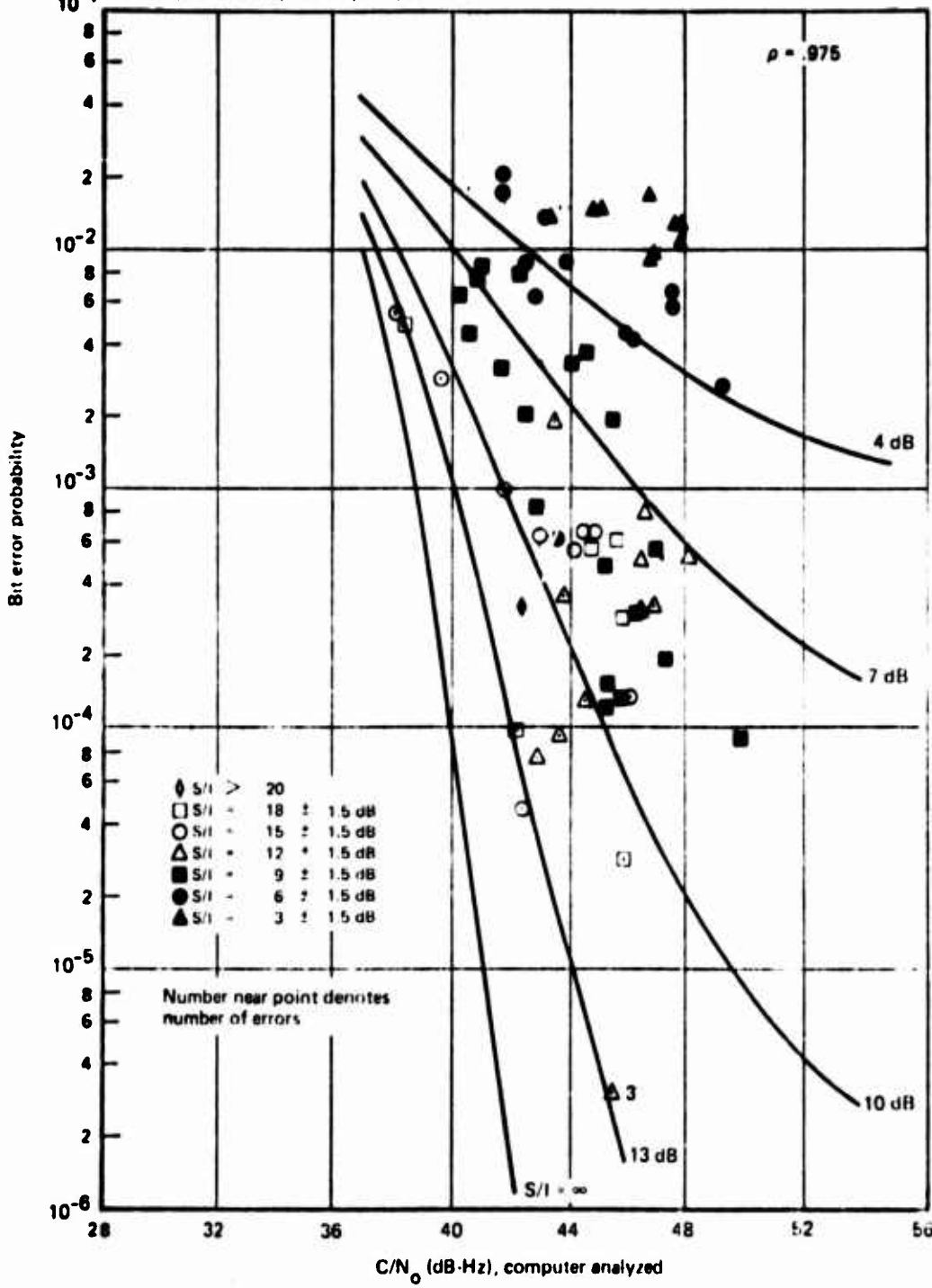


Figure 5-18.—BER Performance, DPSK Demodulator

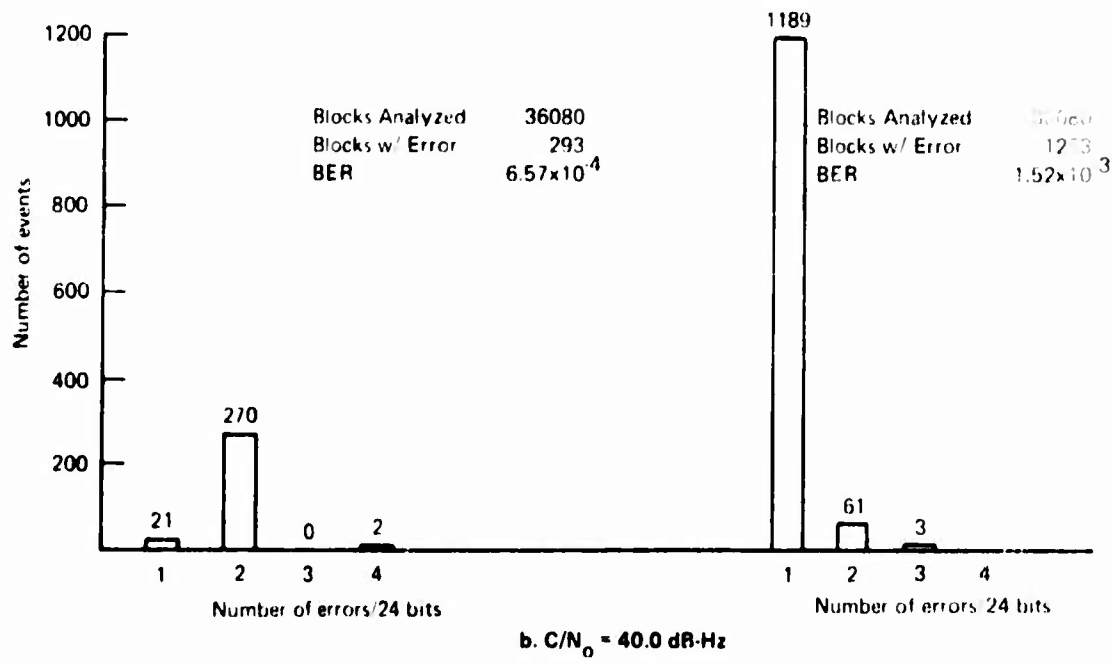
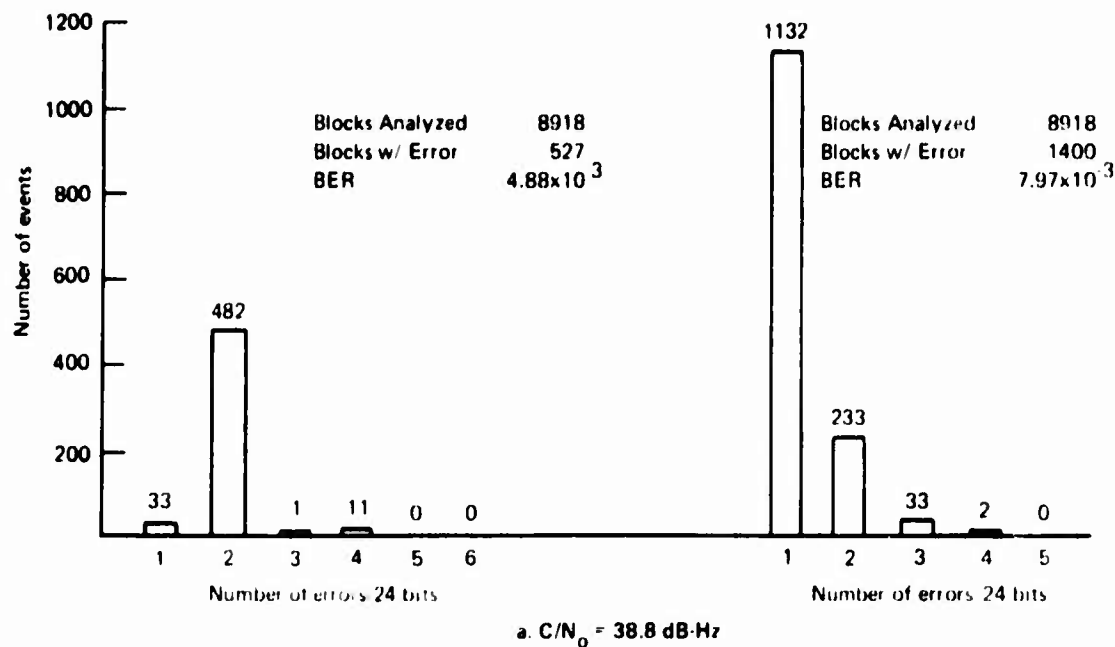


Figure 5-19.—Type I Block Error Histograms

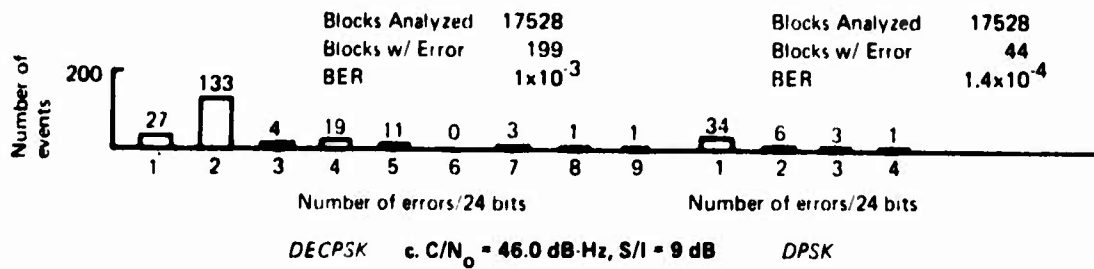
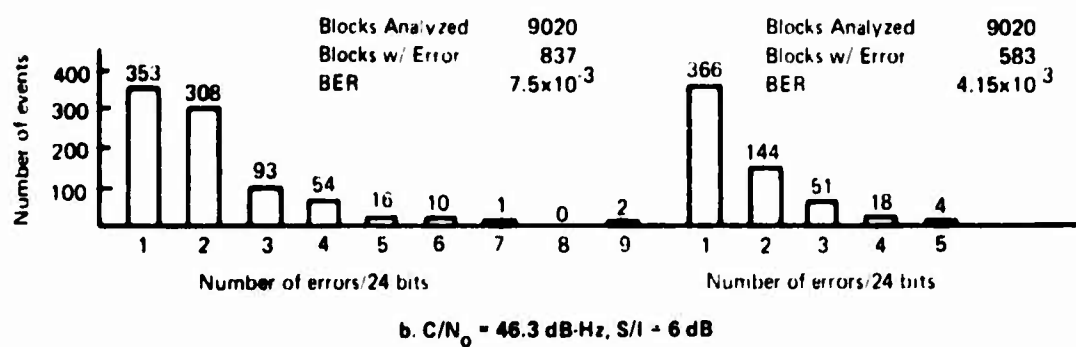
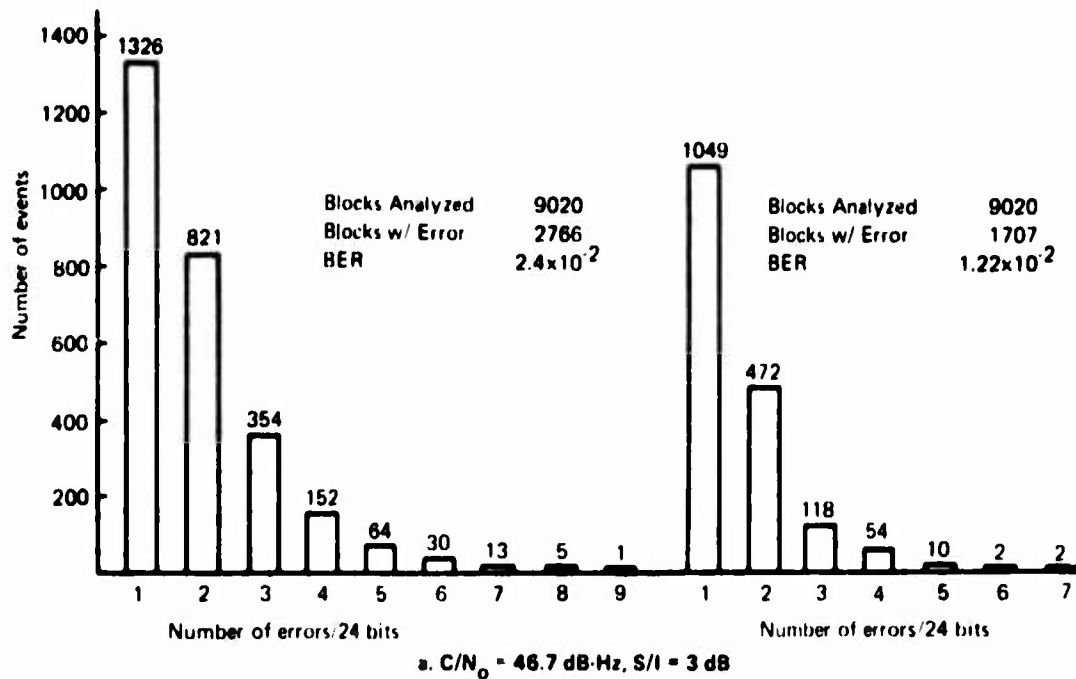


Figure 5-20. -- Type II Block Error Histograms

number of errors per 24 bits and the number of events shown above the bar.) Inspection of this figure reveals a propensity of the DECPSK demodulator to produce paired errors, whereas the DPSK demodulator produces primarily single errors for the selected test conditions, both theoretically supportable results. The DECPSK characteristic results from the differential decoding process in which a single isolated CPSK error begets an error for the following bit also. (Most of the DECPSK single errors recorded in Figure 5-19 are the result of paired errors astraddle adjacent 24 bit blocks, as determined by inspection of the raw data, and are, therefore, not correctly represented in the histogram.)

The Type II block error histograms of Figure 5-20 present results from three test conditions with S/I as the primary parameter. For all cases an increase in frequency of burst error events is observed, most noticeable at low S/I. Another significant result observed here is an increase of DECPSK single errors with decreasing S/I. It is postulated that the majority of single error events result from Costas loop cycle slips induced by the strong multipath component. A cycle slip event lasting for less than one symbol duration induces a single isolated error due to a 180° loop phase shift and consequent inversion of the data. Study of the raw data from which the histograms were constructed shows that most triple block errors result from one pair and one single, while most quadruple block errors result from two pairs, a rather predictable result.

Again with reference to Figure 5-20 one can see that single errors continue to dominate the DPSK results at low S/I values, but the apparent relative frequency of paired errors increased with decreasing S/I. The latter observation may be misleading, however, because two isolated errors within a block appear the same in the histogram as paired errors.

In the Aerosat situation, S/I is expected to be greater than 10 dB for most flight geometries, based on the aeronautical satellite system performance requirements for antennas. Thus, the block error statistics for both types of demodulators should appear approximately as shown in Figure 5-20(c) for the worst expected multipath condition.

The data analysis software also outputs inter-error spacing histograms which tabulate the frequency of occurrence of particular spacings between bit errors for each test segment. Examples of this type of data will be included in the final report.

#### 5.4 RANGING MODEM TEST RESULTS AND ANALYSIS

The TSC digital ranging modem and the NASA PLACE tone ranging modem were tested under Type I and Type II conditions to obtain data of performance as a function of C/N<sub>0</sub> and S/I. The test was implemented as ranging relative to a nominal trajectory rather than absolute ranging. This test configuration was sufficient to meet the test objective and obviated the need for synchronized clocks, accurate satellite orbit determination and accurate knowledge of aircraft location as would be implied by an absolute range measurement configuration.

#### **5.4.1 DATA ANALYSIS PROCEDURES**

The digitized raw ranging data from both modems were analyzed on a CDC 6600 computer using a common ranging data analysis program. The output data rate from the TSC modem is approximately five range readings/sec, thus providing 300 measurements/min. The TSC ranging analysis time segments were chosen to be approximately one minute in duration. This provides an adequate sample size for analysis (300 points) with reasonable assurance that the actual aircraft trajectory would deviate little from the nominal trajectory over this time interval.

The maximum output data rate from the NASA PLAC<sup>E</sup> ranging modem, however, is only one range measurement every 6.4 seconds or approximately 9.4 measurements/min. To obtain meaningful results from these data the processed test segment duration was selected to be as great as possible. Thus, the sample size is determined by the duration of intervals for which valid data were available (up to 12 minutes in one case).

The ranging measurements and associated times are processed as follows for both modems. A second order curve is fitted to the data from each sample in the least square error sense. This curve is assumed to be the aircraft trajectory against which the measured data are compared. Specifically, the mean and standard deviation of the difference between measured data points and the best fit curve are computed for each sample time interval. Additionally, a range error histogram is formed from the test data and a chi-squared goodness-of-fit test is performed to determine the probability that the range errors are normally distributed about the best fit curve.

Computations of CN<sub>0</sub> and ST for the ranging data analysis are performed as explained in Section 5.1.2.

#### **5.4.2 TSC DIGITAL RANGING MODEM**

The TSC digital ranging modem employs a sidetone ranging technique in which the highest tone (the clock tone) is successively divided by two until the lowest tone of 76 Hz is produced. All of these tones are then combined by digital techniques and phase modulated onto a carrier. Two operating bandwidth modes are provided, a wideband mode with a clock frequency of 156 kHz and a narrowband mode with a 19 kHz clock. Another modem parameter is "clock tone weighting" which pertains to the method whereby the tones are combined. The airborne modem, set for the selected mode and clock weighting, phase locks to the received carrier and tones. Range ambiguity is resolved to within 2100 nautical miles via the 76 Hz tone. Range measurement resolution is 7.5 meters (determined by the internal 40 MHz clock) so that noise caused phase jitter of the highest ranging tone will be the limiting factor on range measurement accuracy. Measurements of time difference between the received and locally generated codes are output in a serial bit stream and recorded on analog tape for later data processing.

Reduced RMS range error data for Type I tests performed in the January, February and March test series are presented in Figure 5-21. The processed data were edited by inspecting ranging data plots and rejecting time segments which displayed abrupt discontinuities. The discontinuities result from failure of the modem to correctly resolve ambiguity. The

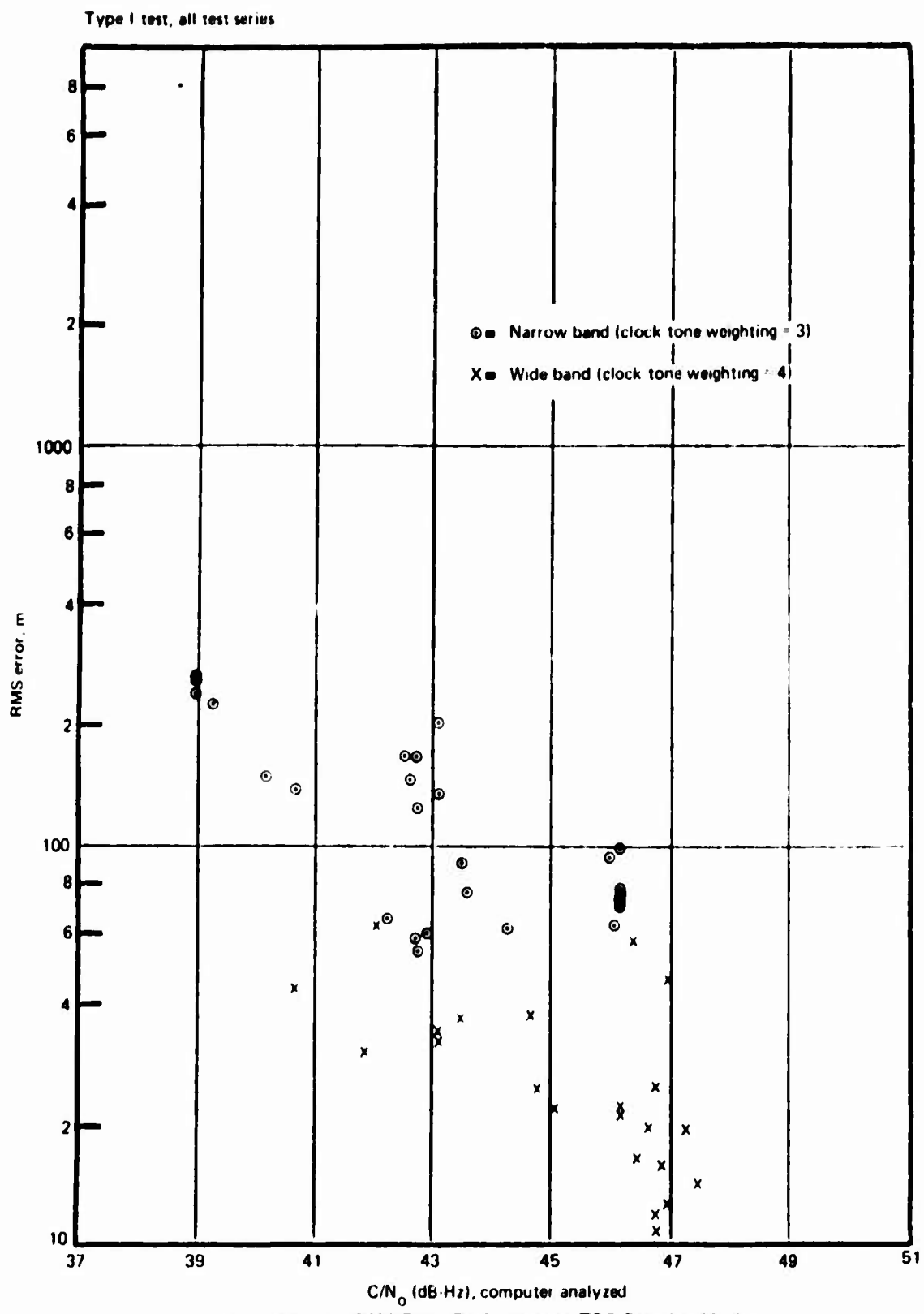


Figure 5-21.—RMS Error Performance, TSC Ranging Modem

ambiguity resolution problem is evident in both wideband and narrowband modes particularly at  $C/N_0$  values below 43 dB-Hz. The data points plotted in Figure 5-21, although somewhat scattered, show improving performance with increasing  $C/N_0$  and best performance for the wideband mode.

TSC is preparing theoretical and laboratory baseline measurements data for comparison with the airborne experimental results. These data, however, were not available in time for inclusion in this report.

Type II test data for the TSC ranging modem are presented in Figure 5-22 where RMS error is plotted as a function of  $C/N_0$  and computer analyzed S/I values are shown adjacent each data point. The data points plotted in Figure 5-22 are limited to those for which S/I is relatively high because the low S/I cases were censored due to the poor ambiguity resolution performance of the modem under heavy multipath conditions. Because of the required censoring and the inherent scattering of the data as seen in Figure 5-21 for the Type I tests, it is difficult to draw conclusions, concerning range error performance versus S/I, for this modem.

The data presented herein for the TSC ranging modem are from the 1975 test series only. The data from the 1974 test series cannot be processed because of incompatibilities between the modem output data and the telemetry equipment employed for reformatting the analog tapes due to waveform anomalies in the modem output data stream. This problem was resolved for the 1975 test series by a change in modem operating procedures to use only those modem modes without waveform anomalies in the output data stream.

#### 5.4.3 NASA PLACE RANGING MODEM

The NASA PLACE ranging system employs CW tones to provide a non-ambiguous range measurements of approximately 6300 nmi. A total of four translated tones, equivalent to 25 Hz, 175 Hz, 1225 Hz, and 8575 Hz are phase modulated onto a carrier and transmitted from the ground station to the airplane via ATS-6. The airborne modem acts as a transponder, demodulating, filtering and retransmitting the received tones to the ground station via the return satellite link at intervals of 64 or 6.4 seconds as determined by the ground station polling cycle. The returned tones are demodulated and then processed by the ground station computer to determine the round trip delay, hence two way range to the airplane. These range measurements and their associated times are then recorded on digital magnetic tapes for additional off-line processing as described under Section 5.4.1.

The processed NASA PLACE ranging data are presented in Table 5-1. It is important to note that these data are in terms of two way RMS range error as opposed to the one-way range error data presented for the TSC ranging modem. Computed  $C/N_0$  as measured at the aircraft are also shown for reference. The cases with largest  $C/N_0$  unexpectedly have the greatest rms range error, though at the level of difference observed, experimental uncertainty cannot be ignored. Also the total link performance is dependent on the aircraft - satellite link as well; nothing is known about actual return link  $C/N_0$ . It was also determined that S/I for all cases was in excess of 19 dB.

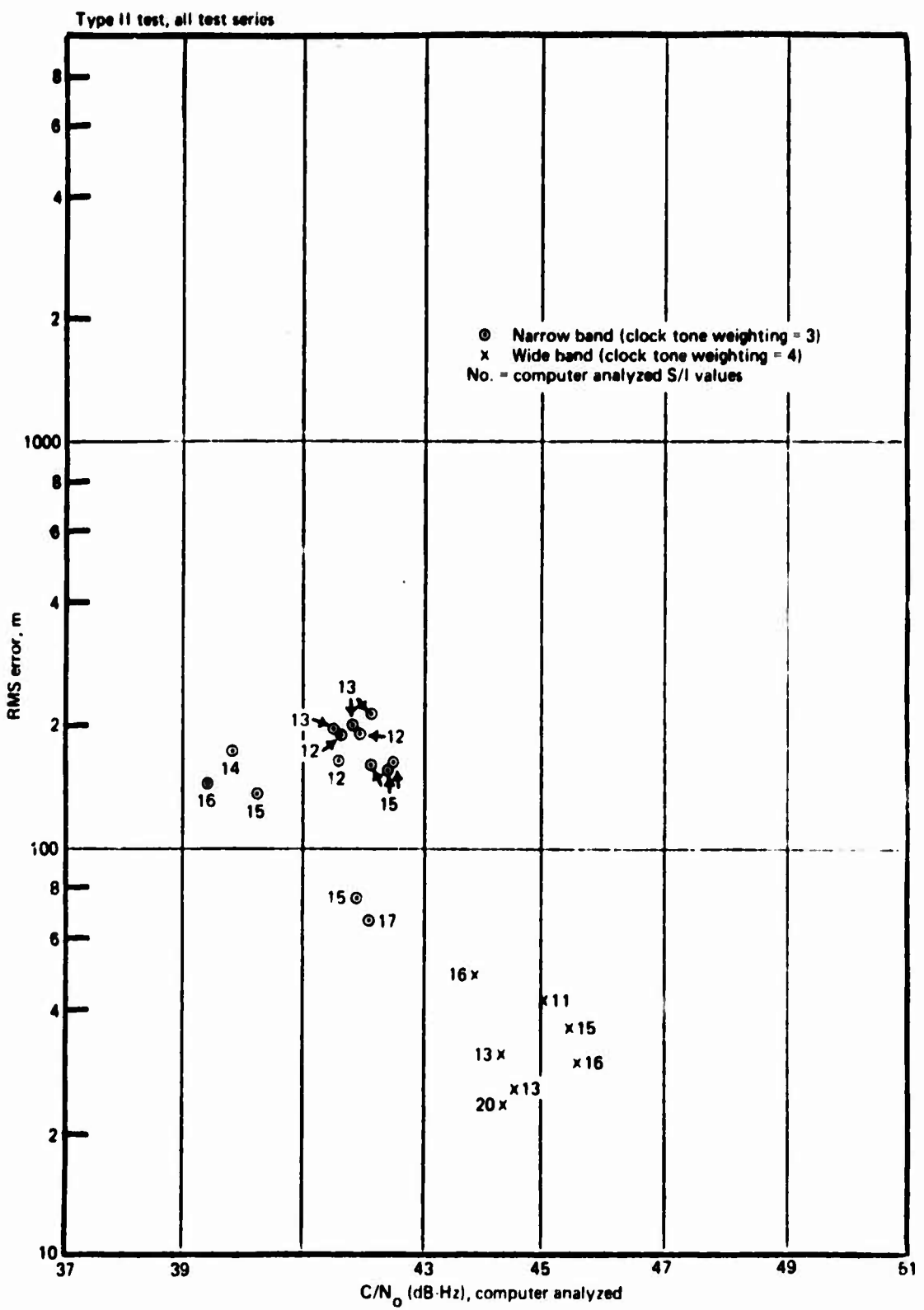


Figure 5-22.—RMS Error Performance, TSC Ranging Modem

*Table 5-1.-PLACE Ranging Model Results*

Date	Start time	Stop time	Data points analyzed	RMS error (meters)	Test type	C/N <sub>0</sub> dB-Hz
11-13-74	9:41:29	9:45:59	32	298	II	42.0
11-13-74	10:11:35	10:15:59	23	332	II	44.5
3-27-75	12:20:20	12:33:00	120	334	II	44.6
3-28-75	13:53:30	13:58:31	45	236	I	42.7
3-31-75	12:17:19	12:20:44	27	263	II	42.0

Most of the NASA PLACE ranging data obtained have been processed and included in Table 5-1. A small amount of data remains to be processed. Reasons for the limited amount of useful data include the relatively low data rate, failure of the system to operate satisfactorily with forward path C/N<sub>0</sub> below 43 dB-Hz and some test transmission formats that replaced the PLACE S&R signal with a CW carrier.

## 6.0 ANTENNA EVALUATION TEST RESULTS AND ANALYSIS

Analyzed test results are presented for the 3-antenna slot-dipole system (LWSD/RWSI/TOP), phased array, patch, and crossed-slot antennas.

### 6.1 DATA ANALYSIS PROCEDURES

The parameters required for data presentation are antenna gain, multipath rejection ratio (S/I), elevation angle and relative bearing angle to ATS-6.

#### 6.1.1 BEARING AND ELEVATION ANGLES

During test conduct, aircraft magnetic heading was manually logged each 30 seconds during circular flights and as required during linear flight paths. INS track data was also manually logged for reference purposes. Magnetic heading, pitch, roll and time code were recorded on tape and stripped out on chart paper for data analysis. The relative bearing to the satellite is derived from the aircraft heading data and known satellite direction. Elevation angles are also computed based on known aircraft and satellite locations.

Aircraft roll angle stripouts were examined whenever such information was available, and data points were discarded if roll exceeded  $\pm 5^\circ$ . During normal data runs, only infrequent purges were required. Aircraft pitch angle was normally between  $4^\circ$  and  $6^\circ$  (nose up) during data acquisition. This flight attitude is considered nominal and no adjustments or data censoring was made due to pitch angle considerations.

#### 6.1.2 ANTENNA GAIN CALCULATION

The relative gain of the antennas can be deduced by comparison of the received power levels at the antenna terminals. Furthermore absolute gain can be estimated by using the quad-helix as a standard, since it is known to provide 15.5 dB gain to RHC polarized signals when optimally pointed. The received signal strength,  $S_A$ , at the antenna terminals is calculated from the measured  $C/N_0$  and the calculated equivalent noise power density at the antenna, i.e.,

$$S_A = -204.0 + (NF_{op})_{\text{antenna}} + C/N_0, \text{ dBW} \quad (6.1)$$

$(NF_{op})_{\text{antenna}}$  is the operating noise figure, as referred to an antenna terminal, and can be calculated by the equation

$$(NF_{op})_{\text{antenna}} = NF_{op} + L \quad (6.2)$$

where  $L$  is the total loss between the antenna and the preamplifier expressed in dB and  $NF_{op}$  is the system operating noise figure referred to the preamplifier input terminal of a receiving channel.  $NF_{op}$  is measured for each receiving system during the pre- and post-flight calibration periods by using the channel calibrator. A conventional Y-factor noise figure measuring technique is employed. The losses  $L$  are available from system calibration data such as RF cable and component insertion loss measurements.

For linear flight paths the received  $C/N_0$  value is derived for each antenna by computer analysis of the detected envelope signal as described in Section 5.1. Since the aircraft/satellite geometry remains essentially fixed for several minutes for linear flight paths, averaging of the computed  $C/N_0$  values is employed to reduce the statistical variability associated with individual  $C/N_0$  samples obtained from the detected envelope signal analysis process. Manual real-time  $C/N_0$  measurements were also logged to serve as a check on analyzed results and for use when analyzed results are unavailable.

For circular flight paths, the aircraft/satellite geometry is continually changing, hence averaging of the computed  $C/N_0$  samples cannot be applied directly. Some reduction in the sample variance of  $C/N_0$  fluctuations can be achieved by noting that  $N_0$  is, for practical purposes, independent of aircraft/satellite geometry. An additional computer program is therefore used to compute the average noise floor from the sample values. The  $C/N_0$  values are then computed as the ratio between the signal strength,  $C$ , from individual samples and the average noise floor computed over many samples.

Quad-helix gain calibration data is not available for all segments since (a) quad-helix azimuthal steering is restricted to  $\pm 110^\circ$  from the nose, and (b) operational procedures and RF subsystem hardware constraints sometimes precluded acquisition of quad-helix reference gain data. However, additional information is sometimes available from signal strength measurements made during other tests in adjacent time periods. These allow the expected ATS-6 signal strength for a certain test area, especially along the modem evaluation Type II test path at an elevation angle of  $15^\circ$ , to be determined. These data have on occasion been used to augment the normal quad-helix antenna gain calibration data.

#### 6.1.3 MULTIPATH REJECTION RATIO CALCULATION

The S/I obtained for the various antennas is derived by computer analysis of the detected envelope signal as described in Section 5.1. S/I values of up to 20 dB, which represents the approximate multipath resolution capability of the analysis technique, can be calculated.

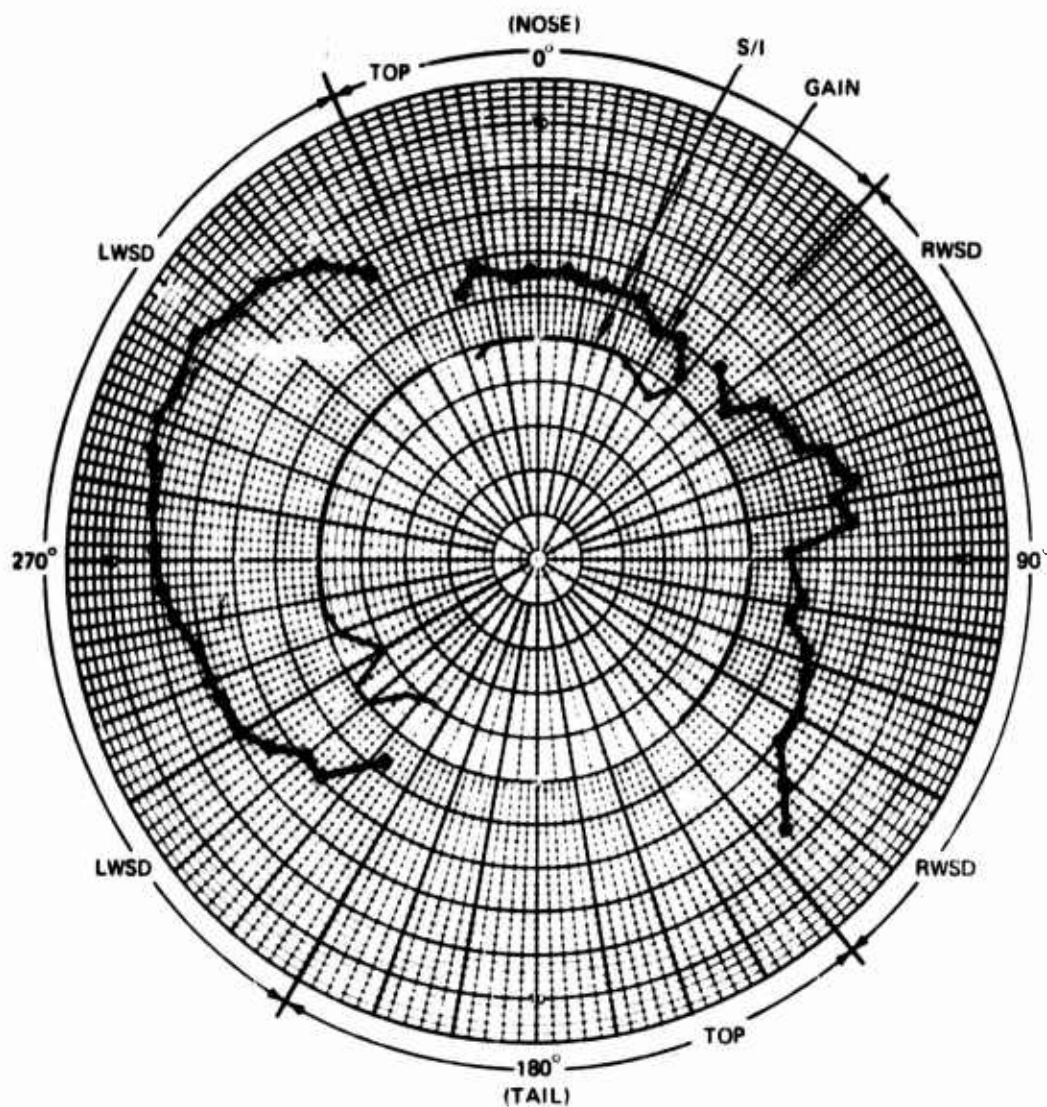
### 6.2 ANTENNA TEST RESULTS

#### 6.2.1 SLOT-DIPOLE ANTENNAS

Analyzed results for the April 1 and March 25, 1975 tests are plotted in Figures 6-1 and 6-2.

Table 6-1 summarizes the results for the April 1 flight and shows the data smoothing described above to obtain adjusted  $C/N_0$ , and thence antenna gain. The tests were conducted in the same area and therefore provide cross checks on each other by virtue of test redundancy. Both tests were flown at a nominal ATS-6 elevation angle of  $15^\circ$ . The actual elevation angle of the satellite to an antenna will be modified by the aircraft bank angle with the magnitude of this effect dependent upon heading relative to the satellite. Aircraft roll and pitch data was not acquired for either of the above tests due to an incorrect switch governing the operation of the instrumentation gyro sensor. However, both tests are known to be well flown and this deficiency is not considered to be of major importance.

**Gain Scale:** 2 dB per major division, origin at -10 dB  
**S/I Scale:** 4 dB per major division, origin at 0 dB



Elev. Angle: 15° (Nominal)  
Turn Direction: Counter Clockwise  
Location: 39°53N, 34°46W

Figure 6-1. – Gain and S/I, Slot Dipole Antennas, April 1, 1975

**Table 6-1. Antenna Test Summary, Slot Dipole System**

Date of the Test: April 1, 1975  
 Location of the test: 39° 53' North, 34° 46' West  
 The elevation angle: 14.5 Deg  
 Mag. Variation: 20.0 Deg West  
 A/C to ATS 6 Bearing Angle: 249.1 Deg True

Time gmt	Rel brdg (Deg)	Comput C/NO (dB-Hz)	Noise change (dB)	Adj. C/NO (dB Hz)	Rec'd signal (-dBW)	Ant gain (dB)	Ant S/I (dB)
1223.13	216	44.2	-0.15	44.1	149.5	1.8	16.0
1223.32	224	45.9	0.65	46.5	147.1	4.3	17.0
1223.43	229	46.6	-0.32	46.3	147.3	4.0	20.0
1223.54	234	47.4	-0.02	47.4	146.2	5.1	20.0
1224.07	239	47.7	0.40	48.1	145.5	5.9	16.0
1224.22	249	48.6	-0.15	48.5	145.1	6.2	19.0
1224.35	255	48.9	-0.27	48.6	145.0	6.4	20.0
1224.47	260	48.9	0.47	49.4	144.2	7.1	20.0
1225.00	264	50.2	0.43	49.8	143.8	7.5	20.0
1226.10	271	50.2	-0.18	50.0	143.6	7.7	20.0
1227.05	277	50.4	-0.14	50.3	143.3	8.0	20.0
1227.30	285	50.5	0.40	50.9	142.7	8.6	20.0
1227.42	289	51.2	-0.22	51.0	142.6	8.7	20.0
1228.00	294	50.5	0.06	50.6	143.0	8.3	20.0
1228.20	302	50.8	0.05	50.8	142.8	8.6	20.0
1228.45	309	49.6	0.37	50.0	143.6	7.7	20.0
1228.58	315	49.8	-0.09	49.8	143.8	7.5	20.0
1229.23	322	49.1	-0.12	48.9	144.7	6.7	20.0
1229.40	329	47.6	-0.52	47.1	146.5	4.8	20.0
Above data for LWSD at NF (Preamp) = 3.00 DB and I.L. = 7.40 DB							
1230.13	343	43.6	0.62	44.2	149.0	2.3	19.5
1230.31	347	44.8	0.27	45.1	148.1	3.2	20.0
1231.22	355	44.8	-0.27	44.5	148.7	2.6	20.0
1231.34	358	44.9	-0.33	44.6	148.6	2.7	20.0
1232.00	6	44.7	-0.02	44.7	148.5	2.8	20.0
1232.12	9	44.5	-0.02	44.5	148.7	2.6	20.0
1232.24	14	44.3	0.06	44.4	148.8	2.5	20.0
1232.50	23	44.3	0.12	44.4	148.8	2.5	20.0
1233.02	29	43.5	0.02	43.6	149.6	1.7	19.0
1233.15	35	44.0	0.28	43.7	149.5	1.9	18.5
1233.27	40	42.7	-0.26	42.5	150.7	0.6	20.0
Above data for top at NF (Preamp) = 3.00 DB and I.L. = 7.00 DB							
1233.46	46	43.7	0.16	43.9	149.3	2.0	20.0
1233.58	55	43.3	-0.36	42.9	150.3	1.0	20.0
1234.24	58	44.2	0.34	44.6	148.6	2.7	20.0
1234.36	63	44.9	0.01	44.9	148.3	3.0	20.0
1234.48	69	45.5	-0.35	45.1	148.1	3.3	20.0

*Table 6-1.—Antenna Test Summary, Slot Dipole System (Cont.)*

Time gm:	Rel brg (Deg)	Comput C/NO (dB-Hz)	Noise change (dB)	Adj. C/NO (dB-Hz)	Rec'd signal (-dBW)	Ant gain (dB)	Ant S/I (dB)
1235.01	71	46.2	-0.01	46.2	147.0	4.3	20.0
1235.14	75	46.1	0.41	46.5	146.7	4.6	20.0
1235.26	78	47.4	-0.25	47.2	146.0	5.3	20.0
1236.16	80	46.2	-0.02	46.2	147.0	4.3	20.0
1236.29	85	47.0	-0.17	46.8	146.4	4.9	20.0
1237.06	90	44.4	-0.57	43.8	149.4	1.9	20.0
1237.18	100	44.5	0.09	44.6	148.6	2.7	20.0
1237.31	104	44.6	-0.42	44.2	149.0	2.4	20.0
1237.44	109	45.8	-0.47	45.4	147.8	3.5	20.0
1237.56	113	45.7	0.02	45.6	147.6	3.8	20.0
1238.09	121	46.1	0.13	46.3	146.9	4.4	20.0
1238.21	127	45.9	0.34	46.2	147.0	4.4	20.0
1238.34	132	46.9	0.70	47.6	145.6	5.8	20.0
1238.46	137	49.0	0.24	49.2	144.0	7.3	20.0

Above data for RWSD. I.C. = 100 dB and I.L. = 7.80 DB

On April 1, the circular flight path was counterclockwise as viewed from the top, i.e., the airplane heading is decreasing and the relative bearing to the satellite is gradually increasing during the test. The normal bank angle for this circular path would be somewhat less than 5° and would effectively increase the elevation angle for the LWSD and decrease it for the RWSD. On this particular flight, westerly winds of approximately 150 knots were experienced at altitude. A discussion with flight personnel confirms that a compensating banking maneuver could be expected which would further increase the effective elevation angle for the LWSD, but would reduce bank angle during the RWSD illumination portion. As a result it is estimated that the broadside effective elevation angle for the LWSD is approximately 20° while that for the RWSD is between 10° and 15°. At the lower elevation angles the antenna gain is very sensitive to small changes in elevation angle. The foregoing effects appear to explain the gain asymmetry in Figure 6-1.

On March 25, the circular path was clockwise. The resultant bank angle would therefore be expected to have the opposite effect on bank angle for the two side-mounted antennas (increase for RWSD, decrease for LWSD). Because wind velocity was less than on April 1, any compensating bank angle due to cross wind should be less for this test. Again the effects of bank angle seem to be present in the data of Figure 6-2. Comparison with Figure 6-1 also reveals the complementary nature of the measured antenna gains which is attributed to the opposite direction of circular flight for the two tests.

A third test result corresponding to an elevation angle of 19° is presented in Figure 6-3. This test was conducted on Nov. 21, 1974 with the circular portion being in a clockwise direction. The aircraft parameter data (Figure 6-4) shows that the average bank angle was near 0° for the major portion of the test with only a few excursions in excess of 5°. The pitch angle was in the range of 3° to 7°, nose up attitude. The results agree reasonably well with the "higher

**Gain Scale:** 2 dB per major division, origin at -10 dB  
**S/I Scale:** 4 dB per major division, origin at 0 dB

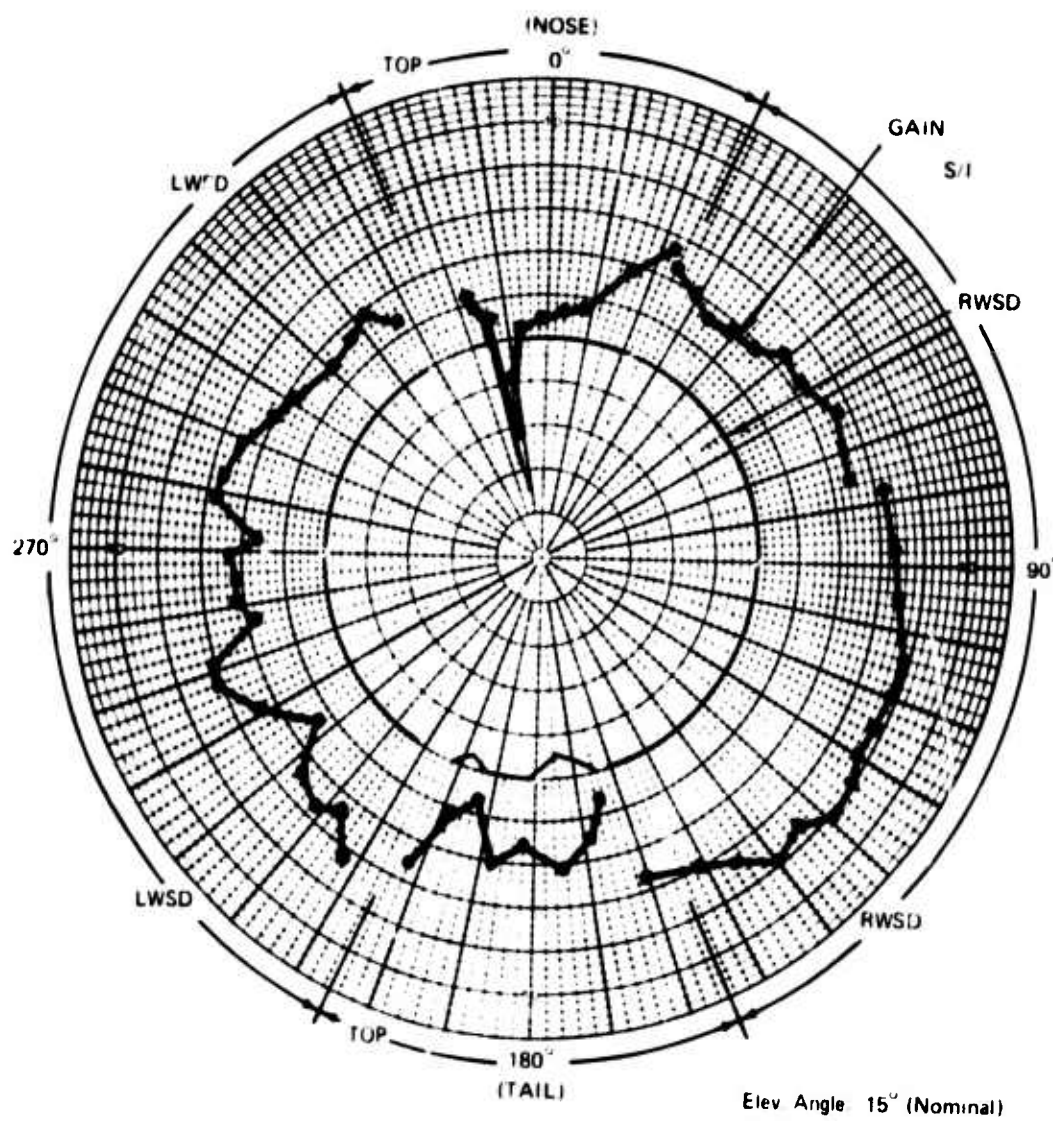


*Figure 6.2. Gain and S/I, Slot Dipole Antennas, March 25, 1975*

**Gain Scale:** 2 dB per major division, origin at -10 dB  
**S/I Scale:** 4 dB per major division, origin at 0 dB

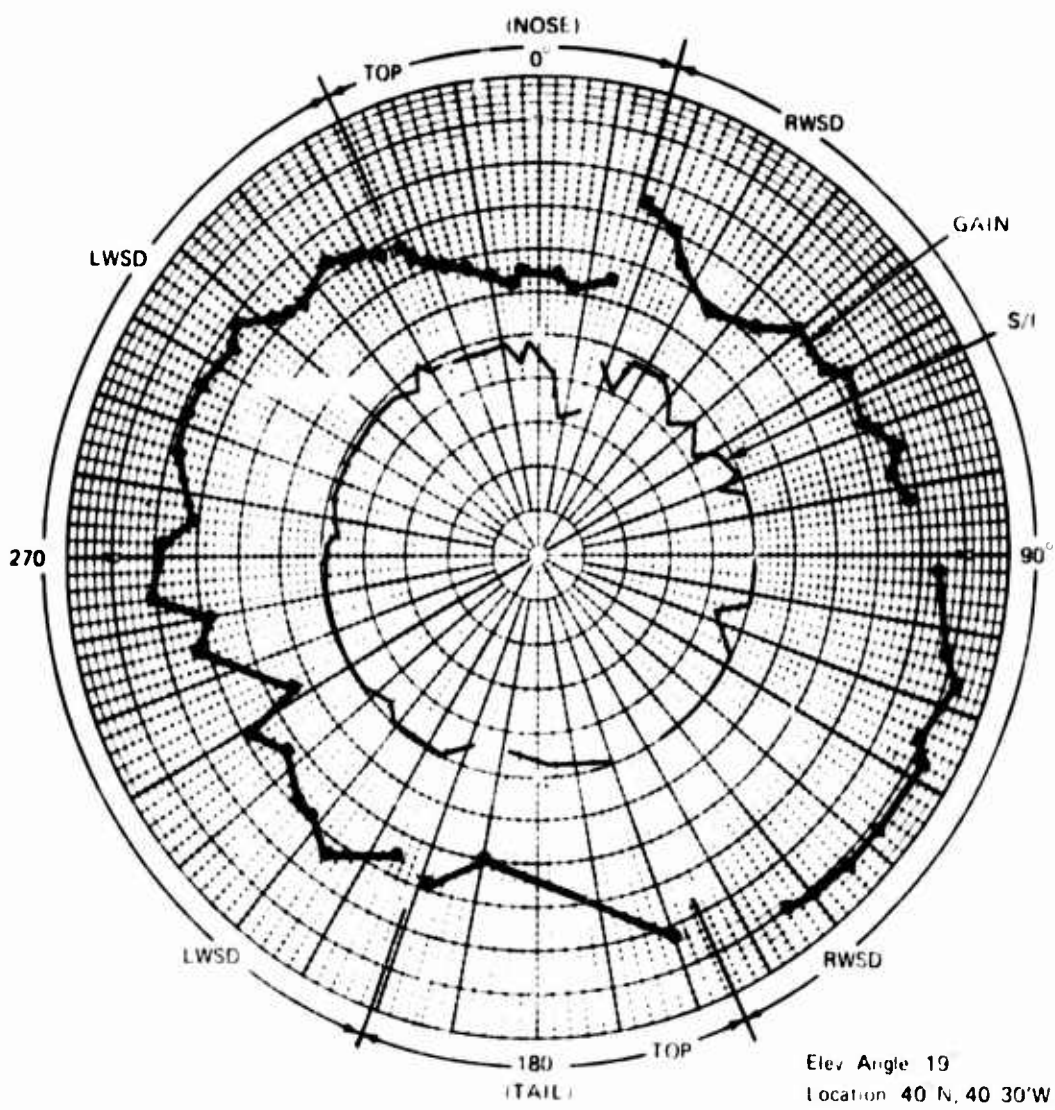


Figure 6.3. Gain and S/I, Slot Dipole Antennas, November 21, 1974

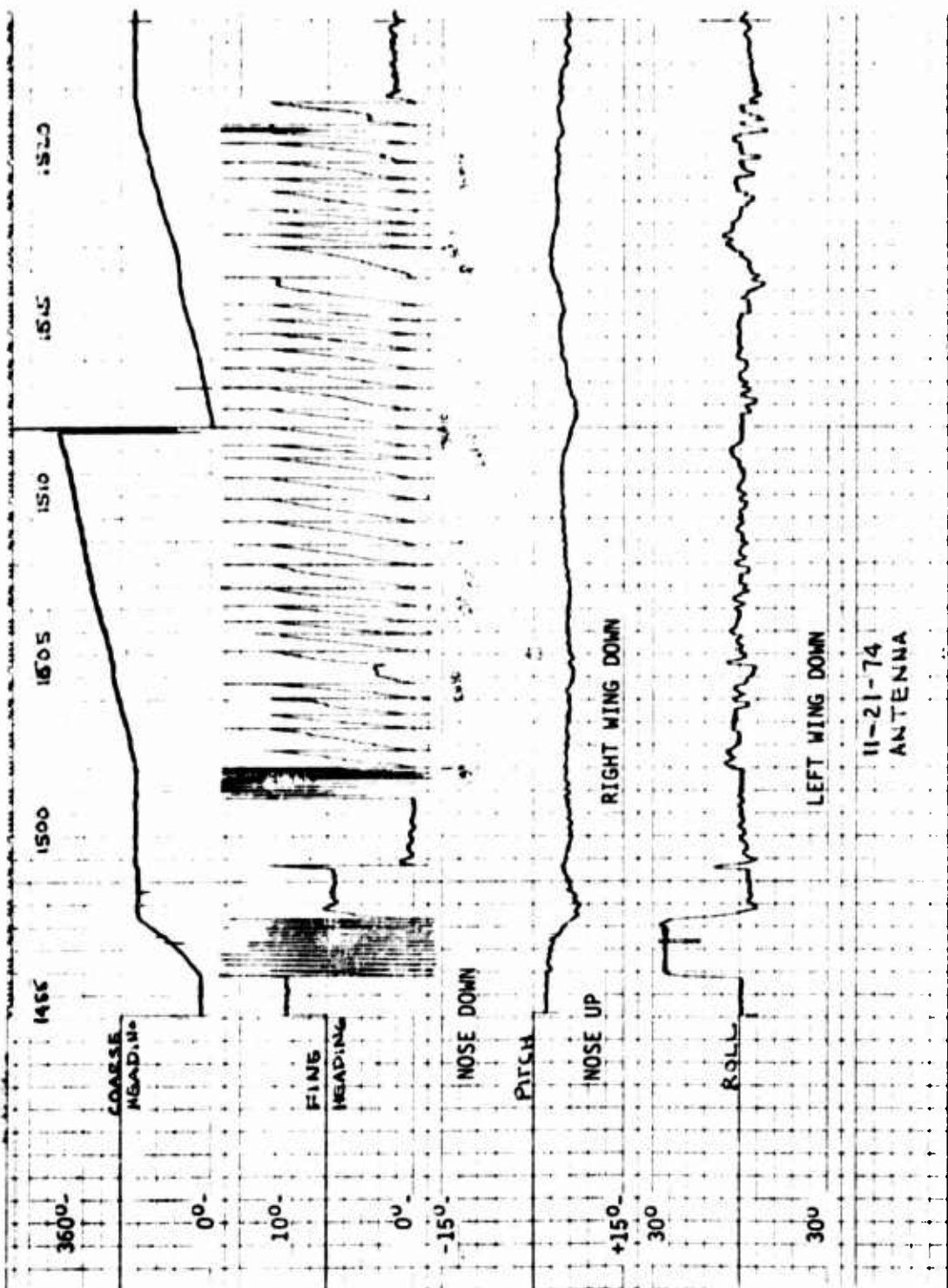


Figure 6-4.—Aircraft Heading, Pitch and Roll Data, November 21, 1974

elevation angle" portions of the March 25 and April 1 tests but a higher than expected gain was observed for the RWSD between  $90^\circ$  and  $160^\circ$  from the nose. For the clockwise flight path used, data for these angles was acquired on the northeast quadrant of the circle. The test area was near the 3-dB contour of the ATS-6 antenna pattern, and pattern overlays show that maximum ATS-6 signal would be expected in the northeast quadrant. This may explain the unexpectedly large apparent gain for this portion of the test. Sufficient cross checks are not available to positively identify the reason for the observed effect.

A composite gain pattern derived from the foregoing three tests is shown in Figure 6-5. The LWSD data is primarily taken from the April 1 test, the RWSD is essentially that of the March 25 test and the TOP data is a weighted combination of all three. This represents an experimental composite gain conic for the slot dipole system for an elevation angle of about  $20^\circ$ . For reference purposes the antenna range scale model gain conic obtained from radiation distribution plots is given and is seen to agree reasonably well with the experimental data.

Figure 6-6 plots gain and S/I for the top-right-left slot dipole system for the September 24, 1974 test. The nominal elevation angle to ATS-6 was  $27.5^\circ$ . It is observed that in general the antenna gain is slightly larger than that of the  $20^\circ$  elevation composite shown in Figure 6-5. This is expected due to physical placement of the antennas.

Also shown on Figures 6-1, 6-2, 6-3, and 6-6 are measured S/I, the direct signal-to-multipath power ratio. As previously mentioned, the measurement procedure has poor resolution for S/I above 20 dB, and points with an estimated S/I larger than 20 db are plotted at the 20 dB level. For all cases it is observed that S/I is generally greater than 20 dB, with occasional dips into the 15-20 dB range, and some more severe drops in the vicinity of the nose for the top-mounted antenna. This performance is in general agreement with antenna range measurements, and results both from the fact that the elevation angle is greater than  $20^\circ$  and the fact that the wing-root location provides natural multipath shielding. The rather large S/I values observed are consistent also with observed results for Type I digital data tests, where the BER curves have the same character as predicted for a purely additive noise environment.

### 6.2.2 PHASED ARRAY ANTENNA

One portion of the phased array antenna data was acquired from "straight-line" flight segments as described in Section 3.3. Test results are presented in Table 6-2 and Figure 6-7. There are a total of three groups of data, collected from the following dates and locations:

1. Ground test at NAFEC on January 21, 1975 at an elevation angle of  $40^\circ$ .
2. March 27, 1975 over the north Atlantic at elevation angles between  $10^\circ$  and  $15^\circ$ .
3. January 27, 1975 over the north Atlantic at elevation angles between  $15^\circ$  and  $28^\circ$ .

During each straight-line segment, the optimum beam position for maximum signal reception was selected. The beam positions are identified according to the manufacturer's nomenclature. Since quad-helix gain calibration data is not available for all straight-line segments, the phased array gain values sometimes utilize signal strength calibration measurements of the

**Gain Scale: 2 dB per major division, origin at -10 dB**

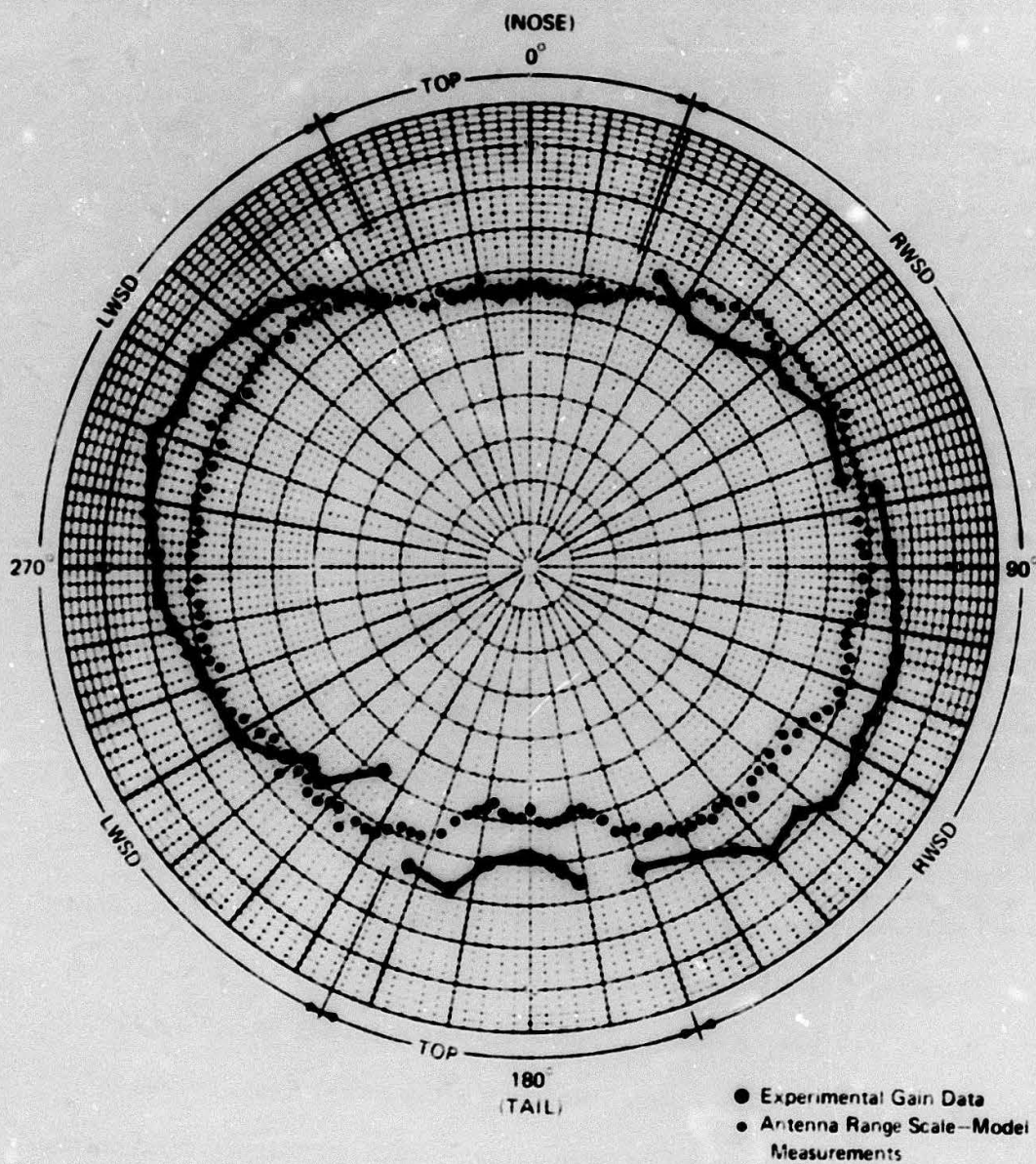


**Figure 6-5.—Slot-Dipole System Composite Gain at 20° Elevation**

**Gain Scale** 2 dB per major division, origin at -10 dB  
**S/I Scale** 4 dB per major division, origin at 0 dB

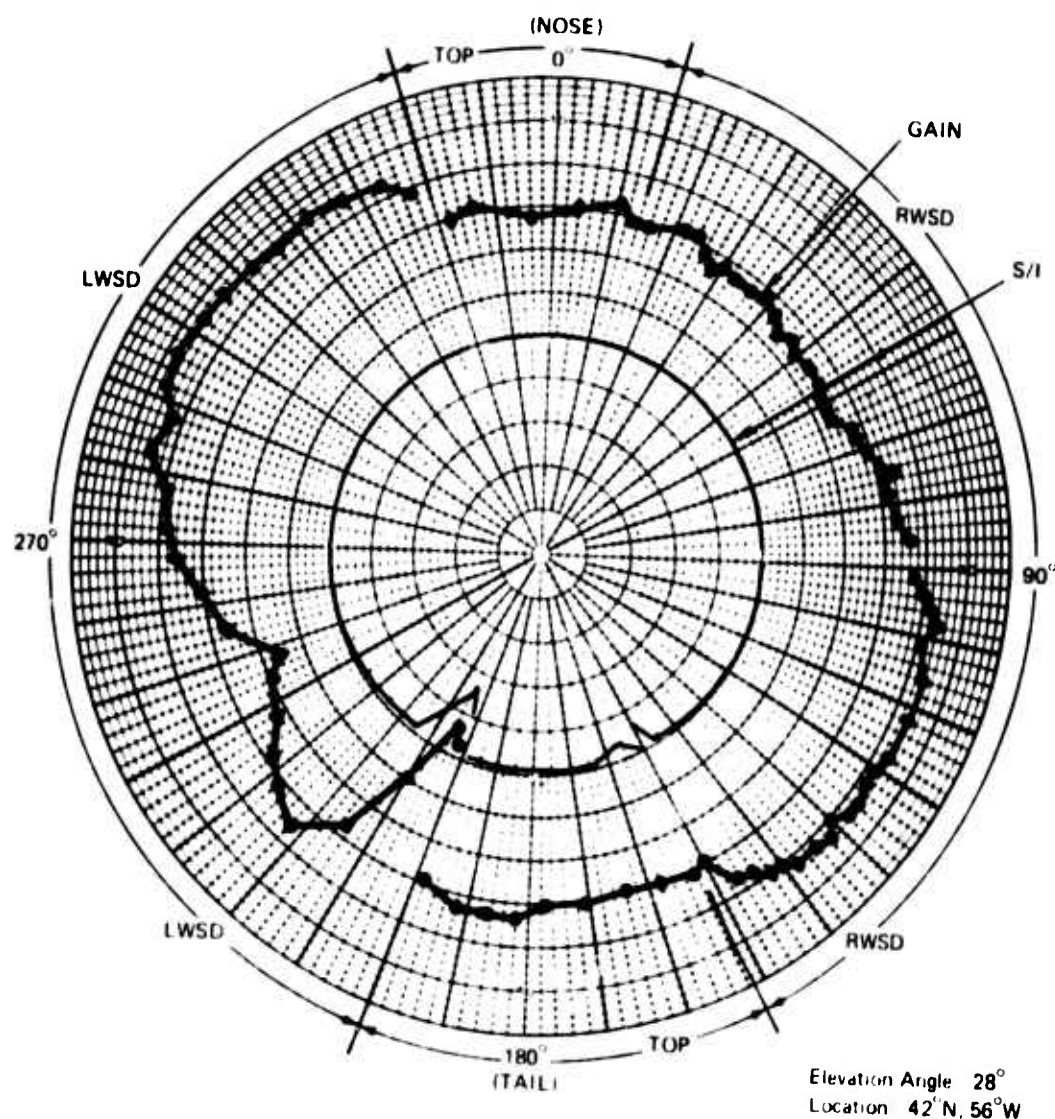


*Figure 6-6. - Gain and S/I, Slot Dipole Antennas, September 24, 1974*

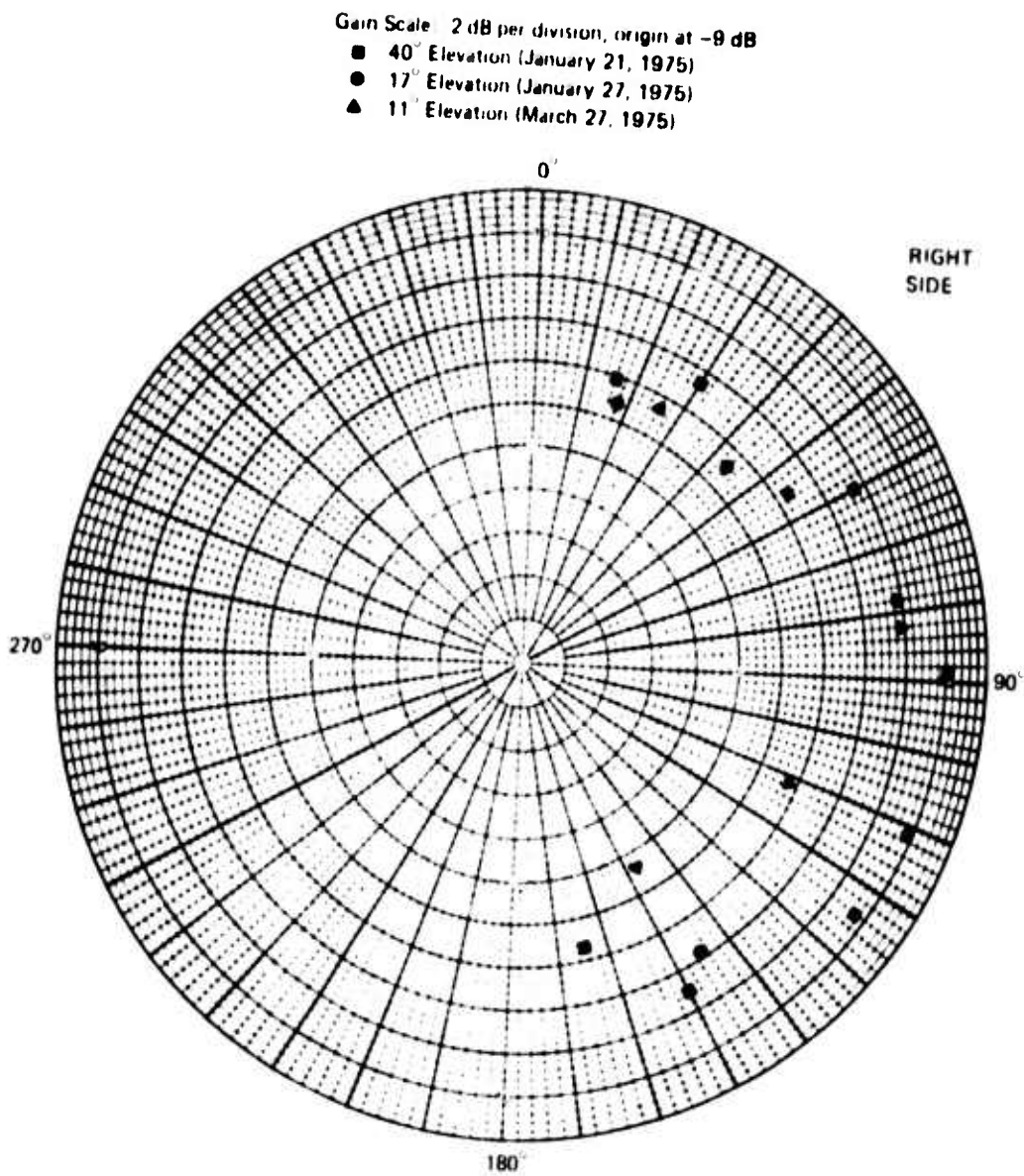


*Figure 6-7. Phased Array Gain Data for "Straight-Line" Flight Segments*

**ATS-6 downlink which were made at other times or locations during the same test. These cases have been identified by an asterisk in Table 6-2.**

Two tests were also conducted on normal circular-track antenna flights on September 24, 1974 and November 21, 1974. Due to the antenna's location, data is only acquirable in the right-hand hemisphere. For the test of September 24, at 27° elevation, the beam position was manually optimized at a bearing angle of 90°. Results for gain and S/I are shown in Figure 6-8. It is observed that with beam pointing properly optimized the array provides gain in the 10-11 dB region over a broadside sector. As the azimuth changes toward 0° or 180° the gain reduces as expected. The measured S/I for this antenna was in excess of 20 dB, probably an expected result due to the narrow roll-plane beamwidth.

**Table 6-2.-Phased Array Antenna Gain Data**

ATS-6 direction		Optimum antenna beam position	C/N <sub>0</sub> (dB-Hz)		Received signal level (-dBW)	Antenna gain (dB)
Relative bearing	Elev.		Real time meas'd	Computer analyzed		
<b>(a) NAFEC Ground Test January 21, 1975</b>						
180°	40°	7	42.9	N/A	149.2	5.8
30°	40°	6	45.1	"	147	7.4
60°	40°	5	47.2	"	144.9	9.5
89°	40°	4	48.7	"	143.4	12.1
124°	40°	5	49.1	"	144.0	11.5*
150°	40°	6	45.7	"	146.4	9.1*
164°	40°	7	42.1	"	150.0	5.5*
<b>(b) Flight Test, March 27, 1975</b>						
260°	120°	3	46.6	45.0	146.7	5.3
55°	110°	2	48.5	46.4	145.3	6.5
82°	100°	1	50.0	49.9	142.5	9.7
111°	110°	2	46.0	45.4	146.3	5.5*
147°	120°	4	43.2	42.5	149.2	2.8*
<b>(c) Flight Test, January 27, 1975</b>						
180°	160°	4	41.4	41.6	150.5	4.8*
44°	170°	2	42.9	42.7	149.4	5.1*
78°	180°	2	49.2	49.0	143.1	9.7
111°	170°	2	51.8	51.5	140.6	11.7*
145°	160°	3	47.9	47.6	144.5	7.8*

\* Indicates that direct gain calibration using quad-helix was not available. ATS-6 downlink calibration measurements made at other times and locations during the same test have been used.

**Gain Scale** 2dB per major division, origin at -10 dB  
**S I Scale** 4 dB per major division, origin at 0 dB

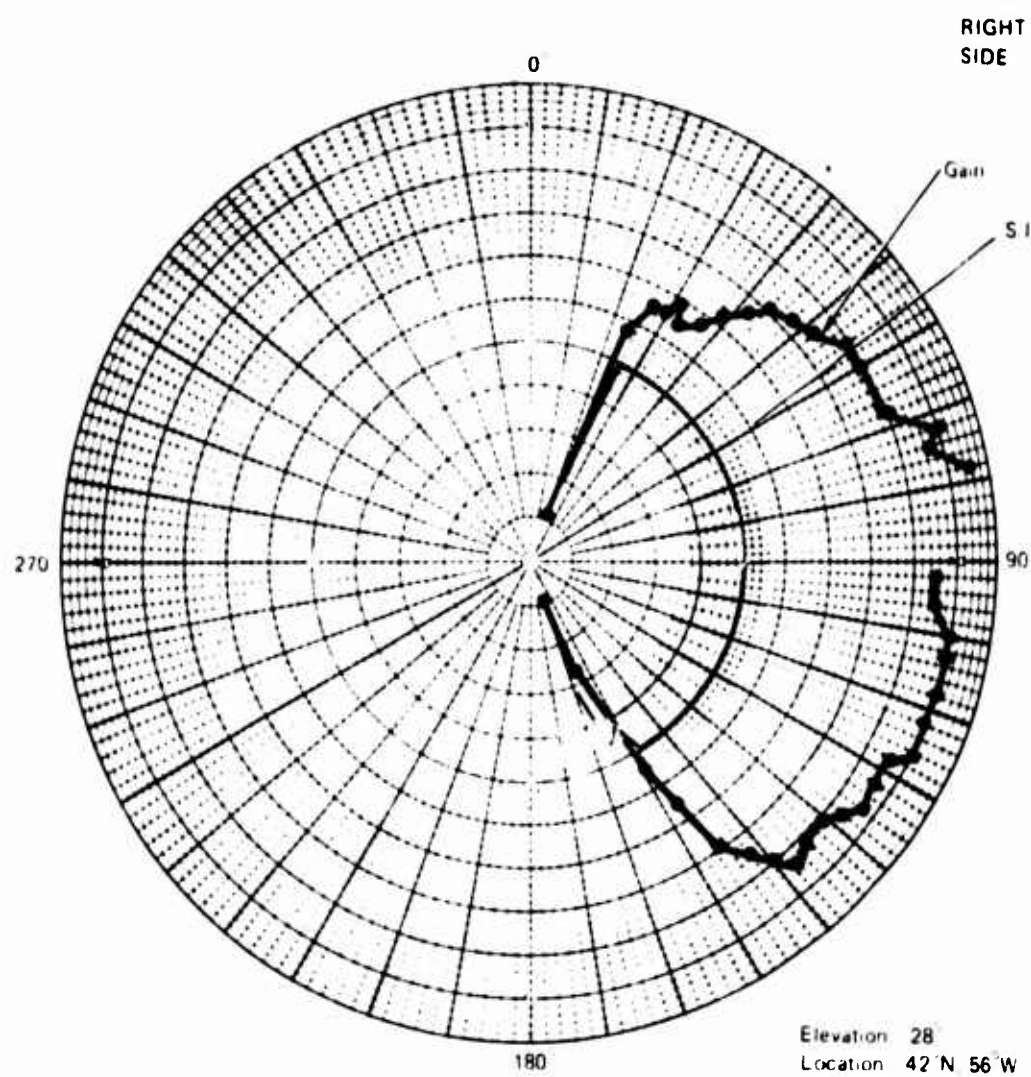


*Figure 6-8. Gain and S/I, Phased Array, September 24, 1974*

Figure 6-9 shows data obtained on November 21. Here the elevation beam position was left at position 5 throughout, which was determined to be optimum at the initial bearing angles. The optimum elevation beam position is dependent upon the azimuthal angle as discussed previously in Section 3.3. Consequently, while elevation beam position 5 is best at certain azimuth angles, it is sub-optimum in the broadside direction when the elevation angle is 190. The dual-lobe behavior of Figure 6-9 is predictable from conic patterns for the phased array. Also, it is interesting to note S/I varies in a manner very similar to that of antenna gain.

### 6.2.3 PATCH ANTENNA

Test results obtained with the patch antenna from January 21, January 27, and March 27, 1975 are tabulated in Table 6-3. This data was measured on straight-line flight segments (or ground tests). Entries marked with an asterisk are without quad-helix gain calibration and should probably be suspected due to the abnormally low gain values. Gain is apparently greatest in the forward direction at higher elevation angles, a result predictable from its location.

*Table 6-3.-Patch Antenna Gain Data*

ATS 6 direction		C/N <sub>0</sub> (dB-Hz)		Received signal level (dBW)	Antenna gain (dB)
Relative bearing	Elev.	Real time meas'd	Computer analyzed		
(a) NAFEC Ground Test, January 21, 1975					
0°	40°	47.5	N/A	151.6	3.7
16°	40°	47.5	N/A	151.6	3.4
164°	40°	45.9	N/A	153.2	2.3*
(b) Flight Test, March 27, 1975					
180°	15°	40.0	39.0	160.1	-8.1*
156°	13°	39.0	—	160.1	-8.1*
24°	13°	47.4	47.0	152.1	0.0
352°	14°	47.5	46.1	153.1	-1.0
(c) Flight Test, January 27, 1975					
178°	15°	42.4	41.7	157.4	-5.1*

\* Indicates that direct gain calibration using quad-helix was not available. ATS-6 downlink calibration measurements made at other times and locations during the same test have been used.

A circular-path result obtained at 190° elevation angle is shown in Figure 6-10. Again the gain is largest in the over-the-nose direction, averaging about 2.5 dB. As bearing moves over the left wing and to the rear, the gain gradually diminishes to the -1 to -2 dB level. S/I is typically 10 to 15 dB, occasionally reaching 20 dB. Although antenna range patterns are not available for this antenna as installed, the peak gain figure seems reasonable given the element design and its intended broad coverage region.

**Gain Scale:** 2 dB per division, origin at -10 dB  
**S/I Scale:** 4 dB per division, origin at 0 dB

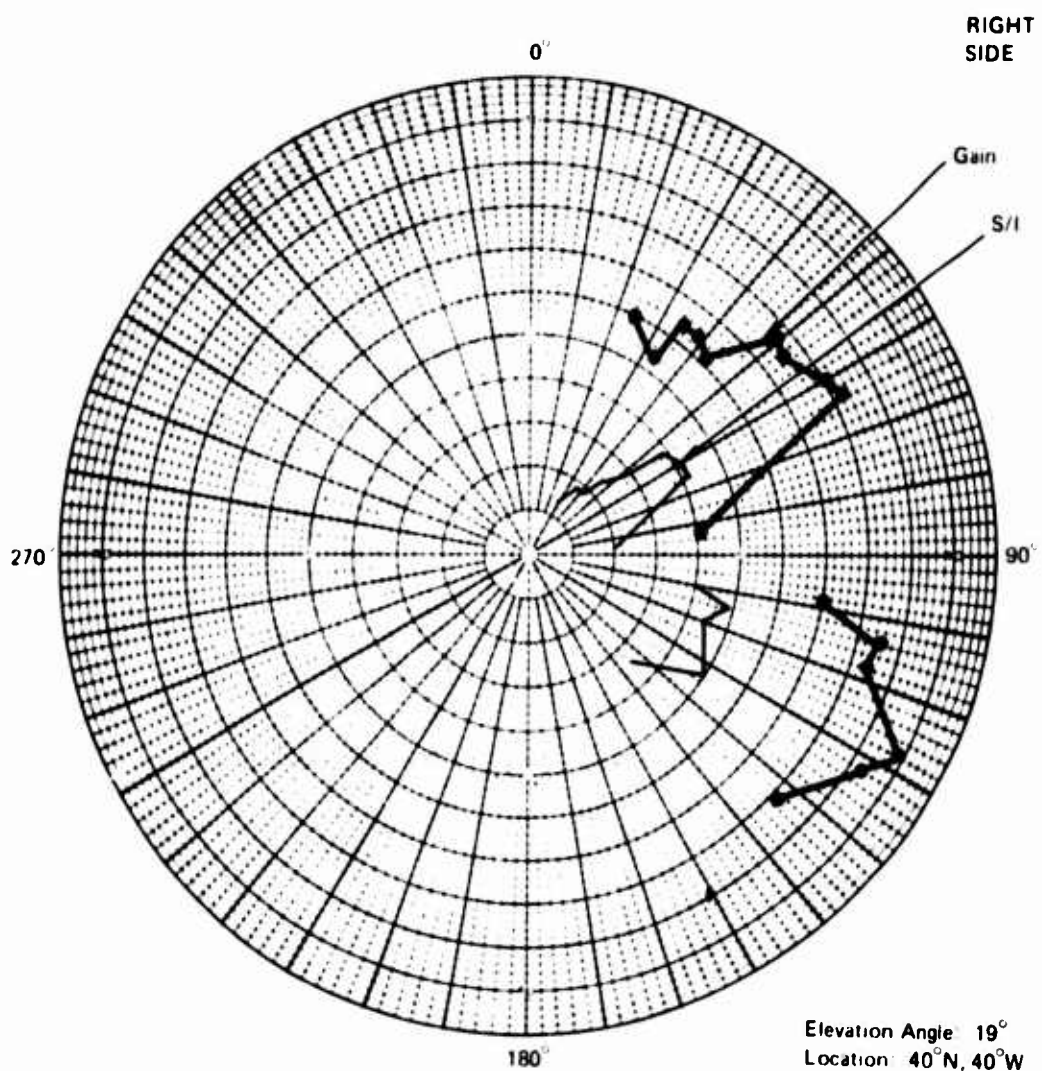


*Figure 6-9. Gain and S/I, Phased Array, November 21, 1974*

Gain Scale - 2 dB per division, origin at -18 dB  
S/I Scale - 4 dB per division, origin at 0 dB

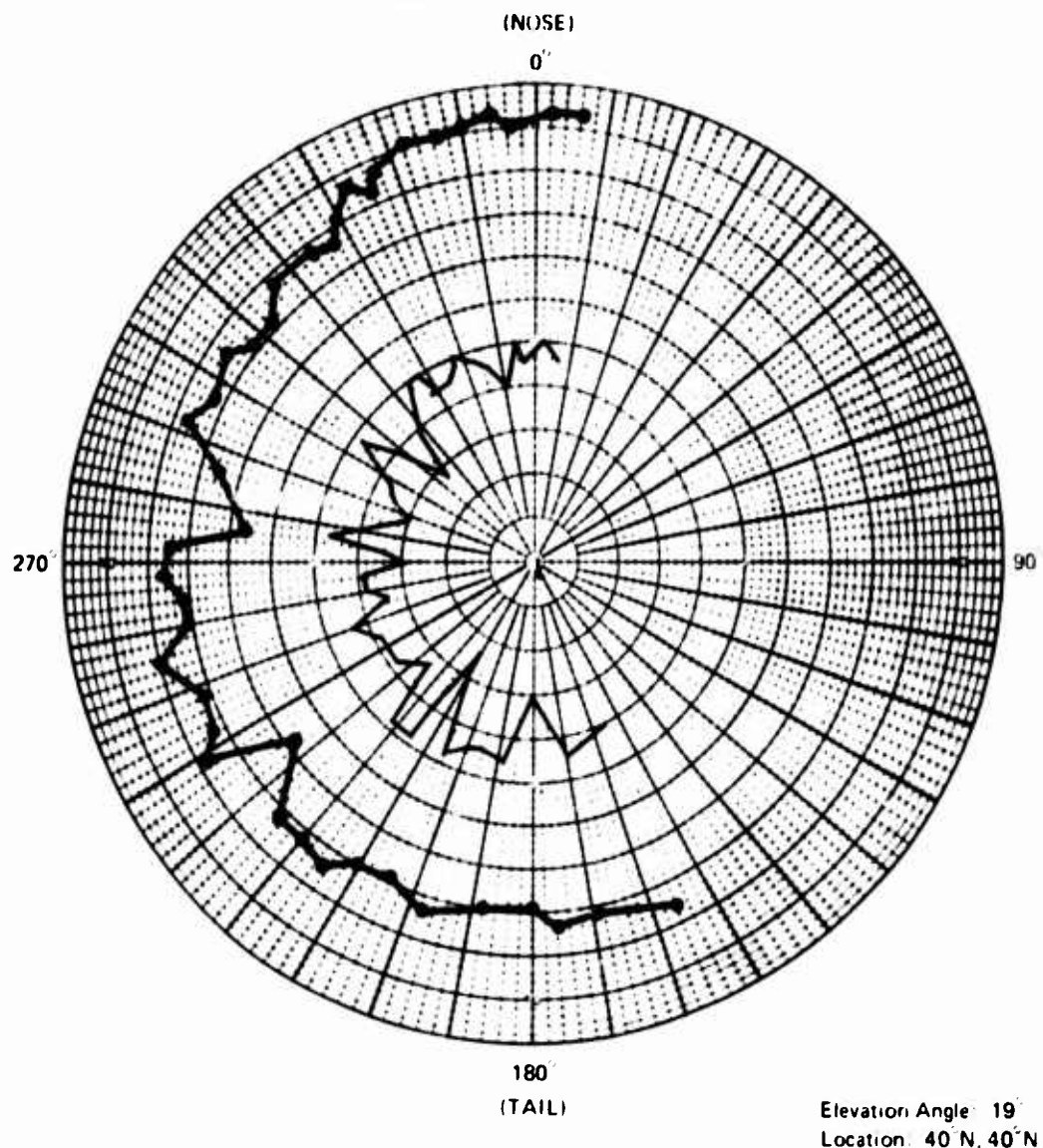


Figure 6-10. --Gain and S/I, Patch Antenna, November 21, 1974

#### **6.2.4 CROSSED-SLOT ANTENNA**

Two test results are presented in Figure 6-11 and 6-12 for the TSC crossed-slot antenna. The tests were conducted on March 25 and April 1, 1975, concurrently with the slot dipole antenna test. Both the antenna gain pattern and the computed S/I ratio are shown. The test results indicate that the antenna has roughly -6 dB gain and S/I of more than 10 dB. The antenna gain is about 6 dB below the expected value and is regarded as indicative of a probable antenna malfunction.

Due to its inherently broader pattern and fuselage location, the S/I values obtained are in general lower than for the slot dipole antennas or the phased array. The S/I for the crossed-slot attained the highest values in the forward direction and on both sides over the wings. For the counterclockwise flight path and postulated bank angles as discussed in Section 6.2.1, the shielding of the right wing would be increased and that for the left wing would be reduced for the April 1 test (Figure 6-11) and vice versa for the March 25 test (Figure 6-12). Multipath shielding in the forward direction would be provided by the fuselage. The observed S/I characteristics therefore appear to be in qualitative accord with expectations.

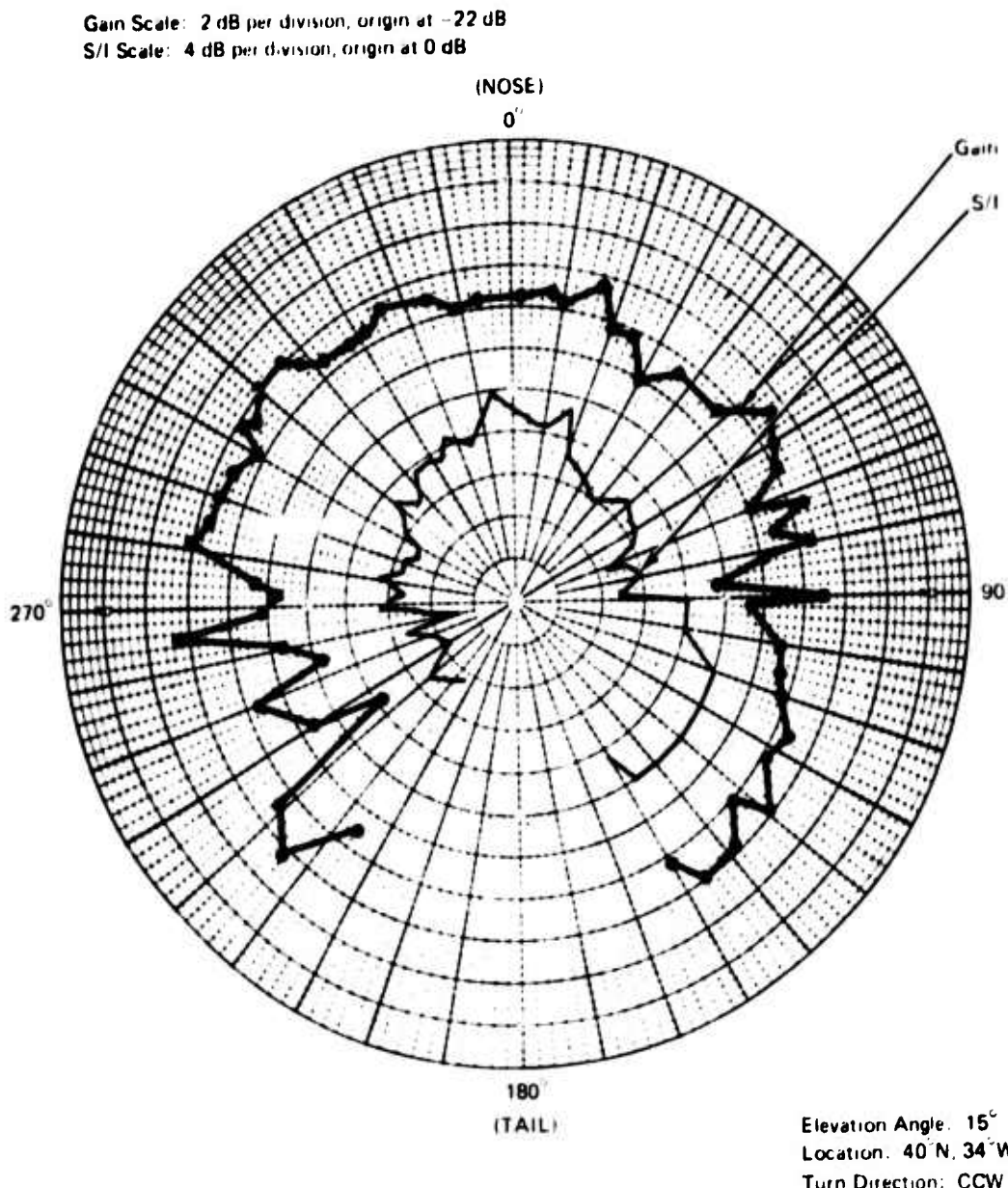
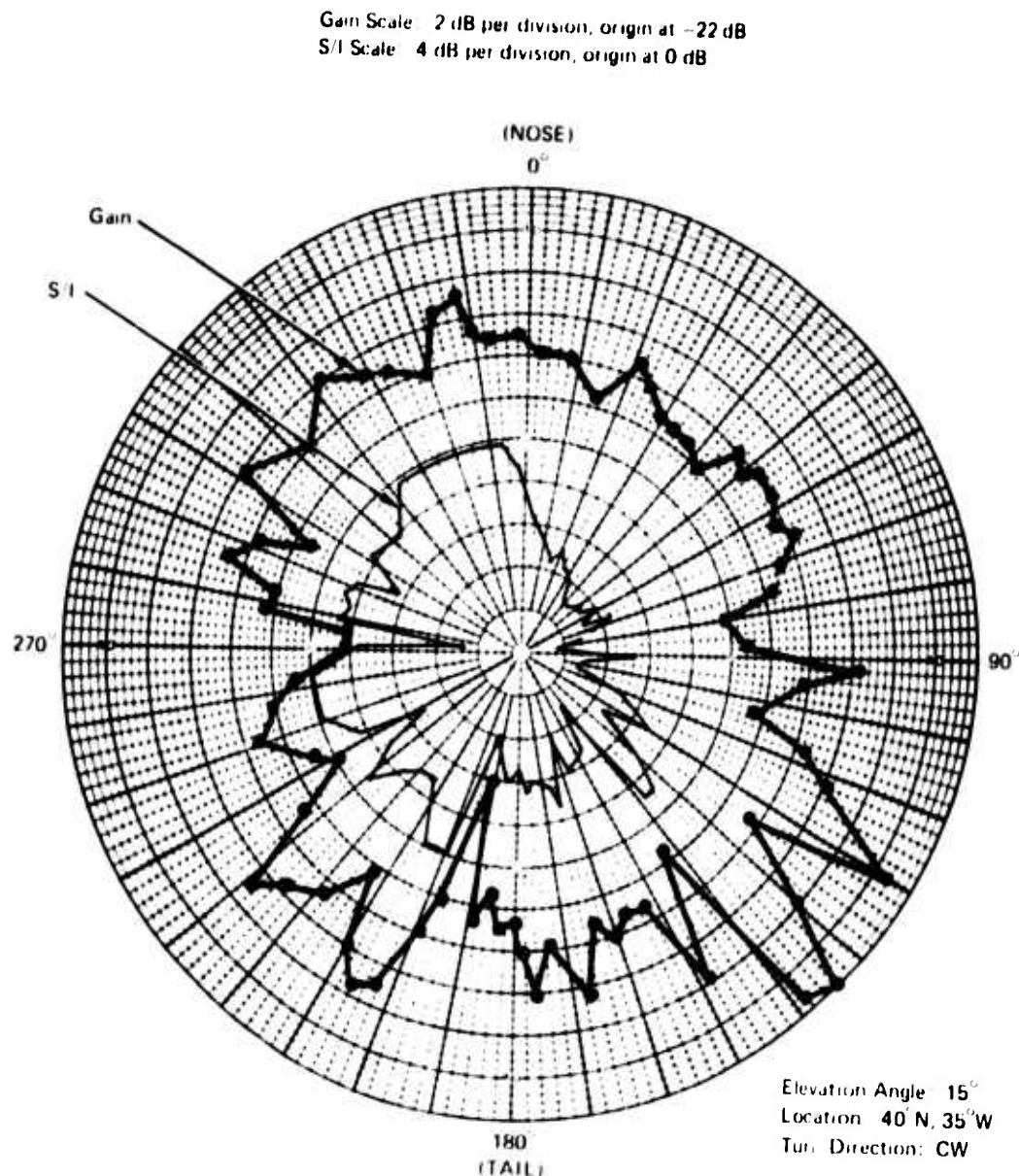


Figure 6-11. — Gain and S/I, Crossed Slot, April 1, 1975



*Figure 6 12. Gain and S/I, Crossed Slot, March 25, 1975*

## **REFERENCES**

- 2-1 Integrated Test Plan for ATS-F L-Band Experiment, NASA/GSFC Report No. TP-750-73-1, September 1973.**
- 2-2 Master ATS-6 Aeronautical Test Plan Document, Program Task II F(b), Contract DOT-TSC-707, The Boeing Company, July 19, 1974.**
- 2-3 R.E. Munson, "Conformal Microstrip Antennas and Microstrip Phased Arrays," IEEE Trans on Antennas and Propagation, January, 1974.**
- 2-4 G.G. Sanford, "Conformal Microstrip Phased Array for Aircraft Tests with ATS-6," Nat'l Electronics Conf., Chicago, Illinois, 1974.**
- 2-5 G.G. Sanford and L. Klein, "Development and Test of Conformal Microstrip Airborne Phased Array for use with the ATS-6 Satellite," IEE Conf on Antennas for Aircraft and Spacecraft, London, England, June, 1975.**
- 2-6 ATS-5 Multipath/Ranging/Digital Data L-Band Experimental Program, Contract FA69WA-2109, Boeing Document D6-60177, April 1973.**
- 2-7 Olsson, T. and Stapleton, B.P., "L-Band Orthogonal-Mode Crossed-Slot Antenna and VHF Crossed-Loop Antenna," Contract DOT-TSC-130, August 1972.**
- 3-1 Task I - Development of Test Equipment Configuration, Interim Technical Report, Contract DOT-TSC-707, November 5, 1973.**
- 3-2 Task IV - Data Reduction and Analysis Plan, Contract DOT-TSC-707, February 25, 1974.**
- 4-1 P.A. Bello, "Aeronautical Channel Characterization," IEEE Trans. on Comm., Vol. COM-21, No. 5, May 1973.**
- 4-2 H. Staras, "Rough Surface Scattering on a Communication Link," Radio Science, Vol. 3 (new series), No. 6, 1968.**
- 4-3 ATS-5 Multipath/Ranging/Digital Data L-Band Experimental Program, Phase V - Multipath/Ranging Analysis and Results, Contract FA69WA-2109, FAA Report FAA-RD-73-57-V, Boeing Document D6-60181.**
- 4-4 P. Beckman and A. Spizzichino, *The Scattering of Electromagnetic Waves From Rough Surfaces*, Macmillian Co., New York, 1963.**
- 4-5 A.J. Mallincrodt, "Propagation Errors," in *Satellite Based Navigation Traffic Control and Communications to Mobile Terminals*, unpublished short course notes, October 1969.**

## **REFERENCES (Continued)**

- 4-6 C. Cox and W. Munk, Slopes of the Sea Surface Deduced from Photographs of Sun Glitter, University of California Press, Berkley and Los Angeles, 1956.**
- 4-7 W.H. Peake, Satellite to Aircraft Multipath Signals Over the Ocean, Final Report 3266-2, Ohio State University Electro-Science Laboratory, May 1974.**
- 4-8 U.S. Aeronautical L-Band Satellite Technology Test Program – Results of 1974 Fall Test Series, Contract DOT-TSC-707, Interim Technical Report, December 1, 1974.**
- 5-1 P. Milner and J.S. Golab, "Intelligibility of Voice Transmissions through a Satellite Relay System," The 89th Meeting of the Acoustical Society of America, University of Texas, April 1975.**
- 5-2 U.S. Aeronautical L-Band Satellite Test Program – DR&A Software Description, Contract DOT-TSC-707, Interim Technical Report, April 1, 1975.**
- 5-3 ATS-5 Multipath/Ranging/Digital Data L-Band Experimental Program – Phase IVD, Volume 1: Satellite/Aircraft L-Band Data Communication Tests – Appendix C, Contract FA69WA-2109, The Boeing Company, April 1973.**
- 5-4 J.C. Blair, "A Comparative Study of Coherent Phase Shift Keying and Noncoherent Frequency Shift Keying in a Multipath Environment," Ph.D. dissertation, University of Pennsylvania, 1969.**
- 5-5 J.C. Blair and J.F. Balcewicz, "Results of an Experimental Study of Coherent PSK in a Multipath Environment," EASCON '68 Record, pp. 607-614.**
- 5-6 J.J. Jones, "Multichannel FSK and DPSK Reception with Three-Component Multipath," IEEE Trans. on Communication Technology, December 1968, pp. 808-821.**
- 5-7 P.A. Bello and B.D. Nellin, "The Influence of Fading Spectrum on the Binary Error Probabilities of Incoherent and Differentially Coherent Matched Filter Receivers," IRE Trans. on Communications Systems, June 1962, pp. 160-168.**
- 5-8 L.A. Frasco and H.D. Goldfein, "Signal Design for Aeronautical Channels," IEEE Trans. on Communications, May 1973, pp. 534-547.**

## **REPORT OF INVENTIONS APPENDIX**

**A diligent review of the work performed under this contract has revealed no new innovation,  
discovery, improvement, or invention.**